

## ABSTRACT

Title of Dissertation: **NEW MESSENGERS & NEW PHYSICS:  
A SURVEY OF THE HIGH-ENERGY UNIVERSE**

Milena Crnogorčević  
Doctor of Philosophy, 2023

Dissertation Directed by: Prof. Massimo Ricotti  
Department of Astronomy, University of Maryland

Studying the origins of the high-energy emission in the Universe can profoundly affect our fundamental understanding of the cosmic origin and its evolution at the most extreme scales. In this dissertation, I explore the high-energy observations of different astrophysical systems to inform our understanding of the theoretical frameworks used to describe them. I harness the current multimessenger infrastructure to investigate questions ranging from new physics and transient astronomy to compact objects and extended emission in the gamma-ray, gravitational-wave, and neutrino skies.

The focus in the first part of this dissertation is on utilizing the *Fermi* Large Area Telescope (LAT) low-energy (LLE) technique to search for the light axion-like-particle (ALP) within the MeV gamma-ray emission of long gamma-ray bursts (GRBs). We perform a data-driven sensitivity analysis to determine distances for which detection of an ALP signal is possible with the LLE technique, which, in contrast to the standard LAT analysis, allows for a larger effective area for energies down to 30 MeV. Assuming an ALP mass  $m_a \lesssim 10^{-10}$  eV and ALP-photon coupling

$g_{a\gamma} = 5.3 \times 10^{-12}$  GeV $^{-1}$ , we find that the distance limit ranges from  $\sim 0.5$  to  $\sim 10$  Mpc. We demonstrate that the sensitivity of the LLE technique to detecting light ALPs is comparable to the standard LAT analysis, making it an excellent complementary—yet independent—way to search for ALPs with *Fermi*.

Next, we select a candidate sample of twenty-four GRBs and conduct a model comparison analysis in which we consider different GRB spectral models with and without an ALP signal component. We find that including an ALP contribution does not result in any statistically significant improvement of the fits to the data. Motivated by the delay between the ALP emission time and the time of the jet break-out associated with its ordinary long-GRB emission, we conduct a novel search for ALPs within time windows that *precede* the main-episode gamma-ray emission of a long GRB, focusing on the sample of sources with known precursor emission detected with LAT and LLE. We report no statistically significant detection of ALPs within the GRB precursor emission and discuss the parts of the ALP parameter space probed with this method.

Multimessenger astronomy is at the heart of the remainder of this dissertation. First, I present a follow-up search for excess emission of X-rays with the *Swift* Burst Alert Telescope (*Swift*-BAT) and that of gamma rays with the *Fermi* Gamma-ray Burst Monitor (*Fermi*-GBM), in spatial and temporal correspondence to gravitational-wave events reported by the LIGO/Virgo/Kagra (LVK) Collaboration. In collaboration with the *Fermi*-GBM Team, we combine the observations from these two instruments to determine whether there is any statistically significant excess emission around the given gravitational-wave trigger. We report no new joint detections but present the joint flux upper limits.

Finally, I present the results of the cross-correlation studies between the unresolved *Fermi*-LAT gamma-ray and the IceCube neutrino skies. We report no positive cross-correlation in the

real-data sky maps. We then combine simulation and observation techniques to place upper limits on the fraction of neutrinos produced in proton-proton or proton- $\gamma$  interactions that occur in blazars. Assuming all gamma rays from unresolved blazars are produced from neutral pions via proton-proton interactions, we find that—for energies above 10 GeV—up to 60% of the unresolved blazar population may contribute to the diffuse neutrino background (the fraction is 30% for proton- $\gamma$  interactions). We also include predictions for the improved sensitivity considering 20 years of IceCube data.

**NEW MESSENGERS & NEW PHYSICS: A SURVEY OF THE  
HIGH-ENERGY UNIVERSE**

by

Milena Crnogorčević

Dissertation submitted to the Faculty of the Graduate School of the  
University of Maryland, College Park in partial fulfillment  
of the requirements for the degree of  
Doctor of Philosophy  
2023

**Advisory Committee:**

Professor Massimo Ricotti, Chair  
Dr. Regina Caputo, Advisor  
Professor Cole Miller, Committee Member  
Dr. Christopher Karwin, External Examiner  
Professor Peter Shawhan, Dean's Representative

© Copyright by  
**Milena Crnogorčević**  
2023

## Preface

All work presented in this dissertation is either published or under a journal or collaborations review. The research in Chapter 3 is published in Physical Review D as “Searching for Axion-Like Particles from Core-Collapse Supernovae with *Fermi*-LAT’s Low Energy Technique” [1]. The work in Chapter 4 is funded through the *Fermi* Guest Investigator Program Cycle 15 (P.I. Milena Crnogorčević) and is currently undergoing the *Fermi*-LAT Collaboration review. This work has been presented in multiple conferences and meetings, including the *Fermi*-LAT Collaboration Meeting and the 241st AAS Meeting in Seattle, WA. Chapter 5 is currently undergoing the review of three collaborations involved in the paper (*Fermi*-GBM, *Swift*-BAT, and LVK), and will be submitted to the Astrophysical Journal shortly as “A Joint *Fermi*-GBM and *Swift*-BAT Analysis of Gravitational-Wave Events from the Third Gravitational-wave Observing Run”. Although this work will contain many authors and members of different collaborations, I was entirely in charge of the *Swift*-BAT side of the analysis. I also collaborated with the *Fermi* and LVK teams to combine the results. Alongside Dr. Joshua Wood and Dr. Corrine Fletcher, I am a corresponding author on this paper. The work summarized in Chapter 5 has been presented multiple times, including the APS April Meeting 2022, the 241st AAS Meeting, and the HEAD meeting 2023. Finally, Chapter 6 is published in the Astrophysical Journal as “A Cross-correlation Study between IceCube Neutrino Events and the *Fermi* Unresolved Gamma-ray Sky” [2]. I am the second author of this paper and I have significantly contributed to the *Fermi*-LAT data preparation, development and testing of the cross-correlation analysis pipeline, and the in-

terpretation of results. Each chapter is presented here with minor modifications from published or submitted versions.

*Let me keep my distance, always, from those  
who think they have the answers.*

— “Mysteries, Yes,” Mary Oliver

## Dedication

To all the curious kids  
with a fire in their belly  
and a tremble in their voice

## Acknowledgments

My graduate school experience is a story of many ups, but also many downs. In the past six years, I crossed paths with some of the most inspiring and caring people, perfected FaceTiming different time zones, mastered thinking in different languages, and grew intellectually and emotionally to reach places I thought impossible when I started. At the same time, the world seemed to crumble daily, and sometimes I crumbled with it too. I am immensely grateful to everyone who cheered for me through the good times, and held me high through the not-so-good ones: it is never lost on me that it takes a village, and I am forever grateful for mine.

To my advisor, Regina Caputo: thank you for your immense patience, understanding, guidance, and support throughout the past years. It has been an absolute honor to be your graduate student. You have advocated for me and provided everything I needed to succeed, and this thesis would not have been possible without you. To many more years of collaboration and friendship!

To my on-campus advisor, Massimo Ricotti: very few people care about their students as much as you do, and I am immensely grateful I got to be one of them. Thank you for trusting my abilities more than I do—in astronomy, volleyball, and Italian. I am a more confident astronomer and person thanks to you.

To my thesis committee: Cole Miller, thank you for providing me with invaluable feedback on my science and presentation skills. I have learned so much from you—about astronomy, volleyball, work-life balancing, and so many things in between. Chris Reynolds, you may have

escaped to the other side of the pond for my defense—nevertheless, I am so grateful for your scientific insights and incredibly kind words of encouragement and support. Thank you for introducing me to Julia—it has been such a joy to have a fellow graduate student with whom I could share my research interests. To Peter Shawhan and Chris Karwin: thank you for taking the time to read my thesis and be a member of my dissertation committee.

To my co-advisor, Manuel Meyer: you have been an invaluable and continuous source of support and guidance in the last few years. Thank you for taking a chance on me and for sharing your expertise. The future of ALPs is bright, and I am excited about our ongoing collaboration.

To my Goddard research group—Carolyn Kierans, Michela Negro, Henrike Fleischhack, Zac Metzler, Kavic Kumar, Sam Wasti, and Amanda Steinhebel; and friends and collaborators—Alyson Joens, Liz Hays, Judy Racusin, Brad Cenko, Julie McEnery, Sylvia Zhu (now at DESY), and Amy Lien (now at UTampa)—I am immensely grateful for you and your support. Thanks to my *Fermi*-LAT collaborators Nicola Omodei, Michael Gustafsson, Eric Charles, Miguel Sánchez-Conde, Mattia DiMauro, and many more for all the support throughout my time in the *Fermi* Collaboration. To the *Swifties*<sup>1</sup>, Aaron Tohuvavohu and Jimmy DeLaunay, thank you for stepping in when I needed help. To Ke Fang and Michael Larson—thank you. To Josh Wood, Cori Fletcher, Rachel Hamburg, and Peter Veres, I loved every moment of working with you. Josh Wood, one day I hope to be half the mentor you have been to me.

My immense gratitude to my friend and mentor, Michela Negro—the world is too small for your kindness, dedication, curiosity, and expertise: you are my role model, and I cannot wait to see what the future of discovery holds for you. Eric Burns, I cherish your friendship and mentorship—and you are funny sometimes, too. John Beacom, thank you for everything.

---

<sup>1</sup>I am so sorry.

Becca, Teal, Ben, Erica, Joe, Vicente, Alex, Pradip, Zeeve, Dana, Weizhe, Serena, Jordan, Gabe, Carrie, Isiah, Rye, and the rest of my fellow graduate students: every single one of you has made my experience at UMD brighter. To my cohort, you are all rock stars. Laura, thank you for bringing so much joy (and burek) into my life. It takes a special kind of human to be my officemate: Julian, thank you for your nerves of steel and that McFlurry last year. Tomás, keep shining your shiny shine. Ramsey, you are the kindest and most thoughtful person I know—thank you for overthinking things with me. Harrison, I cherish our friendship immensely (but that may change soon if you keep posting IG stories from the French coast). To Geoff and Igor—your kindness and passion for learning know no bounds, and I am so grateful I got to witness it firsthand. Ibrahim, I am in constant awe of you as a person and a physicist (you may be searching for dark matter in the wrong place, though). Julia, I cannot wait to write a paper with you.

To my GRAD-MAP co-conspirators, Andrew and Charlotte, I cannot say enough thanks. I could not have asked for kinder and more committed co-leads: keep shining bright wherever you are. Andrew, Charlotte, Amitava, Katya, Arjun, and Rob—it is one of the biggest privileges of my graduate student experience to call you friends and colleagues. I am so excited to see where our paths cross again in the future. To all the BANG! and ACE members and friends: thank you for making our department a better place. To my beloved *Fermi* Mentoring Program co-organizers Deirdre, Giovanna, Melissa, Michela, Matthew, Cori, Michelle, Janeth, Judy, Rania, and my fellow UWC-er Daniel: I am so grateful for you.

Stuart, everything I write here seems too insignificant to reflect how much gratitude I hold for you and your support throughout the last six years: it is largely thanks to you that I reached this point in my graduate career. Thank you for everything. To Derek and Tad: we may not have interacted very closely during my time in graduate school, but I would be remiss if I did

not mention your names. Thank you for setting the example for all of us with your presence and commitment to improving the systemic injustices in our field—I can only hope we all follow you in this endeavour.

My life as a graduate student at the Astronomy Department would not have been possible without the continuous help and support from the UMD Astronomy Staff—thank you all, and especially those with whom I worked most closely: Susan Lehr, John Cullinan, Olivia Dent, Barbara Hansborough, Dorinda Kimbrell, Lauren Miles, and Natalie Rowe.

To my adopted family, Terrapin Masters Swimming: thank you for being such an extraordinary group of people and teaching me that swimming is a team sport. You are my rock inside and outside the pool. Mollie and Jeff, thank you for welcoming me with open arms into the team and your home—you are one of the kindest people I know. Courtney and Jon, I am so grateful and honored to witness you and your strength, thoughtfulness, and commitment. Laura and Brett, thank you for taking care of me—your favorite third wheel loves you to bits. Marion, you bring so much love, sunshine, ABBA, and happiness into my life—you are my partner in crime (and wine). Ethan, thank you for staying behind to help me with my starts, but even more so—thank you for being such a caring and kind human. Jose, thank you for being a fantastic teammate and friend—I cherish your encouragement and the best WhatsApp stickers (and yet, I still may take a breath under the flags or swim my 50s at a 200 pace). Mitchell, Blake, Marlena, Andy, Zac, Noah, Santiago, Miranda, Teddy, Kim, et al.—I appreciate you all so much. Thank you for being the loudest cheerers and the most loving and supportive teammates I could imagine.

To my friends across the globe and DMV: Ivana, Milja, Nikolina, Matias, Umisha, Adara, Erica, Jiya, Gabbie, Paul, Monica, Henry, Emma, Jing, Ilaria, Winston, Miloš, Nathan, and others, I cherish you and our friendship, always. Thank you to Coach Clayton’s swim club and

especially to Connor, Wentao, Lilian, and Matt—you made my last year of graduate school so much more bearable. To my Middlebury professors—especially Eilat Glikman, Noah Graham, and Anne Goodsell—I would not be here if it were not for you.

To Martin Naunov: I am proud to call you my bestest friend and my forever person. With all my mastery of languages, I cannot put into words how much love, appreciation, and respect I hold for you. My journey through graduate school (and the last 12 years) would not have been possible without your unwavering support and love. To many more years of learning and growing together!

Miljanićima, Magovčevićima i Žugićima—hvala vam na vašoj podršci. Hvala na svemu mojoj najdražoj novskoj ekipi, rodicama Sonji i Tanji. Mom čudu od kume i prijateljice, Elviri. Mojim najdražim kumovima Bosnićima, Ivanovićima, Cvetkovićima, Ćukovićima i Kovačevićima: hvala vam.

Sada, mojim Crnogorčevićima: ova disertacija je rezultat koliko mog truda toliko i vašeg odricanja. Mom bratu, Nikoli—iako mi pada teško to da priznam, u većini slučajeva si u pravu. Hvala ti na neizmjernoj podršci, uvijek iskrenim i dobronamjernim savjetima i beskonačnoj ljubavi i vjeri u moje sposobnosti. Mojim roditeljima, Stevu i Saji—ovaj svijet je mali za svu vašu ljudskost i dobrotu. Vaša podrška i vjera u moje odluke me uvijek gura naprijed: koliko god ste vi ponosni što sam vam ja čerka, toliko ponosa ja nosim u sebi što vas zovem roditeljima. Mojoj voljenoj babi Mileni: nisam stigla da ti kažem zbogom, ali znaj da tvoje ime s ponosom nosim svuda<sup>2</sup>.

---

<sup>2</sup>trans. To Miljanićs, Magovčevićs, and Žugićs—thank you for your support. Thanks to my dearest hometown team, my cousins Sonja and Tanja, for everything. To my wonder-godsister and friend, Elvira. To my beloved godparents Bosnićs, Ivanovićs, Cvetkovićs, Ćukovićs, and Kovačevićs—thank you.

Now, to my family, my Crnogorčevićs: this dissertation is the result of as much of my effort as it is of your sacrifice. To my brother, Nikola—although it is hard for me to admit, you are right most of the time. Thank you for your immense support, honest and compassionate advice, and endless love and confidence in my abilities. To my

I express my acknowledgments and gratitude to the original stewards of the dispossessed locations I inhabited to conduct the work done in this dissertation, including but not limited to the Nacotchtank, Piscataway, Monacan, Occaneechi, Munsee Lenape, Chickasaw, Cherokee, Shawnee, S'atsoyaha, Tamien, Ohlone, Ramaytush, Muwekma, Peoria, Myaamia, Ho-Chunk, Kiikaapoi, Kaskaskia, Duwamish, Suquamish, Snoqualmie, Muckleshoot, Stillaguamish, Anishinabewaki, Wendake-Nionwentsio, Mississauga, Cayuse, Umatilla and Walla Walla people in states and regions now known as Maryland, Washington D. C., Virginia, New York, Alabama, California, Illinois, Wisconsin, Ohio, Washington, and Ontario<sup>3</sup>.

Last but not least, in my dissertation, through their quoted words, I acknowledge scientists, friends, and artists who have—in one way or another—shaped my graduate school experience.

This dissertation is a tribute to you *all*.

Thank you.

---

parents, Stevo and Saja—this world is too small for all of your kindness and virtue. Your unwavering support and trust in my decisions are my constant motivation, and I am just as proud to call you my parents as you are to call me your daughter. To my beloved grandma, Milena: I did not get a chance to say goodbye, but know that I proudly carry your name with me everywhere.

<sup>3</sup><https://native-land.ca/>

## Table of Contents

Preface	ii
Foreword	iv
Dedication	v
Acknowledgements	vi
Table of Contents	xii
List of Tables	xv
List of Figures	xvi
List of Abbreviations	xviii
Chapter 1: Introduction	1
1.1 New physics . . . . .	4
1.2 New messengers . . . . .	6
1.3 Observatories . . . . .	8
1.3.1 The <i>Fermi</i> Observatory . . . . .	9
1.3.2 The Neil Gehrels Swift Observatory ( <i>Swift</i> ) . . . . .	14
1.3.3 LIGO/Virgo/KAGRA . . . . .	15
1.3.4 IceCube . . . . .	17
1.4 This Dissertation . . . . .	18
Chapter 2: Theoretical Foundations: The Curious Case of an Axion	20
2.1 QCD & the story of $\phi$ . . . . .	21
2.2 Axions to the rescue . . . . .	25
2.3 What about ALPs? . . . . .	26
2.3.1 ALP as dark matter . . . . .	27
2.4 Constraining the light ALP properties . . . . .	29
Chapter 3: Searching for ALPs from CCSNe with <i>Fermi</i> LLE Technique	34
3.1 Introduction . . . . .	35
3.2 ALP model . . . . .	38
3.2.1 Conversion Probability . . . . .	40

3.2.2	ALP Model in <i>XSPEC</i>	42
3.3	Data Selection	43
3.3.1	<i>Fermi</i> observatory	43
3.3.2	Time-tagging of a core collapse	44
3.3.3	GRB Selection Criteria	46
3.4	Sensitivity Analysis	47
3.4.1	Background Considerations	49
3.4.2	Simulating the ALP spectrum	51
3.4.3	Sensitivity results	51
3.5	Search for an ALP signal within the selected GRB sample	57
3.5.1	Data Preparation	58
3.5.2	<i>XSPEC</i> analysis	59
3.5.3	ALPs from GRBs: fitting results	60
3.6	Conclusions and Discussion	61
 Chapter 4: Light at the end of the tunnel: ALPs and GRB precursors		67
4.1	Motivation	68
4.2	The life of a GRB	69
4.3	Data Selection	71
4.4	Analysis	72
4.4.1	Bayesian Blocks	73
4.4.2	The ThreeML GRB Analysis	75
4.5	Results	80
4.5.1	LLE GRBs	80
4.5.2	LAT GRBs	83
4.6	Discussion	85
 Chapter 5: A Joint <i>Fermi</i> -GBM and <i>Swift</i> -BAT Analysis of Gravitational-Wave Events from the Third Gravitational-wave Observing Run		89
5.1	Method	92
5.1.1	Gravitational-wave Trigger Selection	93
5.1.2	<i>Fermi</i> -GBM Search Methods	95
5.1.3	<i>Swift</i> -BAT Rates Data Search	97
5.1.4	Combined & Marginal Flux Upper Limits	101
5.1.5	Isotropic-Equivalent Luminosity Upper Limits	101
5.2	Results	102
5.3	Discussion	103
5.3.1	Possible NS in the System	105
5.3.2	Probable BBH Systems	107
5.3.3	Marginal Events	113
5.4	Summary and Future Directions	114
 Chapter 6: A Cross-correlation Study between IceCube Neutrino Events and the <i>Fermi</i> - LAT Unresolved Gamma-ray Sky		118

6.1	An ab-initio introduction to the cross-correlation technique . . . . .	121
6.2	$\nu \times \gamma$ skies . . . . .	123
6.2.1	Data Selection . . . . .	126
6.2.2	Real data maps . . . . .	127
6.2.3	Masking . . . . .	129
6.3	Simulations . . . . .	131
6.3.1	Unresolved blazar population . . . . .	132
6.3.2	Simulated IceCube neutrino maps . . . . .	136
6.3.3	Simulated LAT UGRB maps . . . . .	138
6.4	Results . . . . .	139
6.5	Conclusions . . . . .	147
Chapter 7: Conclusions		150
Chapter 8: What about exoplanets?		155
Chapter A: Appendices for Chapter 3		163
A.1	GRB Models . . . . .	163
Chapter B: Appendices for Chapter 4		165
B.1	Additional plots: LLE precursors . . . . .	165
Chapter C: Appendices for Chapter 5		172
C.1	Flux Upper Limits for BBH Events . . . . .	172
C.2	Isotropic luminosity upper limits . . . . .	190
C.3	Marginal events . . . . .	190
Chapter D: Appendices for Chapter 6		194
D.1	IceCube PSF and CAPS correction . . . . .	194
D.2	Additional plots . . . . .	196
Chapter E: Facilities and Software used in this Dissertation		200
E.1	Facilities . . . . .	200
E.2	Software . . . . .	200

## List of Tables

3.1	Selection criteria applied to GRBs detected by <i>Fermi</i> -LAT between August 2008 to August 2018 . . . . .	47
3.2	24 GRBs that pass the selection criteria . . . . .	48
3.3	Maximum distance to the ALP source to be within reach of the <i>Fermi</i> -LLE sensitivity . . . . .	57
4.1	GRB Precursor selection criteria . . . . .	72
4.2	LLE GRBs with an identified precursor emission . . . . .	82
4.3	LAT GRBs with an identified precursor emission . . . . .	86
5.1	GW events from O3 with $p_{\text{astro}} > 0.5$ . . . . .	94
5.2	Marginal GW events from O3 . . . . .	95
5.3	GRB spectral templates . . . . .	97
5.4	Flux upper-limits for events with a possible NS component . . . . .	108
5.5	Flux upper limits for probable BBH events in O3 . . . . .	112
5.5	(continued) . . . . .	113
5.6	Flux upper limits for marginal GW events in O3 . . . . .	115
6.1	Results of the cross-correlation of real IceCube and <i>Fermi</i> -LAT maps . . . . .	143
6.2	Summary of the sensitivity results . . . . .	145
C.1	0.95 percentile fluxes from different models of BBH emission. . . . .	187
C.1	(continued) . . . . .	188
C.1	(continued) . . . . .	189
C.2	Isotropic-equivalent luminosity upper limits for candidates with a NS component	190
C.3	Isotropic-equivalent luminosity upper limits for BBH events from O3 . . . . .	191

## List of Figures

1.1	Gamma-ray sky maps as seen with the OSO-3 and <i>Fermi</i> -LAT	3
1.2	The <i>Fermi</i> Observatory	10
1.3	<i>Fermi</i> -LAT performance plots	12
1.4	The <i>Swift</i> Observatory and its BAT instrument	15
1.5	Michelson interferometer schematic and LIGO GW detectors	16
1.6	The Ice Cube Neutrino Observatory	18
2.1	The Feynman diagrams demonstrating the ALP-photon oscillations	29
2.2	Constraints on the ALP mass-coupling parameter space	30
3.1	ALP production in a CCSN and its trajectory to the Milky Way	36
3.2	Temporal and energy evolution of ALP-induced CCSNe	38
3.3	ALP-induced CCSNe' gamma-ray spectrum	40
3.4	ALP-photon conversion probability as a function of source position in the sky	42
3.5	Background fluences plotted against the incidence angles to the detector	50
3.6	<i>XSPEC fakeit</i> ALP simulations	52
3.7	Wilks' Theorem as applied to the injected signal sample	55
3.8	Distance limits for a LAT-LLE ALP detection	56
3.9	GRB 101123A $\gamma$ -ray flux with two different overlaid models, with and without ALP component	62
4.1	Conversion map for the GRBs with precursors	77
4.2	Integrated ALP spectrum	78
4.3	$40\text{-M}_\odot$ progenitor ALP-induced emission	79
4.4	GRB 221009A through the ALP lens	84
4.5	GRB 100724B Bayesian Blocks LAT standard analysis	85
5.1	Mass classification of systems with a possible NS component in O3	105
5.2	$5\sigma$ flux upper-limit for events with a possible NS component	109
5.2	(continued)	110
5.3	$5\sigma$ $L_{\text{iso}}$ upper-limits for events with a possible NS component	111
5.4	$5\sigma$ upper-limits as a function of sky position for GW200105\_162426	116
6.1	<i>Fermi</i> -LAT and IceCube all-sky maps	131
6.2	IceCube sensitivity to astrophysical neutrinos	132
6.3	UGRB anisotropy simulation cross-checks	135
6.4	Trials histograms for the four <i>Fermi</i> -LAT energy bins	142
6.5	Expected sensitivity to neutrino signal from p-p interaction and future prediction	144

6.6 Contribution of the unresolved blazars to the astrophysical neutrino flux . . . . .	147
8.1 Expected gamma-ray flux from ALPs produced in a GW170817-like BNS merger	157
8.2 ALP production in BNS mergers and detection scheme . . . . .	158
8.3 ALP parameter space: BNS mergers . . . . .	160
B.1 Identified LLE precursors . . . . .	166
B.1 (continued) . . . . .	167
B.1 (continued) . . . . .	168
B.1 (continued) . . . . .	169
B.1 (continued) . . . . .	170
B.1 (continued) . . . . .	171
C.1 $3\sigma$ flux upper-limit for BBH events in O3 . . . . .	173
C.1 (continued) . . . . .	174
C.1 (continued) . . . . .	175
C.1 (continued) . . . . .	176
C.1 (continued) . . . . .	177
C.1 (continued) . . . . .	178
C.1 (continued) . . . . .	179
C.2 $5\sigma$ flux upper-limit for BBH events in O3 . . . . .	180
C.2 (continued) . . . . .	181
C.2 (continued) . . . . .	182
C.2 (continued) . . . . .	183
C.2 (continued) . . . . .	184
C.2 (continued) . . . . .	185
C.2 (continued) . . . . .	186
C.3 The $3\sigma$ flux upper-limit sky maps for the 6 marginal events . . . . .	192
C.4 The $5\sigma$ flux upper-limit sky maps for the 6 marginal events . . . . .	193
D.1 IceCube PSF analysis results . . . . .	195
D.2 Variation of IceCube sensitivity in the Northern hemisphere for different astrophysical neutrino spectral models . . . . .	196
D.3 IceCube sensitivity as a function of the energy for the Northern hemisphere . .	197
D.4 CAPS for the real <i>Fermi</i> -LAT and IceCube maps . . . . .	198
D.5 Simulated <i>Fermi</i> -LAT UGRB maps . . . . .	199

## List of Abbreviations

1FLE	1st <i>Fermi</i> -LAT low-energy catalog
2LAC	2nd LAT AGN catalog
4FGL	4th <i>Fermi</i> -LAT source catalog
ABRACADABRA	A Broadband/Resonant Approach to Cosmic Axion Detection with an Amplifying B-field Ring Apparatus
ACD	Anticoincidence detector
AGN	Active galactic nucleus
ALP	Axion-like particle
APS	Angular power spectrum
BGO	Bismuth Germanate Oxide (detector)
BH	Black hole
BBH	Binary black hole
BNS	Binary neutron star
BSM	Beyond Standard Model
CAL	Electromagnetic hadoscopic calorimeter
CAPS	Cross-correlation angular power spectrum
CAST	CERN Axion Solar Telescope
CCSN	Core-collapse supernova
CERN	European Organization for Nuclear Research
C.L.	Confidence level
CMB	Cosmic microwave background
CR	Cosmic ray
CP	Charge-parity
CTTE	Continous time-tagged event
CZT	Cadmium Zinc Telluride (detector)
DM	Dark matter
DOM	Digital optical module
DRM	Detector Response Matrices
EBL	Extragalactic background light

EM	Electromagnetism/electromagnetic
FAR	False alarm rate
FoV	Field of view
GBM	Gamma-ray Burst Monitor
GCN	Gamma-ray Coordinates Network
GRB	Gamma-ray burst
GUANO	Gamma-ray Urgent Archiver for Novel Opportunities
GW	Gravitational wave
GWTC	Gravitational-wave Trigger Catalog
HEA	High-energy astrophysics
IC	IceCube
IRF	Instrument response function
KAGRA	Kamioka Gravitational-wave Detector
KSVZ	Kim-Shifman-Vainshtein-Zakharov (theory)
LAT	Large Area Telescope
LIGO	Laser Interferometer Gravitational-Wave Observatory
LLE	LAT Low Energy (technique)
LVK	LIGO/Virgo/KAGRA
MBTA	Multi-Band Template Analysis
MMA	Multimessenger astronomy
NaI	Sodium Iodide (detector)
NITRATES	Non-Imaging Transient Reconstruction And TEmporal Search
NS	Neutron star
NSBH	Neutron star-black hole
PMT	Photomultiplier tube
PSF	Point-spread function
PQ	Peccei-Quinn (theory)
SAA	South Atlantic Anomaly
SHAFT	Search for Halo Axions with Ferromagnetic Toroids
SM	Standard Model

SNR	Signal-to-noise ratio
SSD	Silicon-strip detector
SwiMM	<i>Swift</i> Mass Model
TKR	Tracker/converter
UGRB	Unresolved gamma-ray background
QCD	Quantum chromodynamics
QED	Quantum electrodynamics
QFT	Quantum field theory
WISP	Weakly-interacting sub-eV particle
WIMP	Weakly-interacting massive particle

## Chapter 1: Introduction

*They say the first sentence in any speech is always the hardest. Well, that one's behind me, anyway.*

---

Wislawa Szymborska

High-energy astrophysics (HEA) studies some of the most extreme and mysterious phenomena in the Universe. This field is often referred to as the study of nature-made particle accelerators, featuring physical processes at the most extreme energies that we are unable to reproduce in laboratories on Earth. These astrophysical environments accelerate particles to energies billions to trillions of times greater than that emitted each second from the Sun. As such, the HEA physical systems provide unique conditions to explore and test our understanding of the fundamental principles that govern the creation and evolution of the Universe.

Arguably, the first recorded observation of a high-energy astrophysical event dates back to 4500 BCE, when Indian astronomers observed and noted one of the earliest known supernovae, HB9 [3]. Despite centuries of human interest in observing such extraordinarily bright events, the term HEA—and the field itself—solidified only in the second half of the 20th century, guided by necessary advancements in detector technology. The field of HEA began to take shape in the 1910s, when an Austrian astrophysicist, Victor Hess, measured that the ionization levels in Earth’s atmosphere increased with altitude. The only explanation for such observation,

he thought, was that the outer atmospheric layers had to be excited by high-energy radiation originating outside Earth, i.e., from the cosmos—introducing the concept of “cosmic rays” [4]. Indeed, he was right (as confirmed by the Physics Nobel Prize Committee in 1936.) The discovery of cosmic rays (CRs) is regarded as a pivotal moment that initiated the advancement of HEA.

A few decades passed until the technological advancements took full swing: with the development of new technologies, such as X- and gamma-ray detectors and high-altitude balloons, the field of HEA swiftly became more prominent. The 1960s and 1970s saw significant progress in HEA, with the detection of X- and gamma-ray emission from various astrophysical sources and the launch of dedicated space telescopes. The first cosmic gamma-ray detection was made by Explorer-XI in 1961, detecting photons with energies exceeding 50 MeV. The Explorer-XI’s  $\sim$ 150 hours of observations provided the first all-sky image in gamma rays. This led to an interesting realization: the observed brightness of the gamma-ray sky was significantly higher than that predicted by theory, necessitating additional gamma-ray producing mechanisms that would explain it. In addition to gamma rays produced in interactions of CRs with the interstellar medium, which was believed to be the dominant mechanism of gamma-ray production, other mechanisms were proposed—in particular, the interaction of high-energy CRs with the surrounding medium via inverse Compton scattering and bremmstrahlung emission [5]. The all-sky gamma-ray map observed with the Explorer-XI’s successor—the Orbiting Solar Observatory (OSO-3)—featuring data collected in the late 1960s is shown in Fig. 1.1. An all-sky map from the currently-operating gamma-ray *Fermi* Observatory is also shown for comparison.

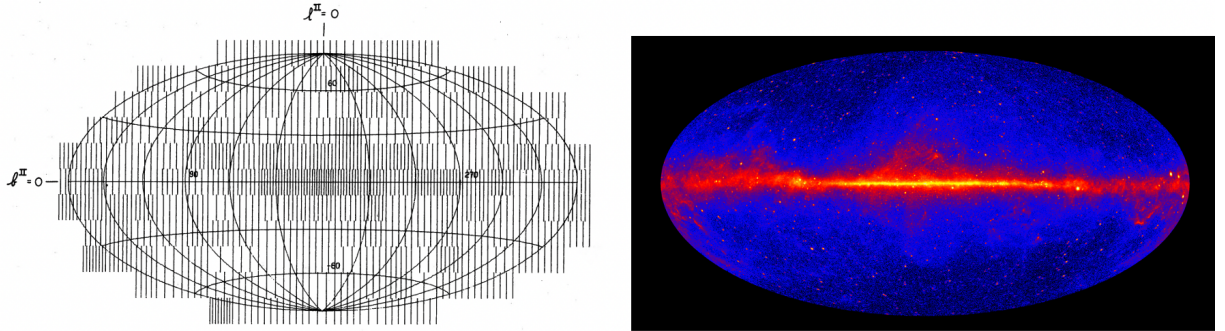


Figure 1.1: *Left:* OSO-3 gamma-ray map adapted from [6]. The density of lines indicates the number of gamma-ray photons per solid angle, with obvious clustering towards the central plane of the Milky Way. *Right:* The *Fermi* Observatory gamma-ray sky (gamma-ray sources shown in red hues.) In addition to the prominent Milky Way plane, a number of bright point sources—mostly coming from distant active galaxies—also pop up, showing the improvement in angular and energy resolution between two instruments [7]. *Credit:* NASA/DOE/*Fermi*-LAT Collaboration.

In 1963, the identification of X-ray emission originating from the Crab Nebula marked a significant milestone in the field of HEA [8]. This X-ray emission, originating from synchrotron processes of fast-moving electrons within the strong magnetic field of a rapidly rotating neutron star (NS) within the Crab Nebula, penetrated through dust and gas that obscure the visible wavelengths and, *for the first time*, gave us a glimpse into a whole new landscape of the previously hidden X-ray Universe. Soon after, in 1968, the Crab Nebula was also identified as the brightest source in the gamma-ray sky [9].

The 1970s and 1980s came to the scene with even more sensitive X- and gamma-ray instruments. The Uhuru satellite mapped the first all-sky X-ray emission, observing previously-unknown X-ray sources, such as X-ray binaries, active galactic nuclei (AGNs), and supernova remnants [10]. In 1967, the Vela satellites detected a series of gamma-ray bursts (GRBs), the origin of which remained a mystery until the 1990s [11]. A plethora of new sources came with the launch of the Einstein and Compton Gamma Ray observatories, shedding light on the physics

of the most extreme environments of NSs and black holes (BHs). Later on, the detection of 24 (!) neutrinos in a little over 13 seconds by three different neutrino detectors (Kamiokande II in Japan, Irvine-Michigan-Brookhaven in the US, and Baksan in then Soviet Union) from the supernova explosion SN1987A was yet another significant accomplishment for HEA, confirming some aspects of the theoretical models of supernova explosions, as well as providing important information about the properties of neutrinos [12–14].

The field of HEA nowadays spans decades in photon energies—from keV to hundreds of TeV—thus relying on several different detection technologies. Such a wide range in energy is comparable to the span of the remainder of astronomy (radio to UV). Even within a single high-energy observation of an event, we may simultaneously see many physical phenomena. The endeavor to characterize such systems is exciting but challenging: one of the most difficult tasks is disentangling different physical processes and finding the culprit responsible for the observed high-energy signature. Often, such investigations lie at the heart of observational HEA research. Or, at least, these questions are central to my thesis work:

*How can we use high-energy observations of astrophysical systems to inform our understanding of the theoretical frameworks we use to describe them? Conversely, can we identify and address the limitations of our theoretical models in describing the observations?*

It is my turn to try.

## 1.1 New physics

The 19th century was regarded as the era of “nothing left to learn in physics”. Newton’s theory of gravity and Maxwell’s equations of electromagnetism governed the interactions of mat-

ter via gravitational and electromagnetic forces. This notion of “nothing left to learn” was shaken by the development of “new physics,” which, at the time, entailed the formalization of the quantum theory by Planck, Einstein, and Bohr [15–17]. In the 1930s, Hideki Yukawa postulated the existence of a meson—a strong force mediator [18], and Enrico Fermi challenged the notion of fundamental particles by invoking the existence of the weak interaction to explain the beta decay of atomic nuclei [19]. The 1950s and 1960s were exhilarating years in experimental physics: physicists conducted many experiments where they smashed particles into each other and learned that we lived in a “particle zoo,” i.e., that there were, in fact, many more fundamental particles than we had previously thought. By the 1970s, physicists developed their version of the periodic table of elements: the Standard Model (SM) of particle physics [20–24].

The theoretical framework of the SM—Quantum Field Theory (QFT)—describes interactions between twelve matter particles (fermions) and six force-carrying particles (bosons) through three fundamental forces: electromagnetic, weak, and strong. Carrying the title of one of the most complete scientific theories, the SM is extraordinarily successful in describing and predicting the behavior of fundamental particles. However, the “nothing left to learn in physics” era that followed the establishment of the SM was short-lived. Despite its outstanding success, a few cracks surfaced from the SM: in particular, its inability to incorporate the theory of general relativity into the framework, describe the nature of dark matter (DM) and dark energy, explain non-zero neutrino masses we observe, or interpret the matter-antimatter asymmetry in the Universe. Some experimental results also may lack SM explanations: for example, the observed mass of the  $W$  boson (weak force mediator) disagrees with the SM prediction at a  $7\sigma$  level [25], while the observed dipole moment of the muon with a disagreement of a  $4.2\sigma$  [26]. Despite the difficulties involved in making these measurements and calculations, they nonetheless cast

doubts on the completeness of the SM. Some other considerations are more nuanced and may only be considered discrepancies in some cases; for example, the strong CP problem that arises in quantum-chromodynamics (QCD) [27].

The strong CP problem is related to a phenomenon known as charge-parity (CP) violation. One of the predictions of the SM is that the strong force should violate CP symmetry, resulting, under certain conditions, in particles and antiparticles behaving differently. However, empirical evidence suggests that this violation is much smaller than predicted by the SM, suggesting that there may be some additional physical mechanisms at play that offset the expected level of CP violation. One of the solutions, the Peccei-Quinn theory, introduces a new scalar field that interacts with the strong force—giving rise to a new particle, the *axion*. The CP problem and the axion solution is presented in detail in Chapter 2. The search for new physics (and axions) is an ongoing effort.

The physical processes occurring inside extreme environments of NSs, BHs, AGNs, blazars, collapsing or merging stars, and other high-energy systems, provide ideal places to search for the still unknown and new physics. Many new-physics models leave distinctive signatures at the highest energies. As a result, using high-energy observations is an excellent way to explore new physics and can yield valuable insights into our most fundamental understanding of the inner workings of the Universe.

## 1.2 New messengers

To understand and truthfully characterize an observation of an astrophysical event, it is in our best interest to look at the system through multiple lenses. Consider the following scenario:

let us assume we detect a very bright gamma-ray flash localized to a point in the sky, lasting  $\sim$ one second. The question arises: what information can we deduce with certainty based solely on such observation? Without having observed many similar events prior to the one in question, the answer is: not much. We may check our observation against some theoretical framework—but we have to keep in mind that our observations often inform our theoretical models. As such, very rarely will our observations *perfectly* match the theory the first time around<sup>1</sup>. Now, let us assume that we also observe this event using, e.g., a radio, optical, infrared, or an X-ray instrument. These complementary observations show us that different physical processes may be responsible for their corresponding observed signatures. For example, a time delay between gamma-rays and X-rays in our example may indicate that the process that caused the gamma-ray emission came before the subsequent X-ray-producing mechanism. Electromagnetic (EM) radiation, from radio to gamma rays, is an information carrier—a messenger. If we also consider other types of messengers, such as gravitational waves (GWs) or neutrinos, we may gain a more complete understanding of the system in question, eventually allowing us to unequivocally claim that what we observed is, in fact, a binary neutron star (BNS) merger. Such is the story of the famous GW170817/GRB 170817A coincident detection [31, 32].

Of course, our observatory resources are limited, and not every bright gamma-ray flash will merit the extraordinary extent of follow-up observations, as was the case for GW170817/GRB 170817A. Nevertheless, the current multimessenger astronomy (MMA) efforts, including the most sensitive GW and neutrino detectors to date and a multitude of follow-up observatories, provide an unprecedented opportunity to expand our understanding of classical physics of the

---

<sup>1</sup>The angular power spectrum of the Cosmic Microwave Background (CMB) may be one of the very few exceptions [28–30].

HEA events and, in turn, help us put constraints on (or discover!) the new physics that may be taking place in these systems.

Long-term efforts in developing new multimessenger observation techniques, in combination with recent coincident detections of EM radiation with GWs (GW170817, [31]) or neutrinos (TXS 0506+056, [33]), resulted in MMA being prominently featured in the Decadal Survey on Astronomy and Astrophysics 2020 [34]. In addition to furthering our understanding of rapid, powerful events in the Universe, MMA also provides an outstanding venue to explore new physics that would otherwise be inaccessible through laboratory experiments or single-messenger astronomical observations. With time, as we increase the sample sizes of observed physical systems and learn more about their unique properties, the multimessenger approach may become superfluous—however, at this time, MMA is undoubtedly one of the most powerful tools to study the nature of astrophysical events in the Universe.

With that in mind, in my thesis, I focus on the following question:

*How can the abundance of data from various instruments and messengers help us characterize the physical properties of the systems in question, in turn allowing us to establish the most stringent limits on classical and new physics?*

### 1.3 Observatories

Hopefully, I have convinced the reader<sup>2</sup> that multi-wavelength and multimessenger efforts provide extensive insights for HEA. Let me now take a moment to introduce and acknowledge the outstanding work of numerous instrumentation teams who designed, built, and are cur-

---

<sup>2</sup>and, if not, please refer to [34] again.

rently operating the instruments used in this thesis. Here, I provide a top-level overview of the observatories and their detectors used in my thesis. Data from the *Fermi* Observatory are used in Chapters 3, 4, 5, and 6, with a special emphasis on the Large Area Telescope (LAT). The Neil Gehrels *Swift* Observatory is featured in Ch. 5, together with the Laser Interferometer Gravitational-Wave Observatory (LIGO), the *Virgo* Observatory, and the Kamioka Gravitational Wave Detector (KAGRA). The IceCube Neutrino Observatory is highlighted in Ch. 6.

### 1.3.1 The *Fermi* Observatory

The *Fermi Gamma-ray Space Telescope* was launched into low-Earth orbit on June 11, 2008. It observes the entire gamma-ray sky every three hours, covering energies from 8 keV to more than 300 GeV. Its scientific goals range from studying the origin of diffuse emission, understanding the origin of CRs, characterizing the environments of supermassive black holes, to time-domain astronomy, including studies of GRBs, solar flares, and magnetars. *Fermi*'s gamma-ray observations of the transient sky, dwarf spheroidal galaxies, and the Galactic Center have provided some of the most stringent limits on the new physics and the particle properties of dark matter [1, 35–37]. The *Fermi* Observatory contains two instruments on board, the Gamma-ray Burst Monitor (GBM, [38]) and the Large Area Telescope (LAT, [39]).

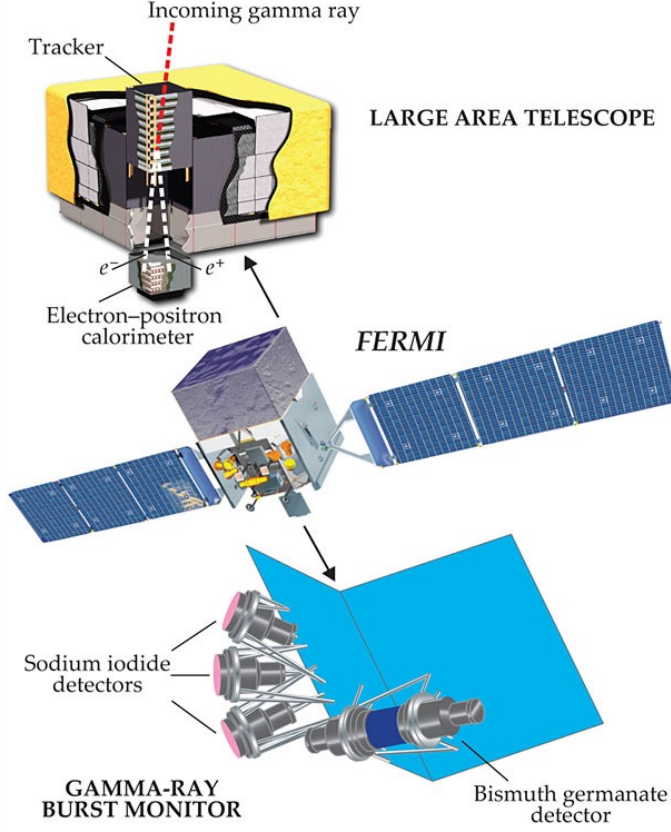


Figure 1.2: The *Fermi* Observatory. Shown are its two instruments onboard, LAT and GBM, with their respective subsystems [38, 39]. Image adapted from [40].

- The LAT is a pair-conversion<sup>3</sup> telescope optimized for gamma-ray observations within the 100 MeV to 300 GeV energy range; however, its sensitivity also allows for a photon detection at energies down to 20 MeV and up to a few TeV. It is composed of three different detector types. A silicon-strip tracker (TKR) provides a dense medium for gamma rays to convert into an  $e^+e^-$  pair. The electron-positron pairs deposit energy in silicon-strip detectors (SSD). Then, the TKR determines the direction of the incoming gamma ray by measuring the trajectory of the electron-positron pair. Without losing much of their original energy in the ionization process within the TKR, the electron-positron pair reaches the much denser calorimeter (CAL). This results in an electromagnetic shower, allowing the CAL to estimate the original gamma-ray photon energy.

---

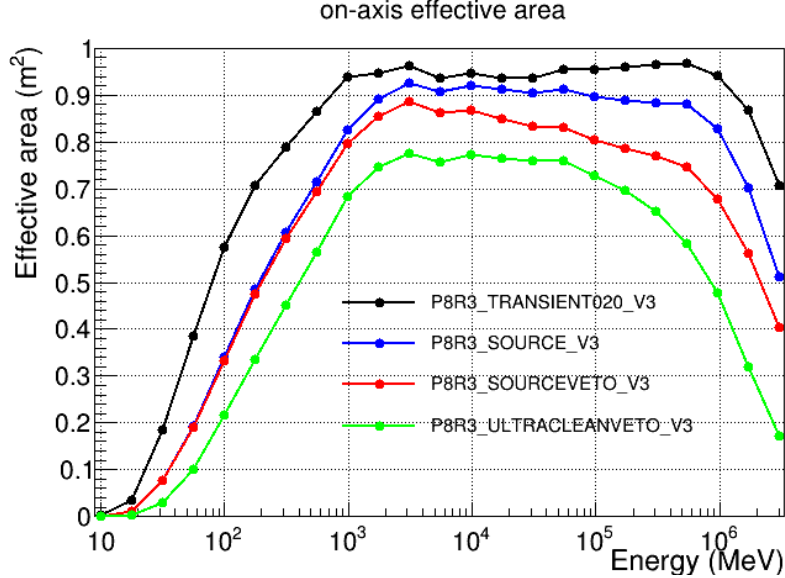
<sup>3</sup> $p + \gamma \rightarrow p + e^+ + e^-$

The third detector type is an anticoincidence detector (ACD) which discriminates between the neutrally-charged gamma-ray photons and charged CRs. The LAT instrument is a  $4 \times 4$  array of CAL+TKR towers encompassed within the ACD's plastic scintillator tiles. The diagram of the LAT instrument onboard *Fermi* is shown in Fig. 1.2.

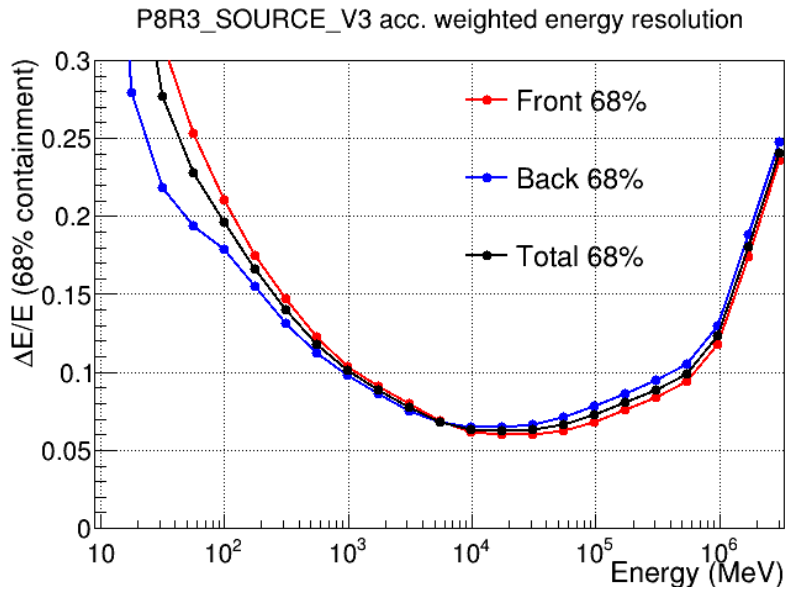
The LAT's effective area,  $A_{\text{eff}}$ , can be expressed as a function of the incoming particle's energy ( $E$ ) and direction ( $\theta, \phi$ ):

$$A_{\text{eff}}(E, \theta, \phi) = A_{\text{geo}}(E, \theta, \phi)P_{\text{conv}}(E, \theta, \phi)\mathcal{E}_{\text{det}}(E, \theta, \phi)\mathcal{E}_{\text{rec}}(E, \theta, \phi), \quad (1.1)$$

where  $A_{\text{geo}}(E, \theta, \phi)$  is the active particle collecting area,  $P_{\text{conv}}(E, \theta, \phi)$  is the conversion probability,  $\mathcal{E}_{\text{det}}(E, \theta, \phi)$  is the detection efficiency of the instrument, and  $\mathcal{E}_{\text{rec}}(E, \theta, \phi)$  is the efficiency of the event reconstruction and background rejection algorithm. As detailed in Chapters 3 and 4, adjusting the background rejection algorithm requirements can result in an increase of the effective area, in turn increasing the number of signal counts (but also the number of background counts). The LAT's  $A_{\text{eff}}$  as a function of energy for an on-axis source is shown in Fig. 1.3.



(a) LAT's effective area.



(b) LAT's energy resolution.

Figure 1.3: *Fermi*-LAT performance plots. *Top*: LAT's effective area as a function of energy for normal incidence photons for different event classification schemes provided by the LAT team. *Bottom*: Acceptance-weighted LAT's energy resolution as a function of energy. Different lines represent different Instrument Response Functions (IRFs), which describe the instrument's performance as a function of multiple parameters including the photon energy, incidence angle, where within the tracker the photon conversion happens, etc. These plots are adapted from the *Fermi*-LAT's performance webpage<sup>4</sup>.

<sup>4</sup>[https://www.slac.stanford.edu/exp/glast/groups/canda/lat\\_Performance.htm](https://www.slac.stanford.edu/exp/glast/groups/canda/lat_Performance.htm), as accessed on March 12, 2023.

Then, the LAT's field of view (FoV) can be expressed in terms of the effective area as

$$\text{FoV} = \frac{\int_{\Omega} A_{\text{eff}}(\Omega) d\Omega}{A_{\text{peak}}}, \quad (1.2)$$

where  $A_{\text{eff}}(\Omega) = A_{\text{eff}}(\theta, \phi)$ ,  $d\Omega = \sin(\theta)d\theta d\phi$ , and  $A_{\text{peak}}$  is the peak effective area at a given energy. The quoted value for the LAT's FoV for the optimal energy coverage is  $\sim 2.4$  sr.

The energy resolution of LAT is 10% at 1 GeV, with a minimum of  $\sim 6\%$  at 10 GeV (Fig. 1.3).

Finally, its spatial 68% confidence-level containment of a 1-GeV photon is  $\sim 1^\circ$ , and can go down to  $\sim 0.2^\circ$  for photons with energies above 10 GeV.

- **GBM.** The GBM is the second instrument onboard *Fermi* whose primary purpose is to observe the temporal and energy evolution of the prompt emission of GRBs. It contains twelve sodium-iodide (NaI) and two bismuth-germanate (BGO) scintillation detectors, covering 8 keV to 1 MeV and 150 keV to 40 MeV in energy, respectively. The NaI detectors are circular disks with a diameter of 12.7 cm and a thickness of 1.27 cm. Each NaI detector is optically coupled to its respective photomultiplier tube (PMT), which generates an electric signal in response to the scintillating light that falls onto the detector. While of the same diameter, the BGO detectors are 12.7 cm thick and are attached to a PMT on both sides of the crystal, resulting in more collected photons. The detectors are arranged so that seven of them (one BGO and six NaI detectors) are placed on each side of the instrument, as shown in Fig. 1.2, ensuring the best sky coverage. The GBM's FoV is  $\sim 9.5$  sr, and the point-source localization accuracy is  $\sim 5^\circ$  [38].

### 1.3.2 The Neil Gehrels Swift Observatory (*Swift*)

The Neil Gehrels Swift Observatory, hereafter referred to as *Swift*, is a space-based observatory launched in November 2004. It consists of three scientific instruments: the X-ray telescope (XRT), the Ultraviolet/Optical Telescope (UVOT), and the Burst Alert Telescope (BAT) [41–43]. We focus on the BAT instrument, as it is the only one used in this thesis.

The BAT is a coded-aperture, large FoV (2.2 sr at >10%; 1.5 sr at >50%; and 0.5 sr >90% coding fraction), hard X-ray instrument on-board *Swift*. The BAT’s coded-aperture technique utilizes a patterned mask to collect light, allowing for a reconstruction of images without the need for traditional focusing optics. Different coding fractions correspond to different sections of the detector plane used to conduct an observation (e.g., a coding fraction of >10% corresponds to <90% of detector area used). BAT’s detector plane contains 32,768 Cadmium-Zinc-Telluride (CZT) detector elements under a coded aperture mask and a graded-Z fringe shield that helps lower the background rate. The coded mask is D-shaped and is composed of around 54,000  $5 \times 5 \times 1$  mm lead tiles with a completely random 50% open-50% closed pattern. The BAT instrument monitors large portions of the sky with the goal of detecting occurrences of transient GRBs, covering the energy range from 15 keV to 350 keV. Once triggered, the BAT can localize a GRB to 1–3 arcmin accuracy, prompting the *Swift* spacecraft to slew and point its two narrow-field instruments—XRT and UVOT—for follow-up observations. The BAT’s localization accuracy is quantified by the instrument’s partial coding fraction, i.e., the fraction of detectors exposed to an event at a given time and sky position. If the coding fraction for a given trigger is 0%, then BAT cannot localize the event. The BAT averages  $\sim$ 90 GRB on-board triggers per year, among which  $\sim$ 10% are short in duration. The diagram depicting the *Swift* Observatory and the BAT

instrument is shown in Fig. 1.4

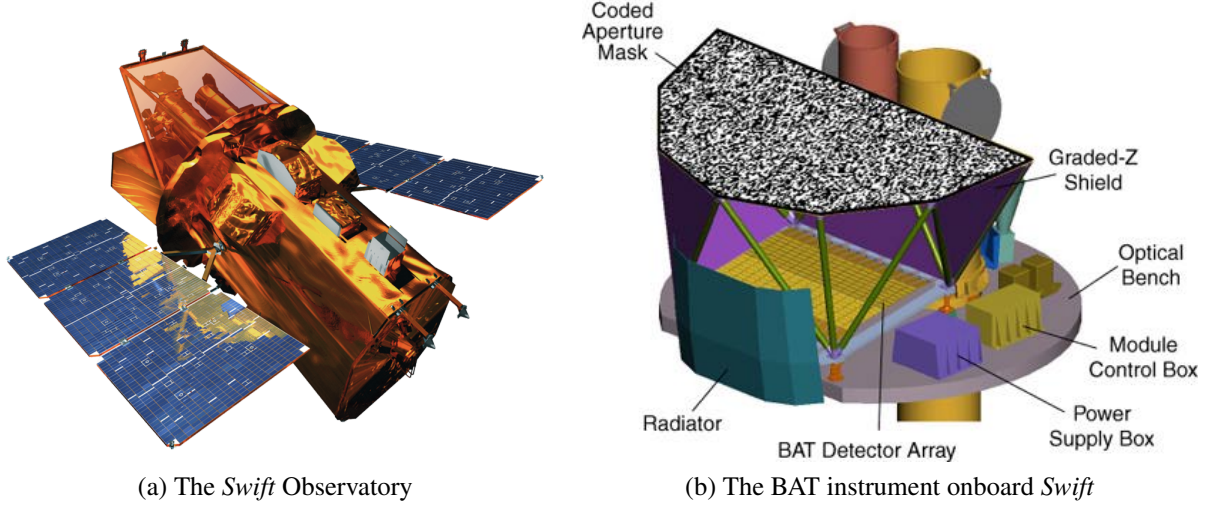


Figure 1.4: *Left:* The Neil Gehrels Swift Observatory with three instruments onboard: UVOT, XRT, and BAT, has been observing GRBs since 2004. *Right:* BAT instrument onboard *Swift* and its subsystems. BAT is a sensitive, large FoV, coded-aperture X-ray instrument. These diagrams are adapted from the *Swift* NASA webpage<sup>5</sup>.

### 1.3.3 LIGO/Virgo/KAGRA

LIGO, Virgo, and KAGRA are laser-interferometric GW detectors designed to measure ever-so-slight changes in the position of test masses (mirrors) [44–46]. The detectors are Michelson interferometers with arm lengths of a few kilometers. A GW passing through these interferometers will cause the arms to stretch and compress, changing their length. The instruments use controlled laser beams sent down the arm paths to measure such changes. These beams reflect from mirrors at the end of each arm and then recombine again at the beam splitter. The measured change in fractional difference—strain  $h$ —between the armlengths  $L_1 \simeq L_2 = L$  is expressed as  $h = (L_1 - L_2)/L$ . Imprinted within the strain are two GW polarizations, the relative orientation of the detector and the incoming GW, and the GW frequencies, providing us with the informa-

---

<sup>5</sup>[https://swift.gsfc.nasa.gov/about\\_swift/](https://swift.gsfc.nasa.gov/about_swift/), as accessed on March 28, 2023.

tion needed to study the source of the GW detected [47]. Figure 1.5 shows the schematic of a Michelson interferometer on the left, and two LIGO detectors in Livingston and Hanford on the right.

The era of Advanced LIGO and Advanced Virgo started as a result of various instrument upgrades between different observing runs (hereafter denoted as  $Ox$ , where  $x \subset 1, 2, 3$ ), including the improvements of the main laser source, mitigation of technical noises, and upgrades of core optics [45, 48]. The Advanced LIGO consists of two 4-km armlengths enhanced Michelson interferometers located in the United States (Hanford, Washington and Livingston, Louisiana). On the other hand, the Advanced Virgo is a single-site, 3-km armlength detector in Cascina, Italy.

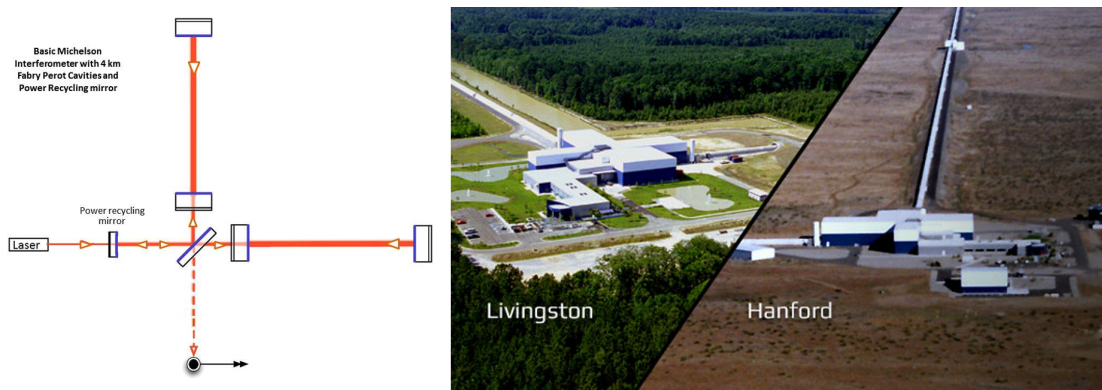


Figure 1.5: *Left:* Michelson interferometer schematic. A light beam from a laser source is split into two at the beam splitter and sent down two paths along the arms. The light is then reflected off mirrors, and recombined to produce an interference signature. The armlength change caused by a GW is encoded within this interference pattern. *Right:* The LIGO detectors in Livingston, LA, and Hanford, WA. The diagram and the photo are adapted from the LIGO webpage<sup>6</sup>.

KAGRA is a 3-km armlength underground detector in Gifu Prefecture, Japan, and has been operating since April 2020 [46]. The median localization volume for the last observing run, O3, is estimated to be  $10^5$  Mpc $^3$  for binary neutron star (BNS) mergers,  $10^6$  Mpc $^3$  for neutron star-black hole (NSBH) mergers, and  $10^7$  Mpc $^3$  for binary black hole (BBH) mergers, with an

---

<sup>6</sup><https://www.ligo.caltech.edu/>, as accessed on March 28, 2023.

improvement of a factor of two for the upcoming O4 run [49].

### 1.3.4 IceCube

The IceCube Neutrino Observatory (hereafter referred to as IceCube) is a large-scale neutrino detector located at the South Pole [50]. IceCube has been collecting data since 2008, with the building stage completed in 2011. It is designed to detect neutrinos of all flavors over an energy range spanning more than seven orders of magnitude, from 10 GeV to more than 1 EeV.

The array of 5,160 digital optical modules (DOMs) is embedded within a cubic kilometer of ice beneath the Antarctic surface, reaching depths of almost 2.5 km. The DOMs are put together into 86 vertical cables—so-called strings—arranged in a hexagonal grid at a distance of 125 m from each other. Eight of the strings near the center are arranged more densely, allowing for lower-energy measurements and a study of neutrino oscillations. The surface component of the IceCube Observatory, i.e., the IceTop, contains 81 stations, each placed atop an IceCube string. Each station contains two water tanks with downward facing PMTs, which serve for vetoing and calibrating the events, as well as detecting cosmic rays (although with a very small FoV of  $\sim 3\%$  of the sky). Figure 1.6 shows the layout of the IceCube Observatory.

IceCube’s experimental foci are two-fold: it studies the 1) high-energy neutrinos (TeV–PeV) produced in violent astrophysical events, and 2) lower-energy neutrinos (GeV) created by CR interactions in the Earth’s atmosphere. When a high-energy neutrino enters the IceCube detector, it collides with the optically clear ice, producing a cascade of charged secondary particles. These secondary particles travel at speeds faster than the phase velocity of light in ice, resulting in Cherenkov radiation. Then, the DOMs equipped with PMTs can detect the Cherenkov light

produced in these interactions, allowing it to recover the original neutrino's energy and direction.

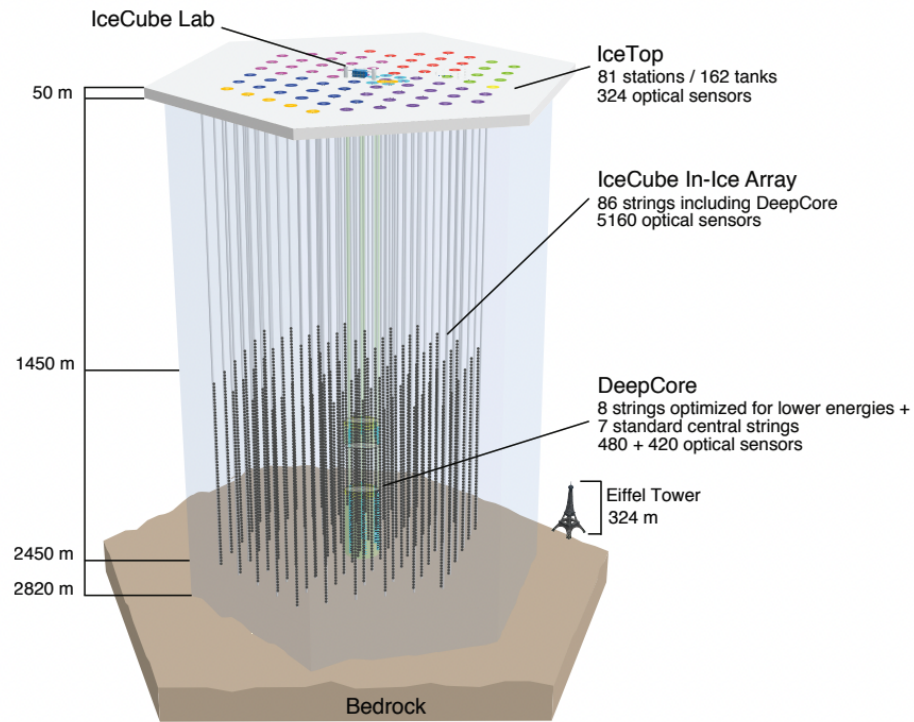


Figure 1.6: The Ice Cube Neutrino Observatory, a cubic-kilometer neutrino detector located at the South Pole. The diagram is adapted from the IceCube science webpage<sup>7</sup>.

## 1.4 This Dissertation

As a graduate student working at the intersection of time-domain, MMA and particle physics, the scientific questions that most intrigue me concern the nature of the high-energy Universe, mainly focusing on the physics Beyond the Standard Model (BSM). Throughout the past few years, I have been intentional in building a strong independent multimessenger portfolio. I hope this is reflected in my dissertation.

The work presented in this dissertation consists of projects related to several high-energy

---

<sup>7</sup><https://icecube.wisc.edu/science/icecube/>, as accessed on March 28, 2023.

astrophysical systems using multiple messengers and instruments. It can be read in two parts: the focus on new-physics searches in Chapters 3 and 4 moves to multimessenger astronomy in Chapters 5 and 6, where LIGO/Virgo/KAGRA and IceCube observations are featured. Chapter 2 provides an overview of the theoretical framework used in Chapters 3 and 4, which are focused on conducting searches for axion-like particles (ALPs) using the observations of GRBs with *Fermi*. Chapter 3 is published in a peer-reviewed journal and Ch. 4 is currently undergoing *Fermi*-LAT Collaboration review. As the lead of the *Swift*-BAT analysis, in Chapter 5 I present the work conducted in collaboration with the GBM Team and the LIGO/Virgo/KAGRA (LVK) Collaboration regarding the offline, follow-up searches for EM counterparts to GW triggers in O3. The results of the cross-correlation studies between the IceCube sky and the LAT unresolved sky are presented in Ch. 6. Chapter 7 provides a summary of the results and in Chapter 8 I share the questions I am most excited to tackle in the coming years. Any collaborative work is presented with an emphasis on my contributions.

Before we proceed, however, a kind warning to the reader. The work presented in this thesis does not exist in a vacuum despite my best attempts to make it self-contained. The research here was built on the shoulders of the scientists that came before me and done in collaboration with many others. Here, I merely list my contributions to different projects in the last few years. To comfortably read this thesis, in addition to a warm cup of tea, some familiarity with particle physics, observational astronomy, and astrostatistics at the graduate student level would be helpful—however, I provide an extensive list of references for the curious reader.

If you have not yet done so, now is the time to grab the aforementioned warm cup of tea. Dear reader, fasten your seatbelts, we are taking off!

## Chapter 2: Theoretical Foundations: The Curious Case of an Axion

*I started to apply [to graduate programs], and my undergraduate advisor said, “You know, graduate schools are often reluctant to accept women. They get married and one thing or another, and they don’t finish. But I don’t think we need to worry about that with you.” I was thinking — “Did I hear what he just said?”*

---

Interview of Helen Quinn by AIP, August 2020

As I sit in my office, trying to talk myself into writing this chapter, I participate in the longest staring contest known to a human: it is me against Professors Peskin and Schroeder’s QFT textbook<sup>1</sup>. If you ask me, it is one of the observational astronomer’s greatest fears. I have given up one too many times and opted to write a more general, math-light overview of axions; however, not motivating it with QFT seems incomplete at this stage. As with most of my writing, there is nothing like an academic deadline to push me into making a rash decision. So, please put on your mathematician’s hat, take a deep breath, and let us dive into it.

---

<sup>1</sup>This, in no way, should be read as a criticism of the textbook authors or its pedagogy. Instead, I instruct the reader to take this as my (one?) moment of self-criticism. I had a chance to speak to Prof. Peskin following my seminar at SLAC. I must say I was starstruck for most of that conversation. Still, as far as I remember, he was an incredibly kind and insightful individual with many interesting questions about my research.

## 2.1 QCD & the story of $\phi$

Quantum Chromodynamics (QCD) is the theoretical framework of the strong interaction, i.e., the force that binds quarks together to form protons, neutrons, and other particles<sup>2</sup>. The force mediator for the strong interaction is a gluon. The QCD Lagrangian,  $\mathcal{L}_{\text{QCD}}$ , that describes the behavior of quarks and gluons and follows from the SM can be written as [51]:

$$\mathcal{L}_{\text{QCD SM}} = -\frac{1}{4}G_{\mu\nu}^a G_a^{\mu\nu} + \sum_{f=1}^{N_f} \bar{q}_f^i [i\gamma^\mu (D_\mu)_{ij} - m_f \delta_{ij}] q_f^j. \quad (2.1)$$

The above QCD Lagrangian contains:

- The first term,  $-\frac{1}{4}G_{\mu\nu}^a G_a^{\mu\nu}$ , is the kinetic energy term, where  $G_{\mu\nu}^a$  represents the field strength tensor for the gluon field describing the magnitude and direction of the strong force;  $\mu$  and  $\nu$  represent the spacetime indices; and  $a$  runs over eight different color charges of the gluon field.
- The second term,  $\sum_{f=1}^{N_f} \bar{q}_f^i i\gamma^\mu (D_\mu)_{ij} q_f^j$ , describes the interaction of quarks with the gluon field. It is summed over quark and antiquark flavors,  $f$ .  $q_f$  represents a quark field of flavor  $f$ , with  $\bar{q}_f$  representing the antiquark field.  $\gamma^\mu$  are the Dirac matrices, and  $D_\mu$  is the covariant derivative that includes the interaction with the gluon field.  $i$  and  $j$  are the color indices of quarks, summed over  $i, j = 1, 2, 3$ .
- The third term,  $-\sum_{f=1}^{N_f} \bar{q}_f^i m_f \delta_{ij} q_f^j$ , is the mass term of quarks, where  $m_f$  represents the mass of the quark of flavor  $f$ .

---

<sup>2</sup>The derivations, notation, and the unit system presented here closely follow [51], with  $\hbar = c = 1$ , unless specified otherwise.

As Peccei and Quinn point out in [52], this Lagrangian—and thus, the strong interaction—is invariant under the CP transformations. So, what is the problem? Unfortunately, the Eq. 2.1 does not represent the full picture of strong interaction. For one, it does not incorporate the origin of the quark mass term that arises after the spontaneous breaking of the electroweak symmetry. The additional mass term can be represented using the mass matrix,  $M$ :

$$\mathcal{L}_{\text{mass}} = -\overline{q_L^i} M_{ij} q_R^j - \overline{q_R^i} (M^\dagger)_{ij} q_L^j, \quad (2.2)$$

where  $q_L$  and  $q_R$  are the left- and right-handed projections of  $q$ . Generally, the  $M$  matrix is non-Hermitian and non-diagonal; however, it is possible to diagonalize it by applying appropriate transformations on the quark fields, leading to the new form of the  $\mathcal{L}_{\text{mass}}$  Lagrangian:

$$\mathcal{L}_{\text{eff}}^{(1)} = \text{Arg det} M \frac{\alpha_3}{8\pi} G_{\mu\nu}^a \bar{G}_a^{\mu\nu}, \quad (2.3)$$

with

$$G_{\mu\nu}^a \bar{G}_a^{\mu\nu} = \frac{1}{2} \epsilon^{\mu\nu\alpha\beta} G_{\mu\nu} G_{\alpha\beta}, \quad (2.4)$$

and

$$\alpha_3 = \frac{g_3^2}{4\pi}, \quad (2.5)$$

where  $g_3$  denotes the coupling constant of the strong interaction. Note that Eq. 2.3 would go to zero—resolving the CP violation—if at least one of the quarks was massless, which is contrary to what we observe.

There is more bad news. Despite modifying the mass term in the original Lagrangian in

Eq. 2.1, this is not the complete story either. As introduced in [53, 54], there is also an additional “ $\Phi$ -vacuum” term, whose Lagrangian can be expressed as

$$\mathcal{L}_{\text{eff}}^{(2)} = \Phi_{\text{QCD}} \frac{\alpha_3}{8\pi} G_{\mu\nu}^a \bar{G}_a^{\mu\nu}. \quad (2.6)$$

Adding Equations 2.3 and 2.6 to the original QCD Langrangian in Eq. 2.1 yields the new effective Lagrangian:

$$\mathcal{L}_{\text{eff}} = \mathcal{L}_{\text{QCD SM}} + \mathcal{L}_{\text{eff}}^{(1)} + \mathcal{L}_{\text{eff}}^{(2)} = \mathcal{L}_{\text{QCD SM}} + \phi \frac{\alpha_3}{8\pi} G_{\mu\nu}^a \bar{G}_a^{\mu\nu}, \quad (2.7)$$

with  $\phi = \text{Arg det}M + \Phi_{\text{QCD}}$ .

The expression for the  $\mathcal{L}_{\text{eff}}$  is no longer CP invariant, causing the **strong CP problem**. The reason for this is as follows: the term  $G_{\mu\nu}^a \bar{G}_a^{\mu\nu}$  can be presented as the product of a strong electric and strong magnetic field,  $\mathbf{E}^a \cdot \mathbf{B}_a$ . We can think of this analogously to the Quantum Electrodynamics’ (QED) electromagnetic tensor,  $F_{\mu\nu}$ , for which it holds that  $F_{\mu\nu} \bar{F}^{\mu\nu} = -\mathbf{E} \cdot \mathbf{B}$ , where  $\mathbf{E}$  and  $\mathbf{B}$  are electric and magnetic fields respectively. Then, to complete the analogy, let us note that the QED vector potential  $A_\mu$  changes the sign under the charge conjugation, while the  $\mathbf{E}$  and  $\mathbf{B}$  are odd and even under parity, respectively. Therefore,  $\mathbf{E} \cdot \mathbf{B}$  changes sign under the combined operation of CP. Analoguously, if we assume that  $A_\mu \rightarrow G_\mu^a$ ,  $\mathbf{E} \rightarrow \mathbf{E}^a$ , and  $\mathbf{B} \rightarrow \mathbf{B}_a$ ,  $G_{\mu\nu}^a \bar{G}_a^{\mu\nu}$  will also change sign under CP, resulting in

$$G_{\mu\nu}^a \bar{G}_a^{\mu\nu} \propto -\mathbf{E}^a \cdot \mathbf{B}_a. \quad (2.8)$$

Since we already established that  $\mathcal{L}_{\text{QCD SM}}$  is CP invariant, looking back at the Eq. 2.7, we can

conclude that the additional term including  $\phi$  causes a CP violation.

An observable consequence of the CP violation in QCD would be a non-zero neutron electric dipole moment,  $d_n$ , which can be expressed as  $d_n = d_0\phi$  with  $d_0$  usually spanning the values on the order of  $10^{-16}$  to  $10^{-17}$  e cm depending on the used properties of the neutron. However, no such observation has been declared yet. Instead, the most stringent upper limit on the value of the neutron electric dipole moment is  $d_n < 1.8 \times 10^{-26}$  e cm, given by the nEDM experiment at the Paul Scherrer Institute in Switzerland [55]. This results in the upper limit on  $\phi$ ,

$$|\phi| < 2.7 \times 10^{-10} \text{ e cm}, \quad (2.9)$$

implying that

$$|\text{Arg det}M + \Phi_{\text{QCD}}| < 2.7 \times 10^{-10} \text{ e cm} \quad (2.10)$$

at a 90% confidence level (CL). As indicated in [54], both  $\text{Arg det}M$  and  $\Phi_{\text{QCD}}$  are predicted to have a magnitude close to 1, requiring that they cancel each other out at a very high accuracy. The question then arises: why *should* they cancel each other? These two parameters seem to be completely independent of each other:  $\text{Arg det}M$  is a result of spontaneous electroweak symmetry breaking, and  $\Phi_{\text{QCD}}$  stems from the characterization of QCD vacuum structure.

Yet again, we stand before a mysterious fine-tuning problem in physics<sup>3</sup>.

---

<sup>3</sup>Some other examples include the cosmological constant problem, the flatness problem, the hierarchy problem, etc. (See, e.g., Ref. [56–58]).

## 2.2 Axions to the rescue

Following the identification of the strong CP problem, physicists Roberto Peccei and Helen Quinn formulated the Peccei-Quinn (PQ) theory in attempt to resolve the fine-tuning in the CP problem [52, 59]. Their approach relied upon introducing a dynamical field to describe the behavior of the  $\phi$  term in Eq. 2.7. In turn, the PQ theory proposed the existence of a new particle, the *axion*, whose field would dynamically adjust itself to cancel out the  $\phi$  term, thereby restoring the CP symmetry. More specifically, the PQ theory suggested that the  $\phi$  term can be expressed as  $\phi = a(x)/f_a$ , where  $a(x)$  is the axion field and  $f_a$  is the axion decay scale, or the energy scale at which the axion field starts to oscillate. When the temperature of the Universe is above this energy scale, the axion field will be in a thermal equilibrium with other particles. However, if the temperature of the Universe is below the  $f_a$  scale, the axion field will oscillate, leading to the emergence of the axion particle. This has interesting implications on cosmology described in detail in Sec. 2.3.1. Substituting the new expression of  $\phi$  into Eq. 2.7 results in

$$\mathcal{L}_{\text{eff}} = \mathcal{L}_{\text{QCD SM}} + \frac{a(x)}{f_a} \frac{\alpha_3}{8\pi} G_{\mu\nu}^a \bar{G}_a^{\mu\nu}. \quad (2.11)$$

In order for the  $\mathcal{L}_{\text{eff}}$  to be invariant under the CP transformation,  $a(x)$  must be a pseudoscalar field. The PQ theory also introduces a new hypothetical Peccei-Quinn symmetry, under which the axion field transforms into  $a(x) \rightarrow a(x) + \alpha f_a$ , where  $\alpha$  is an arbitrary constant determining the phase shift. Introducing this transformation into Eq. 2.11 leads to an anomaly term that describes the interaction between axions and gluons,  $aG\bar{G}$ , providing an effective potential to  $a$ ,

given by:

$$V_{\text{eff}}(a) = \left( \phi + \frac{a}{f_a} \xi \right) \frac{\alpha_3}{8\pi} G_{\mu\nu}^a \bar{G}_a^{\mu\nu}, \quad (2.12)$$

where  $\xi$  is a parameter introduced through the anomaly term of the  $O(1)$ . The groundbreaking result of Peccei and Quinn's work in [52] is their proof that, under this transformation, the  $\langle G\bar{G} \rangle$  is a periodic function which, as shown in [51], leads to the axion-field expectation value in the vacuum, expressed as

$$\langle a(x) \rangle = -\frac{f_a}{\xi} \phi \quad (2.13)$$

at the minimum effective potential. Consequently, the field  $a(x)$  can be written as a sum of the axion physical field,  $a(x)_{\text{ph}}$ , and the axion-field expectation value  $\langle a(x) \rangle$ . Substituting  $a(x) = a(x)_{\text{ph}} + \langle a(x) \rangle$  into the original Lagrangian from Eq. 2.11 will result in  $\langle a(x) \rangle$  canceling out the  $\phi$  term—finally solving the strong CP problem, and at the same time introducing a physical axion field,  $a(x)_{\text{ph}}$ <sup>4</sup>. Further analysis results in a relationship between the axion mass,  $m_a$ , and the axion decay scale,  $f_a$ :

$$m_a \simeq 0.6 \text{ meV} \times \left( \frac{10^{10} \text{ GeV}}{f_a} \right). \quad (2.14)$$

## 2.3 What about ALPs?

Theoretical work done in e.g. [60, 61] (also known as the KSVZ model) suggests that axion should be a very light ( $m_a < 1 \text{ eV}$ ) weakly-interacting particle in order for the PQ mechanism to hold. If we generalize the case of the QCD axion by relaxing the requirement in Eq. 2.14, we introduce the notion of an axion-like particle (ALP). As an immediate consequence, the mass range spanned by an ALP now includes not only the Weakly-interacting Sub-eV Particles (WISPs), but

---

<sup>4</sup>For simplicity,  $a(x)_{\text{ph}}$  is substituted by  $a(x)$  hereafter.

also the Weakly-interacting Massive Particles (WIMPs). On the other hand, ALPs solve the strong CP problem only for the part of their parameter space. Interestingly, ALPs often appear also as SM extensions in string theory. In this dissertation, we focus on the WISP ALPs ( $m_a \lesssim 10^{-10}$  eV).

Similarly to axions, ALPs can have non-zero coupling to photons, allowing us to carry out indirect searches through their interactions with the EM field. The interaction of ALPs with photons can be described by the following Lagrangian,

$$\mathcal{L}_{a\gamma} = -\frac{1}{4}g_{a\gamma}F_{\mu\nu}\bar{F}^{\mu\nu}a = g_{a\gamma}\mathbf{E} \cdot \mathbf{B} a, \quad (2.15)$$

where  $g_{a\gamma}$  is the ALP-photon coupling [62].

### 2.3.1 ALP as dark matter

The existence of DM is extremely well-motivated through various astrophysical observations, including the flattening of galactic rotation curves, gravitational lensing, the fluctuation fields in CMB, and the properties of large-scale structure (see, e.g., Ref. [63]). Our understanding of a DM particle necessitates that, in addition to being weakly interacting and cosmologically stable, a viable candidate should be sufficiently cold to allow for efficient structure formation. The light ALP satisfies the requirement for cosmological stability quite straightforwardly, as its low mass reduces the number and type of possible decay products implying a long lifetime. However, in order to accomplish the necessary coldness, these particles must be produced in non-thermal processes. The most favored means to non-thermally produce ALPs is via the misalignment mechanism (see e.g. Ref. [62] for an overview). This mechanism assumes a non-zero

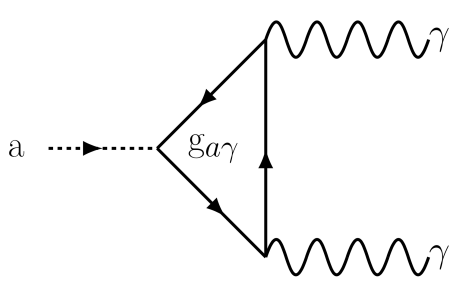
initial state of the fields in the early Universe, with their mass  $m$  evolving as  $m \propto t^{-1}$ . Once these fields reach the given timescale, they oscillate and relax in their potential wells, with oscillation density behaving as  $\rho \propto a^{-3}$ , where  $a$  is the universe scale factor. Such behavior is characteristic of cold dark matter, making these oscillations a realizable candidate for a given range of masses.

Detailed derivations in [62] find that

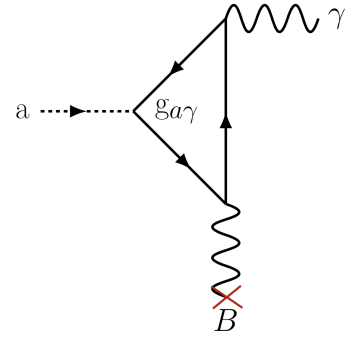
$$\rho_{\phi,0} < 1.17 \frac{\text{keV}}{\text{cm}^3} \times \frac{m_a}{10^{-10} \text{ eV}} \left( \frac{\phi_1}{5.3 \times 10^9 \text{ GeV}} \right)^2, \quad (2.16)$$

where  $\rho_{\phi,0}$  is the dark matter density today. This expression provides constraints on the field value,  $\phi_1$ , at the freeze-out time, as a function of the DM axion mass,  $m_a$ . Following the derivations in [62], the relevant mass range for light ALPs that we consider in this thesis is on the order of  $10^{-10}$  eV. If DM in fact is made of ALPs, most of its mass would be produced via the described misalignment mechanism during the early evolutionary stages of the Universe.

In this thesis, however, we focus on ALPs produced through Primakoff resonant process inside high-energy environments. As suggested in Eq. 3.1, thermal photons convert into ALPs when they enter EM fields of a highly ionized environment created by various astrophysical sources. Once they reach the magnetic field of our Galaxy, they are converted back into photons via the inverse Primakoff process. The Feynman diagrams demonstrating ALP-photon coupling through the aforementioned axion (and generally, ALP) decay and Primakoff processes are shown in Fig. 2.1.



(a) ALP decay in vacuum.



(b) Primakoff process.

Figure 2.1: The Feynman diagrams demonstrating the ALP-photon oscillations. Left panel (a): ALPs can decay into photons in vacuum, or (b) in the presence of an external magnetic field via the Primakoff process.

## 2.4 Constraining the light ALP properties

All ALP searches so far have only resulted in upper limits on its properties described by its mass and coupling to photons, ( $m_a, g_{a\gamma}$ ). Several different techniques have been employed in attempts to detect this particle, ranging from haloscope, light-shining-through-the-wall, and helioscope experiments, to using the astrophysical and cosmological observations to search for indirect ALP signatures. The limits on the light ALP properties are given in Fig. 2.2.

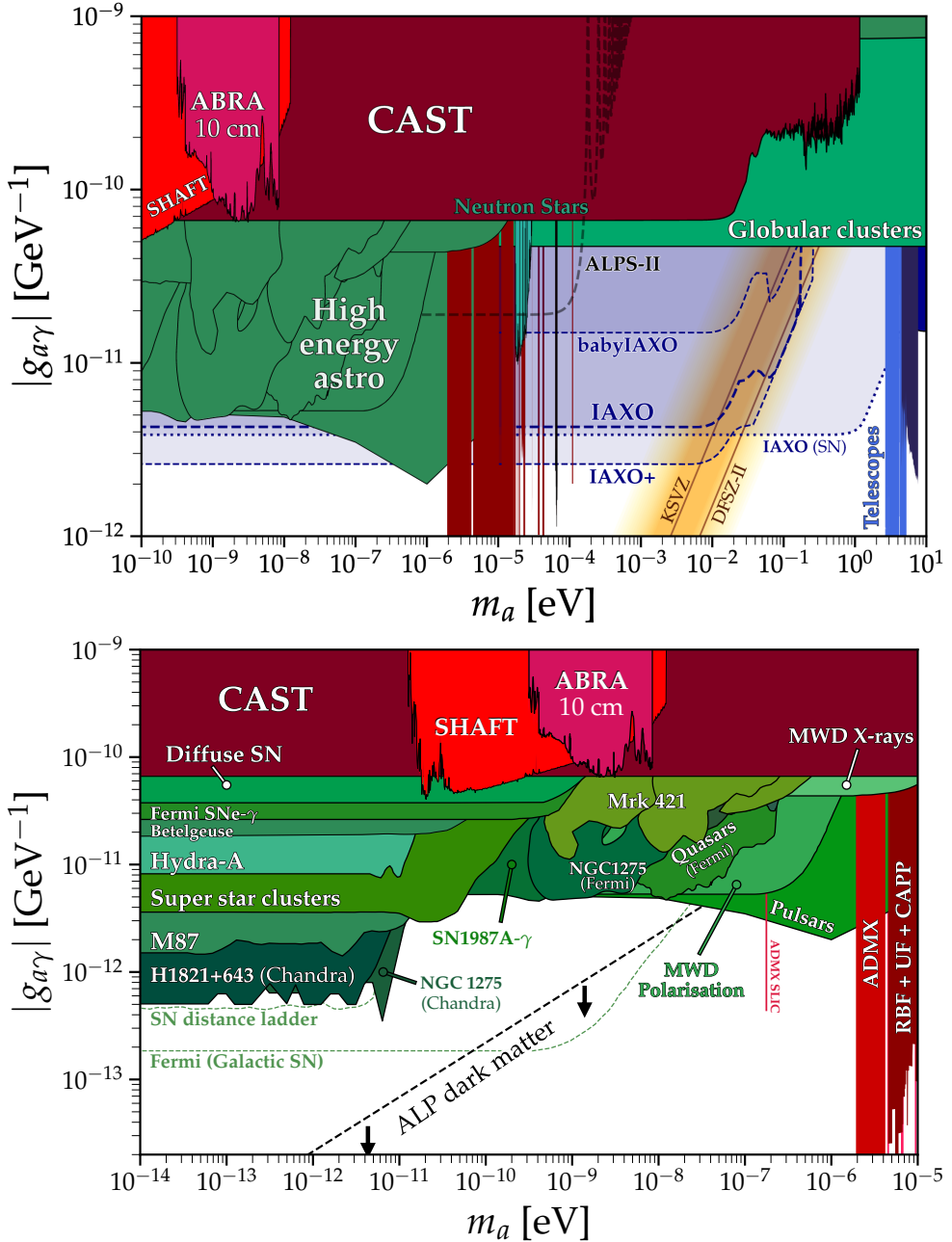


Figure 2.2: *Top:* Constraints on the ALP mass-coupling parameter space. In green are shown the limits placed using the astrophysical observations, and differed shades of red show the limits from haloscope experiments. Purple shades show projected limits from the future light-shining-through-a-wall experiments. Dashed lines are the projected limits for future experiments. *Bottom:* Astrophysical constraints zoom-in. The color scheme follows the one described above. Green dashed lines show projected upper limits in case of an observed astrophysical event. The black dashed line separates the part of the parameter space for which DM can be explained by ALPs.<sup>5</sup>

<sup>5</sup>This plot is produced using the [AxionLimits](#) code by Dr. Ciaran O'Hare, as accessed on March 22, 2023. Additional limits and appropriate references are available within the GitHub repository.

- **Astrophysical observations.** A number of astrophysical systems have been used to put constraints on the ALP properties. For example, thermal photons produced in a core-collapse supernova (CCSN) can convert into ALPs within the local electrostatic fields. The lack of observed ALP-induced GRBs from supernovae has been used to place constraints on the ALP-photon coupling and ALP mass. Similarly, pulsars—highly magnetized NSs—can be an excellent probe into ALPs. Other highly magnetized or jetted objects, such as galaxy clusters and AGNs, also provide important constraints on the properties of light ALPs. Different shades of green in the bottom panel of Fig. 2.2 show several different attempts at using high-energy observations to detect ALPs. Astrophysical searches currently provide the most stringent limits on the light ALP properties [64–86].
- **Helioscopes.** ALPs and axions can be produced in the interior of the Sun. The high-energy photons in the Sun’s plasma can convert into ALPs and axions within the electrostatic fields of charged particles via Primakoff process. Helioscopes are laboratory instruments with a large magnetic field placed at one end, and an X-ray detector on the other. They point at the Sun with the goal of collecting ALPs and axions that would convert into X-ray photons within the instrument’s magnetic field. An example of such instrument is the CERN Axion Solar Telescope (CAST), with a dipole magnet with the field strength of  $\sim 9$  T with limits on coupling shown in Fig. 2.2 [87, 88]. The other experiment shown in the figure is the International Axion Observatory (IAXO) proposed to be built in the Canfranc Underground Laboratory in Spain and is currently in the conceptual design phase [89–92].
- **Haloscopes.** Haloscope experiments use a resonant cavity placed in a strong magnetic field to search for signatures of ALP conversion into microwave photons. The source of ALPs

considered in these searches is typically the Galactic halo (hence the name *haloscope*). The reference microwave photons inside the cavity are set to a specific resonant frequency. ALPs that undergo a conversion into microwave photons will resonate in the cavity, producing a detectable signal. The properties of such signal are determined by the ALP mass and coupling to the photons. Examples of such experiments shown in Fig. 2.2 include A Broadband/Resonant Approach to Cosmic Axion Detection with an Amplifying B-field Ring Apparatus (ABRACADABRA), the Axion Dark Matter eXperiment (ADMX), and Search for Halo Axions with Ferromagnetic Toroids (SHAFT) [93–100].

- **Light-shining-through-a-wall.** The setup for these experiments consists of a laser beam shone through a magnetic field and a wall with a detector placed behind it. Similarly to the experimental approaches already mentioned, the guiding principle for this experiment is reliant on the ALP-photon mixing: in the presence of a strong magnetic field, ALPs and photons can mix together, resulting in a “mixed” particle, or a photon-ALP oscillation. Depending on the magnetic field orientation and strength, the photon-ALP oscillation can convert ALPs into photons, which can then pass through the wall and be detected on the other side. An example of such experiment is the Axion-Like Particle Search (ALPS) experiment, with a proposed successor shown in Fig. 2.2 as ALPS-II.

Here, I list some of the approaches that are most relevant to detecting light ALPs; however, many more experiment designs remain not discussed, such as the observations of CMB, the extragalactic background light (EBL), Solar observations, light-beam dump experiments, etc. I strongly encourage you, the curious reader, to refer to the most up-to-date, comprehensive

database of ALP searches status by Dr. Ciaran O'Hare, [AxionLimits](#)<sup>6</sup>.

---

<sup>6</sup><https://github.com/cajohare/AxionLimits>, as accessed on March 28, 2023.

## Chapter 3: Searching for axion-like particles from core-collapse supernovae with *Fermi* LAT’s low energy technique

*I hope five hundred years from now astronomers aren’t still talking about the same Big Bang model. I think they won’t have done their work if they are... I still believe there may be many really fundamental things about the Universe we don’t know. I think our ignorance is greater than our knowledge.*

---

Interview of Vera Rubin by AIP, April 1989

At last, we are prepared to embark on our quest to search for ALPs. In this chapter, we conduct a sensitivity analysis to determine the limiting distance to which the *Fermi* Gamma-ray Observatory [38, 39] would be able to detect an ALP-induced GRB using the LAT low-energy (LLE) technique [101]<sup>1</sup>. Considering astrophysical background levels from GRBs observed at various incidence angles, we estimate the necessary ALP flux that would lead to a significant detection of the ALP induced GRB. Furthermore, we select a candidate sample of twenty-four GRBs and carry out a model comparison analysis in which we consider different GRB spectral models with and without an ALP signal component.

---

<sup>1</sup>The work in this chapter is published in Physical Review D, under 10.1103/PhysRevD.104.103001 by Crnogorčević et al. It is presented here with minimal modifications.

### 3.1 Introduction

Let us start with a short recapitulation of Chapter 2: the light ALP is a generalized case of the QCD axion, belonging to the family of WISPs (see additional Ref. [102–105] and references within for a review of the QCD axion [52, 59, 106, 107].) The interaction of ALPs with photons can be described by the Lagrangian,

$$\mathcal{L}_{a\gamma} = -g_{a\gamma} \mathbf{E} \cdot \mathbf{B} a, \quad (3.1)$$

where  $g_{a\gamma}$  is the photon-ALP coupling,  $\mathbf{E}$  is the electric field,  $\mathbf{B}$  is the magnetic field, and  $a$  represents the ALP field. When an external magnetic field  $\mathbf{B}$  is present, the two-photon coupling results in a photon-ALP conversion [108]. Photon-ALP oscillations have been invoked to explain the excess of soft X-rays from the center of galaxy clusters [64–67], the monochromatic 3.55-keV line in galaxy clusters [68], the low opacity of the Universe to TeV photons [69–73], anomalous stellar cooling [74–77], as well as the low-energy electronic recoil event excess in XENON1T [109–111]. Furthermore, ALPs are considered one of the leading candidates for cold DM [62, 112–115]. The ALP parameter space has been explored using various experimental approaches, including light-shining-through-the-wall experiments [89], cavity experiments [116], as well as observations of different astrophysical targets, such as Cepheid variable stars [78], star clusters [79, 80], and galaxy clusters [81–84, 86].

In this chapter, we investigate the prospect to detect ALPs that are produced in high-energy environments—in particular, CCSNe—via the Primakoff resonant process [117], and subsequently travel undisturbed until they reach the Galactic magnetic field where they convert into

$\gamma$ -ray photons [118, 119]. Figure 3.1 demonstrates the set-up of the physical system in question. For a 10-solar-mass (hereafter denoted by  $M_\odot$ ) CCSN progenitor, the ALP spectrum should have a thermal shape peaking at around 70 MeV [120–122]. The duration of an ALP-induced burst varies depending on the mass of a progenitor; nevertheless, the signal would be short (on the order of tens of seconds). No other physical processes are predicted to produce such spectral signatures in a CCSN’s  $\gamma$ -ray spectrum. Thus, using observations of a CCSN and, in particular, searching for its presumed associated ALP-induced GRB, can be an excellent probe for constraining the ALP parameter space (e.g. [37, 123]).

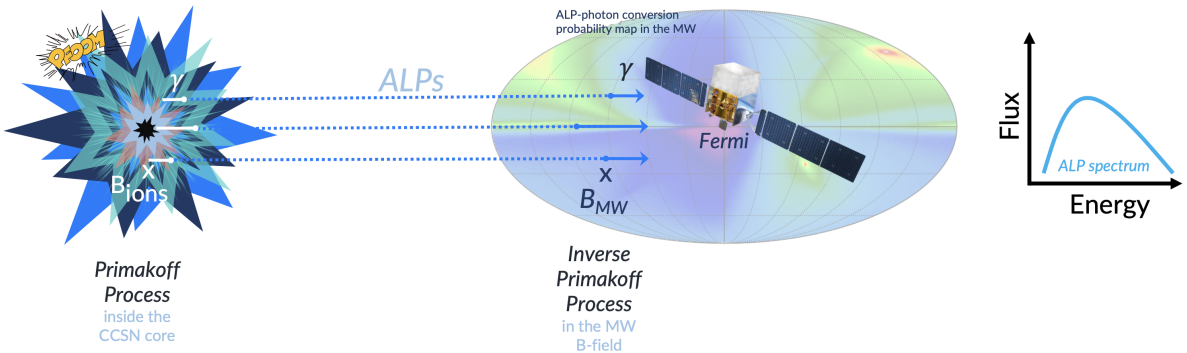


Figure 3.1: Thermal photons produced in a core-collapse are converted into ALPs via Primakoff process in the electrostatic fields of protons and ions (see Fig. 2.1). They travel undisturbed until they reach the Galactic magnetic field, where they undergo the inverse Primakoff process. Photons produced in this conversion may be observed by gamma-ray observatories, for example *Fermi*.

Ordinary GRBs, believed to arise from collimated ultra-relativistic outflows of materials when, e.g., a star collapses, are among the most luminous events in the Universe, spectrally peaking in the keV–MeV energy range [124]. The spectral functions used to characterize the prompt emission of an ordinary GRB are described in Appendix A and are distinct from the ALP spectral signature shown in Fig. 3.3. Depending on the duration of their prompt emission

and their spectral hardness, GRBs are divided into two sub-types: the short-hard, for which the emission duration is less than 2 seconds; and long-soft, with their duration exceeding 2 seconds [125, 126]. To explain differences between the two sub-types with respect to their duration, flux, variability, spectral parameters and evolution, the nature of their progenitors is often invoked [127]. Short-hard GRBs are suspected to originate from compact-object binary mergers (such as two NSs or a NS and a BH [128–130]) and long-soft GRBs are likely associated with Type Ib/c CCSNe [131–136]. Taking into account the predicted duration of an ALP-induced burst (a few tens of seconds), as well as the nature of the hypothesized ALP production site (CCSNe), we are particularly interested in studying the long-soft GRBs.

Using the properties of the ALP spectral emission, we first conduct a sensitivity analysis to determine the limiting distance to which *Fermi* Gamma-ray Observatory [38, 39] would be able to detect an ALP-induced GRB using the LAT low-energy (LLE) technique [101]. Considering astrophysical background levels from GRBs observed at various incidence angles, we estimate the necessary ALP flux that would lead to a significant detection of the ALP induced gamma-ray burst. Secondly, we consider a selected GRB sample and conduct a model comparison between fits that include the ALP spectral component and those that do not. Finally, we discuss the found limiting distances, the feasibility of upper limits on ALP couplings, and the tangibility of ALP detection with *Fermi* or other gamma-ray observatories alike.

This chapter is organized as follows: Section 3.2 provides an overview of the ALP spectral model, derived in [122]. In Section 3.3, we describe the GRB data selection process. In Section 3.4, we conduct a sensitivity study to determine the CCSN distances and photon-ALP couplings that would result in a significant detection of a GRB in the relevant MeV energy range with *Fermi*. Section 3.5 describes the ALP-fitting method for the selected sample of GRBs. Finally,

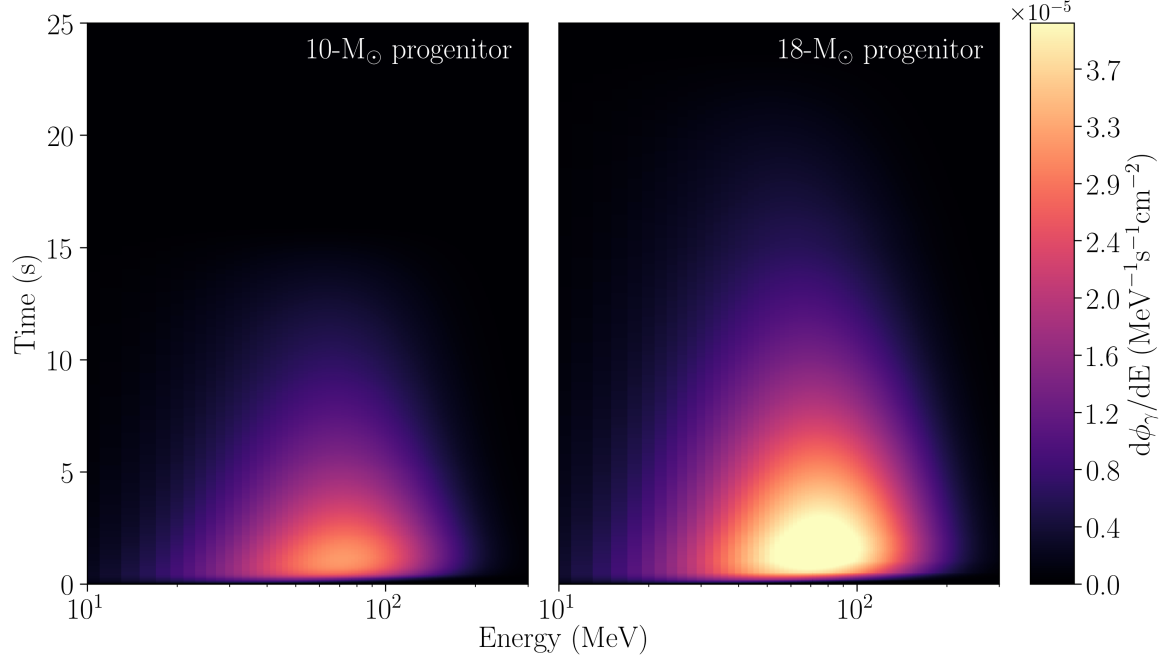


Figure 3.2: Observed evolution of the ALP-induced gamma-ray emission in time and energy in a core-collapse of a  $10 - M_{\odot}$  and  $18 - M_{\odot}$  progenitor, normalized by  $N_{\text{tot}} = 8.4 \times 10^{-54} \text{ cm}^{-2}$ , adapted from [37]. Note that most of the emission occurs in the first ten seconds after the collapse. The  $18 - M_{\odot}$  progenitor is a more energetic source of ALPs with a few-second prolonged emission as compared to the  $10 - M_{\odot}$  progenitor.

Section 3.6 provides the summary and future outlooks for ALP searches within the gamma-ray energy band.

## 3.2 ALP model

To produce a spectral model for an ALP-induced GRB as observed on Earth, we utilize the one-dimensional CCSN model derived in [122] that is, due to the complexity of core-collapse modeling, available for only two distinct progenitor masses ( $10$  and  $18 M_{\odot}$ ). The temporal and energy evolution of an ALP burst emission are shown in Fig. 3.2.

The observed photon flux,  $d\phi_\gamma/dE$ , can be expressed as

$$\frac{d\phi_\gamma}{dE} = \frac{P_{a\gamma}(g_{a\gamma})}{4\pi d^2} \frac{d\dot{N}_a(g_{a\gamma})}{dE}, \quad (3.2)$$

where  $d$  is the luminosity distance to the CCSN;  $P_{a\gamma}$  is the ALP-photon conversion probability, proportional to  $g_{a\gamma}^2$ ; and  $d\dot{N}_a/dE$  is the Primakoff production rate of ALPs per unit energy, also proportional to  $g_{a\gamma}^2$ . This proportionality,  $P_{a\gamma} \propto g_{a\gamma}^2$ , breaks down before  $P_{a\gamma}$  approaches unity [137]. The total flux normalization may then be written as

$$N_{\text{tot}} = 8.4 \times 10^{-54} \text{ cm}^{-2} \left( \frac{d}{10 \text{ Mpc}} \right)^{-2} \times \left( \frac{g_{a\gamma}}{g_0} \right)^4 \times \left( \frac{P_{a\gamma}(g_0)}{0.1} \right), \quad (3.3)$$

with  $g_0 = 10^{-11} \text{ GeV}^{-1}$  denoting an arbitrary reference coupling, roughly corresponding to the current upper limit,  $g_{a\gamma} \lesssim 5.3 \times 10^{-12} \text{ GeV}^{-1}$  [122], for ALP masses ranging from  $m_a \simeq 10^{-12}$  to  $10^{-8} \text{ eV}$  [81, 82, 84, 122, 138]. For lower-mass ALPs, i.e.  $m_a \lesssim 10^{-12} \text{ eV}$ , observations of galaxy clusters provide more stringent constraints,  $g_{a\gamma} \lesssim 6 - 8 \times 10^{-13} \text{ GeV}^{-1}$  [85] (see also [139] and [80, 140]). Furthermore, for masses  $m_a \gtrsim 10^{-10} \text{ eV}$ , the conversion probability  $P_{a\gamma}$  becomes energy-dependent and effectively drops within the MeV energy range considered in this analysis. The observed photon flux can now conveniently be expressed as

$$\frac{d\phi_\gamma}{dE} = N_{\text{tot}} \times \frac{d\dot{N}_a(g_0)}{dE}. \quad (3.4)$$

Using the CCSN model in [122], we obtain the temporal and energy information about the ALP production rates  $d\dot{N}_a(g_0)/dE$  in a CCSN due to the ALP interactions described in Eq. (3.1). Figure 3.2 shows that most of the corresponding ALP-induced gamma-ray emission happens in

the first few tens of seconds for both progenitor masses; hence, by averaging over the time interval of 10 seconds starting at the core-collapse, we obtain the expected spectra shown in Fig. 3.3.

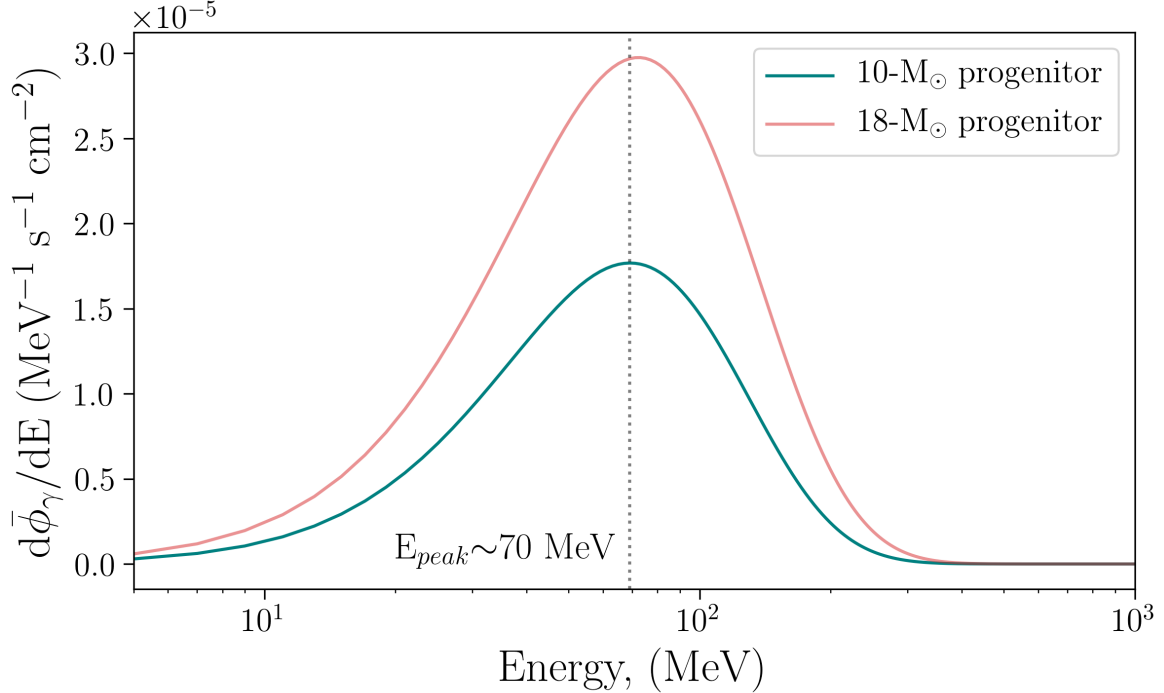


Figure 3.3: The observed ALP-induced gamma-ray spectrum for 10 and  $18-M_\odot$  progenitors integrated and averaged over the first 10 seconds after the collapse for a normalization,  $N_{\text{tot}} = 8.4 \times 10^{-54} \text{ cm}^{-2}$  (see Eq. 3). Note that most of the flux is emitted around 70 MeV.

### 3.2.1 Conversion Probability

The photon-ALP conversion probability,  $P_{a\gamma}$ , is computed numerically to account for variations in the Galactic magnetic field. Following the Milky Way magnetic field model by Jansson & Farrar [141], we compute the conversion probabilities for different positions in the sky, assuming that the photon-ALP mixing happens throughout the entire Galaxy, as done in [123, 142]. The contribution from the turbulent magnetic field component is not included in this analysis since its typical coherence length ( $\sim 10$  pc) is significantly shorter than the ALP-photon oscillation length and can be neglected for the considered ALP mass  $m_a \lesssim 10^{-10}$  eV in most sky regions

[143, 144]. For an emission that passes only through the Galactic magnetic field, the conversion probability is shown in Fig. 3.4, as a function of source’s position in the sky. We assume that  $P_{a\gamma}$  is energy-independent in our analysis, which is valid for low-mass ALPs ( $m_a \lesssim 10^{-10}$  eV), while for larger ALP masses  $P_{a\gamma} = P_{a\gamma}(g_{a\gamma}, m_a, E)$  decreases and starts to oscillate as a function of energy [122].

We do not take into account the photon-ALP conversions that may happen in the intergalactic magnetic field, as such contributions would be negligible and highly uncertain for the nearby sources we consider. For example, if we assume a uniform intergalactic magnetic field strength of  $\sim 1$  nG, a coupling of  $g_{a\gamma} = 5.3 \times 10^{-12}$  GeV $^{-1}$  and a distance of 5 Mpc, we obtain that in the strong-mixing regime (here reached for  $m_a \lesssim 10^{-11}$  eV) [69], the order of the conversion probability,  $\mathcal{O}(P_{a\gamma})$ , is  $10^{-3}$ . Furthermore, considering the conversion probability in an extragalactic source’s host galaxy and, if applicable, its surrounding intracluster medium, would be highly uncertain due to a lack of knowledge of their respective magnetic fields and would have to be taken on a case by case basis. In addition, such consideration would result in an increase of the observed gamma-ray flux [123], resulting in adjustments to Fig. 3.4 with conversion probabilities unlikely reaching values below  $10^{-3}$ ; hence, neglecting them renders our results conservative. Due to case by case differences, we do not take into consideration the ALP-photon conversion that may take place in the magnetic field of the intergalactic medium and within the host galaxy.

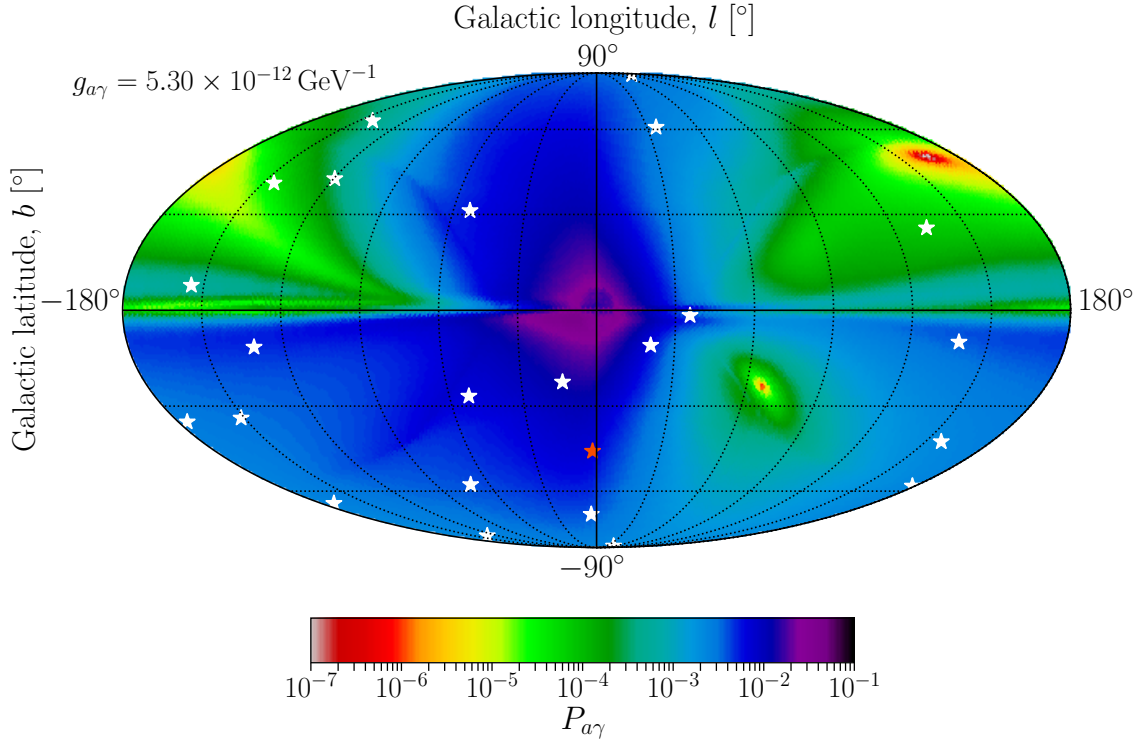


Figure 3.4: ALP-photon conversion probability as a function of source position in the sky. We consider only the ALP conversion into gamma rays within the Milky Way’s coherent magnetic field component, as modeled in [123]. We assume an ALP mass  $m_a = 10^{-10}$  eV and coupling  $g_{a\gamma} = 5.3 \times 10^{-12}$  GeV $^{-1}$ , and energy  $10 < E < 300$  MeV. Note that for this configuration,  $P_{a\gamma,\max} \sim 0.1$  is the maximum conversion probability reached in the central regions of Milky Way. White crosses represent the best localization positions of the GRB sample considered in Sec. 3.5, with the red cross corresponding to GRB 101123A [145].

### 3.2.2 ALP Model in XSPEC

Spectral modeling in this chapter is conducted using the standard high-energy fitting package *XSPEC* [146] and its Python adaptation, *PyXspec*<sup>2</sup>. The ALP spectra shown in Fig. 3.3 are used to write a model function that is inserted into the *XSPEC* model library using the `addPyMod` method. For the model parameters, we consider two different progenitor masses,  $10 M_\odot$  and  $18$

<sup>2</sup><https://heasarc.gsfc.nasa.gov/docs/xanadu/xspec/python/html/index.html>, accessed on April 23, 2019.

$M_\odot$ , with the normalization parameter  $N_{\text{tot}}$ , from Eq. (3.4), left free to vary.

### 3.3 Data Selection

#### 3.3.1 *Fermi* observatory

With its two instruments on board, the GBM [38]) and the LAT, [39], the *Fermi* observatory provides a wide spectral coverage and excellent sensitivity for studying GRBs. The GBM's two different kinds of detectors, NaI and BGO, cover 8 keV to 1 MeV and 150 keV to 40 MeV in energy, respectively. The FoV is  $\sim 9.5$  sr and the point-source localization accuracy is  $\sim 5^\circ$ . On the other hand, LAT is a pair production telescope covering the energy range from 20 MeV to more than 300 GeV, with a FoV of  $\sim 2.4$  sr, and a point-source localization of  $< 1^\circ$ , for energies above 1 GeV. More details about the GBM and LAT instruments can be found in Chapter 1. Figure 3.4 shows the best localization values for the considered GRB sample using either GBM or LAT instruments [145]. Particularly of interest in this paper is the LAT low-energy data (LLE, [101]), due to the energy of the ALP spectral peak at 70 MeV, shown in Fig. 3.3.

The LLE analysis method was developed with the goal of maximizing the effective area of the LAT instrument in the low-energy regime [101]. This is done by relaxing the requirements on background rejection, as compared to the standard LAT transient analysis. This technique is particularly useful for a study of transients, such as GRBs, for energies greater than  $\sim 30$  MeV. The LLE event selection relies upon having at least one reconstructed track within the LAT's tracker/converter, allowing for an estimate of the direction of the incoming photon. Furthermore, all photons pass through the anticoincidence detector which enables cosmic-ray background rejection. Finally, this algorithm requires a non-zero reconstructed energy of the considered event.

Then, for the short and bright transient sources, the background is determined by an “ON” and “OFF” time-interval technique. The background rate during the “OFF” interval is fit by a polynomial function in each energy bin, providing us with an estimate of the background during the “ON” interval. The corresponding LLE response files are produced using Monte Carlo simulations of bright point sources with a specific spectral shape at the sky position of interest. The systematic effects in reconstructing the LLE events are considered in [147], estimating the discrepancy between the LLE selection criteria in the LAT data and in Monte Carlo simulations to be  $\sim 17\%$  for events below 100 MeV. Comparing the flux values reveals that LLE’s flux estimations are on average lower than those from the standard LAT analysis; however, no significant biases are reported for the energy resolution, with that of LLE estimated to  $\sim 40\%$  at 30 MeV and  $\sim 30\%$  at 100 MeV. A detailed description of the LLE technique is provided in [147]. The LLE data is publicly available from the HEASARC website<sup>3</sup>. In Sec. 3.4, we focus on utilizing the LLE data sample; which, in Sec. 3.5, is complemented by the GBM and the standard LAT transient data, when such observations are available.

### 3.3.2 Time-tagging of a core collapse

One of the main challenges for conducting ALP spectral fitting is to observationally approximate the collapse time of a supernova, i.e. the time when most of the ALPs escape the collapse site.

The optimal way to address this challenge is through neutrino detection from the source, as neutrinos and ALPs are expected to arrive at approximately the same time. However, obser-

---

<sup>3</sup><https://heasarc.gsfc.nasa.gov/W3Browse/fermi/fermille.html>, as accessed on December 24, 2019.

vational neutrino data from supernovae are scarce (so far, only SN1987A [122]). Although the current generation of neutrino detectors has significantly improved in sensitivity (e.g. IceCube detection from the blazar TXS 0506+056 at  $z = 0.33$  [33]), no neutrino signal detection is expected from an extragalactic supernova in the near future [148]. This imposes tight limitations on a potential ALP-source distance from which a neutrino signal can be detected, likely to a CCSN in our own Galaxy or in the Local Group, extending up to a few Mpc [148, 149]. Furthermore, if we were to use neutrinos for time-tagging of a core collapse, we would also require a gamma-ray observation of such an event in order to conduct the ALP spectral fitting. For example, the probability for a Galactic SN to occur in the LAT FoV in the next 3 years is  $\lesssim 1\%$ .

Beside neutrino detection, another way to approximate explosion times of supernovae is by using their optical lightcurves [150]. This technique has been used in [37] to search for an ALP-induced gamma-ray burst with the standard LAT data above 60 MeV.

Another possibility to infer the core collapse time is from the time of the ordinary astrophysical GRB. The ordinary bursts are delayed on the order of seconds to minutes with respect to the core collapse, as the jet needs to form and propagate through the stellar envelope (see, e.g., Fig. 10.1 in [151]). Moreover, the ALP-induced gamma-ray emission is approximately isotropic from the source, in contrast to the ordinary GRB jet emission—which also might not be aligned with our line of sight, resulting in a considerably weaker signal if seen off-axis (or even a ‘failed GRB’ [152]). This could imply that not every ALP signal is accompanied by a subsequent ordinary GRB detection. A dedicated study regarding precursor emission (hypothetically, an ALP signal prior to the observed jet emission) to GRBs may address the time-tagging issue in more detail and is the topic of discussion in Chapter 4. In this chapter, we assume that the time when most ALPs escape the collapse site coincides with the GRB signal time window.

### 3.3.3 GRB Selection Criteria

Considering the GRBs detected so far by *Fermi*-LAT [145], with their corresponding optical follow-ups and, in turn, redshift information, we infer that all associated sources are too far (the closest one being over 600 Mpc away) to be considered for a sizable ALP-induced burst observation (see the sensitivity results of Sec. 3.4.3). Thus, in our analysis we instead only consider all the LLE-detected GRBs without redshift information (hereafter referred to as *unassociated* GRBs) as potential ALP signal candidates; albeit, most likely ordinary GRBs of extragalactic origin. With limited information on the origin of the considered GRB sample, we assume they are either induced by an ALP signal or by ordinary astrophysical processes traditionally applied in GRB spectral modeling (see, e.g., [145]). This allows us to start the ALP analysis at the GRB trigger time,  $T_0$ , with the considered time window encompassing either (or both) the traditional GRB emission and the potential ALP signal.

We consider all unassociated GRB detections by *Fermi* LAT from August 2008 to August 2018, as reported in the *Fermi* LAT Second Gamma-Ray Burst Catalog, 2FLGC [145], publicly available on the HEASARC website<sup>4</sup>. Motivated by the energy of the ALP spectral peak at  $\sim 70$  MeV, we further restrict our sample to GRBs with at least  $5\sigma$  detection in LLE alone. Such strong signal in the low-sensitivity region of LAT often indicates a strong signal in either GBM, or standard LAT (or, both), often meriting follow-up observations by optical telescopes. Thus, the  $5\text{-}\sigma$  requirement combined with no redshift information are the most exclusive cut criteria for our sample. We require the source to be within the FoV throughout the entire duration of the burst which, required by the nature of ALP emission, should be a long GRB. For the sensitivity analysis

---

<sup>4</sup><https://heasarc.gsfc.nasa.gov/W3Browse/fermi/fermilgrb.html>

Table 3.1: Selection criteria applied to GRBs detected by *Fermi*-LAT between August 2008 to August 2018. From the initial sample size of 186 GRBs, we narrow down the list of candidates to 24 shown in Table 3.2. The burst duration criterion is not applied to the sensitivity analysis in Sec. 3.4, allowing for the inclusion of three additional short GRBs.

Property	Selection Criterion
Distance	unassociated (no redshift)
Detection significance	$\geq 5\sigma$ in LAT-LLE ( $\gtrsim 30$ MeV)
Observed time interval	$\geq$ duration of the GRB <sup>5</sup>
Burst duration	long GRBs ( $T_{95} \gtrsim 2$ seconds <sup>6</sup> ) (not used in Sec. 3.4)

(Sec. 3.4), in order to somewhat increase our GRB background sample, we drop the GRB duration criterion as we are only concerned with the observed background levels, which are independent from the GRB’s duration. This results in three additional short GRBs (GRB 081024B, GRB 090227B, and GRB 110529A) which can be used as background templates. As such, the spatial distribution of all the considered GRBs, as shown in Fig. 3.4, forms a representative sample of the GRB sources in the sky.

The GRB selection criteria are summarized in Table 3.1. From the initial sample of 186 LAT-detected GRBs, applying the above selection cuts results in a sample of 24 long GRBs, all listed in Table 3.2.

### 3.4 Sensitivity Analysis

We conduct a sensitivity study using the LLE data for two reasons: firstly, to ensure that a manually injected ALP feature can be recognized by our fitting algorithm; secondly, to determine the maximum distance for a given photon-ALP coupling for which the ALP feature is still significantly detectable in LLE. We also find the distance to a CCSN that allows for setting competitive upper limits on the photon-ALP coupling with *Fermi* LLE. In this study, we use a

Table 3.2: List of the 24 GRBs that pass the selection criteria.  $T_{95}$  corresponds to the duration reported in Table III in [145], as seen by GBM. The following columns show the best-fit models listed without an additional ALP component, with uncertainties representing the 90%-confidence interval for the given fit parameter. Also included are the log-likelihood ratio (LLR)  $\Lambda$  values,  $\Lambda = -2 \log(L_{\text{GRB}}/L_{\text{GRB+ALP}})$ , which are derived in Sec. 3.5. We also report the best-fit parameters for the cases in which the Band model (denoted by XSPEC’s grbm) is one of the model components [153], to demonstrate that the parameters do not reproduce the ALP spectral shape which may be reproduced with  $\alpha_1 \sim -2.4$ ,  $\alpha_2 \sim -0.1$ , and  $E_c \sim 30$  MeV. Details of the GRB analysis are described in Sec. 3.5.

GRB	$T_{95}$ (s)	Best model (no ALP)	grbm parameters			LLR
			$\alpha_1$	$\alpha_2$	$E_c$ (keV)	
080825C	22.2	grbm	-0.65 <sup>+0.05</sup> <sub>-0.05</sub>	-2.41 <sup>+0.04</sup> <sub>-0.04</sub>	143 <sup>+13</sup> <sub>-12</sub>	0.2
090217	34.1	grbm	-1.11 <sup>+0.04</sup> <sub>-0.04</sub>	-2.43 <sup>+0.03</sup> <sub>-0.04</sub>	16 <sup>+13</sup> <sub>-8</sub>	0.1
100225A	12.7	grbm	-0.50 <sup>+0.25</sup> <sub>-0.21</sub>	-2.28 <sup>+0.07</sup> <sub>-0.09</sub>	223 <sup>+112</sup> <sub>-68</sub>	0.0
100826A	93.7	grbm + bb	-1.02 <sup>+0.04</sup> <sub>-0.04</sub>	-2.30 <sup>+0.03</sup> <sub>-0.04</sub>	484 <sup>+72</sup> <sub>-63</sub>	0.0
101123A	145.4	grbm + cutoffpl	-1.00 <sup>+0.07</sup> <sub>-0.08</sub>	-1.94 <sup>+0.15</sup> <sub>-0.12</sub>	187 <sup>+74</sup> <sub>-62</sub>	5.8
110721A	21.8	grbm + bb	-1.24 <sup>+0.02</sup> <sub>-0.01</sub>	-2.29 <sup>+0.03</sup> <sub>-0.03</sub>	1000 <sup>+28</sup> <sub>-39</sub>	0.0
120328B	33.5	grbm + cutoffpl	-0.67 <sup>+0.06</sup> <sub>-0.05</sub>	-2.26 <sup>+0.05</sup> <sub>-0.05</sub>	101 <sup>+12</sup> <sub>-13</sub>	0.0
120911B	69.0	grbm	-2.50 <sup>+0.92</sup> <sub>-1.04</sub>	-1.05 <sup>+0.63</sup> <sub>-0.38</sub>	11 <sup>+10</sup> <sub>-2</sub>	0.0
121011A	66.8	grbm	-1.08 <sup>+0.10</sup> <sub>-0.21</sub>	-2.18 <sup>+0.11</sup> <sub>-0.16</sub>	997 <sup>+84</sup> <sub>-26</sub>	0.0
121225B	68.0	grbm	-2.38 <sup>+1.02</sup> <sub>-0.40</sub>	-2.45 <sup>+0.06</sup> <sub>-0.07</sub>	11 <sup>+89</sup> <sub>-3</sub>	0.0
130305A	26.9	grbm	-0.76 <sup>+0.03</sup> <sub>-0.03</sub>	-2.63 <sup>+0.06</sup> <sub>-0.06</sub>	665 <sup>+61</sup> <sub>-55</sub>	0.0
131014A	4.2	grbm	-0.55 <sup>+0.33</sup> <sub>-0.98</sub>	-2.65 <sup>+0.17</sup> <sub>-0.19</sub>	255 <sup>+36</sup> <sub>-11</sub>	0.63
131216A	19.3	grbm + cutoffpl	-0.46 <sup>+0.28</sup> <sub>-0.24</sub>	-2.67 <sup>+1.94</sup> <sub>-0.94</sub>	178 <sup>+77</sup> <sub>-92</sub>	0.0
140102A	4.1	grbm + bb	-1.10 <sup>+0.12</sup> <sub>-0.09</sub>	-2.41 <sup>+0.16</sup> <sub>-0.11</sub>	206 <sup>+65</sup> <sub>-92</sub>	2.3
140110A	9.2	grbm	-2.49 <sup>+1.64</sup> <sub>-1.59</sub>	-2.19 <sup>+0.20</sup> <sub>-0.22</sub>	11 <sup>+23</sup> <sub>-3</sub>	0.0
141207A	22.3	grbm + bb	-1.21 <sup>+0.09</sup> <sub>-0.06</sub>	-2.33 <sup>+0.11</sup> <sub>-0.13</sub>	999 <sup>+18</sup> <sub>-70</sub>	0.0
141222A	2.8	grbm + pow	-1.57 <sup>+0.03</sup> <sub>-0.02</sub>	-2.83 <sup>+0.46</sup> <sub>-1.74</sub>	9971 <sup>+390</sup> <sub>-832</sub>	0.0
150210A	31.3	grbm + pow	-0.52 <sup>+0.04</sup> <sub>-0.05</sub>	-2.91 <sup>+0.11</sup> <sub>-0.38</sub>	1000 <sup>+517</sup> <sub>-234</sub>	0.0
150416A	33.8	grbm	-1.18 <sup>+0.04</sup> <sub>-0.04</sub>	-2.36 <sup>+0.13</sup> <sub>-0.21</sub>	999 <sup>+187</sup> <sub>-269</sub>	0.0
150820A	5.1	grbm	-0.99 <sup>+0.56</sup> <sub>-1.30</sub>	-2.01 <sup>+0.82</sup> <sub>-0.27</sub>	303 <sup>+61</sup> <sub>-39</sub>	0.0
151006A	95.0	grbm	-1.35 <sup>+0.06</sup> <sub>-0.03</sub>	-2.24 <sup>+0.07</sup> <sub>-0.08</sub>	998 <sup>+33</sup> <sub>-84</sub>	0.0
160709A	5.4	grbm + cutoffpl	-1.44 <sup>+0.18</sup> <sub>-0.12</sub>	-2.18 <sup>+0.15</sup> <sub>-0.18</sub>	9940 <sup>+373</sup> <sub>-511</sub>	1.0
160917A	19.2	grbm + bb	-0.78 <sup>+3.45</sup> <sub>-1.40</sub>	-2.39 <sup>+0.20</sup> <sub>-0.10</sub>	994 <sup>+634</sup> <sub>-216</sub>	0.9
170115B	44.8	grbm	-0.80 <sup>+0.02</sup> <sub>-0.04</sub>	-3.00 <sup>+0.10</sup> <sub>-0.07</sub>	1000 <sup>+226</sup> <sub>-106</sub>	2.8

background energy spectrum derived from three different GRB observations and manually inject the ALP-induced gamma-ray signal that is subsequently folded with the instrument response function.

### 3.4.1 Background Considerations

We extract background information for each individual GRB using the analysis tool developed by the LAT team, *gtburst*. This tool allows for a selection of the off-signal intervals, which are fitted in each energy channel with a polynomial function in time, resulting in a fitted background count rate. A detailed description of the GRB analysis process with *gtburst* may be found in Sec. 3.5.

Once we obtain the background count rates, we compute their fluences by conducting spectral fitting using a power-law model, half-Gaussian profile, or a combination thereof to find the lowest, highest, and typical values of background fluences for the LLE data selection, for energies starting at  $\sim 30$  MeV and reaching the GeV energies. In addition to the GRB sample listed in Table 3.2, we include three supplementary short GRBs that pass the remaining selection criteria, GRB 081024B, GRB 090227B, and GRB 110529A. The found fluences for GRB backgrounds are computed and plotted as a function of the incidence angle  $\theta$ , shown in Fig. 3.5. It is important to note that for large incidence angles, the LLE effective area drops significantly, resulting in low count rates. In our sensitivity study, we therefore restrict our analysis to GRBs that are less than  $\sim 70$  degrees off-axis, and conduct a study of the median, the lowest and the highest background fluence values. For these GRBs, the lower background count rates reflect a drop in the effective area for LLE events, and *should therefore not be interpreted as GRBs with necessarily lower*

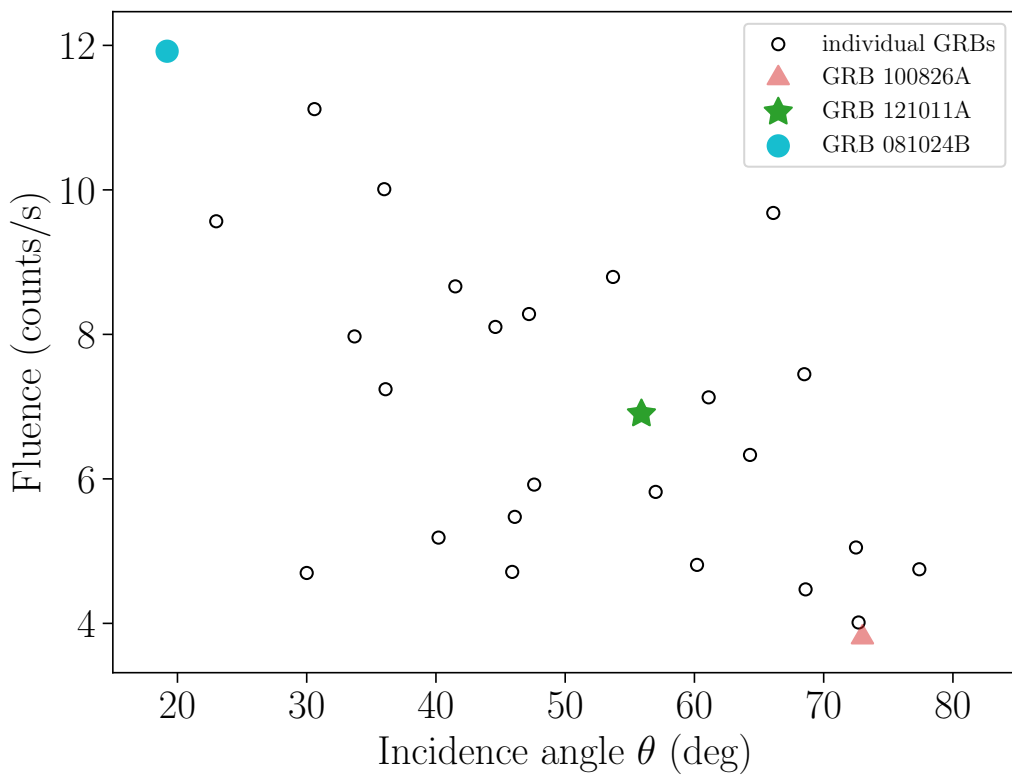


Figure 3.5: Background fluences plotted against the incidence angles to the detector,  $\theta$ . Pink triangle, green star, and blue circle respectively correspond to the lowest, median, and highest background fluences in the sample. Note, however, that low count numbers may be caused by a significant drop in LLE effective area at high  $\theta$ s.

*gamma-ray backgrounds*. Finally, as long GRBs are expected to be uniformly distributed across the sky [145], we may assume a representative ALP-photon conversion probability  $P_{a\gamma}$ , shown in Fig. 3.4, for each considered background in our analysis (albeit, the GRB distribution may be anisotropic if the unassociated sources are very close-by.)

### 3.4.2 Simulating the ALP spectrum

To simulate ALP-induced gamma-ray spectra, we use the *XSPEC*'s `fakeit` function. We consider the ALP spectra in the energy range given by the LLE data file specifications, starting at  $\sim 30$  MeV and reaching the GeV energies. We use the response function and the background observation derived previously from each considered LLE-detected GRB. On top of the scaled ALP-induced gamma-ray signal from Fig. 3.3, we add a realization of the background, taken to be a power-law approximation to the channels' photon rates fits for each considered GRB. The combination of the signal and the background is then passed through the *XSPEC*'s `fakeit` function to create 2000 realizations of spectra corresponding to different normalization values of the ALP signal on top of the observed background levels. An example of a simulation sample resulting from the *XSPEC*'s `fakeit` function is shown in Fig. 3.6.

### 3.4.3 Sensitivity results

To find the *Fermi*-LAT sensitivity to detecting ALP-induced gamma-ray signal originating from a given CCSN using the LLE data, we consider the highest, the lowest, and the median background levels as seen in our GRB sample, respectively corresponding to backgrounds of GRB 081024B, GRB 100826A, and GRB 121011A (also corresponding to the low, high, and

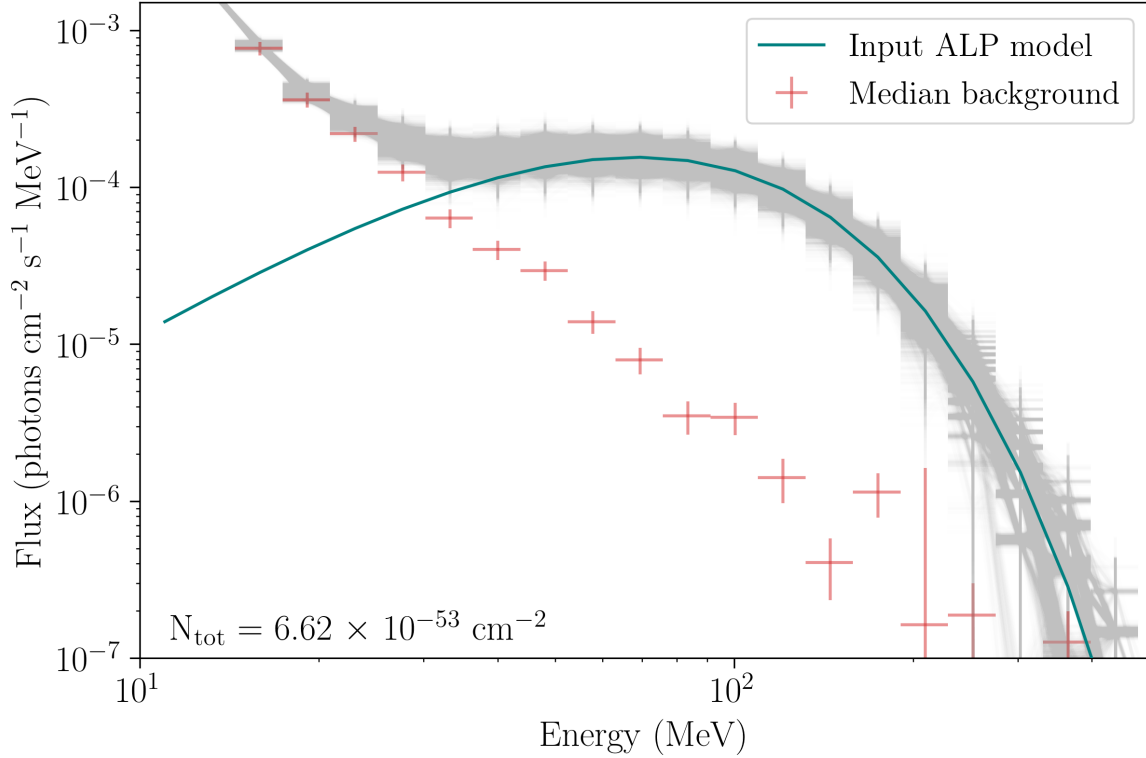


Figure 3.6: *XSPEC fakeit* ALP simulations [146]. Shown in gray is a sample of 2000 realizations of the ALP spectrum for a  $10\text{-M}_\odot$  progenitor and normalization  $N_{\text{tot}} = 6.62 \times 10^{-53} \text{ cm}^{-2}$  (corresponding to a  $\sim 1\text{-Mpc}$  distant CCSN with  $P_{a\gamma} = 0.1$  and  $g_{a\gamma} = 5.3 \times 10^{-12} \text{ GeV}^{-1}$  [122]) on top of the median background, including the background statistical and systematic uncertainties produced with *gtburst*. The solid blue line represents the input ALP signal for the quoted normalization value.

medium  $\theta$ s; see Fig. 3.5). We consider a grid of normalization values for the ALP spectrum,  $N_{\text{tot}}$ , between  $8.4 \times 10^{-60} \text{ cm}^{-2}$  and  $8.4 \times 10^{-50} \text{ cm}^{-2}$ , motivated by *Fermi*-LAT’s expected flux sensitivity. For each of the three background levels, we add the normalized ALP spectrum (60 steps within the range quoted above) and produce 2000 simulations for each data realization for two different progenitor masses (10 and  $18\text{-M}_\odot$ ), resulting in a total of 720,000 simulated spectra. Finally, we conduct spectral fitting for each spectrum, considering two different spectral models. The first model is the ALP model described in Section 3.2 with one free parameter, the total normalization  $N_{\text{tot}}$ , on top of the background model described by a power law with the normalization and power-index as free parameters. The second model is the background-only fit. For both cases, we use *XSPEC*’s `pgstat` statistical method, which describes Poisson data with Gaussian background [154]. Finally, we utilize Wilks’ theorem as applied to the scenario in which the ALP signal: given a large number of realizations of data, the test statistic  $\Lambda = -2 \log(L_{\text{null}}/L_{\text{alternative}})$ , follows a half- $\chi^2$  distribution [155, 156], when no additional ALP signal is injected. In our case,  $L_{\text{null}}$  is the background-only fit,  $L_{\text{alternative}}$  is the ALP model fit, and the difference in the number of degrees of freedom (d.o.f) is one (ALP normalization). For each background consideration, we find a critical signal normalization for which we claim that the ALP model is preferred—taken to be when the log-likelihood analysis indicates half of the  $\Lambda$  values that would have probabilities less than  $5.7 \times 10^{-7}$  if the background-only hypothesis was correct, corresponding to a  $5\sigma$  detection. We use 60 grid steps within the  $N_{\text{tot}}$  normalization range quoted above, with 30 of them a refinement, to accurately determine this “turn-over” point. An example of  $\Lambda$  distributions for a  $10\text{-M}_\odot$  progenitor for the median background (GRB 121011A) is shown in Fig. 3.7.

The values of  $\Lambda$  corresponding to normalization values of  $N_{\text{tot}} = 3.46 \times 10^{-54} \text{ cm}^{-2}$  for

GRB 100826A (lowest background, high  $\theta$ ),  $N_{\text{tot}} = 2.76 \times 10^{-54} \text{ cm}^{-2}$  for GRB 121011A (median background, medium  $\theta$ ), and  $N_{\text{tot}} = 1.51 \times 10^{-54} \text{ cm}^{-2}$  for GRB081024A (highest background, low  $\theta$ ), for a  $10\text{-M}_\odot$  progenitor, favor the ALP model over the background-only model. For a given ALP coupling  $g_{a\gamma}$ , Fig. 3.8 shows the maximum allowed distance to a CCSNe for which a  $5\text{-}\sigma$  ALP signal discovery can be expected (provided the given gamma-ray background and  $P_{a\gamma}$  assumed from Fig. 3.4). On the other hand, if a time- and distance-tagged CCSN is observed without any detected ALP signal, then the yellow curve gives, on average, the expected 90 % CL upper limit to be derived on the ALP coupling  $g_{a\gamma}$ . The right panel of Fig. 3.8 shows an analogous analysis, using the  $18\text{-M}_\odot$  progenitor. For the lowest background (high  $\theta$ ), the corresponding normalization value is  $N_{\text{tot}} = 1.56 \times 10^{-54} \text{ cm}^{-2}$ ; for the median background (medium  $\theta$ ) it is  $N_{\text{tot}} = 1.30 \times 10^{-54} \text{ cm}^{-2}$ ; and finally, for the highest background (low  $\theta$ ) it is  $N_{\text{tot}} = 7.06 \times 10^{-55} \text{ cm}^{-2}$ . The corresponding distance limits for the deduced upper bound on coupling from the SN1987A analysis,  $g_{a\gamma} = 5.3 \times 10^{-12} \text{ GeV}^{-1}$  [122], in addition to a consideration of different conversion probabilities, are summarized in Table 3.3. We remark that at the detection limit, only a few ALP-induced gamma-ray photons would be detected ( $\sim 10$  counts in the LLE sample), which makes it challenging to reliably reconstruct the energy spectrum or to alone trigger a GRB signal detection (considering the look-elsewhere effect in full sky surveys). Finally, we conclude the sensitivity analysis by noting that the distance limit variations in Fig. 3.8 are driven by differences in LLE effective area—thus, the lower background count-rates, shown in Fig. 3.5, are mainly a consequence of decreasing detector acceptances at higher  $\theta$ s.

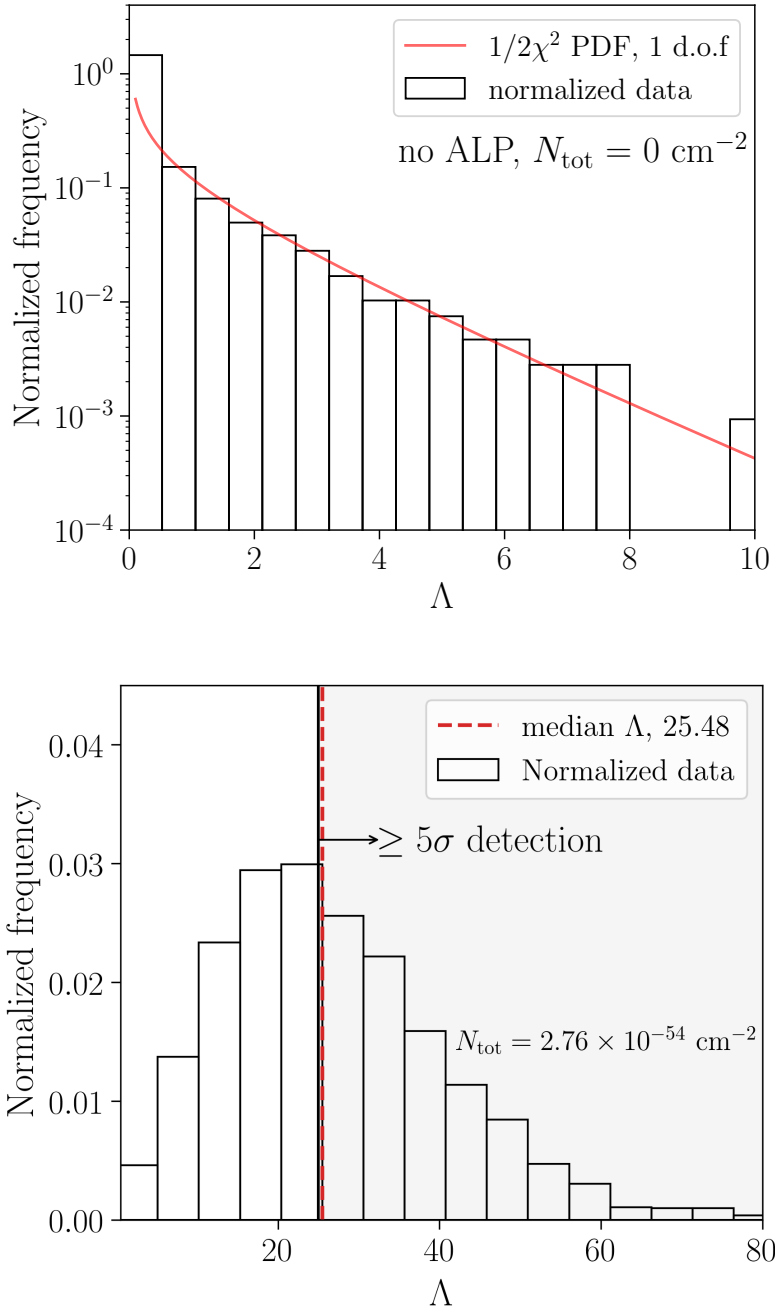


Figure 3.7: Top: demonstration of Wilks' theorem for the considered simulated spectra [155, 156]. The red line is the half- $\chi^2$  distribution with 1 d.o.f. on top of our normalized  $\Lambda$  distribution when no additional ALP signal is injected to the median background. Bottom: the distribution of the same  $\Lambda = -2 \log(L_{\text{null}}/L_{\text{alternative}})$  when an additional ALP signal is injected to the median background. The null model remains the one without an additional ALP component, but the realizations are now drawn from a model with  $N_{\text{tot}} = 2.76 \times 10^{-54} \text{ cm}^{-2}$ , for the case of the median background and a progenitor mass of  $10 M_{\odot}$ . The median  $\Lambda$  represents the median value of the histogram. We determine the sensitivity of our experiment to a deviation from a no-ALP scenario, corresponding to a threshold of  $5\sigma$  or the  $p$ -value of  $5.7 \times 10^{-7}$ .

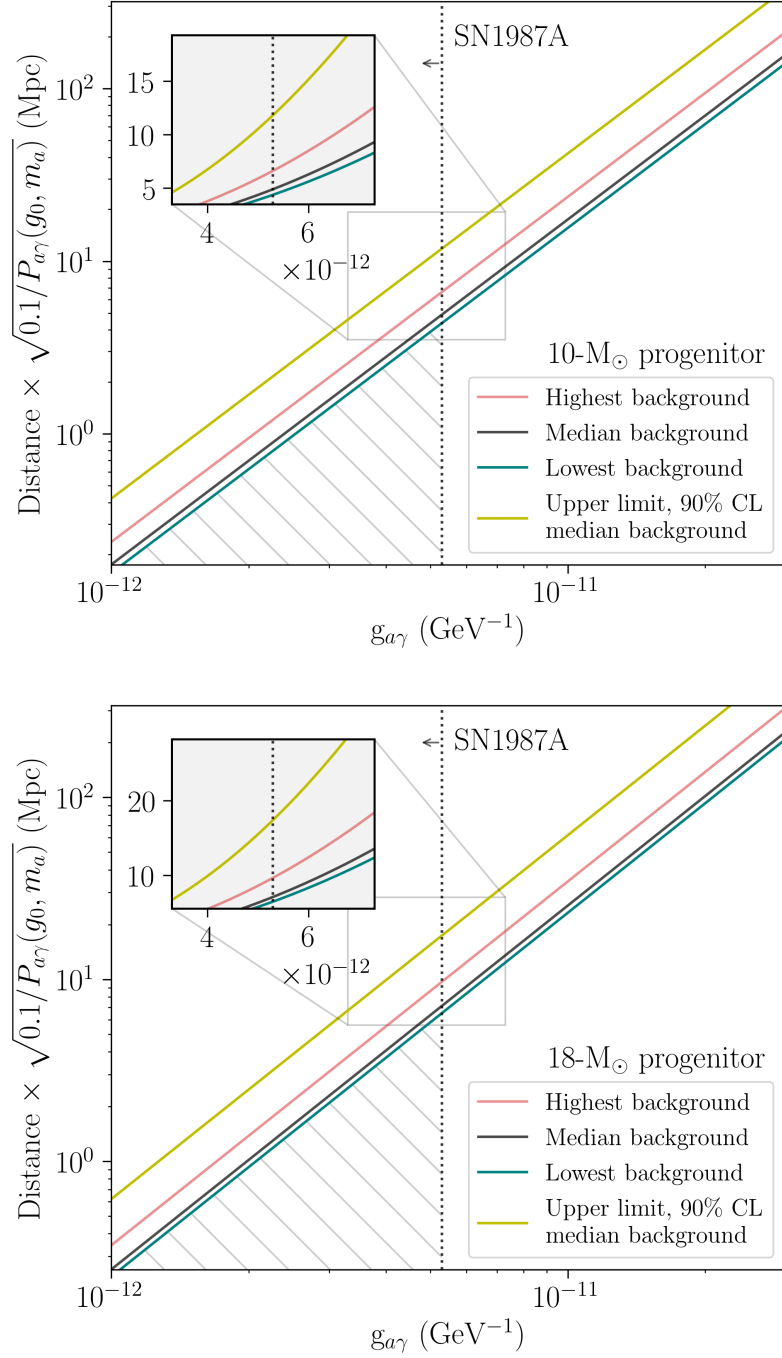


Figure 3.8: Distance limits for a LAT-LLE ALP detection for a  $10\text{-}M_{\odot}$  progenitor (top panel), and an  $18\text{-}M_{\odot}$  progenitor (bottom). The green, black, and red solid lines represent the  $5\sigma$  detection limits on distances with so-far observed background levels from our GRB sample with *Fermi* LLE, while the yellow solid line represents the expected 90% CL upper limit for the median background. The dotted vertical line in each plot shows the upper limit for the ALP-photon coupling,  $g_{a\gamma} = 5.3 \times 10^{-12} \text{ GeV}^{-1}$ , derived in [122]. The hatching in both plots shows the parameter space to which *Fermi* LLE is sensitive, taking into consideration the SN1987A upper limit on the ALP-photon coupling.

Table 3.3: Maximum distance to the ALP source to be within reach of the *Fermi*-LLE sensitivity. We assume the ALP-photon coupling  $g_{a\gamma} = 5.3 \times 10^{-12} \text{ GeV}^{-1}$  [122] for different ALP-photon conversion probabilities,  $P_{a\gamma}$ , as seen in Fig. 3.4. Distance limits are in Mpc, shown for a  $10\text{-M}_\odot$  progenitor on the left, and  $18\text{-M}_\odot$  in parentheses on the right, for different background levels. Note that the different background levels are dependent on the LLE effective area, which decreases with an increase in  $\theta$ , hence lowering the event rate in the detector (see Fig. 3.5). This, however, is not an indicator of the intrinsic GRB background levels, but rather detected counts in the instrument.

Conversion probability $P_\gamma(g_0)$	Distance limit (Mpc)		
	<i>Background level:</i>		
	<i>Low</i>	<i>Median</i>	<i>High</i>
0.1	4.4 (6.5)	4.9 (7.1)	6.6 (9.7)
0.05	3.1 (4.6)	3.5 (5.0)	4.7 (6.9)
0.01	1.4 (2.1)	1.5 (2.3)	2.1 (3.1)
0.001	0.4 (0.7)	0.5 (0.7)	0.7 (1.0)

### 3.5 Search for an ALP signal within the selected GRB sample

We consider the selected sample of unassociated GRBs in Table 3.2 and conduct a spectral fitting for each GRB to find the highest significance for an inclusion of the ALP spectral component. Although it is unlikely that a nearby star’s core-collapse would remain an undetected CCSN to the current optical all-sky surveys, such as [157–162], or that an ordinary GRB would arrive without a time delay to the ALP signal from the core-collapse, we here make the ansatz to search for an ALP signal only within the detected GRB signal time window. We consider a null model to include components commonly used to describe ordinary GRB emission, and compare it to the alternative including the additional ALP component.

### 3.5.1 Data Preparation

The data in our sample was obtained from the public *Fermi Science Support Center* (FSSC) website<sup>7</sup>. To analyze data, we use the *Fermi* Science Tools<sup>8</sup> in combination with the HEAsoft *XSPEC* spectral fitting software<sup>9</sup>. We conduct a combined analysis between GBM, LLE, and standard LAT transient data using the analysis tools commonly used in the high-energy transient community [146].

The GBM analysis is done using *gtburst*<sup>10</sup>. We conduct a binned analysis of the GBM data. Firstly, we compute the overall signal-to-noise ratio (SNR) for twelve GBM detectors and consider the three strongest signals recorded in the NaI detectors and one signal from a BGO detector for the spectral analysis. To determine the background, we use *gtburst* to specify off-signal intervals, fit a polynomial to each channel of the detector, and interpolate these polynomials to compute a background spectrum over a given time interval. For each GBM detector, we consider the same time interval of the burst, determined by visual inspection, approximately corresponding to the flattening of the light curve with the background level. The corresponding GRB duration is listed as  $T_{95}$  in Table 3.2, reflecting the time interval reported in Table III in [145]. Finally, we produce spectral and background files appropriate for the analysis in *XSPEC*.

The preparation of the LLE data follows the same pathway as that of the GBM data. We assume the same burst duration as determined by the GBM value of  $T_{95}$  in Table 3.2.

With its lower number of counts, LAT transient data requires a different approach utilizing an unbinned analysis. Due to the transient nature of the source, we make use of the event class

<sup>7</sup><https://fermi.gsfc.nasa.gov/ssc/data/>, accessed on April 23, 2019.

<sup>8</sup><https://fermi.gsfc.nasa.gov/ssc/data/analysis/software/>, accessed on April 23, 2019.

<sup>9</sup><https://heasarc.gsfc.nasa.gov/lheasoft/>, accessed on April 23, 2019.

<sup>10</sup><https://github.com/giacomov/gtburst>

P8R3\_TRANSIENT020\_v2, analyzed with the corresponding galactic and isotropic diffuse templates<sup>11</sup>, over a time interval determined by the T<sub>95</sub> values referenced in Table 3.2. Using *gtburst*, for most GRBs, we perform a zenith cut of 100°, with a few-degree variation depending on a given source. We conduct a maximum likelihood analysis of the LAT source to obtain a LAT counts map within the considered region of interest (RoI, usually 12°). Once we obtain likelihood fit result parameters using *gtlike*, we proceed onto creating energy-binned background files using *gtbkg* and spectral files of energy-binned signal counts using *gtbin*, both readable by *XSPEC*. Throughout this analysis, we use the point-source localization information provided in the *Fermi* LAT Second GRB Catalog, 2FLGC [145].

### 3.5.2 XSPEC analysis

We conduct a standard spectral fitting procedure of the selected GRB sample [163]. Fitting is conducted in *PyXspec*, an object-oriented Python interface to *XSPEC*<sup>12</sup>. When modeling the spectral shape of a given GRB, we consider models commonly used in GRB spectral fitting, including single power law (denoted `pow` in Table 3.2), power law with a high-energy exponential cut-off (also known as “comptonized model”, `cutoffpl`), the phenomenological Band function [153] (`grbm`), or a combination thereof. We also include a consideration of an additional thermal component in the form of a blackbody spectrum (`bb`), as suggested in [163, 164]. Appendix A provides the details about the used models. We apply *XSPEC*’s `pgstat` statistical method [154] and find the fit with the lowest test statistic (in *XSPEC* denoted by `PG-statistic`), obtaining profile log-likelihood (LL) values from the combined GBM, LLE and LAT transient data. We

---

<sup>11</sup><https://fermi.gsfc.nasa.gov/ssc/data/access/lat/BackgroundModels.html>, as accessed on April 23, 2019.

<sup>12</sup><https://heasarc.gsfc.nasa.gov/xanadu/xspec/python/html/index.html>, accessed on April 23, 2019.

note that the ALP spectral model may be well-reproduced for a specific range of parameters of the Band function; in particular, for a  $10\text{-M}_\odot$  progenitor in Fig. 3.3 the corresponding Band model parameters are  $\alpha_1 \simeq 2.4$ ,  $\alpha_2 \simeq -0.1$ , and  $E_c \simeq 30$  MeV. However, in the considered GRB sample, these parameter values are not reached, as shown in Table 3.2, and are not expected for ordinary GRB spectral shapes. Similarly, the ALP spectral shape can be reproduced reasonably well with a blackbody function described by a peak temperature of  $\sim 70$  MeV; however, all the GRBs listed in Table 3.2 that are best fit by including a blackbody spectral component (GRBs 100826A, 110721A, 140102A, and 160917A) peak at the keV temperatures. For each model, we step through the neighboring fit parameter values to ensure that the best-fit parameters found from the maximum LL analysis are likely global, and not local minima.

To compare two nested models, we apply the log-likelihood ratio (LLR) test  $\Lambda = -2 \log(L_{\text{GRB}}/L_{\text{GRB+ALP}})$ , with  $L_{\text{GRB}}$  corresponding to the likelihood of the null hypothesis, i.e. the GRB model constituting of commonly used functions for ordinary GRB emission.  $L_{\text{GRB+ALP}}$  corresponds to the alternative hypothesis, constituting of an ALP signal added on top of the null model, with all the considered parameters left free to vary. Table 3.2 contains results of the model comparison of our data sample, using the  $10\text{-M}_\odot$ -progenitor ALP spectral model. We note that the  $18\text{-M}_\odot$ -progenitor has an almost identical spectral shape, leaving the results essentially independent on these two progenitors masses.

### 3.5.3 ALPs from GRBs: fitting results

None of the GRBs in the considered sample showed a significant improvement in the fit when including the additional ALP signal component. The model comparison for one GRB,

101123A, indicates a  $\Lambda$  value of 5.8, corresponding to  $\sim 2.4\sigma$  detection, pre-trials. The data and the fitted models for GRB 101123A are shown in Fig. 3.9 with an inplot showing the difference between the best null model and the alternative model with the additional ALP component.

This alternative best-fit hypothesis has an ALP component with the normalization  $N_{\text{tot}} = 4.9 \times 10^{-52} \text{ cm}^{-2}$ . Applying the coupling  $g_{a\gamma} = 5.3 \times 10^{-12} \text{ GeV}^{-1}$  and a conversion probability  $P_{a\gamma} = 0.01$  (see Fig. 3.4 for this GRB's sky position), we find that the corresponding distance would be  $\sim 120$  kpc. Note that GRB 101123A was observed strongly off-axis, at an incidence angle of  $\sim 80^\circ$ . Under such conditions, LLE's effective area decreases significantly. Thus, even a source with such a large  $N_{\text{tot}}$  value of the ALP component results in only few counts and no reconstructed energies above  $\sim 50$  MeV.

We then include the trials factor [165], to take into account the size of the considered parameter space, and express the global significance by  $p_{\text{global}} = 1 - (1 - p_{\text{local}})^{N_{\text{trials}}}$ . From the local  $p$ -value,  $p_{\text{local}} = 1.6 \times 10^{-4}$  and the number of GRB trials in our sample,  $N_{\text{trials}} = 24$ , this results in a global  $p$ -value of  $\sim 0.3$ , further indicating that this observation is not statistically significant.

### 3.6 Conclusions and Discussion

In this paper, we consider the light ALPs produced via the Primakoff process in a collapse of a massive star which, by converting into photons in the Galactic magnetic field, could produce an observable gamma-ray flux. The duration of an ALP burst is expected to be on the order of  $\sim 10$  seconds. Due to its uncertain and likely negligible effect, we do not take into consideration the ALP-photon conversion that may take place in the magnetic field of the intergalactic medium and,

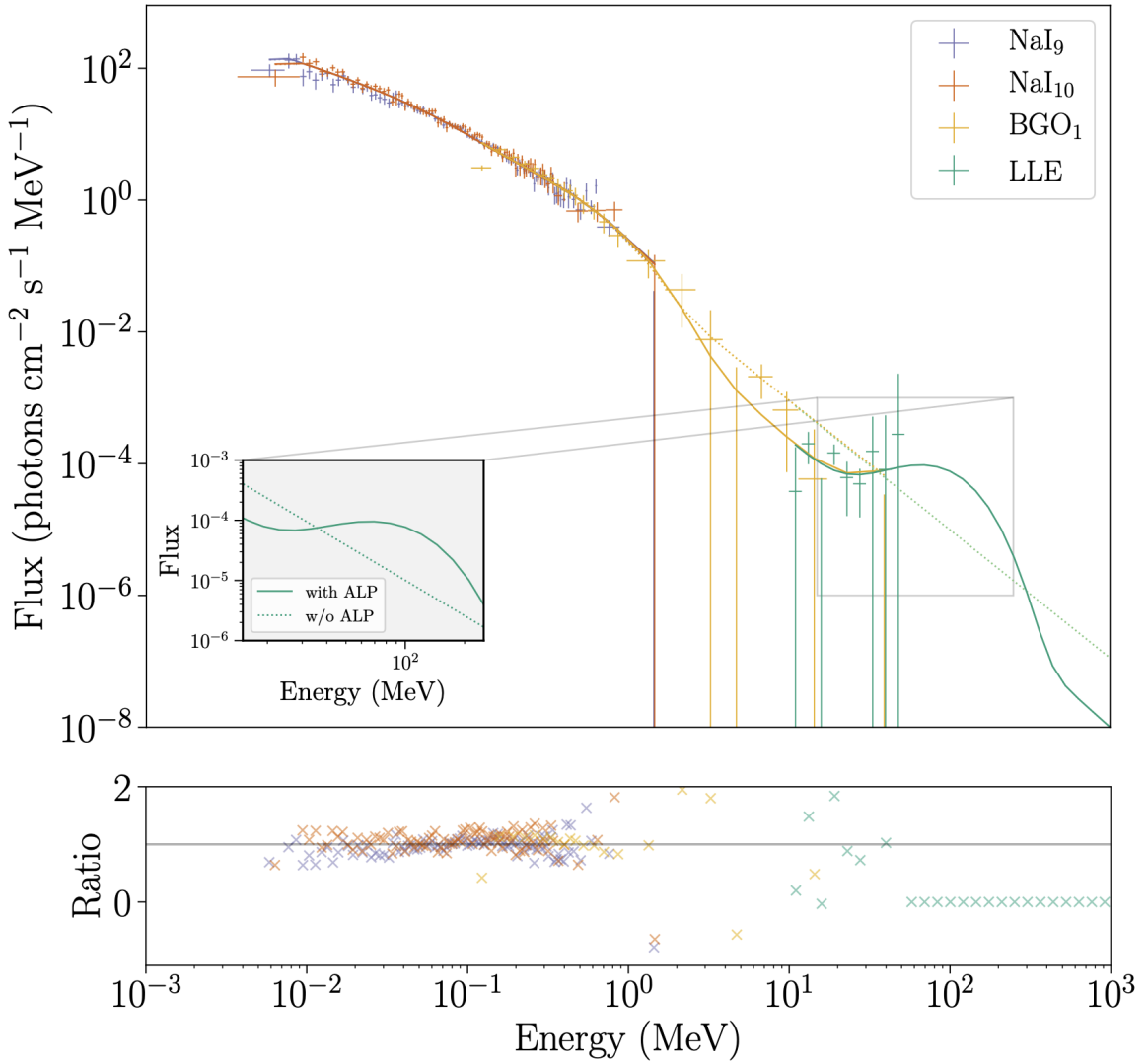


Figure 3.9: GRB 101123A  $\gamma$ -ray flux with two different overlaid models. Different colors represent counts obtained by different detectors: purple, red, yellow, and blue correspond to NaI<sub>9</sub>, NaI<sub>10</sub>, and BGO<sub>1</sub> detectors on GBM respectively; and green corresponds to the LLE transient data. The solid lines represent unfolded model fits for each instrument when the additional ALP component is included, whereas the dotted lines are the best-fit model without the additional ALP component. The inplot shows the difference between the alternative and the null model in more detail: the solid green line represents the alternative model and the dotted line is the null model. The alternative model is composed of a Band function, exponential cut-off function, and the ALP signal. Finally, the lower panel shows the ratio of the observed data to the corresponding model that includes the ALP component, i.e. data/model. For plotting purposes only, the GBM data is shown binned, whilst LLE data is shown with the original binning provided by the instrument.

due to a lack of magnetic field models, we do not take into consideration ALP-photon conversions that may take place within the host galaxy. In fact, the contribution from the host galaxy would increase the observed gamma-ray flux, rendering our current results conservative. Furthermore, due to the complexity of core-collapse modeling, we only consider two CCSN progenitor masses: 10 and  $18 M_{\odot}$  [122]. However, theoretical considerations suggest that long GRBs are produced in explosions of very massive ( $\gtrsim 20 M_{\odot}$ , [166]) stars which, in turn, would produce a higher number of ALPs as compared to a lower mass progenitor. Thus, the combination of our magnetic field and progenitor mass choices renders our reported results conservative.

We find the sensitivity of the *Fermi*-LAT instrument using the LLE data sample including energies  $\gtrsim 30$  MeV to detect ALP-induced gamma-ray emission from CCSNe for ALP masses  $m_a \lesssim 10^{-10}$  eV. In particular, we consider a sample of GRB backgrounds and compute the maximum allowed distance to core-collapsing stars that still give statistically significant,  $5\sigma$ , ALP-signal detection. For the lowest background, we obtain that the limiting distance is  $\sim 3$  Mpc for the conversion probability,  $P_{a\gamma} = 0.05$ , for a  $10-M_{\odot}$  progenitor, and  $\sim 5$  Mpc for an  $18-M_{\odot}$  progenitor, for a coupling of  $g_{a\gamma} = 5.3 \times 10^{-12}$  GeV $^{-1}$  [122]. For the highest background count, the farthest distance corresponds to  $\sim 5$  Mpc and  $\sim 7$  Mpc; and for the median background, it is  $\sim 3.5$  Mpc and  $\sim 5$  Mpc for 10- and  $18-M_{\odot}$  progenitors respectively. Finally, the distance limits reported in this paper, in addition to the observed background levels, are driven by LLE effective area variation that tends to decrease for observations at larger instrumental incidence angles—and thus lower background count rates. These limiting distances for an ALP-signal detection from a CCSN for different conversion probabilities and axion-photon couplings  $g_{a\gamma}$  are shown in Table 3.3 and Fig 3.8. The results found in this paper by utilizing the LLE data cut technique and its resulting data sample are comparable to those done with the standard LAT analysis in [123]. As

such, conducting a search for an ALP signal from a close-by CCSN using the LLE technique, independent from or in parallel with the standard LAT analysis, can be a useful way of probing the ALP parameter space. Furthermore, the distance limits found in this investigation may be complemented by utilizing the upper energy range of the better-resolved GBM data, or the rest of the LAT transient data, to search for the tail distribution from the ALP-induced gamma-ray emission.

Finally, we consider a sample of unassociated, thus potentially nearby, LLE-detected GRBs (see Table 3.2). We conduct a spectral model fitting for each candidate using the *XSPEC* library models commonly used for GRB spectral modeling. Once the best-fit for an ordinary GRB spectrum is determined, we conduct an analogous modelling procedure by introducing an additional ALP spectral component. We find that all of the GRB emissions in our sample are well-fitted by commonly used GRB spectral models and that introducing an additional ALP spectral component does not result in a statistically significant improvement.

In this chapter, we assume that the ALP-induced gamma-ray signal itself triggers the GRB observation, i.e., that the ALP signal from a CCSN coincides with the ordinary GRB signal, which is unlikely to be the case. The main source of uncertainty is determining the core-collapse time, and thus the expected arrival time of any ALP-induced GRB. Therefore, an interesting investigation would be a dedicated search for potential ALP induced gamma-ray photons arriving before the GRB trigger times. As suggested in [150], using optical lightcurves to predict explosion times may be another way of attempting these analyses, as done in [37]. Nevertheless, the optimal resolution for the time-tagging issue is using neutrino detection from a CCSN, followed by a search for ALP emission in the coincident gamma-ray observation; although, at this time, no such coincident detection has been confirmed in association with a GRB.

The GRB model comparison analysis does not allow for a deduction of the limits on the ALP coupling,  $g_{a\gamma}$ . In order to obtain such information, we would require the GRBs' distance information, as done in [37]. With the current and upcoming optical surveys such as ASAS-SN [167], ZTF [168], TESS [169], and the Vera C. Rubin Observatory [170], the number of the observed nearby CCSNe (e.g.  $z < 0.02$  or 100 Mpc), [37]) is likely to increase. This, in turn, would improve the probability of *Fermi* detecting their corresponding GRBs, allowing for a statistically significant study of such sources in the context of ALP searches and limits on the relevant ALP coupling space. An example of such an analysis determining the upper limits on the ALP coupling is shown in [37].

Furthermore, with the new generation of gamma-ray instruments, such as e-ASTROGAM [171], ComPair [172], PANGU [173], or alike, the improved sensitivity and angular resolution particularly at energies relevant to the ALP signal ( $< 100$  MeV) and FoV's similar to *Fermi* LAT, the search for ALP-induced GRBs will be substantially improved. In particular, observatories such as AMEGO [174], with its excellent sensitivity, angular and energy resolution, low energy threshold, and a large field of view, will allow for the most stringent constraints on the ALP parameter space, surpassing the limits of the current ALP laboratory experiments<sup>13</sup>.

Finally, besides CCSNe, additional astrophysical objects may be considered as sites of ALP production. In particular, a production of ALPs has been hypothesized during NS mergers; albeit further theoretical work is needed to constrain the expected ALP spectrum from such events [175]. Taking into consideration the most recent observations from NS mergers using e.g. LIGO/Virgo [176], as well as a rapid development of the field of MMA, using GWs may be yet

---

<sup>13</sup>[https://www.snowmass21.org/docs/files/summaries/CF/SNOWMASS21-CF3\\_CF2\\_Regina\\_Caputo-122.pdf](https://www.snowmass21.org/docs/files/summaries/CF/SNOWMASS21-CF3_CF2_Regina_Caputo-122.pdf), as accessed on April 6, 2021.

another probe into the production time and nature of ALPs in the future (see [Epilogue](#)).

## Chapter 4: Light at the end of the tunnel: ALPs and GRB precursors

*This world needs those who could find a tunnel that has no light at the end of it, and hold it up like a telescope to know the darkness also contains truths that could bring the light to its knees.*

---

Andrea Gibson

In this chapter, we further investigate the properties of GRB emission in the context of ALP searches with *Fermi* LAT<sup>1</sup>. In particular, we apply the hypothesis that the ALP emission should precede that of the jet outbreak after a collapse of a massive star. With the observationally suggested causal connection between CCSNe and long GRBs, we conduct a spectral analysis of the *Fermi*-observed long GRBs through identifying a sample exhibiting signs of *precursor* emission. This approach provides a previously unexplored venue in the context of ALP searches. To avoid redundancy, parts of the introduction, observatory, model-fitting, and the LLE technique details presented in the paper are omitted here. I proceed assuming that the reader is convinced that ALPs are plausibly real and gamma-ray observations of GRBs can provide insights into their properties (see Chapters 2 and 3 for more detail).

---

<sup>1</sup>The work in this chapter is currently undergoing the internal review from the *Fermi*-LAT Collaboration and is presented here with minimal modifications. This work has been previously shared on a number of occasions, including the *Fermi* Collaboration Meetings and the 241st AAS Conference. The work conducted here is funded through the *Fermi* Cycle-15 Guest Investigator Program, PI: M. Crnogorčević.

## 4.1 Motivation

As established in Chapter 3, the arrival time of the ALP burst from a CCSN follows that of neutrinos. However, due to the sensitivity limitations of the current generation of neutrino detectors, we expect no significant neutrino signal from a distant CCSN. While Galactic CCSNe would be an excellent probe into the nature of ALPs, not only are they infrequent ( $\sim 1$  per century) but they also have to occur inside the FoV of the current gamma-ray instruments to provide the necessary data to search for the ALPs, making this approach unpromising at this time [123]. Other techniques have been employed to determine the CCSN collapse time—and consequently, the ALP explosion time—including the consideration of the optical observations of the nearby CCSNe [37] or long GRBs [1]. Combined with theoretical models, these investigations indicate that the gamma-ray emission from the ordinary long GRB is delayed by a few seconds to hours with respect to the time of the star’s collapse [133].

In this chapter, we conduct a novel search for ALPs within a time window that precedes the main-episode gamma-ray emission formed in the jet, focusing on the long GRBs with known *precursors* detected with the *Fermi*-LAT instrument. Motivated by the delay between the time of the core-collapse of a massive star, i.e. the ALP emission time ( $T_a$ ); and the time of the jet break-out associated with its ordinary long GRB emission ( $T_{\text{GRB}}$ ), we conduct an investigation of the gamma-ray emission that occurs prior to the prompt emission of a long GRB.

The chapter is organized as follows. Section 4.2 provides an overview of theoretical models of different GRB emission phases. In Section 4.3, we present the data selection process and the precursor consideration. In Section 4.4.2, we describe the ALP model used in our analysis. Section 4.5 summarizes the results of the spectral fitting in our precursor sample, with a special

emphasis on the recently-detected GRB 221009A. Finally, Section 4.6 provides the summary and a discussion of the results.

## 4.2 The life of a GRB

The observed variability and diverse lightcurve structure indicate that GRB emission is a complex phenomenon<sup>2</sup> The most commonly used model assumes that a GRB is powered by a BH produced either in a CCSN or a BHNS merger event. This BH is engulfed in an accretion disk, whose gravitational energy or, alternatively, the accretion of magnetic flux can result in a formation of a jet. Some models indicate that a millisecond magnetar could also power jets by extracting its spin-down energy. In a BNS merger event, a jet may be formed during the NS’s short-lived hypermassive stage that forms soon before the system’s final collapse into a BH. Although numerous theoretical models have been put forward, at this time, we still need a clearer understanding of the properties of the central engine that fuels the jet’s formation. Nevertheless, once it is formed, the jet’s journey—firstly through its local environment and later through the intergalactic space—may commence.

The GRB emission is characterized through its two most energetic phases: 1) the prompt gamma-ray phase, originating from the ultra-relativistic matter outflows, and 2) the afterglow phase, caused by collisions of the released material with the surrounding medium and resulting in a wide-wavelength (radio to X-ray) emission. In addition to these two phases, some GRBs also exhibit an early onset emission prior to the prompt phase, often referred to as the *precursor emission*. Precursor emission consists of one or multiple faint gamma-ray flashes prior to the main prompt episode.

---

<sup>2</sup>The GRB review presented here is in large part based on [177] and references within.

**The prompt phase.** The prompt phase of the GRB emission is believed to originate from the internal shock processes. Due to different densities within the jet, parts of it will travel at different Lorentz factors causing them to eventually interact and produce internal shocks. Areas with very high densities and pressures are formed in these interactions, resulting in powerful local magnetic fields. Electrons and positrons from the jet repeatedly enter these magnetic fields and are accelerated in a process known as Fermi acceleration. However, the Fermi acceleration cannot last indefinitely—electrons will eventually start losing energy as they interact with magnetic fields through synchrotron interactions and thus emit photons that we observe as the GRB prompt emission. Other processes, albeit to a lesser extent, may also be present, such as the synchrotron self-Compton emission or potential cascades of Fermi-accelerated hadrons.

**The afterglow phase.** The GRB’s afterglow phase results from shocks produced in the jet’s interactions with the material expelled in the explosion, as well as the material in the interstellar medium. As it propagates, the jet compresses the gas and dust in its path, resulting in external shocks—both in forward and reverse directions (within the jet’s frame of reference). The forward-moving shock will accelerate electrons and result in the high-energy afterglow emission. The reverse, slower-moving shock will also accelerate particles—but to lower energies, resulting in the emission of UV and optical photons. These processes, however, are much more complicated than described here—and many additional components may be at play (see, e.g., for a review). The afterglow emission can last for days to weeks after the initial burst of gamma rays. Its properties provide essential information about the nature of the surrounding environment and the physical processes that drive the explosion.

**The precursor phase.** Finally, the precursor phase is the least understood among the GRB phases. Several theoretical models have been proposed to address the astrophysical origin of

the precursor emission, including the internal and external shock models, photospheric emission model, magnetic reconnection, mini-jets, geometrically thin shells, supra-photospheric model, and gravitational lensing; however, no single model can be used to explain the precursor's astrophysical origin fully. To further complicate things, different works have used conflicting definitions of precursors. While some models are very good at explaining, e.g., the duration of the precursor, they may not be so good at explaining its spectral properties. Still, due to the different definitions of precursors, comparing distinct theoretical models is a challenging task.

In this chapter, we adopt the following definition: an ALP-induced precursor is an observed excess of gamma-rays from a GRB, lasting at most 50 seconds and after which the observed flux returns to the background level. We impose no duration requirement on the quiescent interval between two pulses. The precursor duration is motivated by the expected duration of an ALP burst from a CCSN. Following the quiescent interval, which can span seconds to minutes, we observe another flash of gamma rays associated with the jet emission. We impose no requirements on whether the ALP-induced precursor triggers the detection algorithm onboard *Fermi*-LAT: either or both ALP-induced precursor and jet emission can trigger a detection in our work.

### 4.3 Data Selection

Firstly, we consider a total of 93 GRBs detected with the LLE technique from August 2008 to December 2022, as reported in the *Fermi*-LAT Second Gamma-Ray Burst Catalog, 2FLGC, or notices published via the Gamma-ray Coordinates Network (GCN) Circulars (see Section 3.3 for more details about the LLE technique). Separately, we consider a total of 238 GRBs observed with *Fermi*-LAT in the same time frame. A total of 17 GRBs were observed with the LLE

Table 4.1: Selection criteria applied to a total of 255 GRBs detected by *Fermi*-LAT between August 2008 and December 2022.

Property	Selection Criterion
Observed time interval	inside LAT FoV for $\sim 1000$ s prior to the trigger time $T_0$
Burst duration	long GRBs ( $T_{90} \gtrsim 2$ seconds)
Precursor confirmed	BB algorithm (see 4.4.1)
GBM precursor	no temporal coincidence

selection cut only. The same selection criteria are applied to both the LAT- and LLE-detected GRBs and are summarized in Table 3.1.

We consider the selected GRBs in Table 4.2 and 4.3 and conduct a time-resolved spectral fitting for each separated pulse observed in the sample to find the highest significance for of the ALP spectral fit. We consider a null model to include components commonly used to describe ordinary GRB emission, and compare it to the alternative including the additional ALP component.

We also note that, although the precursors have been identified in the GBM data for a number of observed GRBs (see, e.g., thesis work by Sylvia Zhu in [178]), such emission cannot be explained by the ALP model used in our analysis. Precursors observed with GBM spectrally peak in the keV energy range, and as such must be explained by astrophysical processes different from the ALP-photon conversion models described in this chapter.

## 4.4 Analysis

**Data preparation.** We obtain the LAT and LLE lightcurve data from the publicly accessible *Fermi Science Support Center* (FSSC) website<sup>3</sup>. The lightcurve analysis is done using the

---

<sup>3</sup><https://fermi.gsfc.nasa.gov/ssc/data/>, last accessed on February 28, 2023.

*Fermi* Science Tools<sup>4</sup>, as integrated within the ThreeML software package<sup>5</sup>, which we use to conduct the LLE precursor spectral analysis. The response functions for the LLE lightcurves are done using Monte Carlo simulations of a bright source at the position of the observed GRB (see Sec. 3.4).

#### 4.4.1 Bayesian Blocks

To search for precursor emission within LAT and LLE GRB lightcurves, we utilize the Bayesian Block (BB) analysis method, a non-parametric algorithm used for detecting and characterizing structures in data, particularly useful for detecting excess emission for transient sources in the *Fermi*-LAT observations. Developed in [179] and modified in [180, 181], this analysis tool is applied to segment the data based on sudden changes in the count rate.

The algorithm relies on the Bayesian statistics, i.e., it assigns a prior probability distribution to the number of blocks, and updates this prior based on the data. A smaller probability is assigned to a larger number of blocks (ideally, we would not want a connect-the-dots outcome, i.e.,  $n - 1$  blocks for  $n$  data points) and is given by the following expression:

$$P = P_0 \gamma^{N_{\text{blocks}}}, \quad (4.1)$$

where  $P$  is the prior probability distribution for the number of blocks (i.e., the prior assigned before seeing any data),  $P_0$  is the normalization constant, and  $\gamma$  is the “penalty” parameter for increasing the number of blocks typically set between 0 and 1, with smaller value corresponding

---

<sup>4</sup><https://fermi.gsfc.nasa.gov/ssc/data/analysis/software/>, last accessed on February 28, 2023.

<sup>5</sup><https://github.com/threeML>, last accessed on March 19, 2023.

to a larger number of blocks,  $N_{\text{blocks}}$ . The Bayes' factor is then used to compare two different hypotheses: if we have two models,  $M_1$  and  $M_2$ , with their prior probabilities  $P(M_1|D)$  and  $P(M_2|D)$ , the Bayes' factor is then given by

$$\mathcal{K} = \frac{P(M_1|D)}{P(M_2|D)} = \frac{P(D|M_1)P(M_2)}{P(D|M_2)P(M_1)} \quad (4.2)$$

by the Bayes' theorem<sup>6</sup>. Then,

$$\mathcal{K} = \frac{\mathcal{L}_1 P(M_2)}{\mathcal{L}_2 P(M_1)} = \frac{\mathcal{L}_1}{\mathcal{L}_2} \gamma^{(N_{\text{blocks},2} - N_{\text{blocks},1})}, \quad (4.3)$$

where  $D$  is the observed data and  $\mathcal{L}_x$  is the likelihood of the model  $M_x$  ( $x \in 1, 2$ ). Scargle *et al.* [179] determine, through simulations of the unbinned GRB data, that the prior, *ncp-prior*, is given by

$$ncp\_prior = 4 - 75.53p_0N^{-0.478}, \quad (4.4)$$

where  $p_0$  is the false positive rate, and  $N$  is the number of events. Additionally, in contrast to the standard BB algorithm in [179], which identifies the excess signal via comparison to the constant count rate in the data, the code used in our analysis is modified to account for LAT's changing exposure to avoid misidentifying the instrument-caused fluctuations as a real astrophysical signal by applying the IRFs [181]. This adjustment is of particular importance for LAT-related analyses. In contrast to, e.g., GBM, where we can retrieve multiple independent data sets from different detectors, we only have one observation for LAT. Thus, we cannot do a cross-check to search for detector-specific effects and have to carefully account for the instrument response.

---

<sup>6</sup> $P(A|B) = P(B|A)P(A)/P(B)$ .

**Lightcurve analysis.** We consider all the GRBs observed with *Fermi*-LAT and analyze their corresponding lightcurves. We define a 2000-second “search” time window centered at the trigger time determined by LAT,  $T_0$ , along with two ”off-pulse“ windows, spanning a few-hundred-second interval outside the time of the main pulse (and anything that may seem like a precursor). A polynomial function (usually of the zeroth or first order) is then fit to the gamma-ray counts in the off-pulse windows to estimate the background level during the “on-pulse”. To correct for the effects of the Earth’s atmosphere in the observed gamma-ray data, this background level is multiplied by the cosine of the LAT zenith angle relative to the source location in the sky, determined from the given observation of the GRB in question.

Once the background is fit, we proceed to conduct the BB analysis. Analogously to [179], we select a  $p_0 = 0.05$ , which is appropriate for the *unbinned* LLE and LAT data. By visual inspection of each lightcurve, we determine a GRB sample with a potential precursor emission, resulting in a selection of seven LLE-detected GRBs listed in Table 4.2 and 7 GRBs using the standard LAT event cuts (Table 4.3). Once the data have been segmented using the BB algorithm, we conduct a time-resolved spectral analysis on each time window separately.

#### 4.4.2 The ThreeML GRB Analysis

The Multi-Mission Maximum Likelihood software, or ThreeML, is an open-source Python package that allows for a multi-mission analysis of the X-ray, gamma-ray, and neutrino data<sup>7</sup>. It is widely used in the single- and multi-messenger community, providing a user-friendly, Python-based interface for likelihood model fitting and comparison. The ThreeML contains a suite

---

<sup>7</sup>The ThreeML package is publicly available at <https://github.com/threeML/threeML>, with the corresponding documentation at <https://threeML.readthedocs.io/en/stable/>, as accessed on March 12, 2023.

of built-in models for spectral and time-series analysis but also allows for user-defined models to carry out parameter estimation with maximum likelihood (ML) and Bayesian methods. I note that, while the *XSPEC* approach to *Fermi*-LAT and LLE data analysis used in Chapter 3 applies to the study presented here, I opt to build the ALP-search pipeline within the `ThreeML` framework in anticipation of the future multi-wavelength and messenger efforts for which this package was primarily designed.

**The ALP model in `ThreeML`.** Analogously to Sec. 3.2, we define the ALP spectral model using the tabulated form for each progenitor mass within `threeML` via the Python `astromodels` package, with the normalization value,  $N_{\text{tot}}$ , left free to vary. In addition to the previously considered  $10\text{-M}_\odot$  and  $18\text{-M}_\odot$  progenitors in Chapter 3, we also include the recently tabulated ALP spectral signature for a  $40\text{-M}_\odot$  progenitor<sup>8</sup>. We generate the ALP spectra as seen on Earth by scaling the observed photon flux by a normalization factor  $N_{\text{tot}} \propto P_{a\gamma}(g_0)g_{a\gamma}^4/d^2$ , where  $P_{a\gamma}$  is the ALP-photon conversion probability,  $g_0$  is the reference coupling strength ( $g_0 = 10^{-11}$  GeV $^{-1}$ ), and  $d$  is the luminosity distance to the GRB. We numerically calculate the ALP-photon conversion probability,  $P_{a\gamma}$ , in the Milky Way magnetic field, assuming the Jansson & Ferrar field model ([141], also see Sec. 3.2.1). Tables 4.2 and 4.3 summarize the  $P_{a\gamma}$  values for each GRB in our sample and Fig. 4.1 places each GRB onto the conversion probability map. Our work does not take into account the ALP-photon oscillations that may take place in the intergalactic magnetic field, as such contribution would be negligible in our analysis, for reasons outlined in Chapter 3. The input ALP model (now integrated over time, as per the `ThreeML` requirement, in contrast to Chapter 3) is shown in Fig. 4.2. For completeness of this thesis, in Fig. 4.3, I include the temporal and energy evolution plot for the  $40\text{-M}_\odot$  progenitor to complement Fig. 3.2.

---

<sup>8</sup>M. Meyer, M. Giannotti, and T. Fischer, private communication.

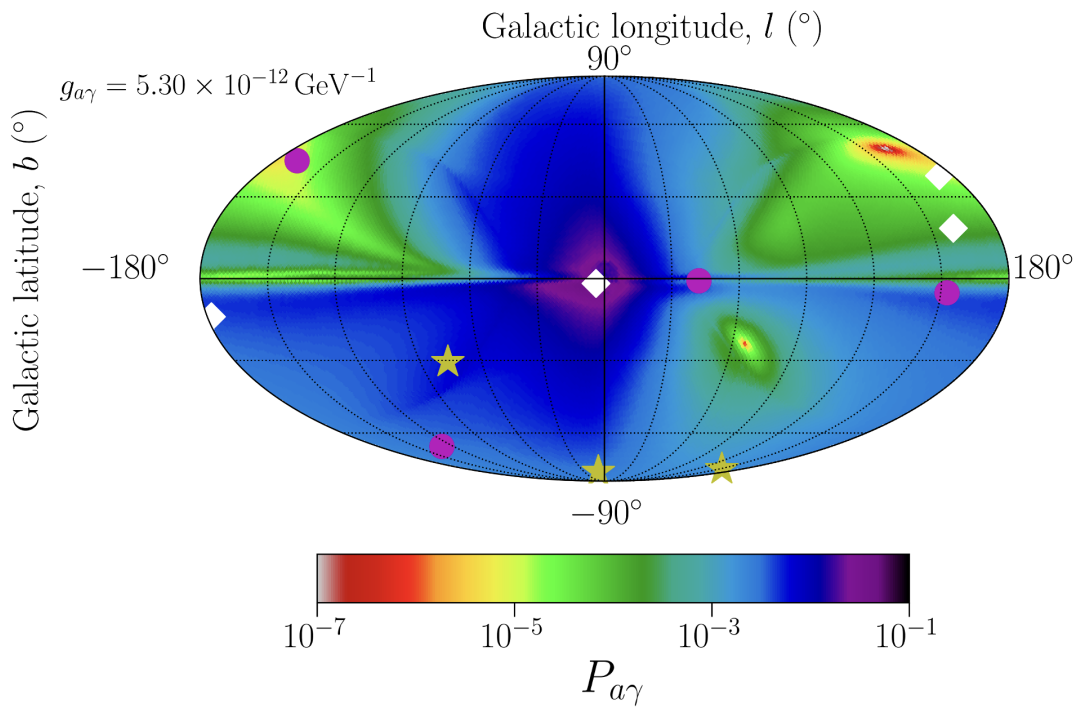


Figure 4.1: Analogous to Fig. 3.4, for an ALP mass  $m_a = 10^{-10}$  eV and coupling  $g_{a\gamma} = 5.3 \times 10^{-12} \text{ GeV}^{-1}$ , and energy  $10 < E < 300$  MeV. Note that for this configuration,  $P_{a\gamma,\max} \sim 0.1$  is the maximum conversion probability reached in the central regions of Milky Way. Yellow stars correspond to GRBs with precursors both in LAT and LLE. White diamonds represent precursor GRBs only detected in LLE, and cyan circles are precursor GRBs only detected in LAT.

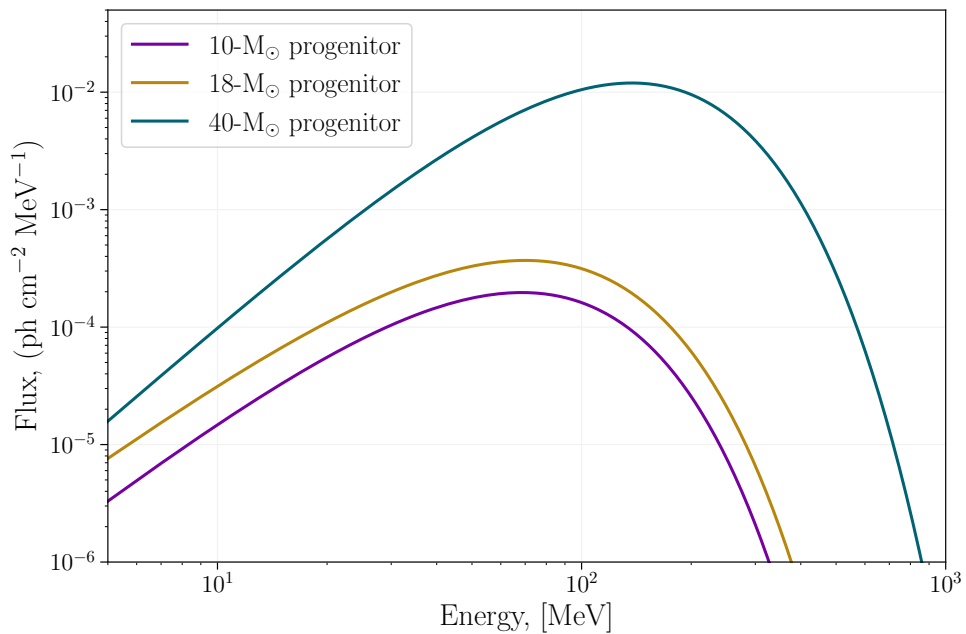


Figure 4.2: The observed ALP-induced gamma-ray spectrum for 10-, 18-, and 40- $M_{\odot}$  progenitor mass integrated over the explosion time for an arbitrary normalization  $N_{\text{tot}} = 8.4^{-54} \text{ cm}^{-2}$ . Note that, for the 40- $M_{\odot}$  progenitor, the peak is shifted to the right compared to the lower-mass progenitors, peaking at  $\sim 150$  MeV.

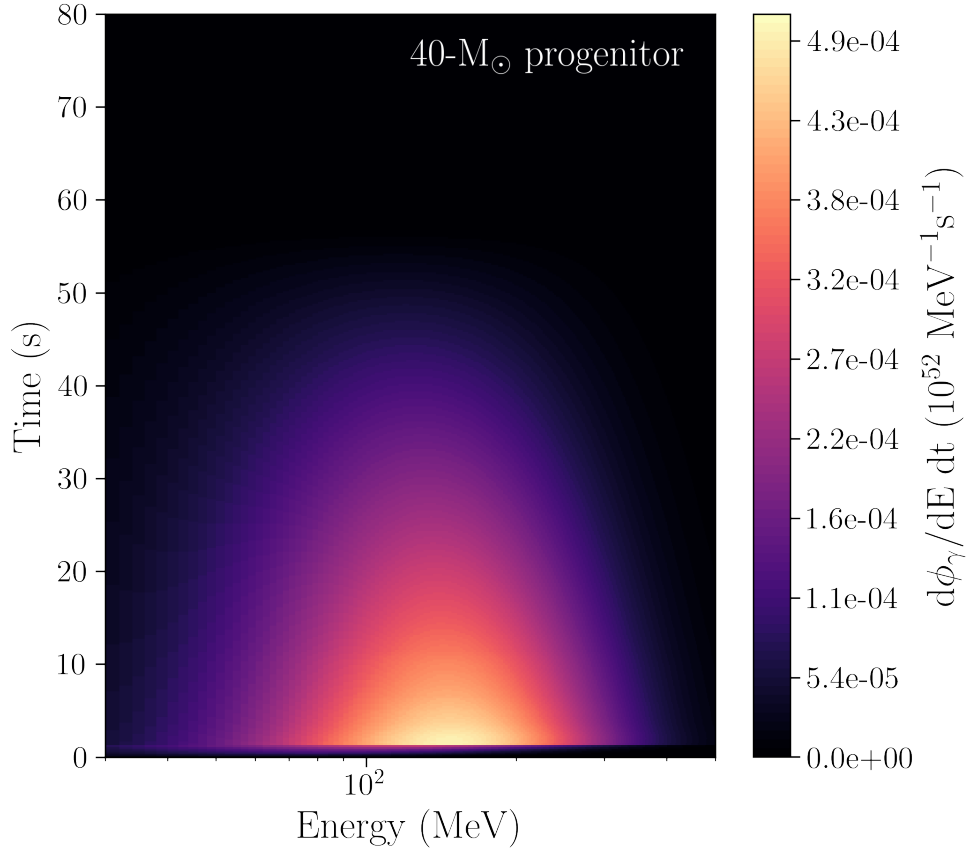


Figure 4.3: Observed evolution of the ALP-induced gamma-ray emission in time and energy in a core-collapse of a  $40\text{-M}_\odot$  progenitor, normalized by  $N_{\text{tot}} = 8.4^{-54} \text{ cm}^{-2}$ . In this case, most of emission happens within the first  $\sim 40$  seconds after the collapse. The temporall and energy evolution can be compared to Fig. 3.2 which demonstrates these properties for the lower-mass progenitors.

**Commonly-used GRB models.** Similarly to Sec. 3.2, we also consider models commonly used in GRB spectral fitting, which are used to also describe physical processes that may account for the precursor emission, such as the phenomenological Band function, power law, comptonized model, or a combination thereof. See Appendix A for more details. It is worth noting that, if a spectrum is best fit by a power law or a comptonized function, this may be motivated by a low-count statistic of the given observation as both of these models are limiting cases of the Band function. Furthermore, neither of the functions we use for standard GRB fitting is correlated to a single physical process that would explain it; rather, all of them are empirically motivated.

**Model comparison.** To compare two models, we apply the Bayesian Information Criterion (BIC) which, for a given model, can be calculated as  $BIC = -\log(\mathcal{L}_i) + k_i \log(N)$ , where  $\mathcal{L}_i$  is the likelihood of model  $i$ ,  $k_i$  is the number of free parameters, and  $N$  is the number of energy channels. When comparing two models, the one with the lower BIC value is preferred. BIC difference exceeding 10 units indicates a very strong preference for the model with the lower BIC. Once we determine the best-fit model for a given precursor, we add an ALP spectral component and test the goodness of the fit.

## 4.5 Results

Here, we present the results of the model comparison analysis.

### 4.5.1 LLE GRBs

A total of 7 GRBs observed using the *Fermi* LLE technique passes the criteria in Table 4.1, all listed in Table 4.2, with their corresponding LAT trigger time,  $T_0$ , precursor time intervals

relative to  $T_0$ , position in the sky, distance (where available), the best-fit model, the ALP-photon conversion probability at the given position, and the corresponding ALP normalization. All GRBs in our sample are better fit by ordinarily used GRB models. Due to some GRBs' measured redshift, the ALP peak may be redshifted outside the LLE energy coverage (e.g., GRB 090323, GRB 120624B, GRB 160625B, and GRB 170214A), resulting in arbitrarily small best-fit ALP normalization values. The lightcurves, their corresponding Bayesian Block representations, and the spectral fits including the ALP component, are shown in Appendix B.

#### 4.5.1.1 Honorable mention: GRB 221009A

GRB 221009A is a long gamma-ray burst that was detected on October 9th, 2022, 14:10:17 UT, by the Burst Alert Telescope (BAT) onboard the *Neil Gehrels Swift Observatory* [182]. Following the BAT notice, the GBM Team reported a spatially coincident detection  $\sim$ 55 minutes before the BAT trigger time. Subsequent spectral analyses confirmed that the BAT instrument triggered once GRB 221009A entered its FoV during an exceptionally bright afterglow phase, with the GBM detection corresponding to the prompt-emission phase[183]. The brightest GRB observed to date, GRB 221009A, is located nearby ( $z = 0.151$ ) at low Galactic latitude ( $b = 4.3^\circ$ ), deeming it an excellent probe into the physical processes both at the explosion site as well as in the Milky Way, in turn setting off numerous follow-up observation initiatives [184].

GRB 221009A lightcurve observed both with *Fermi*- LAT and GBM exhibit a clear multi-episode structure during the prompt-emission phase. The first peak—hereafter referred to as the precursor—lasts for  $\sim$ 10 seconds, and the second, multi-peaked episode spans a few hundred seconds. The precursor episode, however, is not observed with the standard LAT analysis and is only seen when

GRB Name	$T_0$ (MET)	Precursor w.r.t. $T_0$ (s)	(RA, Dec)	$z$	Best fit	BIC (null)	$\Delta$ BIC	$P_{\alpha\gamma}$	$N_{\text{tot}}$ , (cm $^{-2}$ MeV $^{-1}$ s $^{-1}$ )
<b>090323</b>	259459364.630	(-4, 26)	190.75, 17.07	3.57	p1	56.27	4.2	$\sim 10^{-3}$	$\sim 0$
<b>100724B</b>	301624928.090	(5, 27)	123.59, 75.86	-	p1	58.66	3.8	$\sim 10^{-2}$	$(1.52 \pm 0.19) \times 10^{-1}$
<b>120624B</b>	362269436.930	(-268, -237)	170.91, 8.94	2.2	p1	69.24	3.8	$\sim 3 \times 10^{-2}$	$(1.2 \pm 0.7) \times 10^{-4}$
130504C	389402940.520	(14, 22)	91.55, 3.78	-	p1	41.06	3.9	$\sim 10^{-1}$	$(0.9^{+1.8}_{-0.9}) \times 10^{-1}$
160625B	488587220.275	(184, 191)	308.57, 6.93	1.406	p1	74.32	4.6	$\sim 10^{-4}$	$\sim 0$
170214A	508779271.920,	(6, 24)	256.32, -1.88	2.53	p1	70.12	16.1	$\sim 10^{-2}$	$\sim 0$
221009A	687014224.990	(-1, 5)	288.26, 19.78	0.1505	Band	39.76	33.9	$\sim 4 \times 10^{-4}$	$(1.5 \pm 0.4) \times 10^{-1}$

Table 4.2: Out of 93 GRBs detected with LLE, 7 pass the selection criteria imposed in Table 4.1. The time of the LAT trigger is given in the MET format, with the relevant precursor time window denoted relative to the trigger time. The BIC value is given for the null hypothesis (i.e., for a model without an ALP spectral component). The alternative hypothesis includes the ALP component. The difference between BICs is then calculated to determine which model fits the observations better. Between the two models, a better fit is the one with the lower BIC value. Conversion probability values (Fig. 3.4) and the normalization value,  $N_{\text{tot}}$  deduced from the best fit that has the ALP component. The given value of normalization is in units of  $10^{-52}$  cm $^{-2}$  MeV $^{-1}$  s $^{-1}$ . In bold are shown GRBs observed both with the LLE and the LAT standard data cuts.

applying the LLE event cut. The duration of the afterglow phase is currently still being worked out. Nevertheless, a fascinating report in the afterglow phase was made by the LHAASO Team, with a possible  $10\sigma$  detection of an 18-TeV photon  $\sim$ 2000 seconds after the GBM trigger [185]. Considering the distance to the source, the survival probability of such high-energy photon is extremely low—opening the venue to some new physics speculations, including ALPs (see, e.g., [186–188]).

Although the precursor seen in GRB 221009A is the one with the highest count statistics, the resulting upper limit on the ALP-photon coupling is not constraining ( $g_{a\gamma} < 3.9 \times 10^{-10}$  GeV $^{-1}$ , see Eq. 3.3 and Fig. 3.8). This is partly due to the low ALP-photon conversion probability in the direction of the GRB 221009A ( $\sim 10^{-4}$ ), and partly due to the sizeable distance to the GRB ( $\sim 720$  Mpc in luminosity distance, assuming the  $\Lambda$ CDM model).

#### 4.5.2 LAT GRBs.

Unsurprisingly, finding a precursor emission within standard LAT observations of GRBs proved to be a challenging task. Namely, we are heavily limited by the low-count statistic. With that, we relax the requirements on the precursor definition: in particular, we no longer require that the emission goes all the way down to the background level between the precursor and prompt emission. Instead, we also consider GRBs, for which two peaks are separated by a time of constant-level emission that is weaker than the peaks themselves. An example of such GRB is shown in Fig. 4.5. We only carry out the fits with the 40-solar-mass progenitor for LAT precursors, as it is the only model with an ALP signature that peaks in the standard LAT energy range.

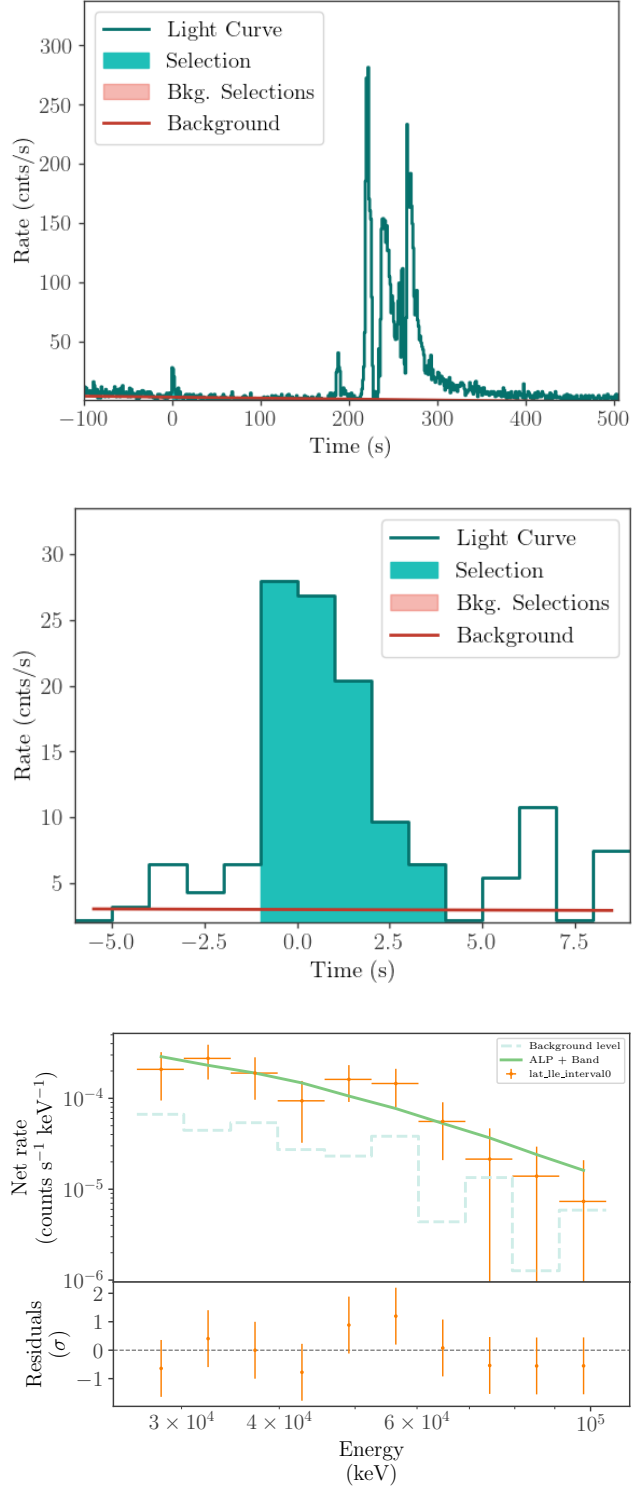


Figure 4.4: Top: LLE lightcurve depicting the prompt emission as seen with LLE. The red horizontal line is the background fit. Middle: BB analysis zoomed in on the precursor. Shaded teal area represents the time interval in which we conduct the spectral fitting. Bottom: the best fit model, including the ALP component.

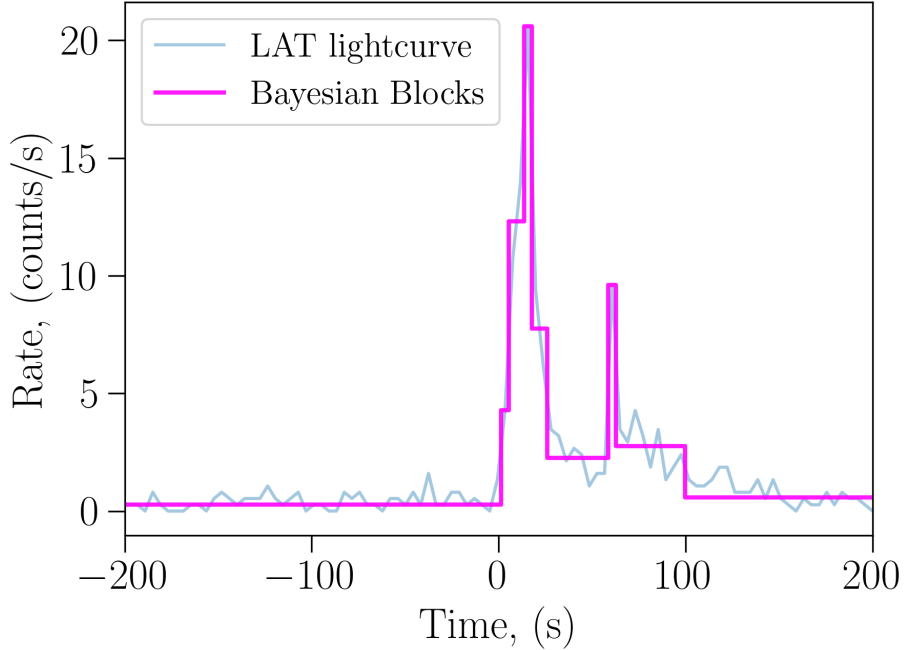


Figure 4.5: GRB 100724B observed lightcurve (pale blue) with Bayesian blocks overlaid in magenta. There is a clear separation between two peaks, however, the emission during the quiescent period does not go all the way down to background levels.

Using the standard LAT data cut and applying the selection criteria to the LAT-detected GRBs results in a total of 7 GRBs to consider. Similarly to the LLE analysis, the properties of the GRBs and the fitting results are shown in Table 4.3. The nearest GRB (at  $\sim 4600$  Mpc), in the direction of a relatively high ALP-photon conversion probability,  $\sim 10^{-2}$ , only allows for a weak constraint on the coupling, down to  $g_{a\gamma} = 1.8 \times 10^{-10}$  GeV $^{-1}$ .

## 4.6 Discussion

Searching for ALPs in precursor emission in long GRBs is a well-motivated approach to constraining the properties of these particles. This is guided by the expected temporal delay between the time we expect to observe ALPs and a jet breakout, which is usually associated with

GRB Name	$T_0$ (MET)	Precursor w.r.t. $T_0$ (s)	RA, Dec	$z$	Best fit	BIC (null)	$\Delta \text{BIC}$	$P_{\alpha\gamma}$	$N_{\text{tot}}$ (cm $^{-2}$ MeV $^{-1}$ s $^{-1}$ )
090323	259459364.630	(-1, 53)	190.75, 17.07	3.57	Band	33.87	1.8 Band+alp	$\sim 10^{-3}$	$\sim 0$
090328	259925808.510	(-1, 38)	90.67, -41.95	0.74	p <sub>1</sub>	98.6	1.1 Band+alp	$\sim 10^{-2}$	$(5.5 \pm 2.2) \times 10^{-3}$
090720B	269802178.900	(-5, 5)	203.638, -51.198	-	unconstrained	N/A	N/A	N/A	N/A
090902B	273582310.320	(-1, 48)	264.95, 27.33	1.82	Band	3974.0	733 Band + alp	$\sim 3 \times 10^{-2}$	$7.0 \pm 0.4) \times 10^{-4}$
100724B	301624928.090	(-1, 50)	123.59, 75.86	N/A	p <sub>1</sub>	135.11	43.6	$\sim 8 \times 10^{-3}$	$\sim 0$
120624B	362269436.930	(-275, 240)	170.91, 8.94	2.2	unconstrained	N/A	N/A	$\sim 2 \times 10^{-3}$	N/A
130821A	398794231.010	(-900, -840)	314.23, -11.52	N/A	unconstrained	N/A	N/A	$\sim 9 \times 10^{-4}$	N/A
								$\sim 8 \times 10^{-6}$	N/A

Table 4.3: Out of 255 GRBs detected with LAT, a total of 7 pass the selection criteria imposed in Table 4.1. The time of LAT trigger is given in the MET format, with the relevant precursor time window denoted relative to the trigger time. The BIC value is given for the null hypothesis (i.e., for a model without an ALP spectral component). The alternative hypothesis includes the ALP component. The difference between BICs is then calculated to determine which model fits the observations better. Between two models, a better fit is the one with the lower BIC value. Conversion probability values (Fig. 3.4) and the normalization value,  $N_{\text{tot}}$  deduced from the best fit that has the ALP component. The given value of normalization is in units of  $10^{-52}$  cm $^{-2}$  MeV $^{-1}$  s $^{-1}$ . Due to low number of counts, we are unable to constrain a best fit model for three of the GRBs.

the prompt emission of a long GRB.

We start by selecting the sample of long GRBs with a likely precursor using a modified version of the Bayesian block approach. We account for the LAT’s changing exposure, which could lead to the misidentification of excess signals if left untreated. This is particularly relevant for instruments we cannot conduct a cross-check between different detectors. Applying the selection criteria to a total of 255 GRBs observed either with LAT and/or LLE results in a sample space of 14 long GRBs, seven observed in LLE and 7 in LAT (three of which were observed with both).

We then employ the `threeML` package to conduct time-resolved spectral fits of the identified precursors. In anticipation of future multiwavelength and messenger efforts, we develop an ALP search pipeline under the `threeML` framework. We fit three different ALP spectral models characterized by different progenitor masses (10, 18, and 40 solar masses) for the LLE-detected GRBs. For LAT-only detections, we conduct the ALP spectral modeling only with the 40 solar mass model, as it is the only one with the peak within the standard LAT energy coverage.

We report no significant detections. We, however, demonstrate that our approach can yield limits on the ALP-photon coupling. Our most stringent upper limit comes from the precursor observation of GRB 221009A, excluding all the values of  $g_{a\gamma} > 3.9 \times 10^{-10}$  for ALP masses  $< 10^{-10}$  eV. This limit is not particularly constraining due to the distance to the source and its location in the sky, which governs the ALP-photon conversion probability.

Employing our technique, nevertheless, can be interesting in the context of different objects—for example, pulsars or variable AGN. Furthermore, additional searches may be done for populations of long GRBs with a precursor emission redshifted to X-rays or soft gamma rays, where the current instruments are more sensitive. Finally, our work again calls for investment into an improved sensitivity to the MeV sky in the future.

*Intermission*

# Chapter 5: A Joint *Fermi*-GBM and *Swift*-BAT Analysis of Gravitational-Wave Events from the Third Gravitational-wave Ob- serving Run

*Just sent you a DoorDash gift card so you don't have to worry about dinner.*

---

Courtney Randolph, during one of my low points in graduate school

The detection of GW170817 [31] coincident with the short gamma-ray burst GRB 170817A [189, 190] was a ground-breaking discovery for the era of MMA<sup>1</sup>. This event marked the first detection of a BNS merger by the LIGO and Virgo instruments, as well as the only confirmed GW event with an EM counterpart to date. Since then, the search for EM emission from more of these extreme events has been at the forefront of MMA, particularly in the gamma-ray energy band since GRB 170817A demonstrated that the merger of two NSs is a progenitor of short GRBs [191]. GWs have also been observed from the mergers of other compact objects, such as binary black hole (BBH) and NSBH systems [49, 192–194]; however, no additional EM counterparts have been confirmed as other counterpart candidates have so far been inconclusive [195–197] or

---

<sup>1</sup>The work in this chapter is currently in the final internal review stage by the three collaborations and is presented here with minimal modifications. The paper is a collaborative work between the *Fermi*-GBM and *Swift*-BAT teams, and the LVK Collaboration. Together with Dr. Corrine Fletcher and Dr. Joshua Wood, I am the contact author, having done all the data analysis from the *Swift*-BAT side and shared the responsibility of combining the results. For completeness, a condensed version of the *Fermi*-GBM analysis steps is included; however, this chapter focuses on the *Swift*-BAT and combined analysis. Significant contributors to the work in the paper under review are also Dr. Rachel Hamburg and Dr. Peter Veres.

are still under debate [198–202].

The second observing run (O2), running from November 2016 to August 2017, resulted in the detection of GW170817, the EM counterpart GRB 170817A and the kilonova AT 2017gfo [32, 203–207]. GRB 170817A was initially discovered by the on-board trigger algorithm of *Fermi*-GBM, with an additional detection by INTEGRAL [190]. The energy range of *Fermi*-GBM combined with its wide FoV and rapid alert abilities makes it an ideal platform to search for gamma-ray counterparts to GW events in real time. Additionally, *Fermi*-GBM provides continuous time tagged event (CTTE) data with a 6-hour latency that enables sensitive searches for short GRBs on the ground. Two of these searches are the Untargeted Search, a blind search of *Fermi*-GBM data for short GRBs, and the Targeted Search, which uses an external time to search for a short GRB [208, 209]. Following O2, the LIGO Scientific and Virgo Collaboration published its first catalog (GWTC-1; [192]) using a full reanalysis of data from both O1 and O2. It contained a total of 11 GW events with a probability of astrophysical compact binary coalescence origin  $p_{\text{astro}} > 0.5$ , but no other EM counterparts were reported by *Fermi*-GBM [210].

In addition to the *Fermi*-GBM, the *Swift*-BAT provides excellent sensitivity to detecting hard X-ray and gamma-ray transient sources [211]. *Swift*-BAT primarily runs in a survey mode that continuously evaluates rate increases and potential GRB triggers. An increase in the observed photon rate triggers on-board image processing algorithms that can provide  $\sim$ arcminute localizations for GRBs. For each significantly detected event, the data transferred to the ground contains information regarding the count arrival time, its location, and energy within the 15–350 keV range. However, if an event does not trigger an on-board detection, the available data for offline ground searches is contained within continuous rate light curves in four energy channels (15–25 keV, 25–50 keV, 50–100 keV, and 100–350 keV) with three time binnings (64 ms,

1 s, and 1.6 s).

In this chapter, we use the *Swift*-BAT continuous collection of the rate data to search for un-triggered or sub-threshold short GRBs around GW event times, analogous to the GBM Targeted Search. Although *Swift*-BAT has been used to search for public and sub-threshold GW events during the LVK observing runs, this is the first systematic search in all events from an observing run. The Gamma-ray Urgent Archiver for Novel Opportunities (GUANO) pipeline [212] is a novel way to recover the event-level data from *Swift*-BAT without onboard triggers and thus enable significantly more sensitive searches. However, GUANO is not used in this chapter’s work because it only began regular successful operations in December 2019, resulting in incomplete data availability for the GW events considered here.

The third observing run (O3) of the LVK occurred from April 2019 to March 2020 with a month-long commissioning break during October 2019. It benefited from improvements to the sensitivity and duty cycle of the GW detectors made after the conclusion of the O2 run [193, 213]. This observing run provided 56 public GW candidate events in real-time with information from their preliminary analysis. More detailed analyses were published in a series of catalogs (GWTC-2; [193], GWTC-2.1; [194], GWTC-3; [49]) with GWTC-3 providing a cumulative list of 79 GW candidates from O3 with  $p_{\text{astro}} > 0.5$ . This represents an 8-fold increase in the number of GW candidates with  $p_{\text{astro}} > 0.5$ .

Among these events was the detection of a second confident event classified as a BNS merger, GW190425, whose total mass is larger than that known from Galactic NS binaries [214]. Additionally, GW190917\_114630, GW191219\_163120, and GW200115\_042309 provided the first detections of events classified as NSBH systems with  $p_{\text{astro}} > 0.5$ . A fourth possible NSBH event, GW200105\_162426, fell just outside the  $p_{\text{astro}} > 0.5$  event criteria in

GWTC-3. There were also two confident detections with ambiguous classifications, GW190814 and GW200210\_092254, that represent a BH merging with either a light BH or a heavy NS. GW190814 is particularly intriguing since its secondary component mass is either the lightest BH or the heaviest NS observed to date [215]. An overwhelming majority of the remaining events are most likely BBHs in origin.

The goal of this chapter is to search for coincident short GRB counterparts to GW events from the cumulative set of O3 events presented in GWTC-3 and discussed in Section 5.1.1. Section 5.1.2 provides a brief overview of the *Fermi*-GBM searches. Section 5.1.3 describes the *Swift*-BAT sub-threshold search. Section 5.1.4 presents the results from both *Fermi*-GBM and *Swift*-BAT for the marginal GW events identified in Section 5.1.1. Furthermore, Section 5.3 divides the discussion of GW events with  $p_{\text{astro}} > 0.5$  into three groups depending on their estimated component masses  $m_1$  and  $m_2$ . For systems with a possible NS component ( $m_2 \leq 3 M_\odot$  in  $\geq 5\%$  of posterior samples), we present the flux and isotropic equivalent luminosity upper limits from both *Fermi*-GBM and *Swift*-BAT (Section 5.3.1). We discuss upper limits to the marginal GW events in Section 5.3.3. Finally, in Section 5.4 we summarize our results and discuss future plans for using the sub-threshold searches for GW events.

## 5.1 Method

In this section, we summarize the set of GW events that we analyze from GWTC-3. We also present the search methods used to find coincident gamma-ray and hard X-ray emission with *Fermi*-GBM and *Swift*-BAT.

### 5.1.1 Gravitational-wave Trigger Selection

The analysis reported here focuses on GW candidates identified during O3. These were selected by four separate analysis pipelines, referred to as GstLAL, Multi-Band Template Analysis (MBTA), PyCBC, and cWB, and published in GWTC-3 [49]. Each pipeline calculates both a False Alarm Rate (FAR) from a background noise hypothesis and a probability of astrophysical origin ( $p_{\text{astro}}$ ) for each event assuming a compact binary coalescence source. Events with  $p_{\text{astro}} > 0.5$  in any pipeline are selected for detailed analysis with a full estimation of the potential astrophysical source parameters. The one exception to this are events identified by the minimally modeled cWB pipeline, which requires a time-matched confirmation of candidates with  $p_{\text{astro}} > 0.1$  in one of the other pipelines in order to ensure the event originated from a compact binary coalescence. In total there were 79 events identified with  $p_{\text{astro}} > 0.5$  during O3. Table 5.1 shows the candidate identifier, date, time, and  $p_{\text{astro}}$  for these events.

The remaining subset of events with an FAR below  $2 \text{ yr}^{-1}$  and  $p_{\text{astro}} \leq 0.5$  in a given pipeline are considered marginal event candidates. As of GWTC-3, there are 6 marginal candidates which cannot be attributed to instrumental or environmental causes (Table 5.2). We exclude these events from our main analysis and discussion to focus on the events with  $p_{\text{astro}} > 0.5$  since these events have a stronger possibility of astrophysical origin; however, we did perform separate searches for gamma-ray counterparts for each marginal candidate since the existence of a counterpart could potentially prove an astrophysical origin.

Table 5.1: GW events from O3 with  $p_{\text{astro}} > 0.5$ .

Event Name	Date	Time (UTC)	$p_{\text{astro}}$	Event Name	Date	Time (UTC)	$p_{\text{astro}}$
GW190403_051519	04-03-2019	05:15:19	0.60	GW191103_012549	11-03-2019	01:25:49	0.94
GW190408_181802	04-08-2019	18:18:02	>0.99	GW191105_143521	11-05-2019	14:35:21	>0.99
GW190412	04-12-2019	05:30:44	>0.99	GW191109_010717	11-09-2019	01:07:17	>0.99
GW190413_052954	04-13-2019	05:29:54	0.92	GW191113_071753	11-13-2019	07:17:53	0.68
GW190413_134308	04-13-2019	13:43:08	0.99	GW191126_115259	11-26-2019	11:52:59	0.70
GW190421_213856	04-21-2019	21:38:56	>0.99	GW191127_050227	11-27-2019	05:02:27	0.74
GW190425	04-25-2019	08:18:05	0.69	GW191129_134029	11-29-2019	13:40:29	>0.99
GW190426_190642	04-26-2019	19:06:42	0.73	GW191204_110529	12-04-2019	11:05:29	0.74
GW190503_185404	05-03-2019	18:54:04	>0.99	GW191204_171526	12-04-2019	17:15:26	>0.99
GW190512_180714	05-12-2019	18:07:14	>0.99	GW191215_223052	12-15-2019	22:30:52	>0.99
GW190513_205428	05-13-2019	20:54:28	>0.99	GW191216_213338	12-16-2019	21:33:38	>0.99
GW190514_065416	05-14-2019	06:54:16	0.75	GW191219_163120	12-19-2019	16:31:20	0.82
GW190517_055101	05-17-2019	05:51:01	>0.99	GW191222_033537	12-22-2019	03:35:37	>0.99
GW190519_153544	05-19-2019	15:35:44	>0.99	GW191230_180458	12-30-2019	18:04:58	0.96
GW190521	05-21-2019	03:02:29	>0.99	GW200112_155838	01-12-2020	15:58:38	>0.99
GW190521_074359	05-21-2019	07:43:59	>0.99	GW200115_042309	01-15-2020	04:23:09	>0.99
GW190527_092055	05-27-2019	09:20:55	0.83	GW200128_022011	01-28-2020	02:20:11	>0.99
GW190602_175927	06-02-2019	17:59:27	>0.99	GW200129_065458	01-29-2020	06:54:58	>0.99
GW190620_030421	06-20-2019	03:04:21	0.99	GW200202_154313	02-02-2020	15:43:13	>0.99
GW190630_185205	06-30-2019	18:52:05	>0.99	GW200208_130117	02-08-2020	13:01:17	>0.99
GW190701_203306	07-01-2019	20:33:06	>0.99	GW200208_222617	02-08-2020	22:26:17	0.70
GW190706_222641	07-06-2019	22:26:41	>0.99	GW200209_085452	02-09-2020	08:54:52	0.97
GW190707_093326	07-07-2019	09:33:26	>0.99	GW200210_092254	02-10-2020	09:22:54	0.54
GW190708_232457	07-08-2019	23:24:57	>0.99	GW200216_220804	02-16-2020	22:08:04	0.77
GW190719_215514	07-19-2019	21:55:14	0.91	GW200219_094415	02-19-2020	09:44:15	>0.99
GW190720_000836	07-20-2019	00:08:36	>0.99	GW200220_061928	02-20-2020	06:19:28	0.62
GW190725_174728	07-25-2019	17:47:28	0.96	GW200220_124850	02-20-2020	12:48:50	0.83
GW190727_060333	07-27-2019	06:03:33	>0.99	GW200224_222234	02-24-2020	22:22:34	>0.99
GW190728_064510	07-28-2019	06:45:10	>0.99	GW200225_060421	02-25-2020	06:04:21	>0.99
GW190731_140936	07-31-2019	14:09:36	0.83	GW200302_015811	03-02-2020	01:58:11	0.91
GW190803_022701	08-03-2019	02:27:01	0.97	GW200306_093714	03-06-2020	09:37:14	0.81
GW190805_211137	08-05-2019	21:11:37	0.95	GW200308_173609	03-08-2020	17:36:09	0.86
GW190814	08-14-2019	21:10:39	>0.99	GW200311_115853	03-11-2020	11:58:53	>0.99
GW190828_063405	08-28-2019	06:34:05	>0.99	GW200316_215756	03-16-2020	21:57:56	>0.99
GW190828_065509	08-28-2019	06:55:09	>0.99	GW200322_091133	03-22-2020	09:11:33	0.62
GW190910_112807	09-10-2019	11:28:07	>0.99				
GW190915_235702	09-15-2019	23:57:02	>0.99				
GW190916_200658	09-16-2019	20:06:58	0.62				
GW190917_114630	09-17-2019	11:46:30	0.74				
GW190924_021846	09-24-2019	02:18:46	>0.99				
GW190925_232845	09-25-2019	23:28:45	0.99				
GW190926_050336	09-26-2019	05:03:36	0.51				
GW190929_012149	09-29-2019	01:21:49	0.86				
GW190930_133541	09-30-2019	13:35:41	>0.99				

Table 5.2: Marginal GW events from O3 without clear instrumental or environmental causes.

	Event Name	Date	Time (UTC)	$p_{\text{astro}}$	Reference
1	GW190426_152155	04-26-2019	15:21:55	0.14	[194]
2	GW190531_023648	05-31-2019	02:36:48	0.28	[194]
3	GW191118_212859	11-18-2019	21:28:59	0.05	[49]
4	GW200105_162426	01-05-2020	16:24:26	0.36	[49]
5	GW200201_203549	02-01-2020	20:35:49	0.12	[49]
6	GW200311_103121	03-11-2020	10:31:21	0.19	[49]

### 5.1.2 *Fermi*-GBM Search Methods

*Fermi*-GBM consists of fourteen detectors that are strategically positioned to cover the full sky, unocculted by the Earth, and provide an excellent opportunity to observe GRBs [216]. A more detailed description of the instrument can be found in Sec. 1.3. The onboard algorithm triggers a detection whenever incoming count rate is at a level greater than  $4.5\sigma$  above the background rate in at least two NaI detectors. Furthermore, the CTTE data is available for the ground-based follow-up analysis, allowing for Untargeted and Targeted subthreshold searches. The *Fermi*-GBM Untargeted Search is a blind search that automatically scans the CTTE data for a significant count rate increases in at least two NaI detectors. The algorithm was originally developed for detecting terrestrial gamma-ray flashes [217] and has since been adapted to search for short GRBs with fluxes below the on-board triggering threshold.

The Untargeted Search runs through eighteen timescales ranging from 64 ms to 31 s and five energy bins from 27 keV to 985 keV, and short GRB candidates are identified when at least two detectors exceed  $2.5\sigma$  and  $1.25\sigma$  above the background rate. The list of short GRB candidates identified using the Untargeted Search is publicly available through the Gamma-ray Coordinates Network (GCN)<sup>2</sup>. Finally, as this part of the analysis was done independently from the *Swift*-BAT

---

<sup>2</sup>[https://gcn.gsfc.nasa.gov/fermi\\_gbm\\_subthresh\\_archive.html](https://gcn.gsfc.nasa.gov/fermi_gbm_subthresh_archive.html), as accessed on March 12, 2023.

I will not provide any more information, but instead encourage the interested reader to refer to the journal article for further details.

### 5.1.2.1 GBM Targeted Search

The *Fermi*-GBM Targeted Search was developed for multimessenger follow-up observations [208]. It uses CTTE data to scan around an external trigger time for gamma-ray emission typical of a short GRB. Theoretical models predict that GRB emission offset time compared to the GW trigger ranges from 0.01 s to 10 s depending on the conditions producing the gamma-ray emission [218]. As such, for follow-up of the events in Table 5.1, we search from  $-1$  s to  $+30$  s around the GW time to ensure we do not miss unexpectedly delayed gamma-ray emission from a counterpart short GRB, even after accounting for temporal offsets up to 10 s relative to the GW time. Starting 1 s before the GW time provides a comfortable buffer to account for the fact that the trigger times can vary by a few milliseconds for events that are identified by multiple pipelines.

The Targeted Search achieves greater sensitivity than the on-board triggering algorithm by processing the data from all 14 detectors coherently rather than focusing on significant signals present in detector pairs. This allows for the detection of weaker signals below the *Fermi*-GBM on-board triggering threshold [219]. To do this, three spectral templates representing spectrally hard, normal, and soft GRBs (Table 5.3) are folded through the GBM detector responses to produce an expected count rate for a given astrophysical source location and flux.

For GW events without a significant counterpart detection in *Fermi*-GBM we compute the gamma-ray flux upper limits as a function of sky position using the Targeted Search because it

Table 5.3: Spectral templates used by the *Fermi*-GBM Targeted Search.

Template	Type	Parameters
hard	Cut-off Power-law [220]	$E_{\text{peak}} = 1500 \text{ keV}$ , $\alpha = -1.5$
normal	Band [221]	$E_{\text{peak}} = 230 \text{ keV}$ , $\alpha = -1.0$ , $\beta = -2.3$
soft	Band [221]	$E_{\text{peak}} = 70 \text{ keV}$ , $\alpha = -1.9$ , $\beta = -3.7$

is the most sensitive analysis method employed by *Fermi*-GBM. To do this, we use the normal spectral template from Table 5.3 and the 1 s gamma-ray emission duration from the Targeted Search since they are characteristic of typical short GRBs [222, 223]. This results in a set of upper limits for each sky position at times ranging from  $-1$  s to  $+30$  s around the GW time. We then choose the maximum observed upper limit measurement for each sky position, guaranteeing that the specified confidence level of the upper limit applies over the entire search period. We use a  $3\sigma$  upper limit level for reporting upper limits over the full 10–1000 keV energy range of standard GRB flux measurements in *Fermi*-GBM following the convention established in [209]. We also compute a second  $5\sigma$  upper limit over a 15–350 keV range to match the convention used by *Swift*-BAT (see Section 5.1.3.2) when combining the upper limits from both instruments.

### 5.1.3 *Swift*-BAT Rates Data Search

*Swift*-BAT is a coded-aperture instrument and one of the most sensitive GRB detectors currently in operation. A more complete overview of the instrument can be found in 1.3. The on-board *Swift*-BAT GRB triggers are complemented by subsequent on-ground rates and image data processing, in turn allowing for dedicated searches for GRB emission. With no GW events from Table 5.1 triggering an on-board BAT detection, we conduct an offline follow-up analysis from the ground to search for the corresponding hard X-ray counterpart emission. The BAT flight software continuously assesses the signal-to-noise ratio (SNR) of the observed count rates. If an

SNR exceeds the given threshold value determined by a number of rate-trigger criteria [224], the triggering algorithm subsequently checks the corresponding image data for the final confirmation and the localization of the potential burst. The detection is confirmed only if the image SNR threshold is surpassed ( $\gtrsim 6.5$ ) and no other sources have been previously reported at the event localization. For every confirmed detection, BAT records event data containing counts' arrival times, location on the detector plane, and energy. With its large effective area ( $\sim 2600 \text{ cm}^2$  for 100 keV photon detection at launch), the event data volume collected by BAT is too big to be stored on-board and, due to the limitations of the *Swift* downlink bandwidth, it is not possible to transfer all the event data to the ground. As such, until recently, the only way to conduct an offline, on-ground follow-up analysis of untriggered and sub-threshold events relied upon the rates light curves in four energy channels (15–25 keV, 25–50 keV, 50–100 keV, and 100–350 keV) with three time binnings (64 ms, 1 s, and 1.6 s) and their corresponding 64 s images in a single energy bin (15–50 keV). The recently developed GUANO technique circumvents this issue by retrieving BAT event data extending to  $\sim 200$  s long windows surrounding the trigger times from various astrophysical events (e.g., GWs, GRBs, fast radio bursts, neutrinos, etc.; [212]). However, due to a significant number of the considered GW triggers being detected prior to the GUANO deployment in December 2019, we conduct the analysis using only the regular rates data from BAT and leave the analogous study using the GUANO data for the future GW observing runs.

To conduct the untriggered and sub-threshold search for hard X-ray counterparts coincident with the LVK triggers in Table 5.1, we developed a code analogous to [225]. The search process begins by extracting the raw light curves from within the central region of the BAT FoV binned in 64 ms, 1 s, and 1.6 s time intervals. Analogously to the GBM search, we calculate the average background rate and standard deviation,  $\sigma_{\text{bg}}$ , starting at  $-1$  s before the GW trigger time, and

extending to +30 s after. Using the raw light curves, we compute the average background rate,  $r_{\text{bg}}$ , spanning a time window outside the signal interval, and spanning  $\sim 800$  s, excluding the instrument slews or its passing through the South Atlantic Anomaly (SAA) when the instrument does not collect data. The signal significance,  $S$ , is then computed from  $\sigma_{\text{bg}}$ , using

$$S = (r_{\text{sig}} - r_{\text{bg}})/\sigma_{\text{bg}}, \quad (5.1)$$

where  $r_{\text{sig}}$  is the threshold signal rate. The background uncertainty is estimated as

$$\sigma_{\text{bg}} = \sqrt{\frac{1}{N} \sum_{i=1}^N (r_{\text{bg},i} - \bar{r}_{\text{bg}})^2}, \quad (5.2)$$

where  $N$  is the number of data points in the considered portion of the lightcurve,  $r_{\text{bg},i}$  is the  $i^{\text{th}}$  background rate measurement, and  $\bar{r}_{\text{bg}}$  is the mean background rate over the considered time interval. Furthermore, we visually inspect each light curve to ensure that no peaks originate from detector noise. Once this is done, we check whether there are any potential counterparts to the GW event, defined as a  $\geq 5\sigma$  detection above background.

### 5.1.3.1 NITRATES Response Functions

To produce the BAT instrument response functions appropriate for converting from photon counts to a source flux in the rate data domain, we use the Non-Imaging Transient Reconstruction And TEmporal Search (NITRATES; [226]). The NITRATES response modeling takes into account both coded and uncoded parts of the detector, and thus includes responses appropriate for all counts recorded in the rates data. In addition, these responses allow for potential GRB

detection from outside the BAT’s coded FoV, as well as higher sensitivity across the entire FoV. The instrument responses were created by simulating photon beams onto the *Swift* Mass Model (SwiMM) using GEANT4, a particle-interaction simulator software toolkit [227]. We produce Detector Response Matrices (DRMs) for 31 different incident directions, covering the  $\sim 2.2$  sr sky area (corresponding to the 10 % coding fraction) where the responses are well calibrated<sup>3</sup>. For a complete description of the BAT instrument response modeling, see Sec. 5 and Appendix A in [226].

### 5.1.3.2 *Swift*-BAT Flux Upper Limits

For GW events without a  $5\sigma$  detection above background in *Swift*-BAT, we estimate the flux upper limit from the observed photon counts. We compute these limits for each time bin in the search by calculating the necessary number of counts that would result in a  $5\sigma$  detection at that time from the estimated background uncertainty  $\sigma_{\text{bg}}$ , assuming a 1 s emission duration. We then select the largest counts value obtained in the search bins for each GW event since this is guaranteed to satisfy the  $5\sigma$  criteria over the full search window. We convert the photon counts to flux upper limits within the partially coded BAT FoV, over a 15–350 keV energy range as a function of sky position by applying the NITRATES instrument response functions using the normal spectral template (Table 5.3) employed for upper limits computed with the *Fermi*-GBM Targeted Search. This is done over 31 locations in a grid covering the  $\sim 2.2$  sr BAT FoV.

---

<sup>3</sup>DRMs are publicly available on the *Swift*-BAT github: [https://github.com/Swift-BAT/RatesUL/tree/master/rsp\\_NITRATES](https://github.com/Swift-BAT/RatesUL/tree/master/rsp_NITRATES), as accessed on March 13, 2023.

### 5.1.4 Combined & Marginal Flux Upper Limits

For GW events without a detected counterpart in *Fermi*-GBM or *Swift*-BAT, we combine the  $5\sigma$  confidence level flux upper limits to produce a joint flux upper limit skymap using both instruments. We do this by selecting the more constraining upper limit at each sky position since the individual limits result from independent measurements. This allows us to provide a single map for each event that simultaneously leverages the wide FoV provided by *Fermi*-GBM as well as the additional coverage and enhanced sensitivity of *Swift*-BAT.

We also provide marginalized flux upper limits ( $S_{\text{UL,marg}}$ ) that we compute by integrating the upper limits over the sky using the probability density of the GW localization as a prior

$$S_{\text{UL,marg}} = \int S_{\text{UL}} \tilde{\rho}_{\text{GW}} d\Omega, \quad (5.3)$$

where  $S_{\text{UL}}$  is the position-dependent upper limit at a given confidence level and  $\tilde{\rho}_{\text{GW}}$  is the probability density of the GW localization normalized over the visible portion of the sky. This reduces the set of upper limits for each GW event to a single, characteristic upper limit that accounts for the most likely location of the GW source.

### 5.1.5 Isotropic-Equivalent Luminosity Upper Limits

We compute upper limits on the isotropic-equivalent gamma-ray luminosity  $L_{\text{iso}}$  in the cosmological rest-frame energy range of 1 keV–10 MeV for GW events without a detected coun-

terpart in *Fermi*-GBM or *Swift*-BAT according to

$$L_{\text{iso}} = 4\pi D_{\text{L}}^2 S_{\text{UL,marg}}, k, \quad (5.4)$$

where  $D_{\text{L}}$  is the median luminosity distance of the GW event,  $S_{\text{UL,marg}}$  is the marginalized confidence level flux upper limit described in Section 5.1.4, and  $k$  is the standard bolometric correction factor given by

$$k \equiv \frac{\int_{1\text{ keV}/1+z}^{10\text{ MeV}/1+z} E \frac{dN}{dE}(E) dE}{\int_{15\text{ keV}}^{350\text{ keV}} E \frac{dN}{dE}(E) dE}, \quad (5.5)$$

where  $z$  is the redshift inferred from  $D_{\text{L}}$ . In this case,  $\frac{dN}{dE}(E)$  represents the normal spectral shape from Table 5.3, which is used to generate the marginalized flux upper limit. We choose to use the median  $D_{\text{L}}$  with the marginalized flux upper limit instead of marginalizing  $L_{\text{iso}}$  itself from the values estimated for each sky position because doing so incorporates the cuts to select for the higher likelihood modes of GW200308\_173609 and GW200322\_091133 during parameter estimation. This ensures that the results for these two events are not prior dominated [49]. All other events yield similar values for  $L_{\text{iso}}$  regardless of whether we use the individual or median values for  $D_{\text{L}}$  in the calculation.

## 5.2 Results

This section presents the results for the searches from *Fermi*-GBM and *Swift*-BAT for co-incident gamma-ray emission to the GW events presented in Table 5.1. We ran the *Fermi*-GBM Targeted Search on the 79 GW events shown in Table 5.1. *Fermi*-GBM was in the SAA for 15 of those times, therefore the detectors were turned off and no data were obtained. **No significant**

**gamma-ray events were found in coincidence with the GW events.**

We ran the pipeline described in Section 5.1.3 on the 1 s binned light curves from *Swift*-BAT for the 79 candidates listed in Table 5.1. The goal of the pipeline is to examine whether any emission surpasses the  $5\sigma$  threshold above the observed background rate level. We visually inspect each light curve to ensure that no detector noise or malfunction affects the reported results. We identify detector noise as a fast duration peak seen only in some of the energy channels. Once identified, the detector noise is subtracted down to the level of the average background rate. There are 14 candidates for which the data are either unavailable or background dominated because they occurred during either the *Swift*-BAT SAA passage or a slew. Separately, 13 events were within the BAT FoV ( $>10\%$  partial coding) and had image survey data available at the time of interest.

**We report no significant hard X-ray detection in the *Swift*-BAT rate data coincident with the reported GW triggers at the  $5\sigma$  level. We also ran the standard BAT analysis on the survey data (longer timescales,  $\sim 300$  s) for the 13 inside-BAT-FoV events and also report no excess X-ray emission.<sup>4</sup>**

The *Fermi*-GBM and *Swift*-BAT searches were applied separately to the 6 marginal GW events from Table 5.2 in an effort to identify EM counterparts, that could prove an astrophysical origin. No  $5\sigma$  detections were found for any marginal candidates using either the *Fermi*-GBM Targeted or *Swift*-BAT rates data search.

### 5.3 Discussion

Compact binary mergers containing a NS component are the most likely candidates for gamma-ray emission, particularly if the inspiral process results in tidal disruption of the NS and

---

<sup>4</sup><https://heasarc.gsfc.nasa.gov/f-tools/caldb/help/batsurvey.html>

provides both the matter and energy needed to produce photons [228]. In contrast, BBH mergers are not expected to produce gamma-rays outside of a few exotic scenarios (e.g., [229–232]). We therefore choose to divide our discussion into two sections based on the secondary component mass  $m_2$ . We also use the standard convention of  $m_1 > m_2$ :

1. **Events with a possible NS in the system:**  $m_2 \leq 3 M_\odot$  in  $\geq 5\%$  of posterior samples.
2. **Events that are probable BBH systems:**  $m_2 > 3 M_\odot$  in  $> 95\%$  of posterior samples.

The cut  $m_2 \leq 3 M_\odot$  was chosen to include all systems with at least one NS component up to the maximal allowed NS mass of 2.16–3.0  $M_\odot$  [233–236]. It may include a few ambiguous BBH systems due to the uncertainty on the maximum allowed NS mass. We favor this approach over a stricter cut due to the limited number of systems in O3 with light secondary component masses. Additionally, the discussion of the possible BBH class does not suffer from the loss of a few ambiguous events at the margin of selection given the large number of systems with  $m_2 > 3 M_\odot$ .

In Section 5.3.1 we discuss the absence of detections for the 6 events classified with a possible NS component along with the flux upper limits from *Fermi*-GBM and *Swift*-BAT. In Section 5.3.2 we present the large number of BBH systems observed without detected EM emission and present flux upper limits to these events<sup>5</sup>.

---

<sup>5</sup>Testing the theoretical models of the BBH merger EM emission is an immediate and interesting consideration of the results reported here and, in the paper, was done by Dr. Peter Veres. I omit any discussion relating to this analysis as I, personally, did not contribute to this work.

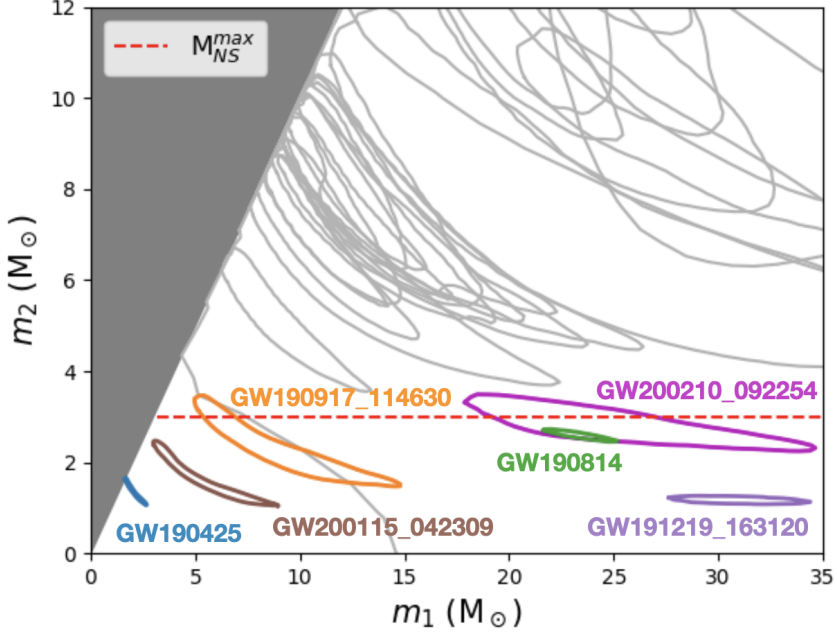


Figure 5.1: The inferred 90% credible regions for the component masses for all GW events identified with  $p_{\text{astro}} > 0.5$  from O3 are shown in grey [49, 193, 194]. The red dashed line marks the upper bound of  $m_2$  allowed for our classification of systems with a possible NS component, which are marked by colored contours.

### 5.3.1 Possible NS in the System

There are 6 events, GW190425, GW190814, GW190917\_114630, GW191219\_163120, GW200115\_042309, and GW200210\_092254, where  $\geq 5\%$  of posterior samples lie below the dashed red line in Figure 5.1. GW190425 is the least massive system presented in the O3 run and the second BNS merger detected by the LVK. It has a primary mass  $m_1 = 2.1^{+0.5}_{-0.4} \text{ M}_\odot$  and a secondary mass of  $m_2 = 1.3^{+0.3}_{-0.2} \text{ M}_\odot$  [194, 214]. GW190814 has a low mass secondary component, estimated at  $m_2 = 2.6^{+0.1}_{-0.1} \text{ M}_\odot$ , while its primary component has an estimated mass of  $m_1 = 23.3^{+1.4}_{-1.4} \text{ M}_\odot$ . It is unclear whether this source is a BBH or a NSBH merger since the secondary component could either be a light BH or a heavy NS [194]. GW190917\_114630 was identified as a BBH merger by the GstLAL pipeline but its secondary component mass

of  $m_2 = 2.1_{-0.4}^{+1.1} M_\odot$  is a strong indicator for a NSBH origin [194]. GW191219\_163120 has a large primary component mass of  $m_1 = 31.1_{-2.8}^{+2.2} M_\odot$  and the lowest secondary component mass  $m_2 = 1.17_{-0.06}^{+0.07} M_\odot$  of all events with a possible NS [49]. It represents a possible NSBH merger. GW200115\_04230 has a primary mass of  $m_1 = 5.9_{-2.5}^{+2.0} M_\odot$  suggesting a low-mass BH and a secondary mass of  $m_2 = 1.44_{-0.29}^{+0.85} M_\odot$  consistent with a NS [49]. GW200210\_092254 possesses a primary component mass of  $m_1 = 24.1_{-4.6}^{+7.5} M_\odot$  and a secondary component mass of  $m_2 = 2.83_{-0.42}^{+0.47} M_\odot$  that could either be a light BH or a heavy NS [49]. It is unclear if this event is a BBH or NSBH merger.

All events except GW191219\_163120 were observable by both *Fermi*-GBM and *Swift*-BAT (Table 5.4). GW191219\_163120 was observed by *Fermi*-GBM but no *Swift*-BAT data are available due to a slewing behavior of the spacecraft at the time of this event. Neither instrument detected an EM counterpart to this set of events. Given that no counterparts were found, we compute the flux upper limits for each GW event using the methods described in Section 5.1. Figure 5.2 shows the combined  $5\sigma$  flux upper limits over the 15–350 keV energy range. Table 5.4 presents the minimum and maximum upper limits over the 90% credible region of the GW localization as well as the marginalized flux upper limits. We use the marginalized  $5\sigma$  flux upper limits to generate upper limits on the isotropic-equivalent luminosity (Figure 5.3) since they incorporate the combined measurement information from *Fermi*-GBM and *Swift*-BAT.

The lack of a confirmed counterpart for the BNS merger GW190425 has three plausible explanations. First, the combined  $\sim$ 60% observational coverage of the total GW localization implies that the GW source may not be visible to *Fermi*-GBM and *Swift*-BAT. Second, GW190425 has an estimated luminosity distance of  $D_L = 0.15_{-0.06}^{+0.08}$  Gpc which is 4 times larger than the distance to GW170817 [192]. This causes the measured luminosity from GW170817 to fall

well below the luminosity upper limit for GW190425 in Figure 5.3, indicating that a counterpart similar to the one for GW170817 would have been unobservable to *Fermi*-GBM or *Swift*-BAT. Finally, the inclination angle of this event is poorly constrained, with the 90% credible level of estimated posterior samples extending to a viewing angle of  $70^\circ$  with respect to the jet axis. This encompasses scenarios where the observed off-axis flux would be below the detection limits, even if the central engine of GW190425 was powerful enough to be detected on-axis by *Fermi*-GBM and *Swift*-BAT at its measured distance.

### 5.3.2 Probable BBH Systems

There are a total of 73 events selected by the criterion of  $m_2 > 3 M_\odot$  in  $> 95\%$  of posterior samples. All of these events have estimated primary and secondary component masses much larger than the maximum expected NS mass of  $3 M_\odot$ . They are therefore likely associated with the mergers of BBH systems.

Of these 73 events, 10 occurred during SAA for *Fermi*-GBM, but had data from *Swift*-BAT. Likewise, *Swift*-BAT does not have data for 9 events either because *Swift*-BAT was in the SAA or slewing, but data are available from *Fermi*-GBM. There are 5 events that do not have data from either *Fermi*-GBM and *Swift*-BAT either due to being in the SAA or slewing. Neither instrument identified an EM counterpart for the events with data coverage. As a result, we compute flux upper limits for each event according to the methods described in Section 5.1. Table 5.5 presents the minimum and maximum upper limits over the 90% credible region of the GW localization as well as the marginalized flux upper limits. Appendix C presents the joint flux upper limit as a function of sky position for the events that have data coverage and Appendix C.2 presents the

Table 5.4: Flux upper limits for the 6 events from O3 with  $p_{\text{astro}} > 0.5$  that are classified with a possible NS component. The  $3\sigma$  confidence level upper limits are computed for the 10–1000 keV energy range of the *Fermi*-GBM instrument over its FoV. The  $5\sigma$  confidence level upper limits are computed for the combined coverage of the *Fermi*-GBM and *Swift*-BAT instruments with both instruments matched to the 15–350 keV energy range of *Swift*-BAT. The columns labeled Min and Max correspond, respectively, to the minimum and maximum upper limit values obtained for points within the 90% confidence level region of the GW event localization. The Marginal upper limit is computed by integrating the upper limits produced at individual locations over the full sky using the GW localization as a weighted prior, normalized to the visible portion of the sky. Also shown is the visible coverage percentage of the full GW localization for *Fermi*-GBM alone, *Swift*-BAT alone, and the combined FoV from both instruments.

Event Name	Coverage [%]			$3\sigma$ Flux U.L. [erg s $^{-1}$ cm $^{-2}$ ]			$5\sigma$ Flux U.L. [erg s $^{-1}$ cm $^{-2}$ ]		
	GBM	BAT	Combined	Min	Max	Marginal	Min	Max	Marginal
GW190425	56.70	10.81	57.81	$1.37 \times 10^{-7}$	$2.47 \times 10^{-7}$	$1.66 \times 10^{-7}$	$6.12 \times 10^{-8}$	$2.31 \times 10^{-7}$	$1.51 \times 10^{-7}$
GW190814	100.00	100.00	100.00	$1.17 \times 10^{-7}$	$1.26 \times 10^{-7}$	$1.21 \times 10^{-7}$	$4.71 \times 10^{-8}$	$7.64 \times 10^{-8}$	$6.26 \times 10^{-8}$
GW190917_114630	88.92	6.56	95.07	$1.48 \times 10^{-7}$	$4.33 \times 10^{-7}$	$2.33 \times 10^{-7}$	$5.26 \times 10^{-8}$	$3.83 \times 10^{-7}$	$2.08 \times 10^{-7}$
GW191219_163120	61.06	N/A	61.06	$1.03 \times 10^{-7}$	$2.36 \times 10^{-7}$	$1.20 \times 10^{-7}$	$1.00 \times 10^{-7}$	$2.27 \times 10^{-7}$	$1.15 \times 10^{-7}$
GW200115_042309	96.26	4.80	96.26	$1.31 \times 10^{-7}$	$2.83 \times 10^{-7}$	$1.78 \times 10^{-7}$	$8.53 \times 10^{-8}$	$2.56 \times 10^{-7}$	$1.60 \times 10^{-7}$
GW200210_092254	61.79	50.55	65.85	$1.28 \times 10^{-7}$	$3.13 \times 10^{-7}$	$2.01 \times 10^{-7}$	$4.41 \times 10^{-8}$	$1.47 \times 10^{-7}$	$9.00 \times 10^{-8}$

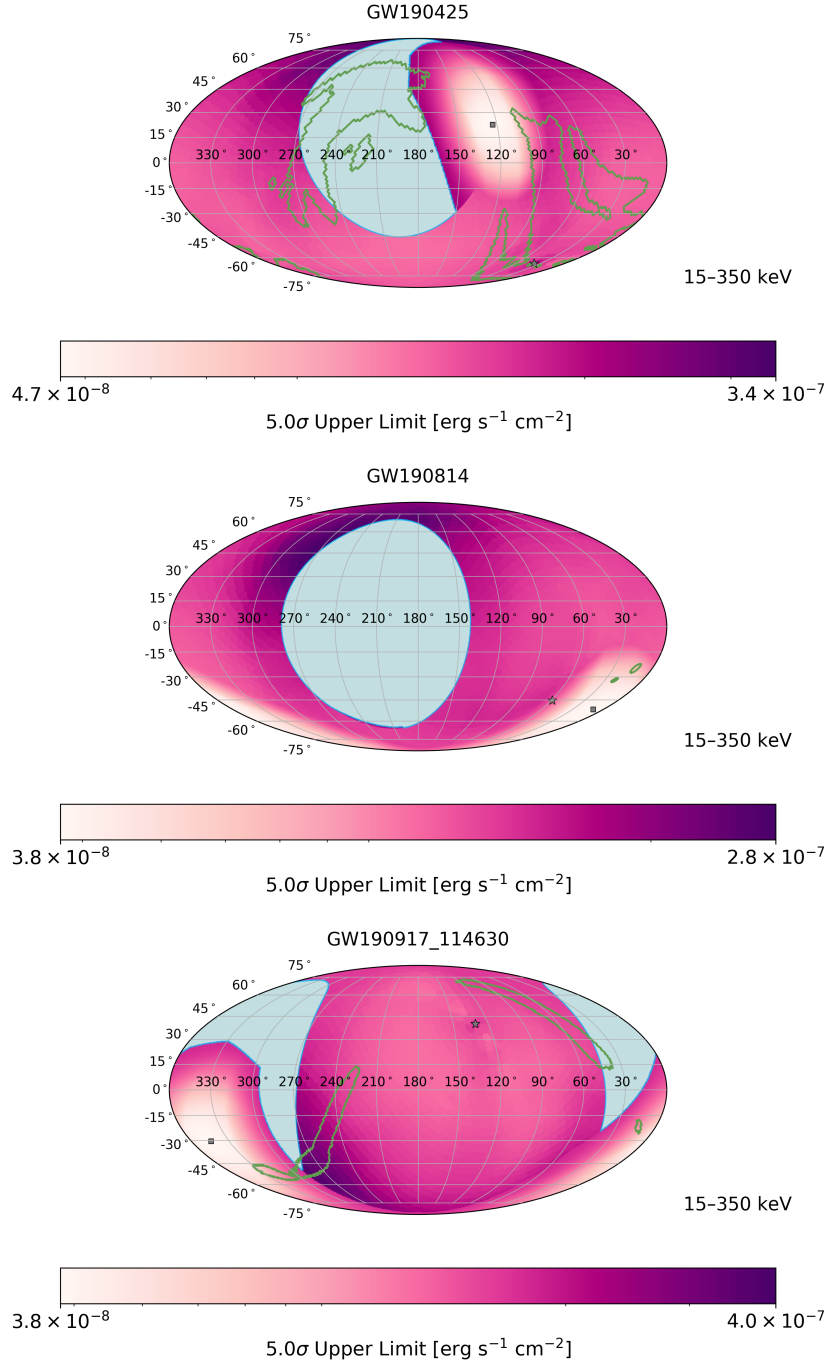
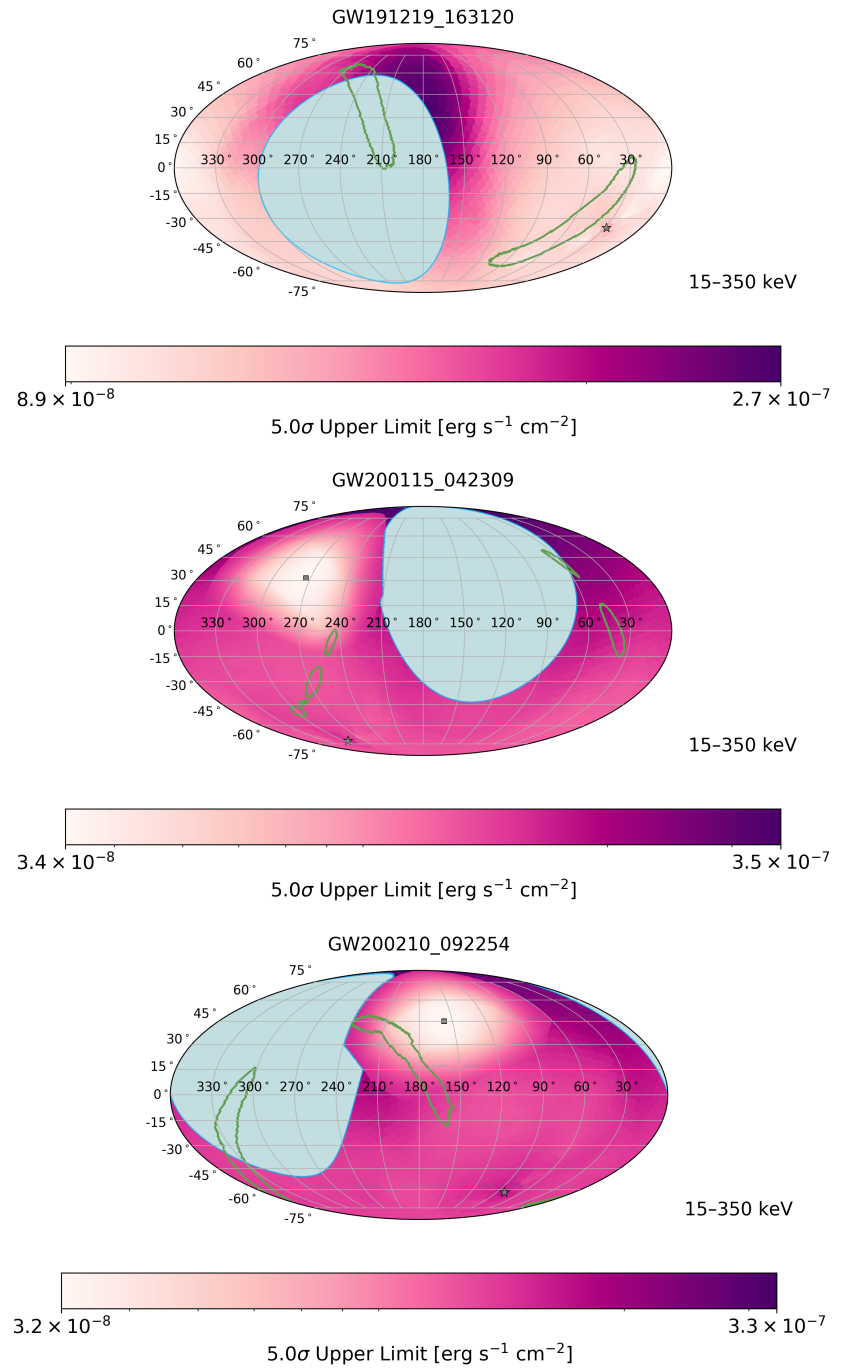


Figure 5.2: The  $5\sigma$  flux upper-limit as a function of sky position for the 6 events from O3 identified with a possible NS component and  $p_{\text{astro}} > 0.5$ . The purple gradient represents the combined *Fermi*-GBM and *Swift*-BAT flux upper limits for source positions at each point on the sky. The star symbol represents the zenith direction of *Fermi*-GBM, the square symbol represents the center of the *Swift*-BAT FoV, and the green contour represents the 90% credible area of the LVK localization. The blue region is the non-visible portion of the sky which is occulted by the Earth for *Fermi*-GBM and outside the *Swift*-BAT FoV.

Figure 5.2: continued.



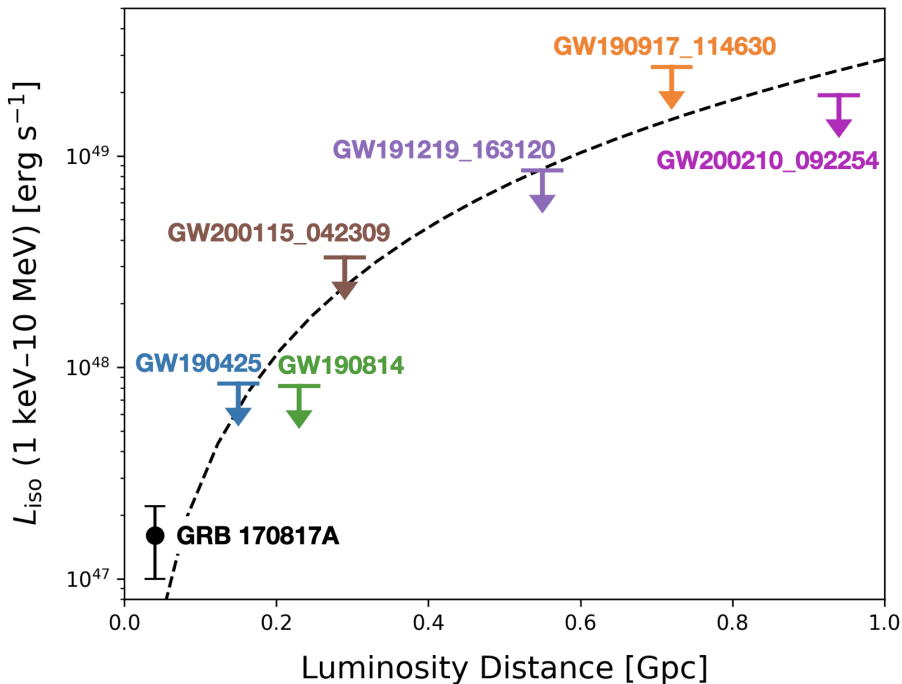


Figure 5.3: The  $5\sigma$  upper-limits on isotropic-equivalent luminosity  $L_{\text{iso}}$  for the 6 events from O3 identified with a possible NS component and  $p_{\text{astro}} > 0.5$ . The black data point is the measured  $L_{\text{iso}}$  from GRB 170817A and the black dashed line is the approximate lower bound for  $L_{\text{iso}}$  of GRBs detected on-board *Fermi*-GBM [191].

corresponding isotropic-equivalent luminosity limits.

Table 5.5: Flux upper limits for possible EM counterparts to probable BBH events detected during O3 with  $p_{\text{astro}} > 0.5$ . The  $3\sigma$  confidence level upper limits are computed for the 10–1000 keV energy range of the *Fermi*-GBM instrument over its FoV. The  $5\sigma$  confidence level upper limits are computed for the combined coverage of the *Fermi*-GBM and *Swift*-BAT instruments with both instruments matched to the 15–350 keV energy range of *Swift*-BAT. The columns labeled Min and Max correspond, respectively, to the minimum and maximum upper limit values obtained for points within the 90% confidence level region of the GW event localization. The Marginal upper limit is computed by integrating the upper limits produced at individual locations over the full sky using the GW localization as a weighted prior, normalized to the visible portion of the sky.

Event Name	Coverage [%]			3 $\sigma$ Flux U.L. [erg s $^{-1}$ cm $^{-2}$ ]			5 $\sigma$ Flux U.L. [erg s $^{-1}$ cm $^{-2}$ ]		
				10–1000 keV			15–350 keV		
	GBM	BAT	Combined	Min	Max	Marginal	Min	Max	Marginal
GW190403_051519	76.61	24.76	82.91	$1.07 \times 10^{-7}$	$3.09 \times 10^{-7}$	$1.78 \times 10^{-7}$	$3.67 \times 10^{-8}$	$2.80 \times 10^{-7}$	$1.50 \times 10^{-7}$
GW190408_181802	SAA	0.00	0.00	-	-	-	-	-	$3.50 \times 10^{-7}$
GW190412	97.27	3.45	99.80	$1.00 \times 10^{-7}$	$1.22 \times 10^{-7}$	$1.11 \times 10^{-7}$	$9.81 \times 10^{-8}$	$1.15 \times 10^{-7}$	$1.07 \times 10^{-7}$
GW190413_052954	33.38	0.05	33.42	$1.21 \times 10^{-7}$	$1.97 \times 10^{-7}$	$1.36 \times 10^{-7}$	$1.15 \times 10^{-7}$	$2.12 \times 10^{-7}$	$1.28 \times 10^{-7}$
GW190413_134308	SAA	6.94	6.94	-	-	-	$7.40 \times 10^{-8}$	$2.10 \times 10^{-7}$	$1.25 \times 10^{-7}$
GW190421_213856	65.97	40.81	99.97	$1.38 \times 10^{-7}$	$1.58 \times 10^{-7}$	$1.44 \times 10^{-7}$	$5.02 \times 10^{-8}$	$2.04 \times 10^{-7}$	$1.30 \times 10^{-7}$
GW190426_190642	88.70	SAA	88.70	$1.10 \times 10^{-7}$	$2.48 \times 10^{-7}$	$1.34 \times 10^{-7}$	$1.09 \times 10^{-7}$	$2.29 \times 10^{-7}$	$1.31 \times 10^{-7}$
GW190503_185404	96.59	SAA	96.59	$1.32 \times 10^{-7}$	$1.36 \times 10^{-7}$	$1.33 \times 10^{-7}$	$1.25 \times 10^{-7}$	$1.28 \times 10^{-7}$	$1.26 \times 10^{-7}$
GW190512_180714	30.95	0.00	30.95	$1.65 \times 10^{-7}$	$1.79 \times 10^{-7}$	$1.76 \times 10^{-7}$	$1.54 \times 10^{-7}$	$1.66 \times 10^{-7}$	$1.64 \times 10^{-7}$
GW190513_205428	84.97	0.00	84.97	$1.07 \times 10^{-7}$	$1.31 \times 10^{-7}$	$1.13 \times 10^{-7}$	$1.06 \times 10^{-7}$	$1.19 \times 10^{-7}$	$1.09 \times 10^{-7}$
GW190514_065416	83.33	68.64	83.75	$1.09 \times 10^{-7}$	$3.03 \times 10^{-7}$	$1.35 \times 10^{-7}$	$3.89 \times 10^{-8}$	$2.79 \times 10^{-7}$	$8.77 \times 10^{-8}$
GW190517_055101	6.81	4.07	10.57	$1.32 \times 10^{-7}$	$1.35 \times 10^{-7}$	$1.34 \times 10^{-7}$	$4.41 \times 10^{-8}$	$1.26 \times 10^{-7}$	$1.02 \times 10^{-7}$
GW190519_153544	40.53	0.00	40.53	$1.13 \times 10^{-7}$	$1.61 \times 10^{-7}$	$1.26 \times 10^{-7}$	$1.06 \times 10^{-7}$	$1.54 \times 10^{-7}$	$1.18 \times 10^{-7}$
GW190521	58.61	61.27	99.98	$1.64 \times 10^{-7}$	$3.54 \times 10^{-7}$	$2.19 \times 10^{-7}$	$4.20 \times 10^{-8}$	$3.20 \times 10^{-7}$	$1.35 \times 10^{-7}$
GW190521_074359	100.00	0.00	100.00	$1.20 \times 10^{-7}$	$1.61 \times 10^{-7}$	$1.51 \times 10^{-7}$	$1.16 \times 10^{-7}$	$1.48 \times 10^{-7}$	$1.40 \times 10^{-7}$
GW190527_092055	72.51	0.05	72.51	$1.14 \times 10^{-7}$	$3.30 \times 10^{-7}$	$1.91 \times 10^{-7}$	$1.10 \times 10^{-7}$	$2.96 \times 10^{-7}$	$1.74 \times 10^{-7}$
GW190602_175927	65.84	SAA	65.84	$1.53 \times 10^{-7}$	$2.08 \times 10^{-7}$	$1.89 \times 10^{-7}$	$1.51 \times 10^{-7}$	$1.92 \times 10^{-7}$	$1.76 \times 10^{-7}$
GW190620_030421	SAA	4.10	4.10	-	-	-	$8.21 \times 10^{-8}$	$1.79 \times 10^{-7}$	$1.39 \times 10^{-7}$
GW190630_185205	78.32	SAA	78.32	$1.17 \times 10^{-7}$	$2.16 \times 10^{-7}$	$1.30 \times 10^{-7}$	$1.08 \times 10^{-7}$	$1.97 \times 10^{-7}$	$1.20 \times 10^{-7}$
GW190701_203306	100.00	99.51	100.00	$1.27 \times 10^{-7}$	$1.33 \times 10^{-7}$	$1.28 \times 10^{-7}$	$1.01 \times 10^{-7}$	$1.20 \times 10^{-7}$	$1.15 \times 10^{-7}$
GW190706_222641	66.90	12.80	73.80	$1.03 \times 10^{-7}$	$2.95 \times 10^{-7}$	$1.63 \times 10^{-7}$	$4.66 \times 10^{-8}$	$2.79 \times 10^{-7}$	$1.53 \times 10^{-7}$
GW190707_093326	42.31	SAA	42.31	$1.38 \times 10^{-7}$	$2.34 \times 10^{-7}$	$1.60 \times 10^{-7}$	$1.30 \times 10^{-7}$	$2.12 \times 10^{-7}$	$1.48 \times 10^{-7}$
GW190708_232457	56.01	SAA	56.01	$1.28 \times 10^{-7}$	$4.24 \times 10^{-7}$	$1.93 \times 10^{-7}$	$1.22 \times 10^{-7}$	$3.77 \times 10^{-7}$	$1.75 \times 10^{-7}$
GW190719_215514	74.97	15.00	89.79	$1.17 \times 10^{-7}$	$3.74 \times 10^{-7}$	$1.85 \times 10^{-7}$	$3.65 \times 10^{-8}$	$3.40 \times 10^{-7}$	$1.60 \times 10^{-7}$
GW190720_000836	87.90	SAA	87.90	$1.08 \times 10^{-7}$	$2.64 \times 10^{-7}$	$1.19 \times 10^{-7}$	$1.01 \times 10^{-7}$	$2.46 \times 10^{-7}$	$1.12 \times 10^{-7}$
GW190725_174728	SAA	SAA	-	-	-	-	-	-	-
GW190727_060333	61.20	0.01	61.20	$1.61 \times 10^{-7}$	$1.93 \times 10^{-7}$	$1.74 \times 10^{-7}$	$1.49 \times 10^{-7}$	$1.72 \times 10^{-7}$	$1.58 \times 10^{-7}$
GW190728_064510	74.03	71.13	74.03	$1.07 \times 10^{-7}$	$2.36 \times 10^{-7}$	$1.21 \times 10^{-7}$	$6.33 \times 10^{-8}$	$2.28 \times 10^{-7}$	$9.27 \times 10^{-8}$
GW190731_140936	61.08	3.17	61.08	$1.20 \times 10^{-7}$	$1.99 \times 10^{-7}$	$1.40 \times 10^{-7}$	$1.13 \times 10^{-7}$	$1.88 \times 10^{-7}$	$1.32 \times 10^{-7}$
GW190803_022701	SAA	47.43	47.43	-	-	-	$7.34 \times 10^{-8}$	$1.47 \times 10^{-7}$	$1.16 \times 10^{-7}$
GW190805_211137	91.07	7.64	98.63	$1.15 \times 10^{-7}$	$1.60 \times 10^{-7}$	$1.43 \times 10^{-7}$	$4.04 \times 10^{-8}$	$1.48 \times 10^{-7}$	$1.27 \times 10^{-7}$
GW190828_063405	90.53	24.93	90.53	$1.34 \times 10^{-7}$	$2.01 \times 10^{-7}$	$1.81 \times 10^{-7}$	$8.58 \times 10^{-8}$	$1.83 \times 10^{-7}$	$1.56 \times 10^{-7}$
GW190828_065509	12.79	8.82	12.79	$1.60 \times 10^{-7}$	$2.98 \times 10^{-7}$	$2.00 \times 10^{-7}$	$5.19 \times 10^{-8}$	$2.67 \times 10^{-7}$	$1.32 \times 10^{-7}$
GW190910_112807	SAA	34.37	34.37	-	-	-	$3.85 \times 10^{-8}$	$1.77 \times 10^{-7}$	$8.11 \times 10^{-8}$
GW190915_235702	94.82	76.04	94.87	$1.59 \times 10^{-7}$	$2.15 \times 10^{-7}$	$1.86 \times 10^{-7}$	$5.59 \times 10^{-8}$	$1.74 \times 10^{-7}$	$1.13 \times 10^{-7}$
GW190916_200658	56.57	0.00	56.57	$1.20 \times 10^{-7}$	$1.61 \times 10^{-7}$	$1.31 \times 10^{-7}$	$1.12 \times 10^{-7}$	$1.42 \times 10^{-7}$	$1.21 \times 10^{-7}$
GW190924_021846	100.00	92.40	100.00	$1.39 \times 10^{-7}$	$1.61 \times 10^{-7}$	$1.47 \times 10^{-7}$	$4.25 \times 10^{-8}$	$1.43 \times 10^{-7}$	$8.43 \times 10^{-8}$
GW190925_232845	SAA	SAA	-	-	-	-	-	-	-
GW190926_050336	60.68	0.02	60.68	$1.53 \times 10^{-7}$	$2.84 \times 10^{-7}$	$2.10 \times 10^{-7}$	$1.43 \times 10^{-7}$	$2.57 \times 10^{-7}$	$1.88 \times 10^{-7}$
GW190929_012149	73.05	34.84	73.05	$1.35 \times 10^{-7}$	$2.25 \times 10^{-7}$	$1.75 \times 10^{-7}$	$4.79 \times 10^{-8}$	$2.14 \times 10^{-7}$	$1.59 \times 10^{-7}$
GW190930_133541	63.05	0.56	63.05	$1.55 \times 10^{-7}$	$2.87 \times 10^{-7}$	$2.39 \times 10^{-7}$	$1.46 \times 10^{-7}$	$2.71 \times 10^{-7}$	$2.25 \times 10^{-7}$

continued on next page

Table 5.5: continued.

Event Name	Coverage [%]			3 $\sigma$ Flux U.L. [erg s $^{-1}$ cm $^{-2}$ ]			5 $\sigma$ Flux U.L. [erg s $^{-1}$ cm $^{-2}$ ]		
				10–1000 keV			15–350 keV		
	GBM	BAT	Combined	Min	Max	Marginal	Min	Max	Marginal
GW191103_012549	76.96	56.21	97.35	$1.57 \times 10^{-7}$	$3.60 \times 10^{-7}$	$1.98 \times 10^{-7}$	$1.25 \times 10^{-7}$	$3.24 \times 10^{-7}$	$1.65 \times 10^{-7}$
GW191105_143521	77.45	8.05	80.39	$1.35 \times 10^{-7}$	$2.01 \times 10^{-7}$	$1.69 \times 10^{-7}$	$1.06 \times 10^{-7}$	$1.91 \times 10^{-7}$	$1.58 \times 10^{-7}$
GW191109_010717	89.38	29.05	89.38	$1.29 \times 10^{-7}$	$2.22 \times 10^{-7}$	$1.55 \times 10^{-7}$	$1.25 \times 10^{-7}$	$2.05 \times 10^{-7}$	$1.47 \times 10^{-7}$
GW191113_071753	72.98	2.27	73.00	$1.53 \times 10^{-7}$	$2.27 \times 10^{-7}$	$1.72 \times 10^{-7}$	$1.45 \times 10^{-7}$	$2.08 \times 10^{-7}$	$1.61 \times 10^{-7}$
GW191126_115259	59.81	7.88	59.81	$1.12 \times 10^{-7}$	$2.09 \times 10^{-7}$	$1.36 \times 10^{-7}$	$7.09 \times 10^{-8}$	$1.96 \times 10^{-7}$	$1.25 \times 10^{-7}$
GW191127_050227	89.03	77.16	89.04	$1.12 \times 10^{-7}$	$2.42 \times 10^{-7}$	$1.40 \times 10^{-7}$	$3.94 \times 10^{-8}$	$2.23 \times 10^{-7}$	$8.96 \times 10^{-8}$
GW191129_134029	SAA	SAA	-	-	-	-	-	-	-
GW191204_110529	48.10	25.20	66.23	$1.09 \times 10^{-7}$	$2.77 \times 10^{-7}$	$1.42 \times 10^{-7}$	$3.10 \times 10^{-8}$	$1.43 \times 10^{-7}$	$1.07 \times 10^{-7}$
GW191204_171526	SAA	87.15	87.15	-	-	-	$2.02 \times 10^{-7}$	$9.13 \times 10^{-7}$	$3.97 \times 10^{-7}$
GW191215_223052	51.87	21.09	51.87	$1.41 \times 10^{-7}$	$1.69 \times 10^{-7}$	$1.53 \times 10^{-7}$	$4.40 \times 10^{-8}$	$1.55 \times 10^{-7}$	$1.29 \times 10^{-7}$
GW191216_213338	94.70	1.76	94.76	$1.40 \times 10^{-7}$	$1.64 \times 10^{-7}$	$1.48 \times 10^{-7}$	$1.26 \times 10^{-7}$	$1.50 \times 10^{-7}$	$1.33 \times 10^{-7}$
GW191222_033537	SAA	0.89	0.89	-	-	-	$1.84 \times 10^{-7}$	$1.92 \times 10^{-7}$	$1.89 \times 10^{-7}$
GW191230_180458	40.80	0.00	40.80	$1.09 \times 10^{-7}$	$1.72 \times 10^{-7}$	$1.39 \times 10^{-7}$	$1.09 \times 10^{-7}$	$1.60 \times 10^{-7}$	$1.33 \times 10^{-7}$
GW200112_155838	SAA	SAA	-	-	-	-	-	-	-
GW200128_022011	45.58	23.04	45.58	$1.22 \times 10^{-7}$	$3.08 \times 10^{-7}$	$1.42 \times 10^{-7}$	$3.29 \times 10^{-8}$	$2.83 \times 10^{-7}$	$1.07 \times 10^{-7}$
GW200129_065458	1.36	1.16	1.36	-	-	$1.42 \times 10^{-7}$	-	-	$6.49 \times 10^{-8}$
GW200202_154313	99.99	SAA	99.99	$1.18 \times 10^{-7}$	$1.26 \times 10^{-7}$	$1.21 \times 10^{-7}$	$1.10 \times 10^{-7}$	$1.18 \times 10^{-7}$	$1.14 \times 10^{-7}$
GW200208_130117	99.70	0.00	99.70	$1.33 \times 10^{-7}$	$1.36 \times 10^{-7}$	$1.36 \times 10^{-7}$	$1.22 \times 10^{-7}$	$1.25 \times 10^{-7}$	$1.25 \times 10^{-7}$
GW200208_222617	SAA	5.85	5.85	-	-	-	$6.09 \times 10^{-8}$	$1.77 \times 10^{-7}$	$1.06 \times 10^{-7}$
GW200209_085452	61.47	7.05	61.63	$1.27 \times 10^{-7}$	$1.69 \times 10^{-7}$	$1.35 \times 10^{-7}$	$3.71 \times 10^{-8}$	$1.28 \times 10^{-7}$	$1.17 \times 10^{-7}$
GW200216_220804	SAA	38.42	38.42	-	-	-	$8.98 \times 10^{-8}$	$1.71 \times 10^{-7}$	$1.47 \times 10^{-7}$
GW200219_094415	20.36	SAA	20.36	$1.37 \times 10^{-7}$	$1.73 \times 10^{-7}$	$1.52 \times 10^{-7}$	$1.29 \times 10^{-7}$	$1.58 \times 10^{-7}$	$1.41 \times 10^{-7}$
GW200220_061928	99.63	0.05	99.65	$1.33 \times 10^{-7}$	$2.12 \times 10^{-7}$	$1.65 \times 10^{-7}$	$1.22 \times 10^{-7}$	$1.87 \times 10^{-7}$	$1.48 \times 10^{-7}$
GW200220_124850	63.37	21.46	80.25	$1.10 \times 10^{-7}$	$2.34 \times 10^{-7}$	$1.28 \times 10^{-7}$	$3.07 \times 10^{-8}$	$2.18 \times 10^{-7}$	$1.10 \times 10^{-7}$
GW200224_222234	SAA	98.76	98.76	-	-	-	$1.13 \times 10^{-7}$	$1.40 \times 10^{-7}$	$1.27 \times 10^{-7}$
GW200225_060421	87.61	1.30	87.61	$1.37 \times 10^{-7}$	$3.32 \times 10^{-7}$	$2.36 \times 10^{-7}$	$1.28 \times 10^{-7}$	$3.10 \times 10^{-7}$	$2.23 \times 10^{-7}$
GW200302_015811	67.41	23.35	67.92	$1.04 \times 10^{-7}$	$3.40 \times 10^{-7}$	$1.62 \times 10^{-7}$	$3.27 \times 10^{-8}$	$1.77 \times 10^{-7}$	$1.19 \times 10^{-7}$
GW200306_093714	72.37	30.46	90.36	$1.18 \times 10^{-7}$	$2.54 \times 10^{-7}$	$1.46 \times 10^{-7}$	$5.38 \times 10^{-8}$	$2.40 \times 10^{-7}$	$1.33 \times 10^{-7}$
GW200308_173609	70.53	4.40	70.89	$1.19 \times 10^{-7}$	$3.39 \times 10^{-7}$	$1.92 \times 10^{-7}$	$8.13 \times 10^{-8}$	$3.20 \times 10^{-7}$	$1.77 \times 10^{-7}$
GW200311_115853	SAA	N/A	-	-	-	-	-	-	-
GW200316_215756	15.69	13.49	15.69	$1.14 \times 10^{-7}$	$1.51 \times 10^{-7}$	$1.34 \times 10^{-7}$	$1.09 \times 10^{-7}$	$1.36 \times 10^{-7}$	$1.22 \times 10^{-7}$
GW200322_091133	75.18	13.82	89.00	$1.06 \times 10^{-7}$	$3.70 \times 10^{-7}$	$1.54 \times 10^{-7}$	$4.49 \times 10^{-8}$	$3.38 \times 10^{-7}$	$1.39 \times 10^{-7}$

### 5.3.3 Marginal Events

Although these events have  $p_{\text{astro}} < 0.5$ , all 6 marginal GW events from Table 5.2 are of interest for EM follow-up. This is because GW200311\_103121 may have a possible BNS origin and the remaining 5 events have possible NSBH origins [49, 194]. In particular, the possible NSBH event GW200105\_162426 was noted as a clear outlier from experimental backgrounds despite not satisfying the  $p_{\text{astro}} > 0.5$  criteria used to identify events with a likely astrophysical origin. It also has the highest observed  $p_{\text{astro}}$  of all the marginal events.

The 5 marginal events with possible NSBH origins were visible to *Fermi*-GBM while the

remaining event, GW200311\\_103121, occurred when *Fermi*-GBM was in the SAA. None of the marginal events have appreciable coverage in *Swift*-BAT. No significant counterparts were found. As with GW190425, this may be due to unfavorable viewing angles with respect to the jet axis, larger observational distances such as the  $0.27^{+0.12}_{-0.11}$  Gpc distance to GW200105\\_162426 [49], and partial sky coverage for events other than GW190426\\_152155. It therefore remains ambiguous as to whether these events are real compact binary coalescences. Nevertheless, we provide in Table 5.6 the flux upper limits for each event calculated according to the same methods described in Section 5.3.1 since they may provide emission model constraints if future analyses can identify an astrophysical progenitor with a favorable viewing angle with respect to the jet axis. Figure 5.4 displays the  $5\sigma$  confidence level flux upper limit map for GW200105\\_162426 since it is the marginal event with the highest probability of having an astrophysical origin. The marginalized  $5\sigma$  flux upper limit of this event yields an isotropic-equivalent luminosity upper limit of  $L_{\text{iso}} = 2.2 \times 10^{48} \text{ erg s}^{-1}$  when combined with its 0.27 Gpc distance. Appendix C.3 provides flux upper-limits as a function of sky position for the remaining marginal events.

## 5.4 Summary and Future Directions

Using the 79 GW candidates with  $p_{\text{astro}} > 0.5$  from O3 that were reported in GWTC-3, we searched for coincident EM counterparts with *Fermi*-GBM and *Swift*-BAT. This represents the most comprehensive follow-up to date of the O3 run in the hard X-ray and gamma-ray regime. We found no significant counterparts in either instrument. For the one BNS event, GW190425, with  $p_{\text{astro}} > 0.5$  there are several possible reasons for the non-detection of a counterpart:

- The combined *Fermi*-GBM and *Swift*-BAT coverage of the GW localization area was

Table 5.6: Flux upper limits for possible EM counterparts to marginal GW events with ( $\text{FAR} < 2 \text{ yr}^{-1}$ ,  $p_{\text{astro}} < 0.5$ ). The  $3\sigma$  confidence level upper limits are computed for the 10–1000 keV energy range of the *Fermi*-GBM instrument over its field-of-view. The  $5\sigma$  confidence level upper limits are computed for the combined coverage of the *Fermi*-GBM and *Swift*-BAT instruments with both instruments matched to the 15–350 keV energy range of *Swift*-BAT. The columns labeled Min and Max correspond, respectively, to the minimum and maximum upper limit values obtained for points within the 90% confidence level region of the GW event localization. The Marginal upper limit is computed by integrating the upper limits produced at individual locations over the full sky using the GW localization as a weighted prior, normalized to the visible portion of the sky. Also shown is the visible coverage percentage of the full GW localization for *Fermi*-GBM alone, *Swift*-BAT alone, and the combined FoV from both instruments.

Event Name	Coverage [%]			$3\sigma$ Flux U.L. [ $\text{erg s}^{-1} \text{cm}^{-2}$ ]			5 $\sigma$ Flux U.L. [ $\text{erg s}^{-1} \text{cm}^{-2}$ ]		
	GBM	BAT	Combined	Min	Max	Marginal	Min	Max	Marginal
GW190426_152155	100.00	SAA	100.00	$1.03 \times 10^{-7}$	$1.65 \times 10^{-7}$	$1.30 \times 10^{-7}$	$1.00 \times 10^{-7}$	$1.53 \times 10^{-7}$	$1.21 \times 10^{-7}$
GW190531_023648	86.90	0.03	86.91	$1.35 \times 10^{-7}$	$2.63 \times 10^{-7}$	$1.74 \times 10^{-7}$	$1.26 \times 10^{-7}$	$2.42 \times 10^{-7}$	$1.60 \times 10^{-7}$
GW191118_212859	93.63	SAA	93.63	$1.07 \times 10^{-7}$	$2.93 \times 10^{-7}$	$1.19 \times 10^{-7}$	$1.05 \times 10^{-7}$	$2.71 \times 10^{-7}$	$1.13 \times 10^{-7}$
GW200105_162426	53.57	3.01	54.36	$1.13 \times 10^{-7}$	$1.53 \times 10^{-7}$	$1.26 \times 10^{-7}$	$1.06 \times 10^{-7}$	$1.69 \times 10^{-7}$	$1.18 \times 10^{-7}$
GW200201_203549	86.01	SAA	86.01	$1.17 \times 10^{-7}$	$1.80 \times 10^{-7}$	$1.31 \times 10^{-7}$	$1.09 \times 10^{-7}$	$1.64 \times 10^{-7}$	$1.22 \times 10^{-7}$
GW200311_103121	0.01	-	-	-	-	-	-	-	$1.09 \times 10^{-7}$

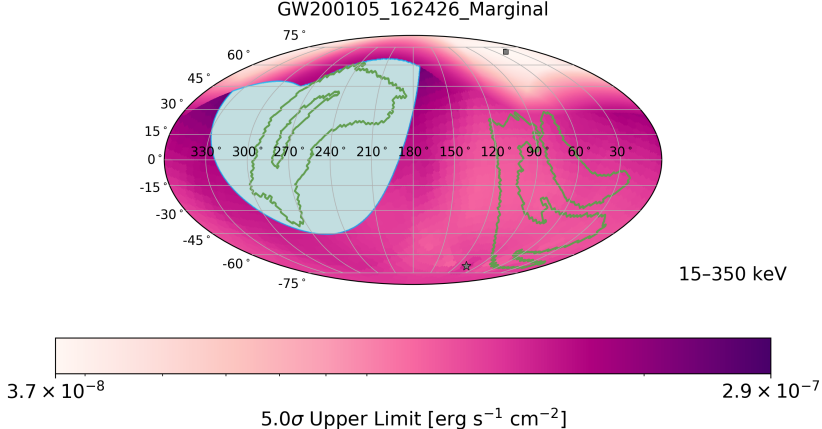


Figure 5.4: The  $5\sigma$  upper-limits as a function of sky position for GW200105\_162426, the marginal GW event with the highest  $p_{\text{astro}}$ . The purple gradient represents the combined *Fermi*-GBM and *Swift*-BAT flux upper limits for source positions at each point on the sky. These are computed at a  $5\sigma$  confidence level for a Band function ( $E_{\text{peak}} = 230 \text{ keV}$ ,  $\alpha = -1.0$ ,  $\beta = -2.3$ ) spectral shape over a 15–350 keV energy range assuming a 1 s emission duration. The star symbol represents the zenith direction of *Fermi*-GBM, the square symbol represents the center of the *Swift*-BAT field-of-view, and the green contour represents the 90% credible area of the LVK localization. The blue region is the non-visible portion of the sky which is occulted by the Earth for *Fermi*-GBM and outside the *Swift*-BAT FoV.

$\sim 60\%$ , meaning that the GW source may have been outside the FoV for both instruments.

- The distance to GW190425 was four times larger than the estimated distance for GW170817, causing the observed flux to be below the detection threshold in both instruments if it had the same intrinsic luminosity and viewing angle as GW170817.
- The viewing angle may have been too far away from the jet axis to detect emission under scenarios with a clean or structured jet.

This event is therefore unconstrained by our observations.

With O4 on the horizon, we expect an increase in GW detections by a factor of 5 [237, 238] and a bountiful regime of EM follow-up data. This will greatly increase the need for further instantaneous, wide FoV gamma-ray/x-ray observations in order to detect the EM counterparts to

these GW events and localize them, especially given the absence of a counterpart detection during O3. Towards this end, the *Fermi*-GBM Targeted Search updates presented in this paper will be used in future LIGO/Virgo/KAGRA observing runs. In the absence of detections, flux upper limits, both marginalized and skymaps, will be provided to the community. Additionally, *Swift*-BAT will provide further sub-threshold searches of GW candidates with enhanced sensitivity through the GUANO pipeline. The work presented here, additionally, will be used to compute flux upper limits with BAT rate data, which is much less computationally expensive compared to GUANO and, thus, crucial for the quick turnaround required for the follow-up observations of GW triggers.

## Chapter 6: A Cross-correlation Study between IceCube Neutrino Events and the *Fermi*-LAT Unresolved Gamma-ray Sky

*When day comes, we ask ourselves, where can we find light in this never-ending shade?*

---

Amanda Gorman

A population of high-energy neutrinos of astrophysical origin has been observed [239], though the sources of the bulk of these events remain unknown [240]<sup>1</sup>. Neutrinos at TeV-PeV energies are produced when relativistic protons interact with matter via hadronuclear interaction (inelastic  $p$ - $p$  scattering) or with radiation via photohadronic processes ( $p$ - $\gamma$  interactions). These processes also produce neutral pions that decay into gamma rays. Since neither signal experiences propagation delay, a simultaneous detection of gamma rays and neutrinos would provide invaluable insights into the nature of the production source.

Blazars are promising sources of high-energy neutrinos. The blazar TXS 0506+056 was identified as the first high-energy neutrino source candidate via the coincidence of its very-high-energy gamma-ray flare with a high-energy neutrino [241] and excess of neutrino events in IceCube's historical data [242]. In addition, an excess of IceCube neutrinos has been found from

---

<sup>1</sup>The work in this chapter is published in the Astrophysical Journal, under *ApJ* 951 83 [2] and is presented here with minimal modifications. The lead author is Dr. Michela Negro. The Ph.D. Candidate Milena Crnogorčević is the second author on the paper and has considerably contributed to the analysis, simulation of the *Fermi*-LAT data, and conducted an in-depth tests of the pipeline. The IceCube data treatment was done in collaboration with Dr. Michael Larson and Dr. Ke Fang.

the direction of the starburst Seyfert galaxy NGC 1068 [243], also detected in gamma rays in the GeV regime. Marginal evidence has been suggested toward spatial coincidences between tidal disruption events and IceCube alert events, albeit with a relatively long delay in neutrino detection [244, 245]. These results suggest that the production of high-energy neutrinos could be related to supermassive black hole activity.

Besides single sources studies in coincidence with IceCube events, significant effort has been directed towards systematic searches of spatial correlation between blazar catalogs and IceCube all-sky data. Searches using gamma-ray blazars, including the second *Fermi* LAT AGN catalog [2LAC, 246] and the *Fermi*-LAT low energy catalog [1FLE, 247], found that resolved blazars contribute less than  $\sim 30\%$  and  $1\%$  of the diffuse flux [248, 249], respectively. Searches with radio-selected blazars using public IceCube data introduced possible positive spatial correlations [250, 251].

Although the sample of resolved blazars includes the brightest sources, the cumulative emission from unresolved sources carries substantial amount of energy. In fact, the spatial distribution of the Unresolved Gamma-ray Background (UGRB) sources and its corresponding anisotropy measurement (most recently measured by [252]) can entirely be accounted for by the gamma-ray emission from isotropically distributed blazars below the LAT sensitivity threshold [253, 254]. At the same time, this very population of blazars accounts for the 20–30% of the total UGRB intensity spectrum [254], which also sees the contribution from other, more numerous and spatially smoother, populations such as star forming galaxies and misaligned AGNs (see, e.g., [255] and [256]). Finally, GeV-TeV photons from extragalactic gamma-ray sources will be attenuated due to pair production, resulting in the brightest neutrino sources being gamma-ray dim [257]. It is therefore crucial to study the contribution of these faint, unresolved gamma-ray

blazars to the diffuse high-energy neutrino flux.

So far, source association studies of astrophysical neutrinos have largely relied upon considering resolved gamma-ray sources; in turn, neglecting all the objects that are too faint to be detected individually, yet still contributing to the total gamma-ray flux. In this work, we determine the level of correlation between the UGRB emission as observed by the *Fermi* over 12 years, and the neutrino event observations conducted in 10 years of IceCube observations [258, 259].

Previous source association involving IceCube data analyses mostly rely on likelihood stacking (e.g., [240]). More recently, the two-point cross-correlation method has also been employed to investigate the physical origins of astrophysical neutrinos. Cross-correlation measurements were primarily introduced to describe the distribution of galaxies in the Universe, relying upon the consideration of excess probabilities of finding two galaxies at some separation, drawn from a random distribution of points [260]. This cross-correlation technique has been extensively adopted to characterize the UGRB in several works studying its connection with the large scale structure of the Universe: from galaxy catalogs [261–263] to galaxy cluster catalogs [264–267], weak lensing from cosmic shear [268–271], and lensing potential of the cosmic-microwave background [272]. A generalization of such methods was utilized in [273], considering association of astrophysical neutrinos with the well-calibrated tracers of the large scale structure obtained from the infrared catalogs.

As such, in this chapter we investigate the sensitivity of the 2D spatial cross-correlation technique to detecting a significant cross-correlation signal between the emission from a population of LAT-unresolved  $\gamma$ -ray blazars and the muon-neutrino events detected by IceCube. To this end, we build a simulation pipeline with the goal of comparing the sensitivity by varying the amount of expected observed neutrino signal given a gamma-ray intensity distribution and as-

suming p-p or p- $\gamma$  interaction. We also investigate the improvement in sensitivity with increased statistics in the IceCube data sample, in view of future advancements and data reprocessing such as IceCube-Gen2 [274]. The chapter is organized as follows. Section 6.1 provides the descriptions of the analysis set-up and the cross-correlation method. We devote Section 6.2.2 to the construction of the data maps, while a description of the procedure to generate simulated maps is laid out in Section 6.3. The results for both the sensitivity study and the real-data cross-correlation analysis are shown in Section 6.4. Finally, the discussion and the conclusions are presented in Section 6.5. Additional considerations and plots are provided in Appendix.

## 6.1 An ab-initio introduction to the cross-correlation technique

**Autocorrelation.** The 2-point autocorrelation function,  $\xi(r)$ , quantifies the probability of finding two signals (e.g., galaxies) at a given spatial distance  $r$ . It can be interpreted as the global measure of clustering at different angular scales, i.e., a measure of whether and to what extent sources follow a random distribution in the sky. The autocorrelation function is defined as the excess probability,  $dP$ , above the expected random spatial distribution of finding an object at a separation  $r$  in the given volume  $dV$  with a given density of objects  $n$ , and can be expressed as

$$dP = n [\xi(r) + 1] dV. \quad (6.1)$$

Depending on the population of interest, the autocorrelation function can be expressed in terms of fluctuation fields,  $\delta(x) = n(x)/\langle n \rangle - 1$ , averaged over the spatial distribution as  $\xi(r) = \langle \delta(x)\delta(r+x) \rangle$ . In spherical symmetry, the angular autocorrelation function,  $i_{\text{ang}}(r)$ , is usually represented through its Legendre transform—the angular power spectrum (APS),  $C_l$ , and is given

by

$$\xi_{\text{ang}}(r) = \sum_{\ell} C_{\ell} \sum_m Y_{\ell m}(x) Y_{\ell m}^*(r + x) = \sum_{\ell} C_{\ell} \frac{2\ell + 1}{4\pi} P_{\ell}(\cos \theta), \quad (6.2)$$

where  $\theta$  is the angular separation between two points,  $\ell$  is the multipole of the harmonic space, and  $Y_{\ell m}$  are the spherical harmonics. To more easily visualize this expression, the reader may think about the APS as a measure of anisotropy associated with each multipole  $\ell$ , corresponding to the overdensity of an angular size  $\theta \sim 180 \text{ deg} / \ell$ .

**Cross-correlation.** Cross-correlation is a more general case of the autocorrelation technique and is used to quantify the similarity between two *different* datasets either in their respective temporal or spatial separations. In astronomy, it has been widely used to characterize signals that would otherwise be difficult to detect.

The cross-correlation angular power spectrum (CAPS) between a field  $\delta_{\alpha}$  and a field  $\delta_{\beta}$  is given by

$$C_{\ell}^{\alpha\beta} = \frac{1}{2\ell + 1} \left\langle \sum_m a_{\ell m}^{\alpha} a_{\ell m}^{\beta} \right\rangle \quad (6.3)$$

averaged over modes  $m$ , with coefficients  $a_{\ell m}$  given by the expansion into spherical harmonics of the fields of interest,

$$\delta_{\alpha}(\mathbf{n}) = \sum_{\ell m} a_{\ell m}^{\alpha} Y_{\ell m}(\mathbf{n}). \quad (6.4)$$

The  $\mathbf{n}$  denotes a given direction in the sky. Analogously to APS, CAPS also measures the anisotropy amplitude associated with different multipoles,  $\ell$ , corresponding to different angular sizes,  $\theta$ . Again, the higher the multipole, the smaller the angular size.

## 6.2 $\nu \times \gamma$ skies

We are now prepared to embark onto our analysis journey. In our study the two fields are represented by the gamma-ray intensity field (in units of  $\text{cm}^{-2}\text{s}^{-1}\text{sr}^{-1}$ ) and the neutrino count fluctuation field:

$$\delta_\gamma(\mathbf{n}) = \Phi_\gamma(\mathbf{n}) \quad \delta_\nu(\mathbf{n}) = \Xi_\nu(\mathbf{n}) \quad (6.5)$$

where  $\Xi_\nu(\mathbf{n})$  is defined later on in Eq. 6.11. The generation of the field maps in HEALPix is described in Sec. 6.2.2 and Sec. 6.3 for real and simulated data respectively. Here, we provide the steps to compute CAPS.

Given a pair of HEALPix<sup>2</sup> [275, 276] maps of equal order, we compute the CAPS using the *PolSpice* statistical toolkit [277–280]. *PolSpice* allows for an automated correction of the angular power spectra for the effect of a mask applied to the maps. Additionally, it provides the covariance matrix,  $V_{\ell\ell'}$ , which carries information about the covariant uncertainties among the power of different angular scales. We remove the monopole and the dipole components using the dedicated *PolSpice*’s routines in order to reduce the contamination on small scales. The CAPS, as given by *PolSpice*, must be corrected by the point spread function (PSF) of both *Fermi*-LAT and IceCube. We also apply a correction for the spatial binning (pixeling) of the maps. The corrected CAPS,  $\overline{C}_\ell^{(\gamma\nu)}$ , is given by

$$\overline{C}_\ell^{(\gamma\nu)} = C_\ell^{(\gamma\nu)} W_\ell^{-1} \quad (6.6)$$

where  $C_\ell^{(\gamma\nu)}$  is the raw CAPS and  $W_\ell = (W_\ell^{\gamma,\text{beam}} W_\ell^{\nu,\text{beam}})(W_\ell^{\text{pix}})^2$ .  $W_{\text{pix}}$  is the “pixel window function” which corrects for the pixellation.  $W_\ell^{\gamma,\text{beam}}$  and  $W_\ell^{\nu,\text{beam}}$  are “beam window functions”

---

<sup>2</sup><http://healpix.sourceforge.net>, as accessed on March 28, 2023.

for *Fermi* and IceCube respectively. They correct for the angular resolution of the instruments and are computed as

$$W^{beam}(E, \ell) = 2\pi \int_0^\pi P_\ell(\cos \theta) \text{PSF}(\theta, E) \sin \theta d\theta \quad (6.7)$$

where  $P_\ell(\cos \theta)$  are the Legendre polynomial of index  $\ell$  for the angular scale  $\theta$ , and  $\text{PSF}(\theta, E)$  is the PSF as a function of angular distance  $\theta$  and energy  $E$ . For *Fermi*-LAT, the  $\text{PSF}(\theta)$  can be obtained for specific  $E_\gamma$  values with `gtpsf` tools<sup>3</sup>, then the bin-averaged beam window function,  $W_E^{beam}(\ell)$ , can be obtained averaging the  $W^{beam}(E, \ell)$  over the energy range considered, weighted by the UGRB intensity spectrum, which is approximately a power law with index  $-2.3$  [281]:

$$W_E^{\gamma, beam}(\ell) = \frac{\int_{E_{min}}^{E_{max}} W^{\gamma, beam}(E, \ell) \frac{dN}{dE} dE}{\int_{E_{min}}^{E_{max}} \frac{dN}{dE} dE}. \quad (6.8)$$

$W_{pix}$  is obtained with the HEALPix routine `pixwin`, and is the same for both the *Fermi* and IceCube maps (since the pixeling order is the same), and it is shown as a gray dashed line in the left plot of Fig. D.1 in the Appendix D.1.

We bin CAPS in multipole space in order to minimize the artificial correlation between adjacent multipoles in the  $C_\ell$  spectrum that is caused by masking the maps. Following the procedure outlined in [252] and [282]<sup>4</sup>, the  $\overline{C}_\ell$  value in the  $\Delta\ell$  bin is computed as the arithmetic mean of the corresponding  $C_\ell$  values. The errors of the binned CAPS is obtained from the associated

---

<sup>3</sup>*Fermi Science Tools* routine, <https://fermi.gsfc.nasa.gov/ssc/data/analysis/software/>, as accessed on April 1, 2023.

<sup>4</sup>The unweighted averaging procedure is validated using Monte Carlo simulations in [282] (see Sec. IV-A of the paper), and also applied in other similar cross-correlation analyses [e.g. 262]

covariance matrices following the procedure adopted from [282].

$$\Delta C_\ell = \sqrt{\sum_{\ell\ell'} \bar{V}_{\ell\ell'} / \Delta \ell^2} \quad (6.9)$$

where  $\bar{V}$  is the covariance matrix given by *PolSpice* and corrected by the window function,  $\bar{V}_{\ell\ell'} = V_{\ell\ell'} W_\ell^{-2} W_{\ell'}^{-2}$ . The covariance matrix computed with *PolSpice* ignores effects due to non-Gaussian contributions. In this work, the cross-correlation measurement is dominated by the shot-noise terms and we expect higher order effects from non-Gaussian contributions to be negligible.

The UGRB angular power spectrum is described by a constant function across the energy range considered in this work [252]. According to the interpretation of the halo model [283]<sup>5</sup>, such observation is dominated by 1-halo term component produced by the emission of isotropically distributed point-like sources. Among possible contributors, blazars are the absolutely dominant population producing the observed anisotropy in the UGRB [254]. On the neutrino side, the cross-correlation of IceCube events with the WISE–2MASS galaxy sample in [273] also shows no deviation from a 1-halo term. As we are testing the spatial correlation between the population of blazars that dominates the UGRB anisotropy and the IceCube events, we also expect a cross-correlation signal to be also dominated by the 1-halo term.

The cross-correlation 1-halo term, usually denoted as  $C_P$ , is computed by fitting the mea-

---

<sup>5</sup>Here, the cross-correlation signal is a sum of a compact 1-halo term (tracing the intra-halo correlation), which is constant as a function of the multipoles, and a more extended 2-halo term, a decreasing function of the multipoles (tracing the inter-halos cross-correlation and representing the signature of correlation with the large-scale structure).

sured CAPS with a constant by minimizing the  $\chi^2$  function defined as

$$\chi^2 = \Delta^T \bar{V}_{\ell\ell'}^{-1} \Delta, \quad \text{where } \Delta^T = (C_{\Delta\ell,1} - C_P, \dots, C_{\Delta\ell,N} - C_P). \quad (6.10)$$

In the fit, we do not consider multipoles below 20 to further exclude any possible contamination from large-scale residuals in the *Fermi*-LAT maps due to mis-modeling of the Galactic foreground and/or the *Fermi*-LAT exposure uncertainty. At high multipoles we are limited by the IceCube PSF, which we estimate to be 0.47 degrees at 68% containment angle for high-energy events. This limits the maximum multipole we can consider in this study to  $\ell \approx 380$ . More details on the estimation of the IceCube PSF profile is given in Appendix D.1.

### 6.2.1 Data Selection

The UGRB anisotropy energy spectrum shows a significant ( $> 4\sigma$ ) detection of anisotropies from point-like sources in the energy range between 1 and  $\sim 25$  GeV [252]. As such, here we only focus on this energy range for the gamma-ray data selection, and we work in four different energy bins (1–2, 2–5, 5–10, and 10–25 GeV). Using the energy-resolved approach is supported by the sizeable photon statistics of the LAT data. Analogously to [252], we consider a sub-selection of events (and their corresponding response functions) with better angular resolution. This selection corresponds to SOURCEVENTO event class and PSF1+PSF2+PSF3 event type<sup>6</sup>. In this study we use 12 years of *Fermi*-LAT Pass 8 data.

We use IceCube’s 10 year public data release [259] derived from a recent time-integrated

---

<sup>6</sup>See [https://fermi.gsfc.nasa.gov/ssc/data/analysis/documentation/Cicerone/Cicerone\\_Data/LAT\\_DP.html](https://fermi.gsfc.nasa.gov/ssc/data/analysis/documentation/Cicerone/Cicerone_Data/LAT_DP.html) for more detail regarding the LAT event selection, as accessed on April 1, 2023.

point source search [284]. This data release, taken between 2008 and 2018, includes a complete set of instrument response functions (“IRFs”) describing the reconstruction behavior of the detector as a probability mapping  $P(E_{proxy}, \Psi, \sigma | E_\nu, \delta)$  where  $E_{proxy}$  is the reconstructed proxy for the energy,  $\Psi$  is the directional reconstruction error,  $\sigma$  is the estimated directional uncertainty,  $E_\nu$  is the true neutrino energy, and  $\delta$  is the source declination<sup>7</sup>. Effective areas binned in true neutrino energy and declination are provided for several “detector seasons” corresponding to different versions of the detector or processing chain (“IC40”, “IC59”, “IC79”, “IC86-I” and “IC86-II+”). IRFs allow users to map neutrino energy and source declination to reconstructed energy proxy, angular uncertainty, and PSF for each season. Reconstructed energy proxies, directions, and angular uncertainties for each observed event are also provided in the data release. To simplify calculations, we consider only the final detector season, “IC86-II+”, spanning six years of data with **uniform** effective area and IRFs.

### 6.2.2 Real data maps

The *Fermi*-LAT UGRB maps have been obtained following the same procedure as in [252], i.e., through finely binning the data in energy (32 *micro* logarithmic bins between 1-25 GeV) to produce intensity maps and then sum the final maps into *macro* bins; as described in Sec. 6.1, we bin the data in four logarithmic energy bins between 1 and 25 GeV. We use version v10r0p5 of the *Fermi Science Tools* to generate all-sky intensity maps in HEALPix format (order 8), as described in Sec. II of [252]. As an example, Fig. 6.1 (middle panel) shows the *Fermi*-LAT UGRB intensity map in the energy bin 2-5 GeV, where the gray areas are masked away as

---

<sup>7</sup>Details on the meaning of each parameter are provided on IceCube’s data release pag, <https://icecube.wisc.edu/science/data-releases/> and in a README file included in the release itself, as accessed on April 1, 2023.

described in Section 6.2.3.

The subtraction procedure of the residual Galactic foreground emission outside the masked region is detailed Sec. I of the Supplemental Online Material of [252]. In this work we use the Galactic diffuse emission model `gll_iem_v7.fits`<sup>8</sup>. For the auto-correlation analysis in [252], the authors test that any residual contamination from the Galactic foreground is negligible above multipole 50: the angular power spectrum flattens after the foreground subtraction in the range of multipoles of interest (see their Fig. 3, left panel, of the Supplemental material). We repeat the test for our energy bins, confirming that this is still the case. In our cross-correlation study, therefore, we do not expect any significant residual contamination from the Galactic foreground.

The IceCube data map are obtained by filling an order 8 HEALPix map with the IceCube data provided in [259], selecting data taken in the 6 years between 2012 and 2018. In order to account for the widely varying IceCube response in declination, we choose to use a fluctuation map  $\Xi$  for the neutrino data. We define the neutrino fluctuation map by normalizing the trial map for each HEALPix band in declination

$$\Xi_{pix}^{\delta} = \frac{N_{pix}^{\delta} - \langle N \rangle^{\delta}}{\langle N \rangle^{\delta}} \quad (6.11)$$

where  $N_{pix}^{\delta}$  is the number of events observed in HEALPix pixel  $pix$  at a declination of  $\delta$  and  $\langle N \rangle^{\delta}$  is the average count over that declination. In Fig. 6.1, the bottom row maps illustrate an example of IceCube simulated counts map (on the left) and the derived fluctuation map (on the right). Fig. 6.1, right panel, illustrates the IceCube fluctuation map with the mask applied.

---

<sup>8</sup>[https://fermi.gsfc.nasa.gov/ssc/data/analysis/software/aux/4fgl/Galactic\\_Diffuse\\_Emission\\_Model\\_for\\_the\\_4FGL\\_Catalog\\_Analysis.pdf](https://fermi.gsfc.nasa.gov/ssc/data/analysis/software/aux/4fgl/Galactic_Diffuse_Emission_Model_for_the_4FGL_Catalog_Analysis.pdf), as accessed on April 1, 2023.

### 6.2.3 Masking

The IceCube effective area for neutrino-like events has a strong dependence on the declination [259]. In the Southern hemisphere ( $\delta - 5^\circ$ ), the IceCube sky is dominated by muons produced in atmospheric air showers. Cuts are applied to remove these backgrounds from the Southern sky, resulting in a high energy threshold. Atmospheric muons from the Northern hemisphere ( $\delta \geq -5^\circ$ ), are blocked by Earth from reaching the IceCube detectors. However, instead of muons, atmospheric neutrinos generated in air showers provide an irreducible background in IceCube's Northern sky. Because the neutrino cross-section increases with energy, Earth limits the number of high energy neutrino events visible in the Northern sky.

In order to optimize our sensitivity to cross-correlations between IceCube's neutrinos and the UGRB, we first study IceCube's expected response as a function of neutrino energy and arrival declination. We expect the UGRB-correlated neutrinos to contribute to IceCube's unresolved astrophysical diffuse flux, so we first compute the expected astrophysical neutrino events. To this end, we weight each energy and declination bin of IceCube's effective area using simple power law parametrized as in IceCube's most recent fit [285],

$$\frac{d\Phi_\nu}{dE_\nu}(E_\nu) = 1.44 \times 10^{-18} \left( \frac{E_\nu}{100 \text{ TeV}} \right)^{-2.37} \text{ GeV}^{-1} \text{ cm}^{-2} \text{ s}^{-1} \text{ sr}^{-1}. \quad (6.12)$$

We use the expected event counts to sample from the provided IRFs, producing  $10^4$  realizations of the IceCube astrophysical diffuse flux binned in reconstructed energy proxy and direction assuming a uniform distribution across each IRF bin. These sampled events are compared to the observed events, building a map of the expected astrophysical contributions to each bin shown in

Fig. 6.2. We see a strong divide between the expected purity of the Northern and Southern skies, with the Northern sky reaching a purity of 10% or higher at high energy proxies. In contrast, the Southern sky purity rarely breaches 1%.

With that in mind, we stipulate that the Northern sky provides a significant advantage for astrophysical searches. We therefore limit our search to  $\delta > -2^\circ$ . Note that this is more stringent than the IceCube definition of the northern hemisphere to prevent from edge effects due to the sudden drop of the instrument effective area around declination  $-5^\circ$ .

We use randomized neutrino data in background generation to match IceCube’s standard methods [284]. This procedure breaks near the poles due to limited event statistics. Hence, we additionally mask out the polar cap ( $\delta > -75^\circ$ ).

Analogous to [252], we apply a 1-deg radius disk-like mask around the resolved gamma-ray sources listed in the 4FGL-DR3 [7] and we mask the sky region within 25 degrees from the Galactic plane. The resulting total mask leaves free about 20% of the sky and is shown in Fig. 6.1. Masking 25 degrees around the galactic plane is a conservative choice also adopted in several other cross-correlation studies [262, 263, 271]. As discussed later on (Sec. 6.2.2), mismodeling of the foreground emission that is subtracted from the data could lead to contamination at small scales. Conservatively masking this emission has demonstrated to be a good procedure to assure subdominant contamination from background subtraction. Furthermore, removing the majority of the bright Galactic emission along the Galactic plane considerably reduces the noise, which affects the variance of the cross-correlation measurement.

The combination of the Southern sky, polar cap, Galactic plane, and 4FGL-DR3 masks are combined into a single mask. All maps are generated in HEALPix format, and we use the *healpy* python package to analyze them. As IceCube’s angular uncertainty is of  $O(0.5^\circ)$  [259],

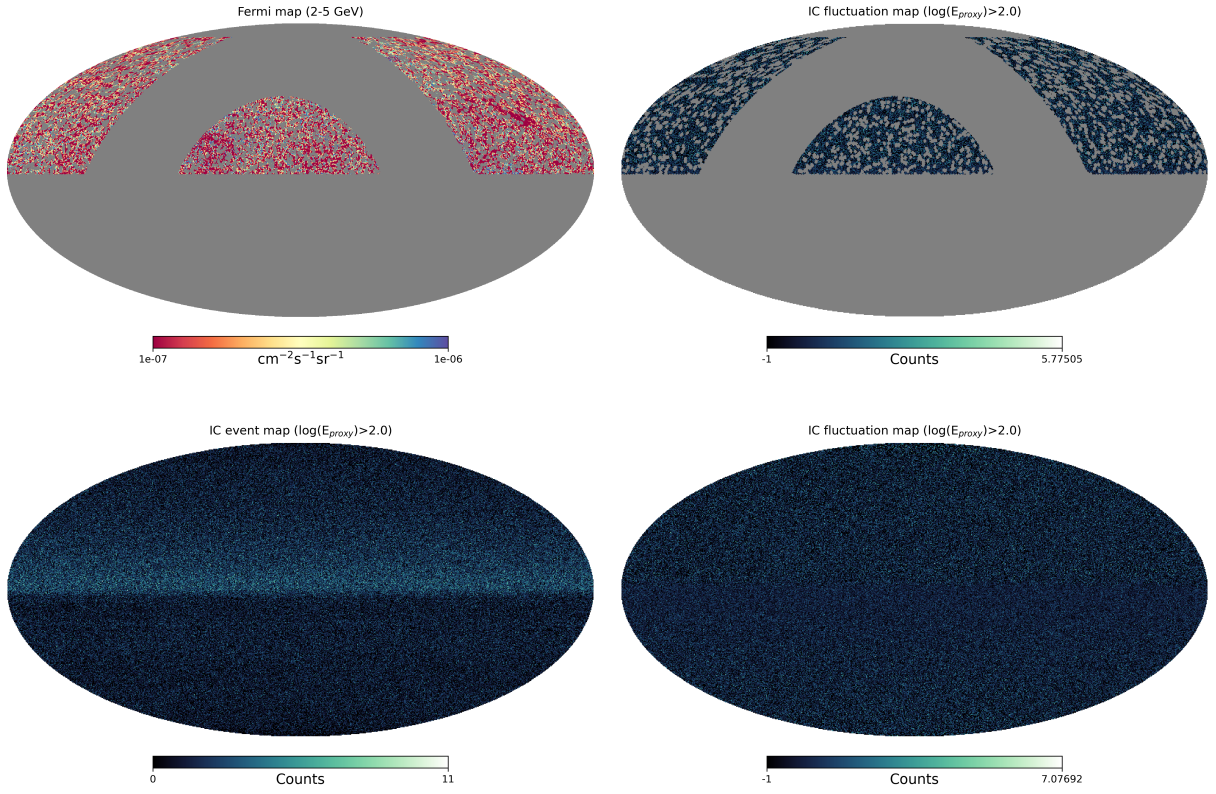


Figure 6.1: Top-left: Example of *Fermi* map in the 2-5 GeV energy bin. Top-right: IceCube (IC) counts fluctuation. For both maps in the top panel, the gray areas show the mask applied, which is the combination of the Southern hemisphere mask, polar cap, Galactic plane, and the 4FGL sources masks. Bottom-left: Example of simulated IceCube (IC) counts map. Bottom-right: Fluctuation IceCube event map derived from the simulated counts map shown on the left. All the maps reported here are in celestial coordinates.

we choose to work with a relatively coarse pixelization defined by an NSIDE of 256 (order 8) corresponding to an average pixel resolution of approximately 0.2 degrees.

### 6.3 Simulations

This analysis searches for a cross-correlation signal between the gamma-ray intensity field (as seen by the LAT) generated by an unresolved population of blazars and a neutrino count fluctuation field (as seen by IceCube) from the same population of blazars assuming a neutrino

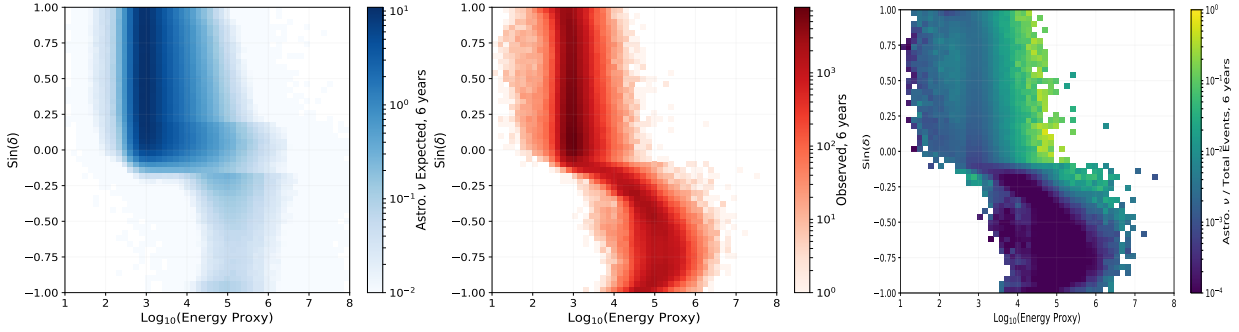


Figure 6.2: Study of the IceCube sensitivity to astrophysical neutrino signal considering the public data between 2012 and 2018. Left: Expected astrophysical neutrino events obtained assuming the latest astrophysical flux measurement by [286]. Middle: observed neutrino events as provided by the latest IceCube data release [259]. Right: Ratio between the expected astrophysical neutrino events and the total expected events: the Northern hemisphere is the far better portion of the sky to search for a signal from astrophysical neutrinos. In all plots Energy Proxy is expressed in GeV.

production from p-p interaction or p- $\gamma$  interactions. Since we are trying to correlate disparate measurements, the resulting value of  $C_P$  is difficult to interpret *a priori*. Hence, we use simulations with known levels of correlation to both determine the sensitivity of our pipeline to the presence of a signal and to convert our measurement of  $C_P$  into an upper limit on the fraction of the UGRB  $\gamma$ -ray flux produced in hadronic interactions. In this Section, we describe the procedure used to build simulated *Fermi*-LAT intensity maps and IceCube counts maps from a synthetic blazar population.

### 6.3.1 Unresolved blazar population

Our goal is to simulate a population of unresolved blazars that, on one hand, reproduces the expected  $\sim 30\%$  of the UGRB intensity spectrum [281], and on the other, matches the measured UGRB anisotropy energy spectrum [252]. To this end, the work in [287] provides two important tools: (1) a simulation of the intrinsic blazar population (detected and undetected sources) that we

can use to simulate both *Fermi* and IceCube maps; (2) a catalog of blazars detected from the simulations via a reliable detection pipeline optimized to recover the preliminary 4FGL catalog (the FL8Y), which we use to construct a mask for the simulated extragalactic sky (see the following Section 6.3.3). The simulation campaign presented in [287] aims to reproduce the observed spectral characteristics and statistics of the resolved extragalactic gamma-ray sources (i.e., blazars). Under the assumption that these sources are uniformly distributed in the  $\gamma$ -ray sky, the authors build blazar populations with: (1) a flux distribution extending an order of magnitude below the *Fermi*-LAT source detection sensitivity; (2) an intrinsic source count distribution (*logN-logS*); and (3) a double broken power-law intrinsic energy spectrum ( $\frac{dN}{dE}$ ) for each source of the form:

$$\frac{d\phi_\gamma}{dE} = K \left[ \left( \frac{E}{E_b(\Gamma)} \right)^{\delta_1} + \left( \frac{E}{E_b(\Gamma)} \right)^{\delta_2} \right]^{-1}, \quad (6.13)$$

with  $\log(E_b(\Gamma)) = 9.25 - 4.11\Gamma$  being the energy (in GeV) of the spectral break and  $\Gamma$  the power-law photon index of blazar's  $\gamma$ -ray spectrum as measured by the LAT [288];  $\delta_1 = 1.7$  and  $\delta_2 = 2.8$  are the spectral indices before and after the break energy, whose values have been found to reproduce the source-count distribution of the Third Catalog of Hard LAT Sources (3FHL, [289]). We refer the curious reader to [287] for further details on the simulation of the blazar population. In this work, we consider the simulation built on the *logN-logS* modeled as a double broken power law (model 2 in Table 2 of [287]).

Despite [287] extensively demonstrates that the population of detected simulated sources gives an adequate representation of the real *Fermi*-LAT extragalactic gamma-ray source population, we still must ensure that the unresolved regime is statistically representative of the real UGRB. We verify that the simulated unresolved blazar population results in an anisotropy power

that corresponds to the observed UGRB anisotropy energy spectrum. In order to do so, we first define a sky mask to cover the detected sources (covered with a disk of 1 degree radius) and the Galactic plane (25 degree bands above and below). Then, we compute the cumulative anisotropy level for each energy bin,  $C_P(\Delta E)$ , from all the sources that fall outside the masked region as

$$C_P(\Delta E) = \frac{1}{4\pi f_{sky}} \sum_{src} [\Phi(\Delta E)]^2 \quad (6.14)$$

where  $f_{sky}$  is the fraction of sky that is unmasked,  $\Phi(\Delta E)$  is the integrated flux in the energy bin considered, and the sum runs over the unmasked sources. Fig. 6.3 (top panel) shows the level of anisotropy of the simulated unresolved blazars compared to the measured anisotropy energy spectrum by [252]. The agreement is satisfying and validates the use of the simulated blazar population by [287] for our study.

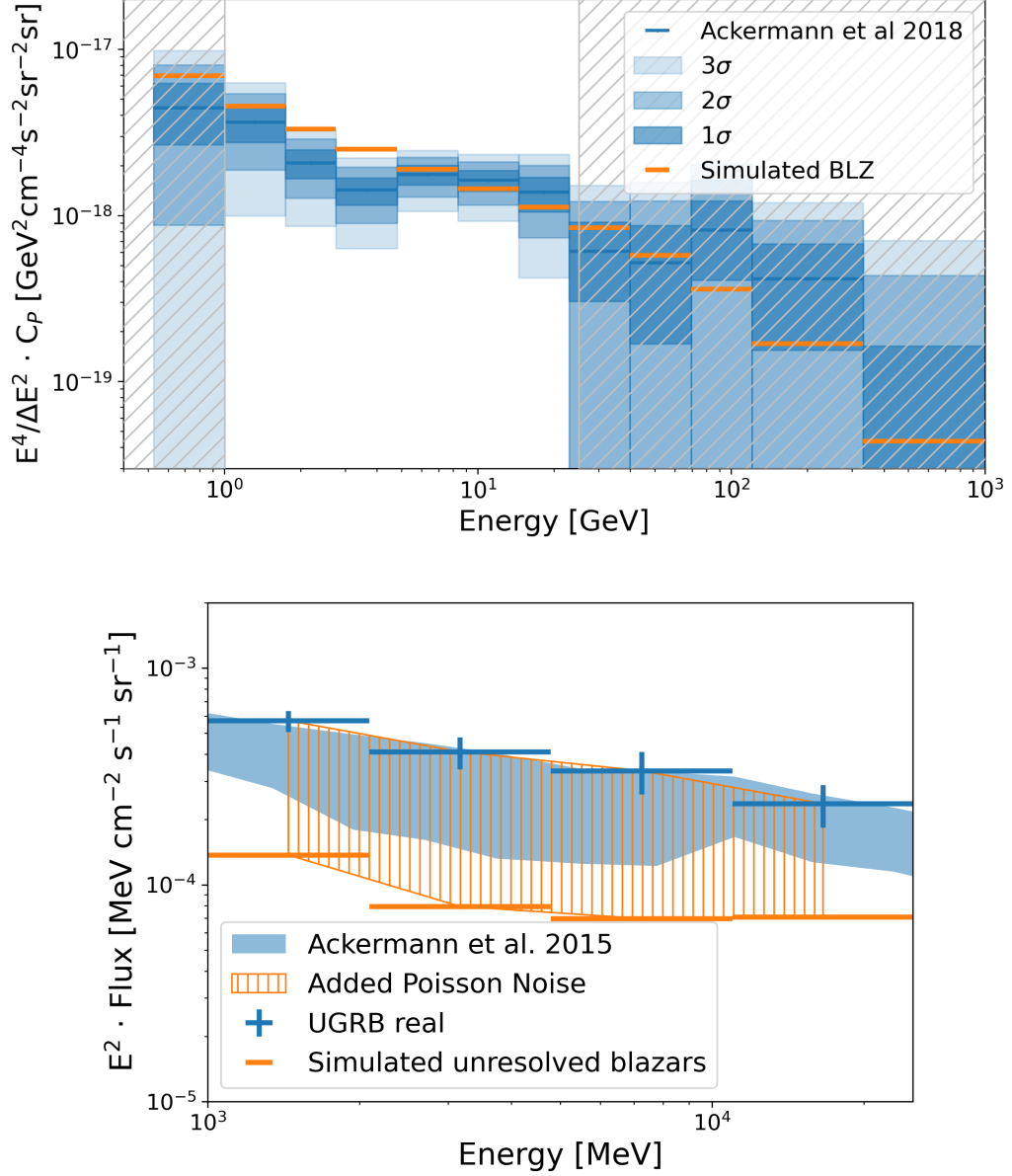


Figure 6.3: Top: Anisotropy power carried by the simulated unresolved blazar population (BLZ, orange) compared to the measured UGRB anisotropy energy spectrum in [252]. Bottom: Photon intensity of the simulated unresolved blazar population (orange lines), the photon intensity of the UGRBs measured from the real data maps (see Sec. 6.2.2) The orange dashed region marks the fraction of the intensity added to the simulated *Fermi* maps as Poisson white noise in order to match the real data intensity in each energy bin. The blue shaded part is the systematic band of the UGRB energy spectrum as presented in [252]. Note that all the intensities are estimated from the *unmasked* region of the sky, according to the mask described in Sec. 6.1

### 6.3.2 Simulated IceCube neutrino maps

We generate neutrino signal from the simulated list of resolved and unresolved blazars using the IceCube response functions provided in the latest release [259], and assuming that all blazars produce neutrinos in  $p$ - $p$  interactions following the same spectra as the  $\gamma$ -rays. We extrapolate the  $\gamma$ -ray spectrum down to IceCube energies and convert the gamma-ray flux into a neutrino flux following the relationship between the all-flavor neutrino flux and the  $\gamma$ -ray flux from [290]:

$$E_\nu^2 \frac{d\phi_\nu}{dE_\nu} \approx \frac{3}{2} \left( E_\gamma^2 \frac{d\phi_\gamma}{dE_\gamma} \right) \Big|_{E_\nu \approx E_\gamma/2} \quad (6.15)$$

We divide the all-flavor neutrino flux by three - implicitly assuming complete mixing of neutrino flavors - since the IceCube release includes only contributions from muon neutrinos. It is important to note that the extrapolation of the gamma-ray spectrum implicitly assumes no energy cutoff or any additional harder component emerging at IceCube's energies. In these latter cases, it is difficult to predict the spectral shape at TeV energies, as these possible scenarios are unconstrained. We therefore opt for the simple extrapolation of the power law defined at GeV energies and discuss variations in sensitivity due to different power-law indices at IceCube energies in Appendix D.2. For each source  $i$ , we calculate the expected number of neutrino events, denoted by  $\mu^i$ , by combining the derived single-flavor neutrino fluxes, the IceCube livetime,  $\Delta t$ , and IceCube effective area,  $A_{\text{eff}}(E_\nu, \delta^i)$ :

$$\mu^i = \Delta t \int A_{\text{eff}}(E_\nu, \delta^i) \left( \frac{d\phi_\nu}{dE_\nu} \right)^i dE_\nu \quad (6.16)$$

where  $\Delta t \sim 6$  years for the “IC86-II+” seasons used here, and  $\frac{d\phi_\nu}{dE_\nu}$  is derived using Eq. 6.15 assuming the  $\gamma$ -ray spectrum in Eq. 6.13. The IceCube effective area is provided as averages  $\bar{A}_{\text{eff}}$  over discrete energy bins  $[E_\nu^{j,\text{min}}, E_\nu^{j,\text{max}}]$ , converting our calculation of  $\mu^i$  into a summation

$$\mu^i = \Delta t \sum_j \bar{A}_{\text{eff}}^j (\delta^i) \int_{E_\nu^{j,\text{min}}}^{E_\nu^{j,\text{max}}} \left( \frac{d\phi_\nu}{dE_\nu} \right)^i dE_\nu \quad (6.17)$$

The number of signal events added to each trial is drawn from a Poisson distribution assuming  $\mu^i$  as mean value. Events are distributed around the source according to the point spread function from the IceCube IRF files.

To produce simulated background measurements, we sample events from the data with Poisson fluctuations, then randomize the right ascension values of the sampled events. This procedure assumes that the backgrounds are local and azimuthally symmetric, that any potential signal would be defined by spatial coincidences which may be broken by the randomization, and that the total rate of events is dominated by atmospheric backgrounds.

Signal events, if present, are added to the trial while removing an equal number of randomly selected background events, ensuring that the total number of observed events in each trial remains consistent with data. The final set of events in the trial are then binned in a HEALPix map.

The obtained counts map is converted into a fluctuation map by following the same declination-dependent procedure adopted for the real data maps (Eq. 6.11).

### 6.3.3 Simulated LAT UGRB maps

From the list of simulated unresolved sources, we generate simulated realizations of *Fermi*-LAT UGRB maps in the four energy bins defined in the previous section. Each of these simulated maps is then cross-correlated with the trial simulated IceCube maps, allowing an energy-resolved study in gamma rays. This is advantageous because the final cross-correlation result may be affected by the SNR of the gamma-ray maps. The SNR improves with increasing energy, but also with the intensity of the UGRB sources, which decreases with increasing energy. We do not know *a priori* which effect will dominate the cross-correlation measurement—as such, energy binning will allow for a blinded sensitivity study.

The integrated flux from each source, in units of  $\text{ph cm}^{-2}\text{s}^{-1}$  is obtained by integrating Eq. 6.13 from  $E_{\min}$  to  $E_{\max}$ . Then, it added to an initially empty HEALPix map in the pixel corresponding to the location of the simulated sources. The flux is converted to intensity in units of  $\text{cm}^{-2}\text{s}^{-1}\text{sr}^{-1}$  dividing by the pixel area. For every source, we apply a convolution with the *Fermi*-LAT PSF, which is function of the energy and the separation angle  $\theta$  form a given sky direction<sup>9</sup>. In agreement with the data selection (Section 6.2.2), we consider the responses for SOURCEVETO (PSF1+PSF2+PSF3) event selection, averaged over the energy bin weighted by the source spectrum.

Once all sources are added into the map, we add a white noise component to match the total UGRB intensity. This is achieved by injecting an isotropic component in the map with value equal to the difference between the true measured total intensity and the total intensity flux given by the simulated unresolved blazars. We illustrate the additional noise component with the

---

<sup>9</sup>See [https://www.slac.stanford.edu/exp/glast/groups/canda/lat\\_Performance.htm](https://www.slac.stanford.edu/exp/glast/groups/canda/lat_Performance.htm) for more information, as accessed on April 1, 2023.

hatched orange band in Fig. 6.3 (bottom panel). Notice that the total intensity from simulated blazars represents roughly 30% of the total UGRB flux, in agreement with the expectations. We then derive a counts map by folding the *Fermi*-LAT exposure map obtained while reducing the real data (see Sec. 6.2.2). A pixel-by-pixel Poisson randomization is applied to the counts map and then converted back to intensity by dividing by the same exposure map.

As discussed earlier, for the case of real *Fermi*-LAT data maps we subtract the Galactic foreground emission assuming a model template. Ideally the subtraction is perfect. In reality there might be some residuals and/or artifacts due to a non-perfect foreground modeling that might affect the small scales anisotropies at low latitudes (where the emission of the Galaxy dominates over the UGRB). This effect can be largely ignored in this case, because of the very conservative mask we adopt to cover the Galactic plane emission. Furthermore, by injecting the Poisson noise component that matches the total intensity of the real data maps into the simulated maps (and hence including any possible small-scale artifact due to mis-modeling of the foreground), we ensure that the correct variance is reproduced when computing the CAPS.

## 6.4 Results

In this section we first summarize simulation results. Then, we compute the cross-correlation of the real data maps.

The number of trials of our simulations, which aims to estimate the sensitivity of the analysis technique to detect a neutrino signal from gamma-ray unresolved blazars, is given by the number of realizations of simulated IceCube event map. We generate 10,000 IceCube map realizations for a range of variations in signal strength,  $\kappa$ , given by

$$\left( \frac{d\phi_\nu}{dE_\nu} \right)^{inj} = \kappa \left( \frac{d\phi_\nu}{dE_\nu} \right). \quad (6.18)$$

The simulated value of  $\kappa$  ranges from 0 - corresponding to the null hypothesis of no correlated signal injected - to ten. The obtained trial distributions for each signal strength are used as likelihood functions to derive the analysis sensitivity. The trials distributions of the  $C_P$  for each *Fermi*-LAT energy bin considered are shown in Fig. 6.4. The distribution for the null hypothesis of having only background events is marked in black, while the colored distributions are the alternate hypotheses where different levels of signal are injected, by varying the parameter  $\kappa$ . As expected the  $C_P$  distributions are approximately Gaussian and therefore we define the likelihood functions as the best-fit Gaussian to the trial distribution for each injected flux:

$$\mathcal{L}^B(C_P) = \frac{1}{\sqrt{2\pi}\sigma_B} e^{-\frac{(C_P - C_P^B)^2}{2\sigma_B^2}} \quad \mathcal{L}^{S_\kappa}(C_P) = \frac{1}{\sqrt{2\pi}\sigma_\kappa} e^{-\frac{(C_P - C_P^{S_\kappa})^2}{2\sigma_\kappa^2}} \quad (6.19)$$

where  $C_P^B$  and  $C_P^{S_\kappa}$  are the Gaussian mean value of the trial distributions for the null and alternate hypotheses, respectively. We interpolate the means and variances as a function of  $\kappa$  to obtain a continuous likelihood as a function of injected signal. A test statistic is calculated from the delta log-likelihood of the likelihood functions evaluated at the median value as:

$$\Delta_\kappa = -2 [\log \mathcal{L}^B(C_P^B) - \log \mathcal{L}^{S_\kappa}(C_P^{S_\kappa})] \quad (6.20)$$

Noting that the background and signal models are nested and linear in the fitted parameter  $\kappa$ , our test statistics  $\Delta_\kappa$  is  $\chi^2$  distributed with one degree of freedom [291]. We derive the sensitivity at 99% confidence level as the  $\kappa$  value where the  $\Delta = 6.67$ . The 99% sensitivity is shown

in Fig. 6.5 (orange arrows). Note how the highest energy bin is the most sensitive to a cross-correlation signal. This can be attributed to the higher signal to noise ratio in the *Fermi*-LAT maps at higher energies (less white noise with respect to the blazars emission).

We also explore the hypothesis of neutrinos produced via proton- $\gamma$  interactions. The procedure to generate the IceCube simulated maps is the same as the one described in Sec. 6.3 except that Eq. 6.15 now reads:

$$E_\nu^2 \frac{dN_\nu}{dE_\nu} \sim \frac{3}{4} \left( E_\gamma^2 \frac{dN_\gamma}{dE_\gamma} \right) |_{E_\nu \sim E_\gamma/2}. \quad (6.21)$$

which is the all-flavor flux assuming perfect mixing of neutrinos after oscillation. To only consider the contributions from muon-neutrinos, the expression in Eq. 6.21 is divided by 3. For completeness, we also perform simulations considering only IceCube events with  $\log(E_{\text{proxy}} [\text{GeV}]) > 4$  in order to test whether enhancing the ratio between astrophysical neutrinos and atmospheric neutrinos could lead to more promising results. However, the final sensitivity was not constrained because the IceCube statistics in the Northern hemisphere above those energies is too low to pick up any cross-correlation signal.

The results of the cross-correlation with real maps are reported in Tab. 6.1. The  $C_P^{\text{real}}$  values are all compatible with zero within the  $1\sigma$  error. We proceed, therefore, to estimate the upper limits for the neutrino signal from unresolved gamma-ray blazars. To do this we follow the same procedure as for the sensitivity calculation, in which we substitute the null hypothesis given by the background simulations with the likelihood whose mean value is equivalent to the measured  $C_P^{\text{real}}$  values as:

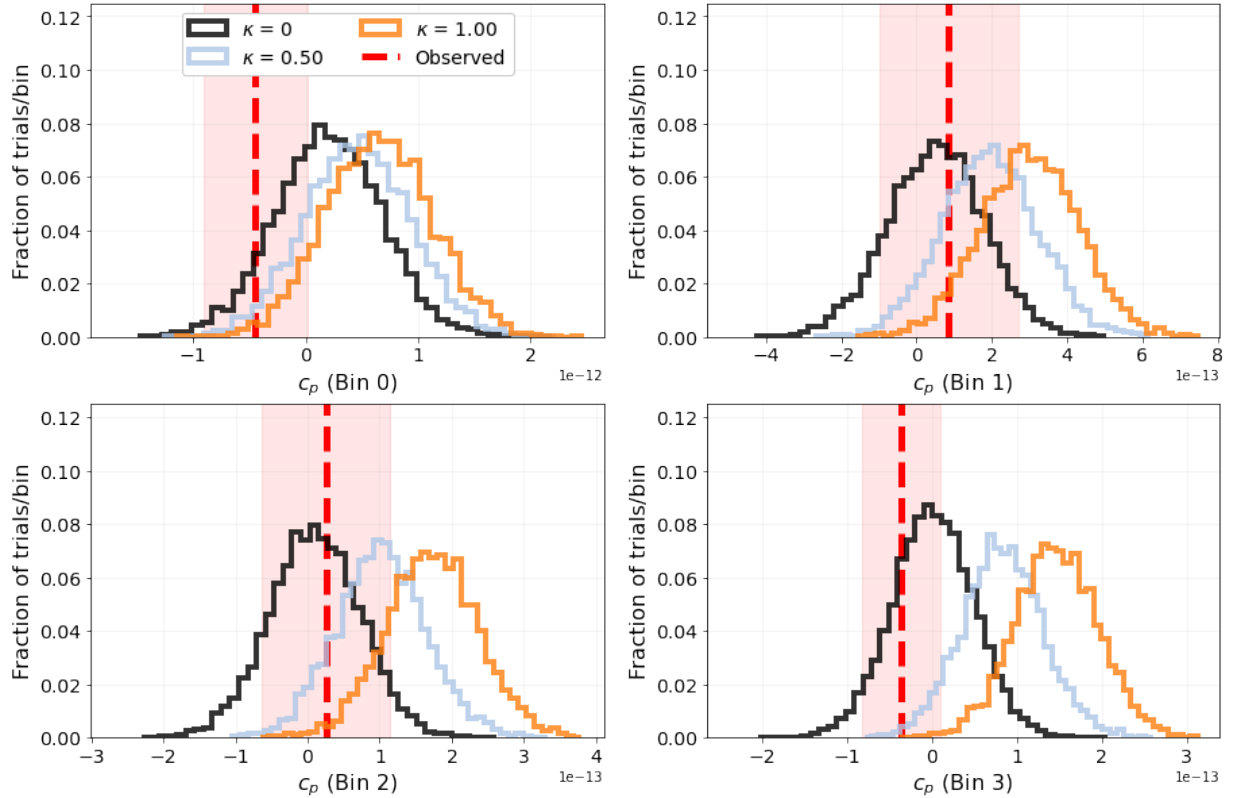


Figure 6.4: Trials histograms for the four *Fermi*-LAT energy bins considered in this study. The black line corresponds to the null hypothesis of having only background events in the IceCube data (no correlation expected). The colored lines are the trials distributions for different values of  $\kappa$ . As we increase the amount of correlated signal, the value of  $C_P$  increases for each energy bin.

Real data CAPS 1-halo term		
<i>Fermi</i> -LAT $\Delta E$	$C_P$	$\delta C_P$
[GeV]	[ $(\text{cm}^{-2}\text{s}^{-1}\text{sr}^{-1}) \text{ sr}$ ]	[ $(\text{cm}^{-2}\text{s}^{-1}\text{sr}^{-1}) \text{ sr}$ ]
1–2	$-4.5 \times 10^{-13}$	$4.6 \times 10^{-13}$
2–5	$8.5 \times 10^{-14}$	$1.8 \times 10^{-13}$
5–10	$2.6 \times 10^{-14}$	$8.9 \times 10^{-14}$
10–25	$-3.5 \times 10^{-14}$	$4.6 \times 10^{-14}$

Table 6.1: Results of the cross-correlation of real IceCube and *Fermi*-LAT maps.

$$\Delta_\kappa = -2 [\log \mathcal{L}^B(C_P^B) - \log \mathcal{L}^{S_\kappa}(C_P^{S_\kappa})] \quad (6.22)$$

In Tab. 6.2 we report the 99% CL sensitivity and upper limit. Note that the  $C_P^{\text{real}}$  in the first and last *Fermi*-LAT energy bins are negative. As shown in the trials distributions in Fig. 6.4, fluctuation to negative values in presence of expected positive correlation is possible. However, we emphasize that a negative 1-halo term could also be interpreted as an anti-correlation. This is unlikely the case as anti-correlation is not supported by the cases of the middle *Fermi*-LAT energy bins, in which we expect the most significant anisotropy signal from unresolved blazars according to [252].

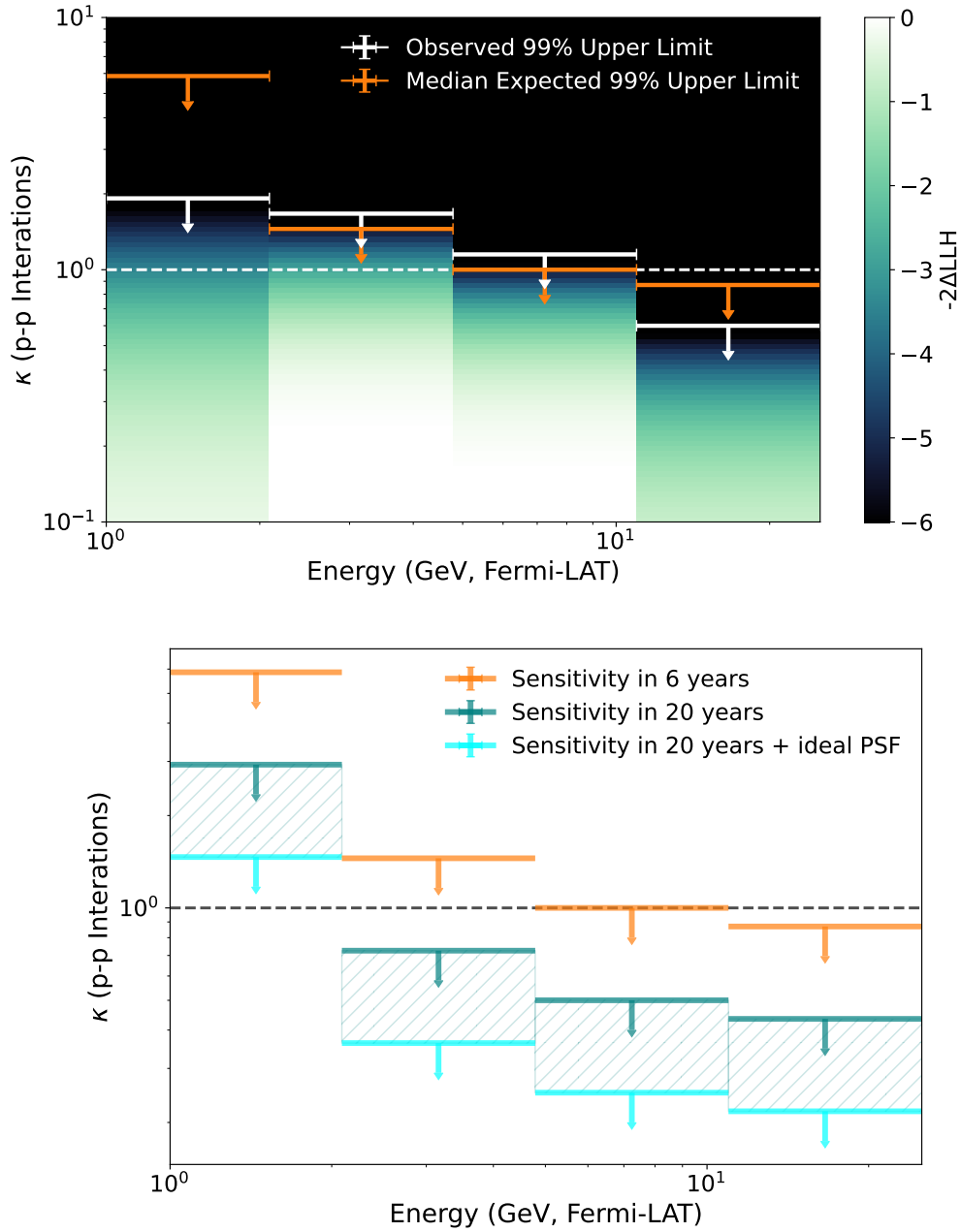


Figure 6.5: Top: Expected sensitivity to neutrino signal from p-p interaction production channel and unblinded upper limits. In orange we mark the 99% C.L. upper limit. In white we mark the data-driven 99% C.L. upper limit. The dashed thin horizontal lines is added to mark the reference value  $\kappa = 1$ . Bottom: Sensitivity projected to 20 years of IceCube data for the p-p interaction. The p- $\gamma$  neutrino production channel can be obtained by scaling the p-p interaction sensitivities by a factor of 2.

The results show that the measured  $C_P$  between the real *Fermi*-LAT and IceCube data

Sensitivity and upper limits summary table				
<i>Fermi</i> -LAT $\Delta E$	Sensitivity		Limit	
[GeV]	p- $\gamma$	p-p	p- $\gamma$	p-p
1–2	< 2.80	< 5.59	< 0.80	< 1.59
2–5	< 0.73	< 1.45	< 0.84	< 1.67
5–10	< 0.50	< 1.00	< 0.58	< 1.15
10–25	< 0.44	< 0.87	< <b>0.30</b>	< <b>0.60</b>

Table 6.2: Summary table of 99% confidence levels sensitivities derived from simulations and upper limits computed from real data maps cross-correlation for p-p and p- $\gamma$  neutrino production channels. We highlight in bold the most stringent limits that we find.

maps fall within the range obtained from the simulations. This further validates the simulation procedure devised for this work. In the case of p-p interactions, only in the highest gamma-ray energy bin we have a constraining upper limit with  $\kappa < 1$ , excluding that all of the gamma-ray emission from the unresolved population of blazars is produced from p-p (p- $\gamma$ ) interactions. In all other cases, we are not sensitive enough to make the same statement. In case of p- $\gamma$  neutrino production channel, the sensitivities and upper limits are the same as for the p-p interaction case but scaled by a factor of 2 (see Eq. 6.21). The lower sensitivity of the cross-correlation involving lower gamma-ray energies is attributable to a combination of higher level of noise and worse angular resolution of the *Fermi*-LAT data.

Furthermore, we estimate the maximum contribution of the unresolved blazars that dominates the anisotropy measurement by translating the upper limit on the parameter  $\kappa$  into a constraint on the intrinsic neutrino flux, which is then compared to the one estimated by IceCube [286]. In order to do so, we derive the neutrino flux from the  $\gamma$ -ray flux using Eq. 6.15 and Eq. 6.21 for p-p and p- $\gamma$  interactions, respectively. Then, we apply the  $\kappa$  factor of the most stringent limits (in bold in Tab. 6.2). As outlined in Sec. 6.3, we consider the  $\gamma$ -ray intrinsic spectra of each unresolved blazar to be described by Eq. 6.13. At IceCube energies (above 100

GeV) this spectrum is a simple power law with index of  $-2.8$ . We estimate that the total  $\gamma$ -ray differential flux at 100 TeV from all the unresolved simulated blazars is about  $6.8 \times 10^{-21} \gamma/\text{cm}^2/\text{s}/\text{sr}/\text{GeV}$ . According to Eq. 6.15, this corresponds to  $1.4 \times 10^{-20} \nu/\text{cm}^2/\text{s}/\text{sr}/\text{GeV}$ . Since we are not omitting energy information in discriminating between signal and background events, our sensitivity is driven by the number of events observed from our assumed spectrum. Using simulations, we estimate 99% of signal events with the assumed spectrum fall between 100 GeV and 50 TeV. Therefore, we report the constraints in this energy range. At 99% C.L. we exclude that the unresolved blazars contribute to the astrophysical neutrino flux more than O(10%) at 1 TeV and O(1%) at 100 TeV. This result is illustrated in Fig. 6.6 and, together with the one obtained from the resolved blazars in the 1FLE catalog [249], suggests that the blazar population, with brightness down to about an order of magnitude below the detection threshold of the *Fermi*-LAT, can contribute to the astrophysical neutrino flux up to a couple of percent at about 100 TeV. We emphasize that any intrinsic energy cutoff and/or any additional components in the blazars spectra above measured TeV energies would not be included in our simulations. Generally, a cutoff would result in a weakening of the quoted limits, while an additional harder component would make the limit more stringent. See the first two figures in Appendix D.2 for further details.

As a final consideration, we estimate the sensitivity of our pipeline for future studies. In particular, we consider 20 years of IceCube statistics, roughly when the IceCube/Gen2 [274] configuration is expected to be in operation. We first assume no improvement in the angular resolution of the instrument to estimate the improvement due to the increased neutrino count statistics only. We also report the ideal scenario of a perfect arrival direction reconstruction: this case can be seen as the lower limit of this sensitivity study. It is worth noting that, even in this “ideal” case, we are still limited by the LAT PSF and the presence of shot noise, which represent

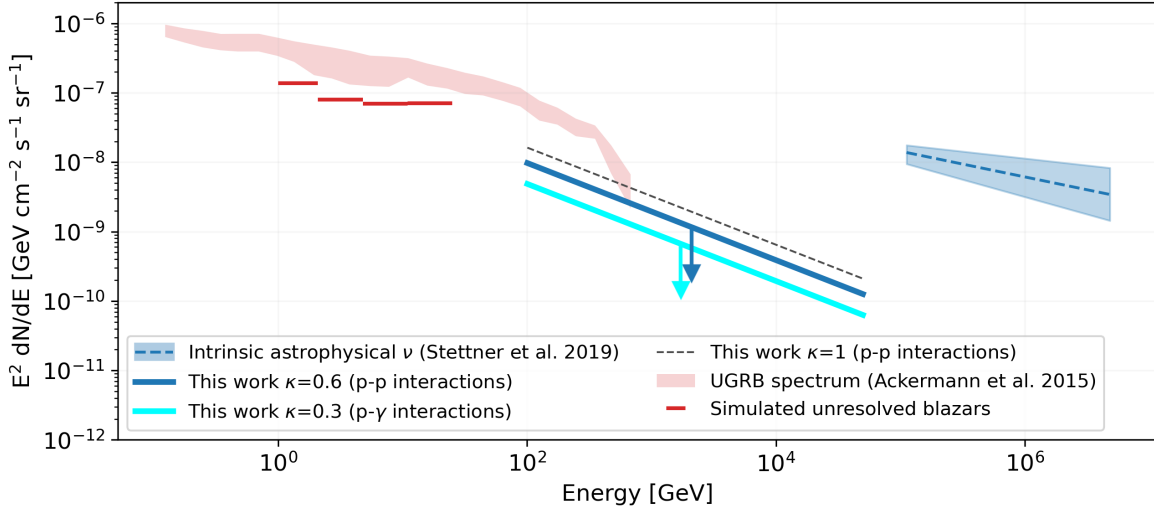


Figure 6.6: Contribution of the unresolved blazars that dominates the anisotropy of the UGRB to the astrophysical neutrino flux.

the lower limit to the predicted sensitivity. The results are shown in Fig. 6.5 (bottom panel).

In this scenario, we do not assume the UGRB signal to change with respect to the current set-up, as *Fermi*-LAT is unlikely be operating at the time of IceCube/Gen2. If it was, we would have a more complete catalog of resolved gamma-ray sources, making it non-trivial to predict how the unresolved component will evolve, i.e., what populations will be dominating the unresolved emission.

## 6.5 Conclusions

This work investigates the possibility to measure the spatial cross-correlation between the IceCube neutrino events (public data release by [259]) and the unresolved gamma-ray background as measured by the LAT. We devise a simulation pipeline for IceCube event map and the *Fermi*-LAT UGRB intensity map, given a list of sources and their intrinsic energy spectra. In this work, we produce simulations from a list of unresolved blazars, to access the possible neutrino signal

from this population of gamma-ray dim blazars.

We test two assumptions to derive our sensitivity to a neutrino-UGRB cross-correlation signal, where neutrinos are produced via 1) p-p, or 2) p- $\gamma$  interactions. We vary the amount of injected signal by scaling the expected neutrino flux given the gamma-ray flux from a simulated unresolved blazar population. Such scaling is encoded in the  $\kappa$  parameter, detailed in Eq. 6.18.

We find that, in the former case, the sensitivity is constraining (below  $\kappa = 1$ ) at gamma-ray energy above 10 GeV; while in the latter case the sensitivity is constraining starting from 2 GeV.

The cross-correlation 1-halo term computed considering the real data maps is compatible with zero within the 68% C.L. We therefore derive upper limits, which show similar trends to those revealed by the sensitivity study. For p-p interactions, the most constraining upper limit is above 10 GeV with a  $\kappa < 0.60$  at the 99% C.L.; for p- $\gamma$  interactions the most constraining upper limit goes down to  $\kappa < 0.30$  at the 99% C.L. Our analysis suggests that under the assumption that no energy cutoff and/or additional harder component is present above *Fermi*-LAT energies, and that all gamma-rays of the unresolved blazars are produced by neutral pions from p-p (p- $\gamma$ ) interactions, up to 60% (30%) of the population may contribute the diffuse neutrino background. We estimate a contribution to the neutrino flux of the order of the percent at 100 TeV (10 percent at 1 TeV) from the unresolved blazars that dominate the UGRB anisotropy spectrum as measured by the LAT.

Recently, the IceCube Collaboration reported a  $\sim 4\sigma$  excess probability for a neutrino source in the direction of the nearby starburst Seyfert galaxy NGC 1068 [243]. This evidence suggests that non-blazar AGNs could also contribute to the astrophysical neutrino flux. The nearby NGC 1068 is detected by the LAT. However, misaligned AGNs are generally faint in the GeV regime and, being more numerous than blazars, contribute to the total UGRB intensity

roughly to the same extent [256]. An analogous study as the one presented here, therefore, can be attempted for misaligned AGNs and will be subject of a future investigation. Furthermore, other smoother UGRB components, such as star forming galaxies, could also contribute and still be consistent with the observed null cross-correlation signal.

Finally, we estimate the projected sensitivity at 20 years of IceCube data. Assuming the current angular resolution, the sensitivity improves to  $\kappa \sim 0.45$  (0.23) for p-p (p- $\gamma$ ) interaction. Such improvement is a factor of about 30% with respect to the sensitivity at 6 years. Therefore, a future study with an enhanced neutrino statistic is worth an attempt.

## Chapter 7: Conclusions

*They say all's well that ends well.*

---

Taylor Swift

At last, we have arrived at our final destination—for now. What have we found? Well, not much—if anything. To many, this dissertation is simply a story of upper limits. Nevertheless, we are getting ever-so-closer to answering our long-standing questions about the nature of the high-energy emission in the Universe. In this dissertation, we have used multiple techniques and messengers to study the most extreme events in the Universe. The dissertation’s first segment focuses on searches for new physics and ALPs.

***Axion-like particles from gamma-ray bursts.*** Constituting  $\sim 27\%$  of the Universe’s energy budget, grasping the particle properties of DM is crucial to understanding the fundamental principles of cosmic formation and evolution. Numerous well-motivated particle (and some non-particle) candidates have been proposed to explain the observed DM signatures, yet the search efforts continue to date. One of the most compelling contenders is the generalized case of the quantum chromodynamics axion, **the light ALP** ( $m_{\text{ALP}} \lesssim 10^{-10}$  eV) [62].

Due to the challenging nature of designing an MeV telescope, many physical processes remain largely unexplored in this energy range. In Chapter 3, for the first time, we demonstrate the use of the *Fermi* LLE technique to search for the ALP spectral signatures within the MeV

gamma-ray emission of long GRBs. Furthermore, we find that the sensitivity of the LLE technique to detecting light ALPs is comparable to the standard LAT analysis, making it an excellent complementary—yet independent—way to search for ALPs with *Fermi*. Finally, the sensitivity pipeline developed for these searches can easily be applied to different instruments, especially to support a strong scientific motivation for future MeV-energy-range observatories, as indicated in [292].

In Chapter 3, assuming an ALP mass  $m_a \lesssim 10^{-10}$  eV and ALP-photon coupling  $g_{a\gamma} = 5.3 \times 10^{-12}$  GeV $^{-1}$ , values considered and deduced in ALP searches from SN1987A, we find that the distance limit ranges from  $\sim 0.5$  to  $\sim 10$  Mpc, depending on the sky location and the CCSN progenitor mass. Furthermore, we select a candidate sample of twenty-four GRBs and carry out a model comparison analysis in which we consider different GRB spectral models with and without an ALP signal component. We find that including an ALP contribution does not result in any statistically significant improvement of the fits to the data. We discuss the statistical method used in our analysis and the underlying physical assumptions, the feasibility of setting upper limits on the ALP-photon coupling, and give an outlook on future telescopes in the context of ALP searches.

The arrival time of the ALP burst from a CCSN should coincide with that of neutrinos and, thus, arrive to Earth prior to the ordinary prompt phase emission. Motivated by the delay between the time of the core collapse of a massive star, i.e., the ALP emission time, and the time of the jet break-out associated with its ordinary long GRB emission, in Chapter 4, we conduct a novel search for ALPs focusing on the sample of sources with known precursor emission detected with LAT and LLE.

We conduct a model comparison analysis of the time-resolved spectral fits to the identified

precursor emission in 14 long GRBs. We conduct the analysis within the threeML framework, where we define ALP tabular models for different masses considered. For LLE-identified precursors, we fit three different ALP spectral models characterized by different progenitor masses (10, 18, and 40 solar masses). For LAT-only precursor identifications, we conduct the ALP spectral modeling only with the 40 solar mass model due to the energy coverage constraints of the standard LAT analysis.

We find all precursors are better fit with the null-hypothesis models or are unconstrained due to the low-count statistics. We show that, for the LLE precursor identified in GRB 221009A, we can exclude all the values of the ALP-photon coupling  $g_{a\gamma} > 3.9 \times 10^{-10}$  for ALP masses  $< 10^{-10} \text{ GeV}^{-1}$ , already considered by other instruments. Nevertheless, this technique can be useful for the nearby long GRBs in the regions of the sky with a high ALP-photon conversion probability.

The second segment of the dissertation is focused on our multimessenger efforts and searches for coincident detections.

***Gamma-ray counterparts to gravitational waves.*** In Chapter 5, we present an offline search for EM counterparts to GW events during the third observing run of the Advanced LIGO and Advanced Virgo detectors. Using the data obtained with *Fermi*-GBM and *Swift*-BAT, we investigate whether there were any corresponding gamma- and X-ray counterparts to events identified in the GWTC-2, GWTC-2.1, and GWTC-3. We report no new coincidences. Using the *Fermi*-GBM Targeted Search and the *Swift*-BAT rate search, we calculate the flux upper limits and joint upper limit skymaps for the associated gamma-ray luminosity of each GW. These limits can provide necessary information to constrain various theoretical models for emitting gamma rays from binary mergers.

**Cross-correlating the neutrino and gamma-ray skies.** The searches for correlation between the high-energy astrophysical neutrinos detected by the IceCube Observatory and gamma-ray photons detected by the *Fermi*-LAT are crucial in understanding the origin of the diffuse high-energy neutrino background. So far, only sources resolved by the LAT have been considered in correlation with IceCube neutrinos, neglecting any emission from sources too faint to be resolved individually. In Chapter 6, we, for the first time, consider a cross-correlation analysis between the *unresolved* gamma-ray background and IceCube events. With no high-confidence cross-correlation result from the real data, we perform a simulation-driven sensitivity study to place upper limits on the fraction of the observed neutrinos produced in p-p or p- $\gamma$  interactions in blazars. Our analysis suggests that under the assumption that there is no intrinsic cutoff or hardening of the spectrum above *Fermi*-LAT energies and that all gamma-rays from the unresolved blazars dominating the UGRB fluctuation field are produced by neutral pions from p-p (p- $\gamma$ ) interactions, up to 60% (30%) of such population may contribute to the total neutrino events observed by IceCube. This translates into an O(1%) maximum contribution to the astrophysical high-energy neutrino flux observed by IceCube at 100 TeV.

*Epilogue*

## Chapter 8: What about exoplanets?

*Books have always had their roots in other books, and they still do.*

---

Dubravka Ugrešić

In my second year of graduate school at the University of Maryland, following what, at the time, I thought was the most challenging exam and the biggest failure of my life—I went to a poetry show of one of my favorite spoken-word poets, Sarah Kay. She opened her performance with the line, “Every great story has a beginning, middle, and end, not necessarily in that order.” Over the last few years, I learned how to play with this notion in my own research. Most of my work, in fact, starts at the end: physical processes we discuss in this thesis happened eons ago, and we are just trying to interpret them and write the story backward. Yet, here we are, a hundred and more pages into my thesis, back to the beginning—a little more knowledgeable, but still asking questions.

Dear Reader: As with much observational astronomy research, the end of my thesis is too just a beginning. The dark sector of the Universe remains elusive, and the multimessenger efforts are still young. Here, I present to you the questions that I am most excited to answer in the following years.

Finally, if you have gotten this far and your name did not appear in my Acknowledgements, it was my mistake—please consider yourself acknowledged. I am grateful for you and your

decision to join me on my journey through the high-energy Universe.

---

Let us now ask the question older than time,

*But what about magnetic fields?!*

Truth be told, having a better understanding of various magnetic fields within physical systems considered in my dissertation is crucial. This is particularly relevant in the context of the ALP searches I present in Chapters 3 and 4. However, I would not be a good astronomer of my generation if I did not ask the following ones:

*OK, but what about exoplanets?! Or binary mergers?*

I admit, the title of this epilogue is misleading—but it caught your attention. I will leave the discussion of exoplanets in the context of DM searches (i.e., “dark exoplanets”) to the experts [293], and instead focus on the latter.

As I (hopefully) convey in this dissertation, the gamma-ray data have been used to set strong constraints on ALPs, one of the leading explanations for DM. In the next few years, I am excited to propose a new approach to probing the ALP parameter space. I will search for gamma rays from ALP production in BNS merger data—that has the potential for a greatly increased sensitivity. This approach takes advantage of the low masses of ALPs, which means they can be abundantly produced in hot, dense astrophysical environments, later converting to gamma rays in intervening astrophysical magnetic fields. My approach leverages the high-statistics GW data from the fourth LVK observing run and the expected multi-wavelength follow-up observations to provide precise search directions and times, as well as accurate characterization of the astrophysical systems. In the next few years, I hope to offer an entirely new method for utilizing LAT

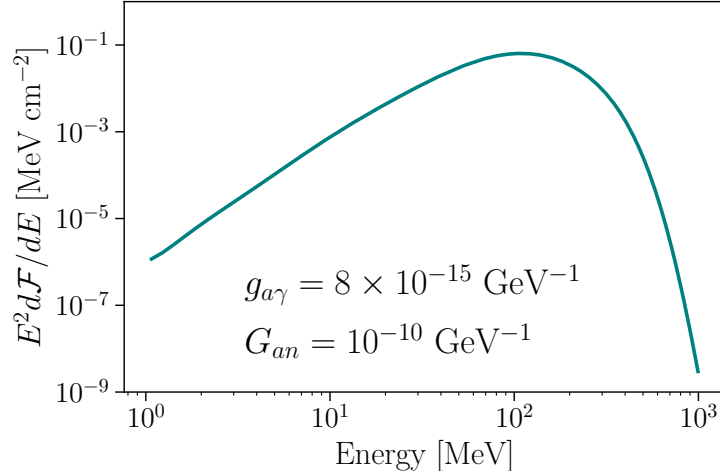


Figure 8.1: Expected gamma-ray flux from ALPs produced in a GW170817-like BNS merger, for possible ALP-photon ( $g_{a\gamma}$ ) and ALP-neutron ( $G_{an}$ ) coupling values and an arbitrary normalization, integrated over 10 seconds (adapted from [294]). Note the peak in the MeV energy range.

in a multimessenger context to place even stronger constraints on ALP properties compared to previous works.

## Out of the dark and into the light: ALPs from BNS mergers

With comparable physical conditions (in particular, temperatures and densities) to those of a CCSN, as well as the high density of nuclear matter, we expect ALPs to be abundantly produced during the hypermassive NS stage of BNS merger, predominantly via coupling to nuclear matter, i.e., the bremsstrahlung process of neutrons ( $n + n \rightarrow n + n + a$ ), described by the coupling constant,  $G_{an}$  [295, 296]. Similarly to CCSNe, once BNS-merger produced ALPs leave the site of production, they will convert into photons in the Galactic magnetic field. Figure 8.1 shows that most of the ALP-induced gamma-ray emission from a GW170817-like BNS merger happens in the MeV energy range and Fig. 8.2 depicts the physical system and processes in question. As no other astrophysical process is known to imprint such a signature in the observed gamma-ray

spectrum during the prompt emission phase of a BNS merger, the detection of such emission would be a conclusive indication of the presence of ALPs.

Although the BNS systems are extreme and complex, we have the unique advantage of multi-wavelength data to supplement the GW observations. These independent observables allow us to break the system's degeneracies, constraining the astrophysics. In a complementary way, I will explore the new-physics effects within the system by investigating possible observable consequences: the unique gamma-ray signature from ALP production during BNS mergers and the subsequent ALP-photon conversion in the Milky Way magnetic field.

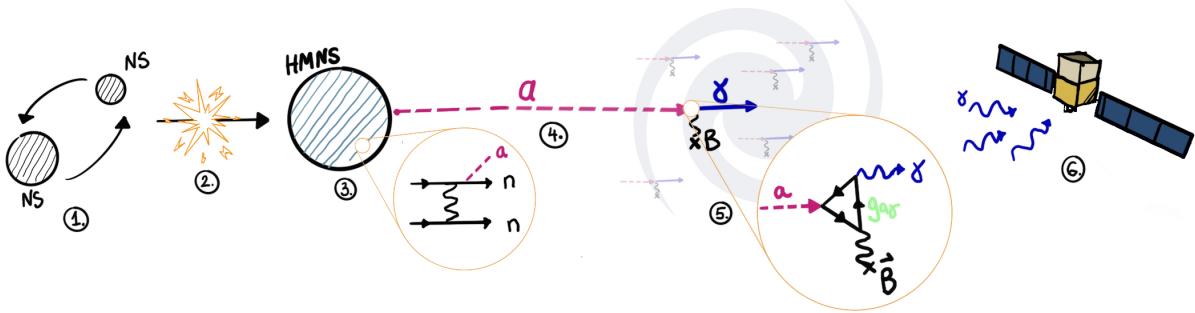


Figure 8.2: ALP production and detection (not to scale). (1) Two NSs orbit each other until the (2) merger, followed by (3) the formation of a hypermassive NS (HMNS). There, ALPs are produced via the neutron-neutron bremsstrahlung process. Once produced, ALPs travel undisturbed (4), until they reach the magnetic field of the Milky Way (5). In the Milky Way's magnetic field, ALPs convert into gamma-rays, which then can be detected by *Fermi* (6).

**Identifying the BNS merger sample:** To determine the maximum distance  $d$  of a BNS merger that would give competitive sensitivity for the detection of ALPs, we note that the number of detected gamma-ray counts roughly scales with  $G_{an}^2 g_{a\gamma}^2 / d^2$ . Thus, for a fixed value of  $G_{an}$ , the sensitivity for  $g_{a\gamma}^2$  scales with  $d$ . A BNS merger located in M33 ( $d = 835$  kpc) could probe couplings  $g_{a\gamma} > 10^{-15}$ , as suggested in [294]. To reach the sensitivity limits comparable to the ones currently imposed by the CCSN observations ( $g_{a\gamma} > 10^{-12}$ ), we may include all the BNS merger events within a distance  $\sim 835$  Mpc, or a redshift of  $z \sim 0.2$ .

So far, the following events have been confirmed to stem from a BNS merger within the allowed redshift range and within LAT’s FoV: 1) GW BNS merger candidate: GW190425 ( $z \sim 0.01$ , 37% instantaneous coverage, given the GW localization map), and 2) using the short GRB follow-up observations, the following kilonovae were identified during the *Fermi* lifetime, consistent with the BNS merger as progenitor: GRB 160821B ( $z \sim 0.16$ ) and GRB 211211A ( $z \sim 0.08$ ). Although in the case of GW170817 LAT was in SAA and not collecting data at the time of merger, we emphasize that GW170817-like event inside the LAT’s FoV in the future would provide an ideal opportunity for a potential ALP detection.

In addition to these three events, with the fourth LVK GW observing run scheduled to start in May 2023 and its unprecedented sensitivity to detecting binary mergers (predicted  $\sim 10$  BNSMs, as compared to a total of 1 in O3), as well as the active involvement from the optical and X-ray community to detecting kilonovae, the sample of considered BNS events is expected to increase throughout the duration of this project.

As the strength of the ALP signal is determined by its normalization  $N(g_{a\gamma})$ ; this, in turn, will allow us to probe the ALP-photon coupling, given the distance to the source ( $N(g_{a\gamma}) \propto g_{a\gamma}^2/d^2$  for a given  $G_{an}$ ). Dotted area in Fig. 8.3 shows the sensitivity of our method to probing the ALP parameter space.

**Modeling the ALP emission from BNS mergers & the current state of theoretical models:** The majority of the ALP emission following a BNS merger is expected to occur during the hypermassive NS phase of the post-merger system. Numerical simulations indicate that this phase may last from a few milliseconds to a few tens of seconds—depending on the initial properties of the binary system—dictating the total energy released through the emission of ALPs. Furthermore, current state-of-the-art models consider different parameters, such as various NS equations

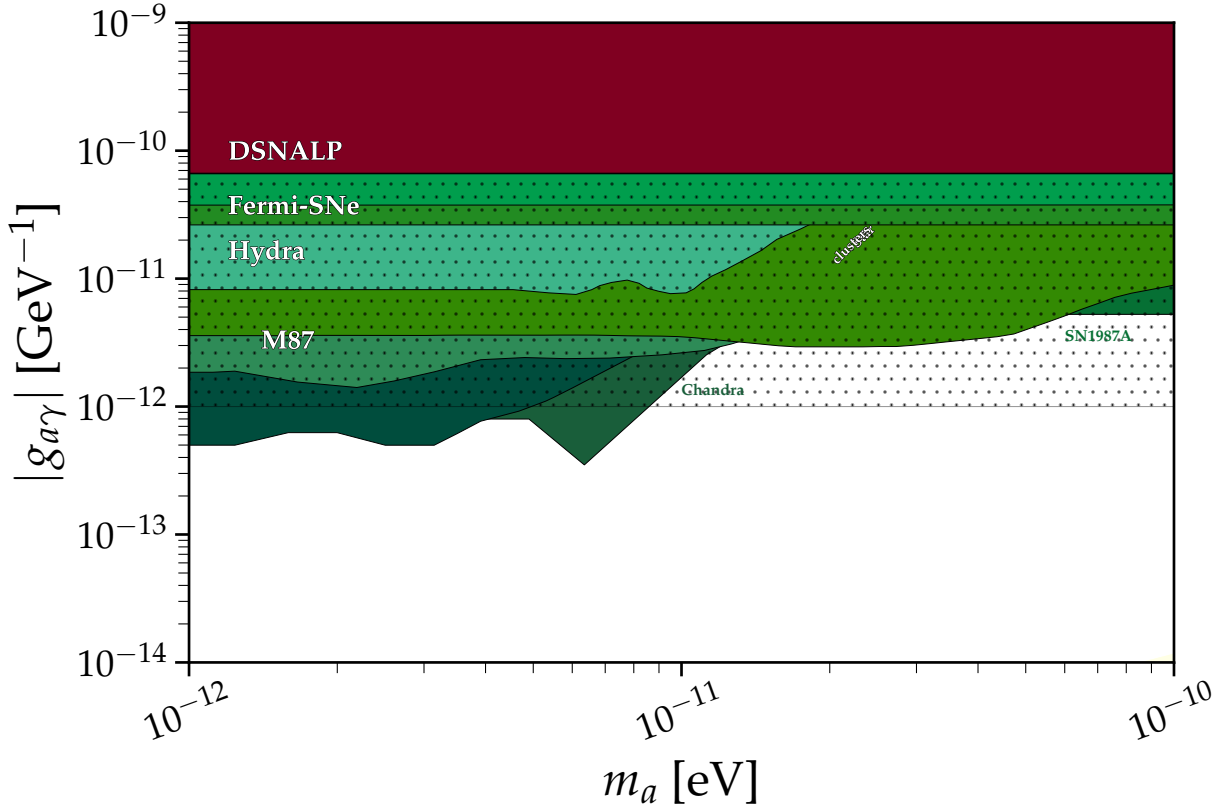


Figure 8.3: Exclusion plot for the ALP parameter space in the range relevant to our searches. Dotted area shows the parameter space to which our method is sensitive.

of state, their initial masses, spins, cooling rates, and magnetic fields. These theoretical considerations, when combined with multimessenger observations of the GW event and the subsequent short GRB, can provide us with a precise life span estimation of the hyper-massive NS (see, e.g., [297–299]). In an extensive study in [175], Harris *et al.* produce a set of most comprehensive ALP emissivity models as well.

**Merits of using the multimessenger approach:** Searching for ALPs from BNS mergers complements the previously-done searches from CCSNe. Taking into consideration the current state of the field, we can expect an abundance of follow-up observations and swift analyses from numerous groups if and when a BNS merger candidate is first detected. Second, the time-tagging from the GW detection will provide us with down to a second uncertainties in time windows

appropriate for ALP searches. In case no GW counterpart is detected, using the numerical modeling from [297] will narrow down the ALP emission time window to an uncertainty of at most a few tens of seconds (as compared to hours, or even days in the case of CCSNe). Third, although BNS mergers are rarer in nature than CCSNe in a given volume, the absence of stellar envelopes in BNSMs allows for no sample selection cuts that are currently required in the CCSN analysis, where only no-envelope (Type Ib/c) CCSNe are considered—making the two sample sizes comparable in a given volume. Finally, this project exploits the infrastructure already set in place for O4; used in a new context (ALPs).

**Setting up for O4 and beyond:** In addition to providing competitive constraints on the ALP parameter space, this work will also lay the groundwork for the future observations and, in particular, provide a pipeline for swift ALP searches following BNS merger detections in O4. As such, there are two possible research pathways considering direct observational consequences that may build on this work: 1) Coincident GW and SGRB detection. In this case, the expected ALP emission can be tagged to  $\sim$ second precision (compared to  $\sim$ hours or more in the case of CCSNe). Combined with the state-of-the-art modeling of the expected ALP spectral signature, this approach will provide a new probe into the allowed ALP parameter space, not yet excluded by the current astrophysical or laboratory experiments; and 2) GW detection without the EM counterpart. For the BNS merger sample within the allowed redshift range ( $z < 0.2$ ), this work provides a novel way of searching for ALPs. Finally, in addition to the excellent ALP time-tagging in a BNS merger gained from the GW observations, current and upcoming instruments will provide a plethora of information regarding other processes in the considered astrophysical systems: e.g., the characterization of BNS magnetic fields (using IXPE in addition to various radio instruments), quick kilonovae identification (with ZTF, Vera Rubin, etc.), and many other on-ground and in-

space observatories, most of which are set on high-alert to follow up on a BNS merger candidate swiftly.

This, dear reader, is what I mean by “New Messengers & New Physics.” That is all from me for now. I hope you enjoyed your cup—or two—of tea.

## Appendix A: Appendices for Chapter 3

### A.1 GRB Models

To fit the selected GRB sample, we use *XSPEC* models that include:

1. Band function (`grbom`, gamma-ray burst continuum), described by

$$A(E) = \begin{cases} KE^{\alpha_1} \exp(-E/E_c), & \text{if } E < E_c(\alpha_1 - \alpha_2) \\ K[(\alpha_1 - \alpha_2)E_c]^{(\alpha_1 - \alpha_2)} \exp(\alpha_2 - \alpha_1)E^{\alpha_2}, & \text{otherwise} \end{cases} \quad (\text{A.1})$$

where  $E$  is the energy in units of keV. Model parameters are  $\alpha_1$ , first power law index;  $\alpha_2$ , second power law index;  $E_c$ , characteristic energy in keV; and  $K$  is the normalization constant in units of photons/keV/cm<sup>2</sup>/s.

2. Power law, (`pow`), described by:

$$A(E) = KE^{-\alpha}, \quad (\text{A.2})$$

where  $\alpha$  is the power-law index.

3. Power law with high energy exponential cut-off, (`cutoffpl`), described by

$$A(E) = KE^{-\alpha} \exp(-E/\beta), \quad (\text{A.3})$$

where  $\beta$  is the e-folding energy of the exponential rolloff (in keV).

4. Blackbody spectrum, (`bb`), described by

$$A(E) = K \frac{E^2}{\exp(E/kT) - 1}, \quad (\text{A.4})$$

where  $kT$  is the temperature in keV.

## Appendix B: Appendices for Chapter 4

### B.1 Additional plots: LLE precursors

Here we present the observed LLE lightcurves for the events in Table 4.2, with their corresponding Bayesian block treatment, as well as the best model fit with the ALP component.

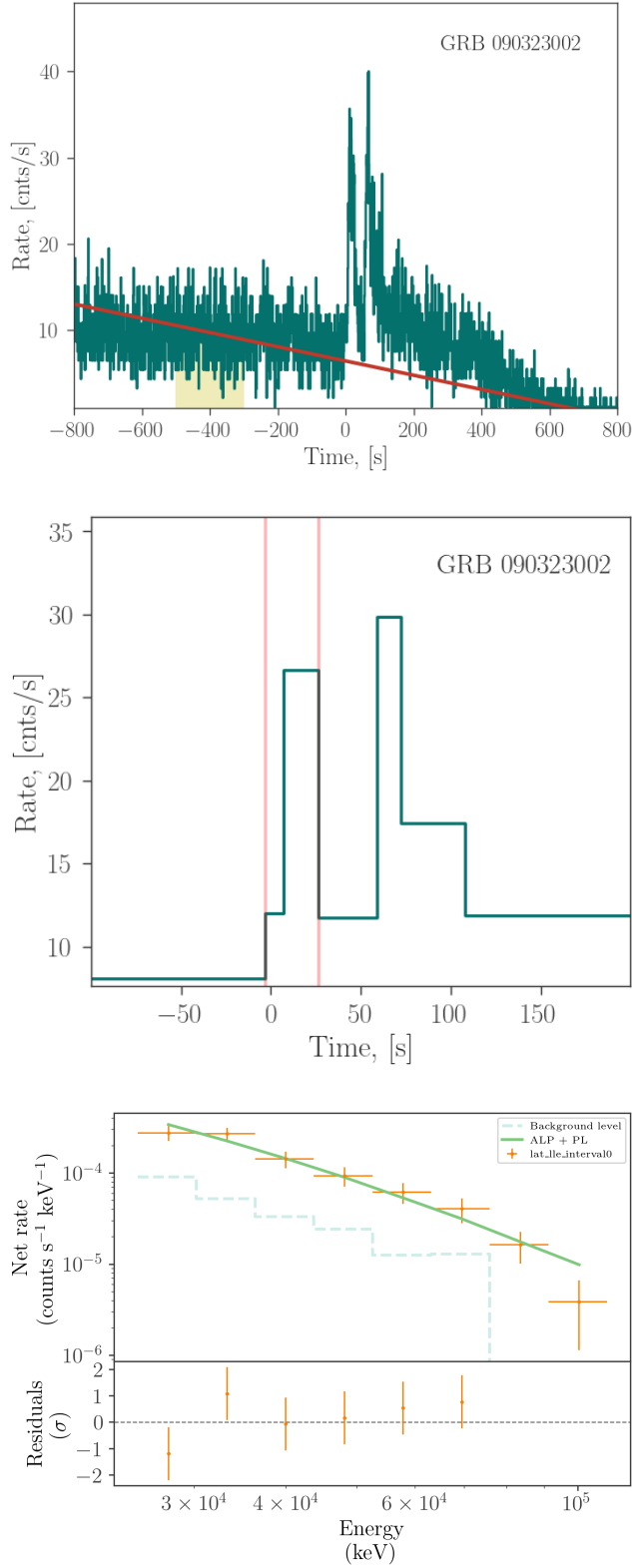


Figure B.1: Top: LLE lightcurve depicting the prompt emission as seen with LLE. The red horizontal line is the background fit. Middle: BB analysis zoomed in on the precursor. The area between the red lines represents the time interval in which we conduct the spectral fitting. Bottom: the best fit model, including the ALP component.

Figure B.1: continued.

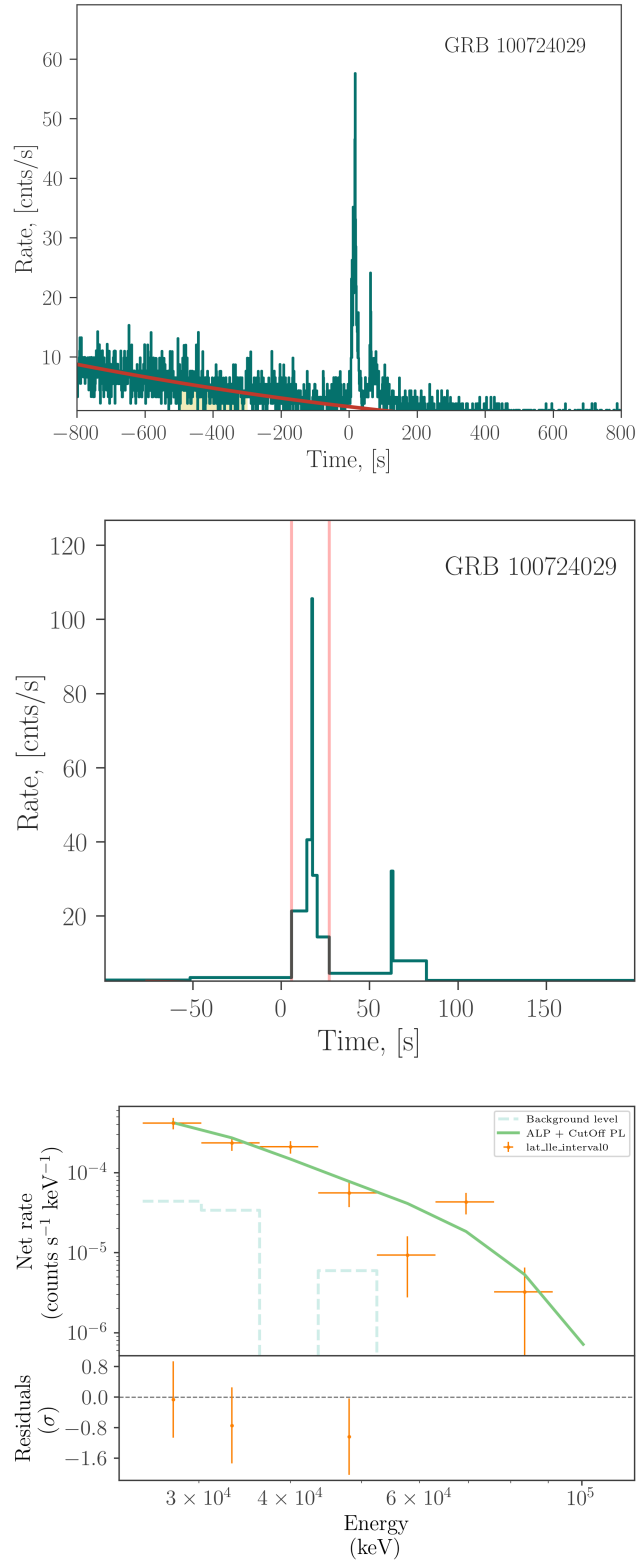


Figure B.1: continued.

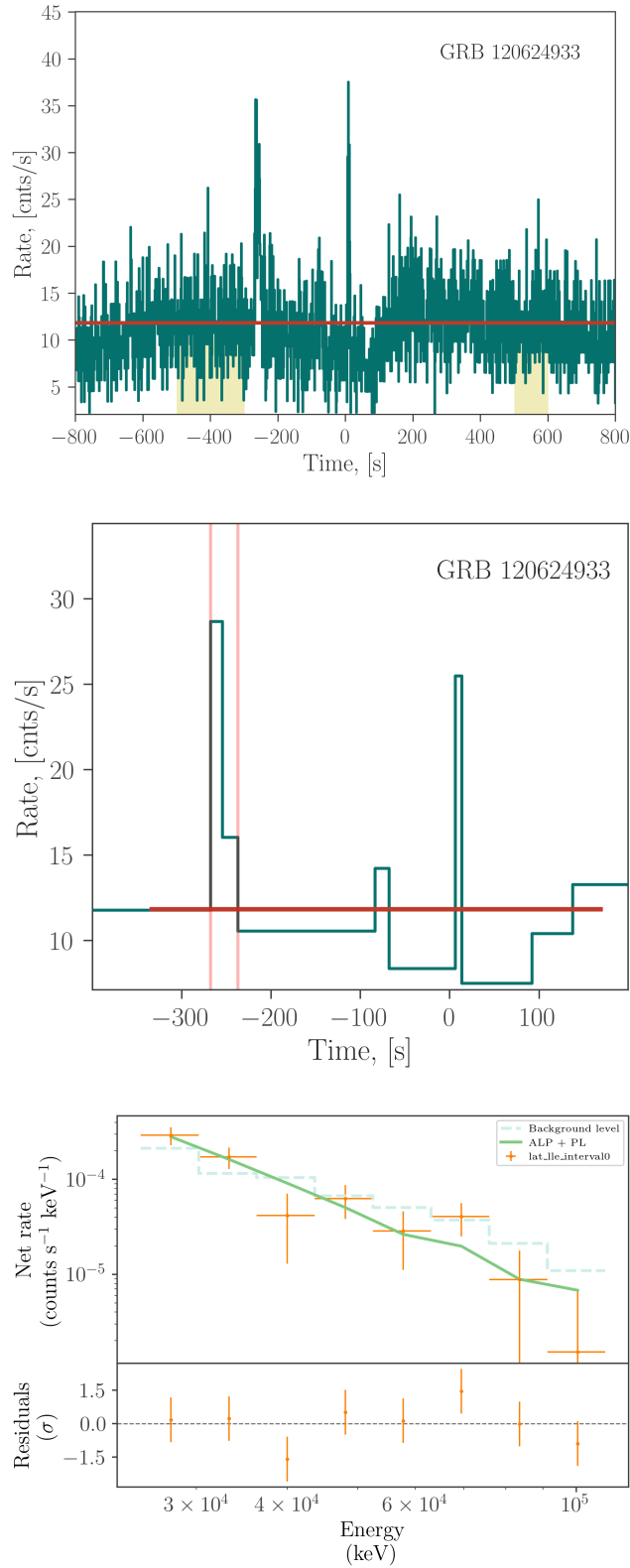


Figure B.1: continued.

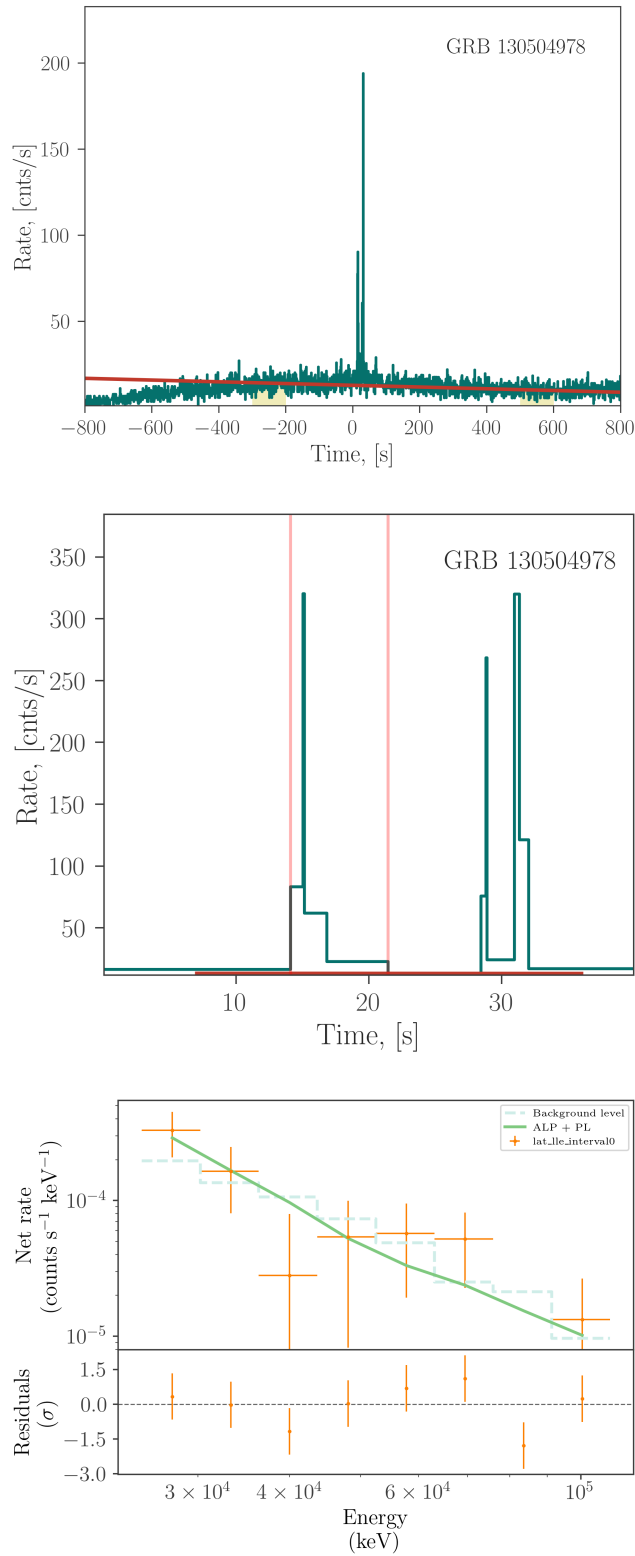


Figure B.1: continued.

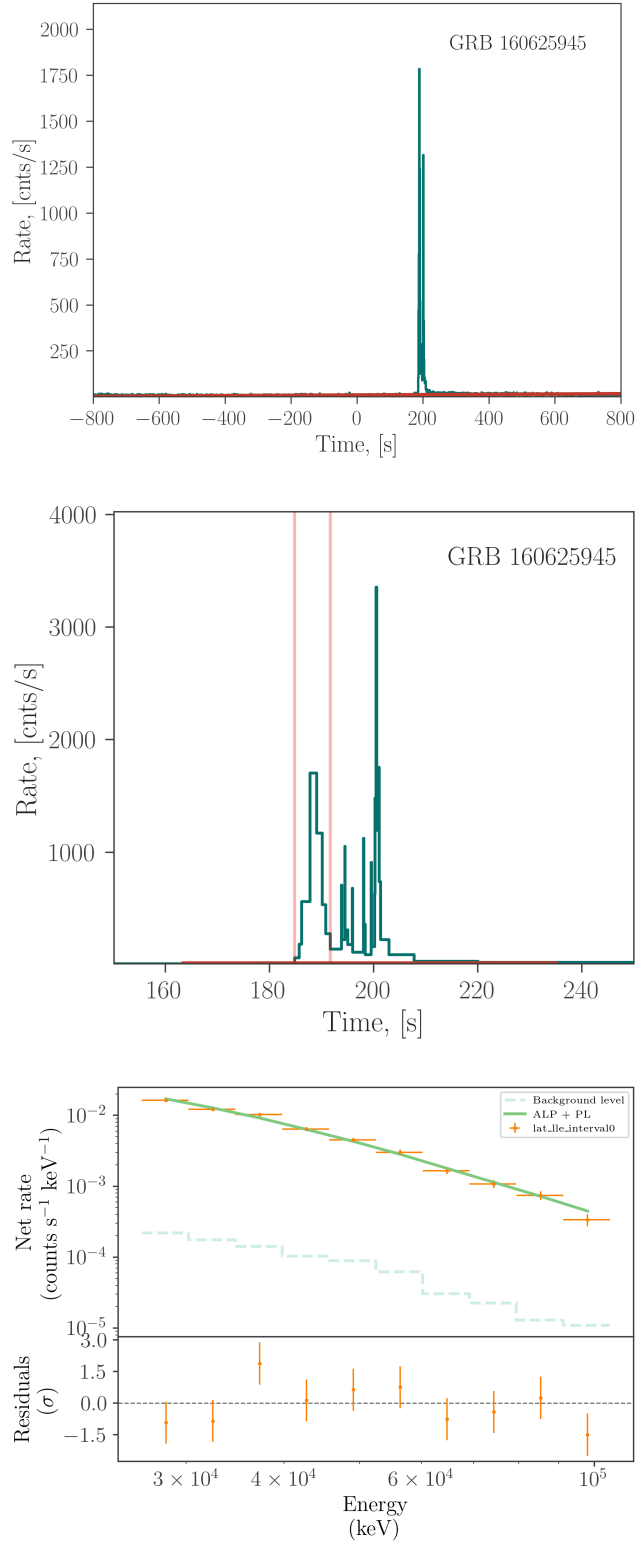
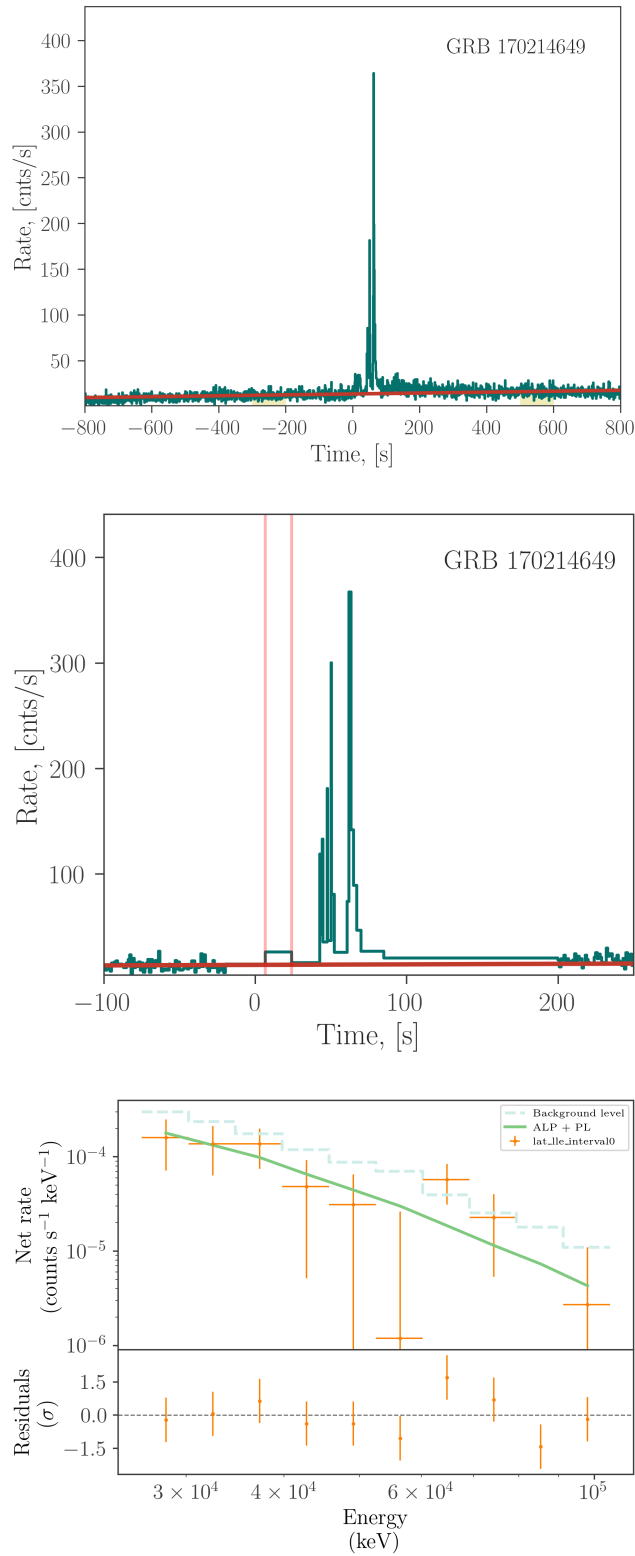


Figure B.1: continued.



## Appendix C: Appendices for Chapter 5

### C.1 Flux Upper Limits for BBH Events

Here we present the flux upper limit maps for the probable BBH events described in Section 5.3.2. These are constructed according to the method in Section 5.1 with Figure C.1 displaying the  $3\sigma$  upper limits computed with *Fermi*-GBM over a 10–1000 keV energy range and Figure C.2 showing the combined  $5\sigma$  upper limits computed with *Fermi*-GBM and *Swift*-BAT over a 15–350 keV energy range. Both sets of upper limits assume the spectral shape of potential emission follows the normal spectral template from Table 5.3 with a 1 s emission duration.

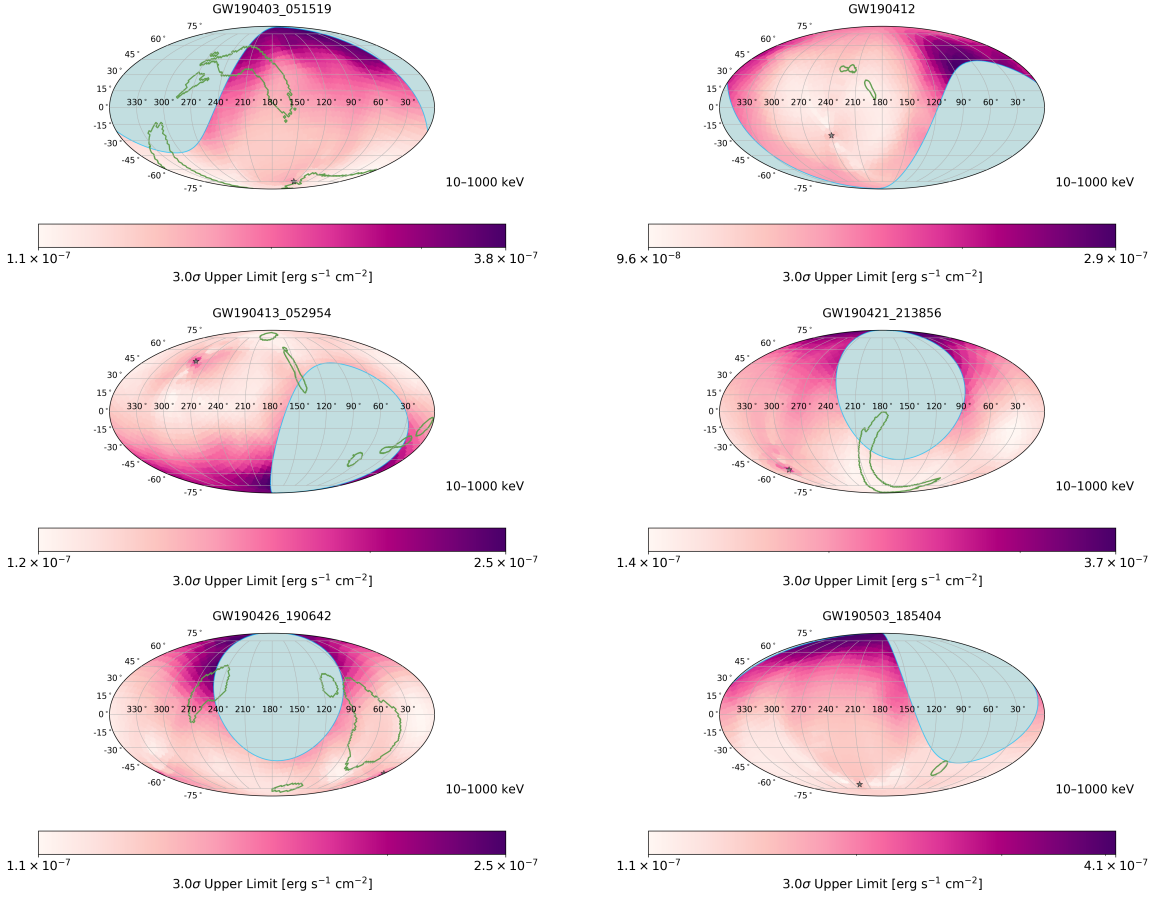


Figure C.1: The  $3\sigma$  flux upper-limit as a function of sky position for events from O3 identified with  $p_{\text{astro}} > 0.5$  and classified as a probable BBH merger in Section 5.3. The purple gradient represents the combined *Fermi*-GBM and *Swift*-BAT flux upper limits for source positions at each point on the sky. The star symbol represents the zenith direction of *Fermi*-GBM, the square symbol represents the center of the *Swift*-BAT FoV, and the green contour represents the 90% credible area of the LVK localization. The blue region is the non-visible portion of the sky which is occulted by the Earth for *Fermi*-GBM and outside the *Swift*-BAT FoV.

Figure C.1: continued.

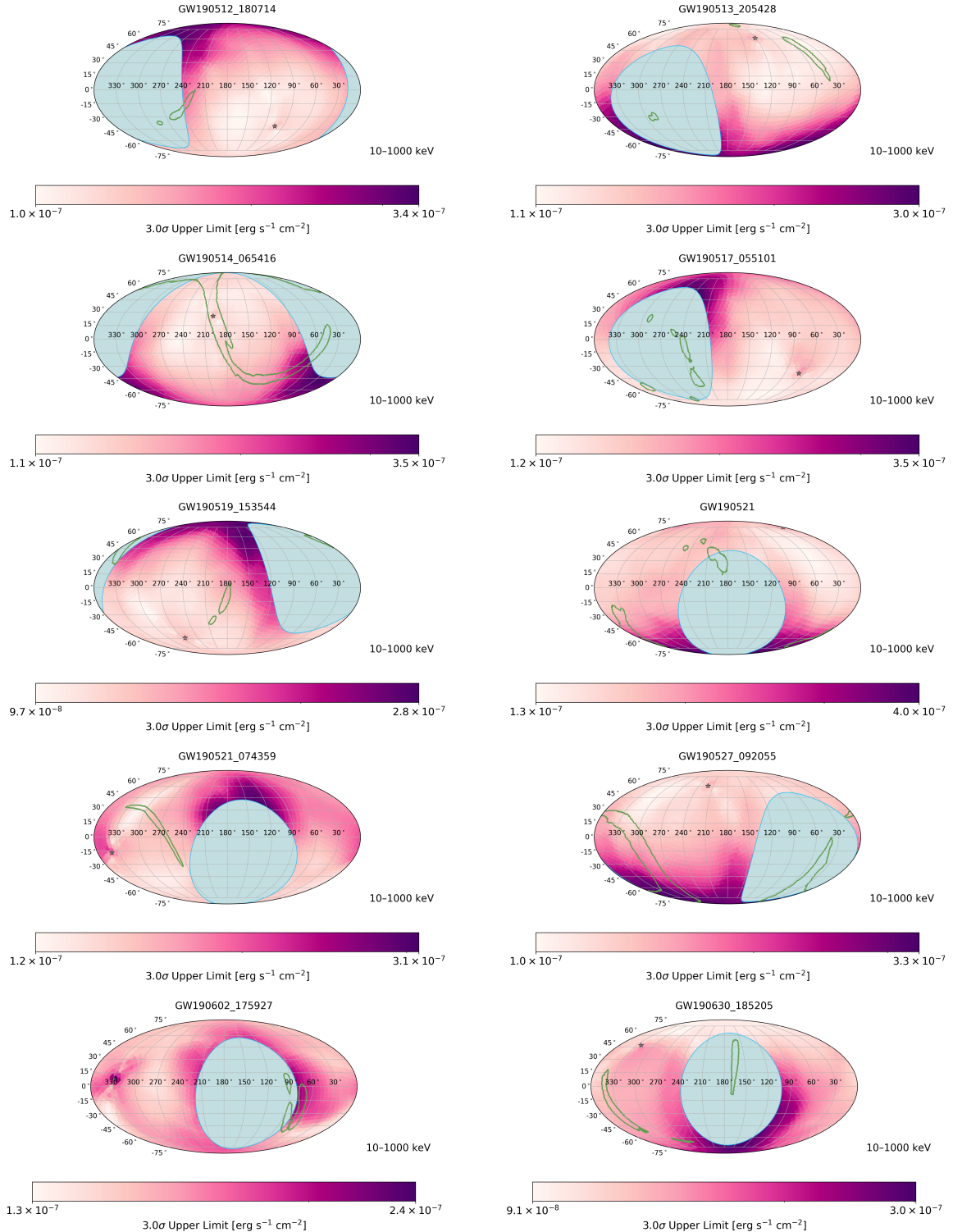


Figure C.1: continued.

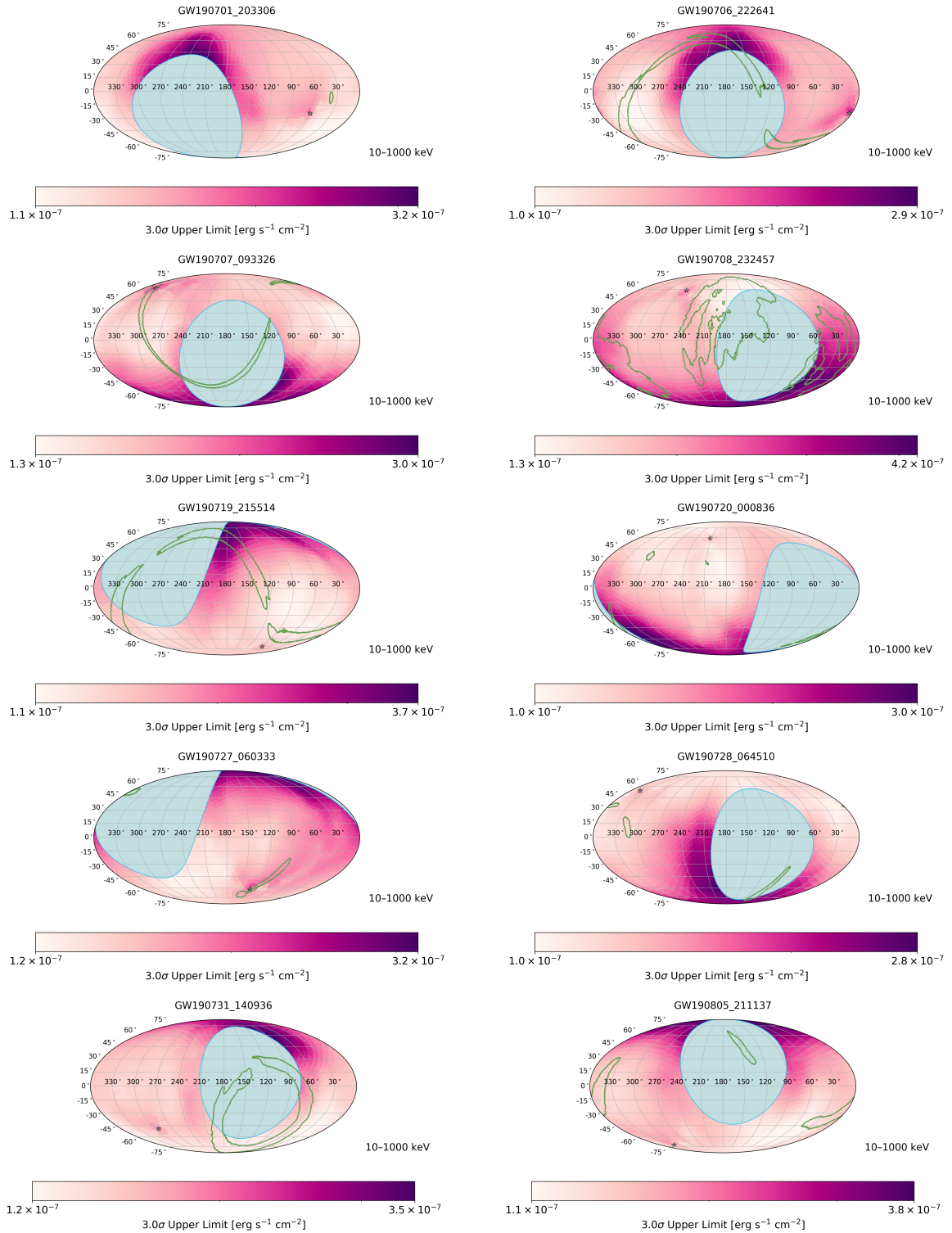


Figure C.1: continued.

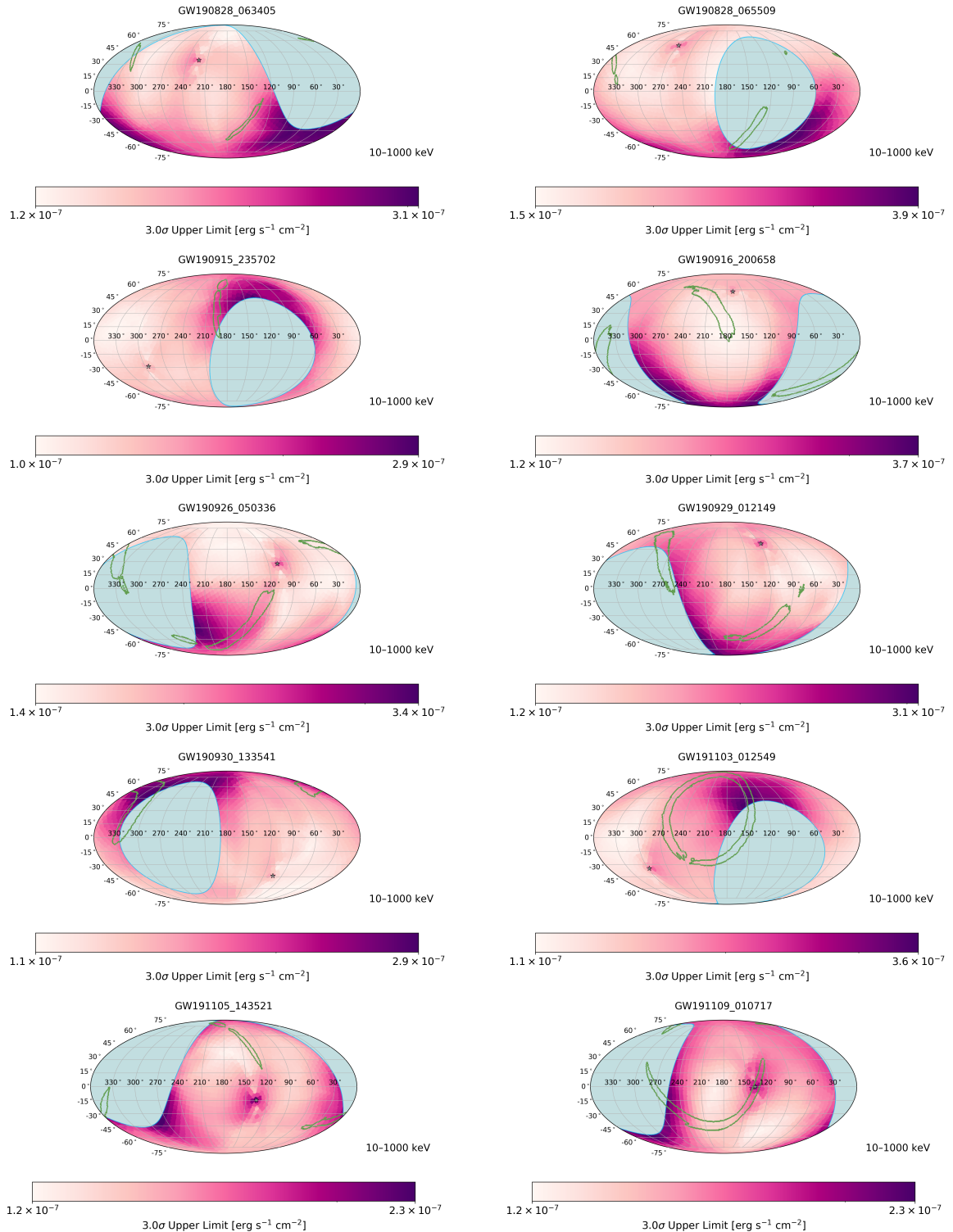


Figure C.1: continued.

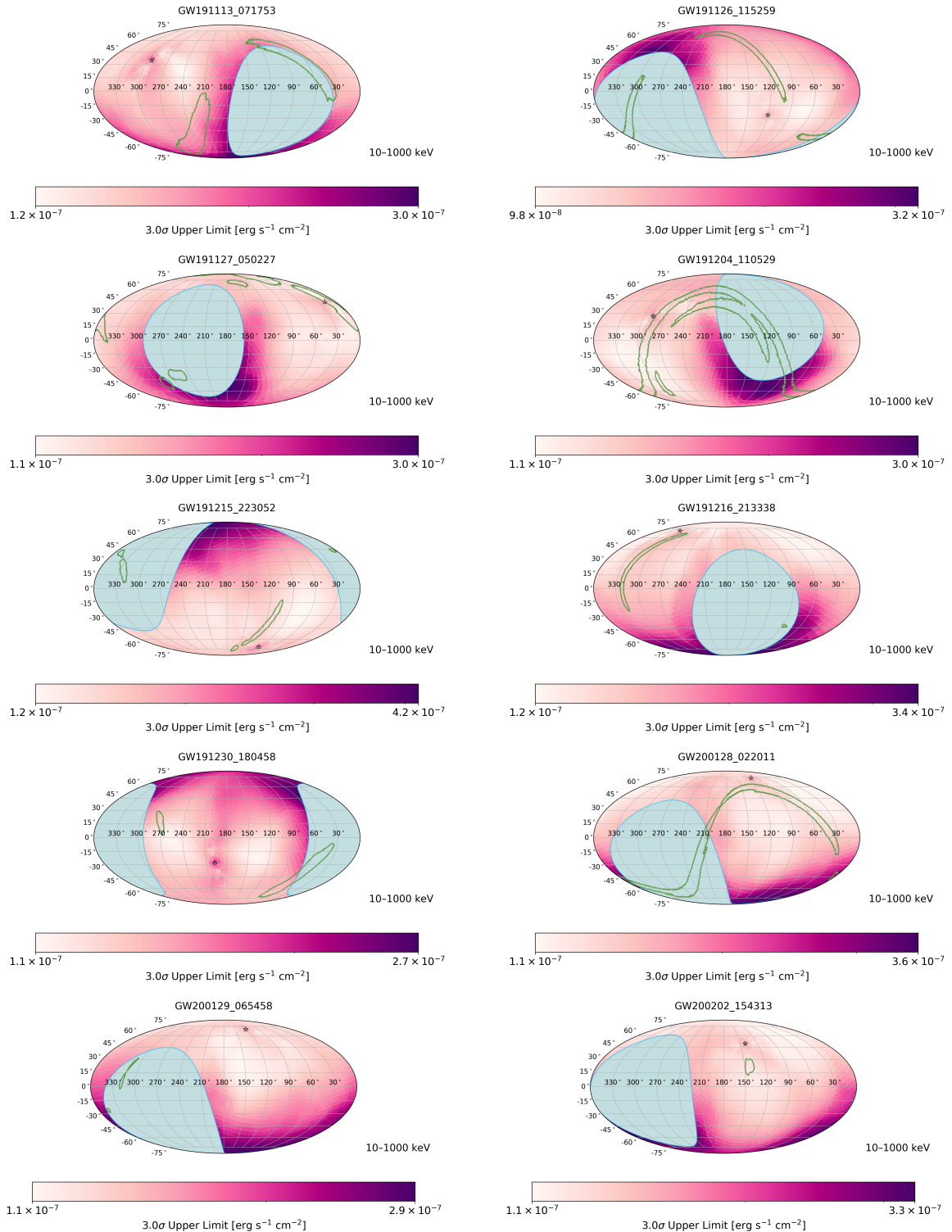


Figure C.1: continued.

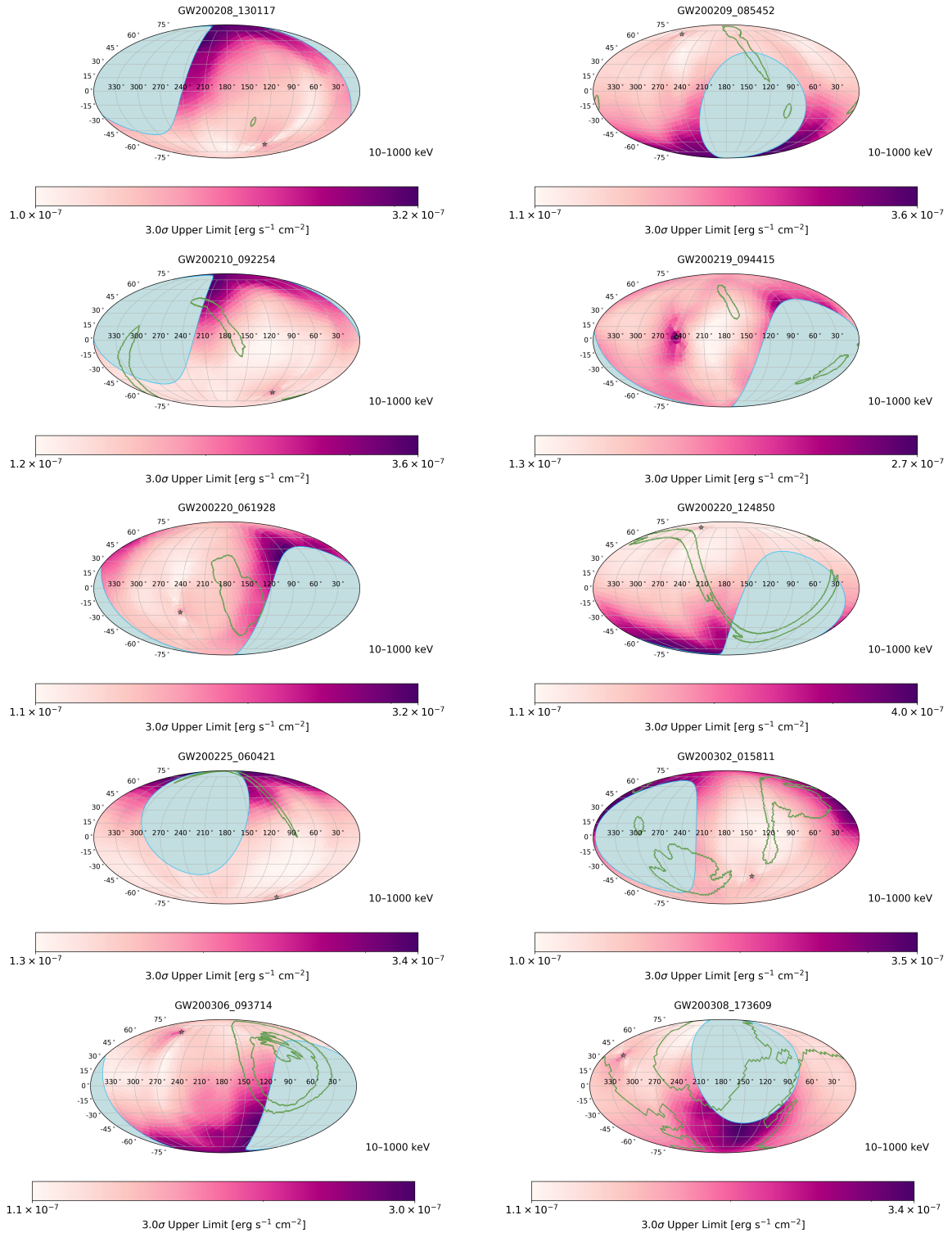
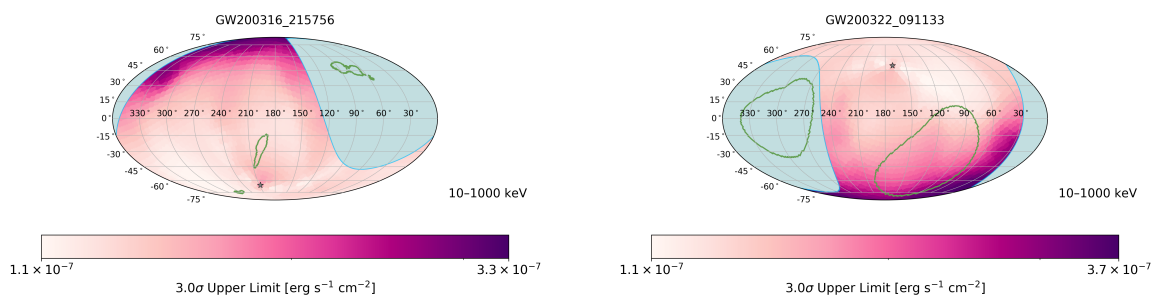


Figure C.1: continued.



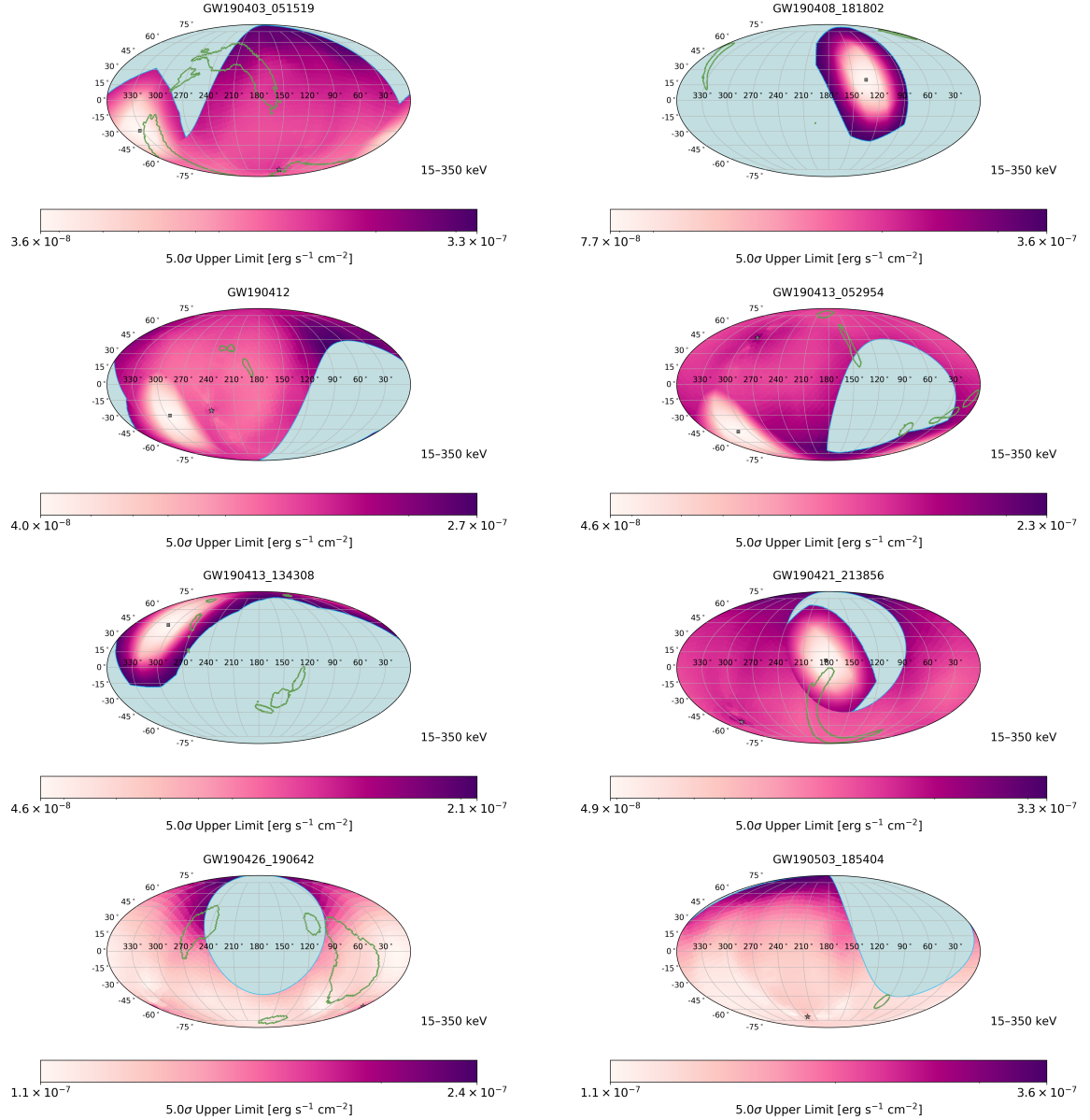


Figure C.2: The  $5\sigma$  flux upper-limit as a function of sky position for events from O3 identified with  $p_{\text{astro}} > 0.5$  and classified as a probable BBH merger in Section 5.3. The purple gradient represents the combined *Fermi*-GBM and *Swift*-BAT flux upper limits for source positions at each point on the sky. The star symbol represents the zenith direction of *Fermi*-GBM, the square symbol represents the center of the *Swift*-BAT FoV, and the green contour represents the 90% credible area of the LVK localization. The blue region is the non-visible portion of the sky which is occulted by the Earth for *Fermi*-GBM and outside the *Swift*-BAT FoV.

Figure C.2: continued.

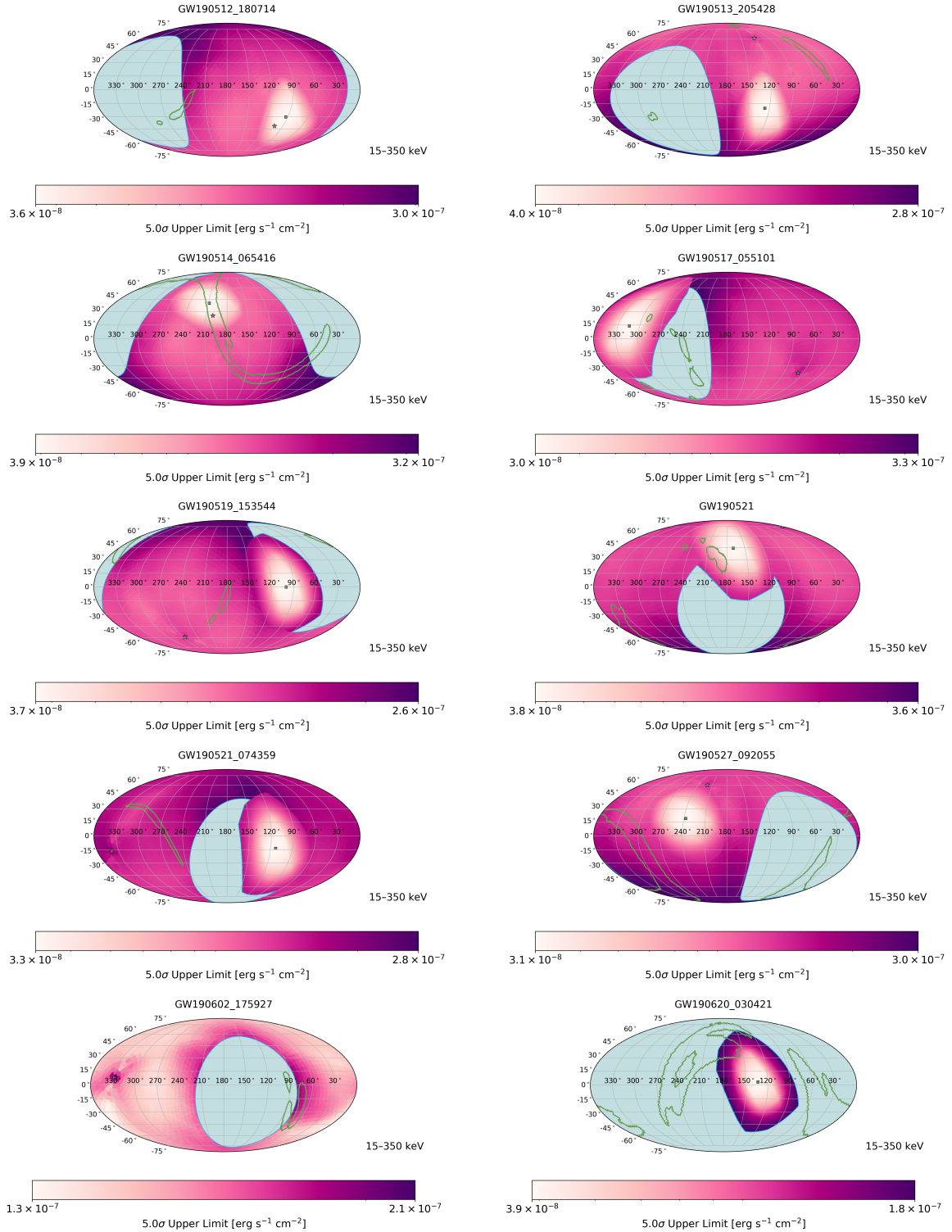


Figure C.2: continued.

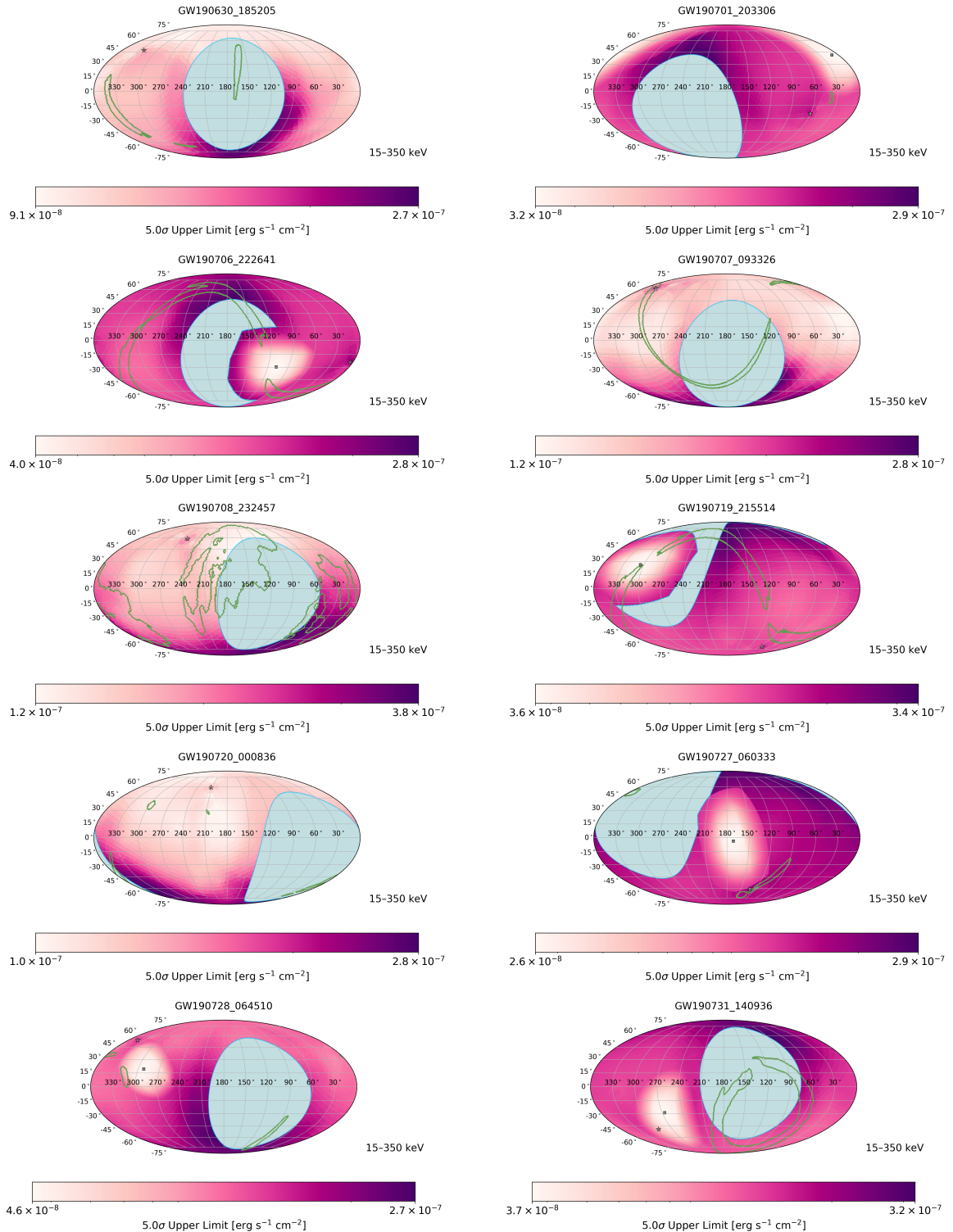


Figure C.2: continued.

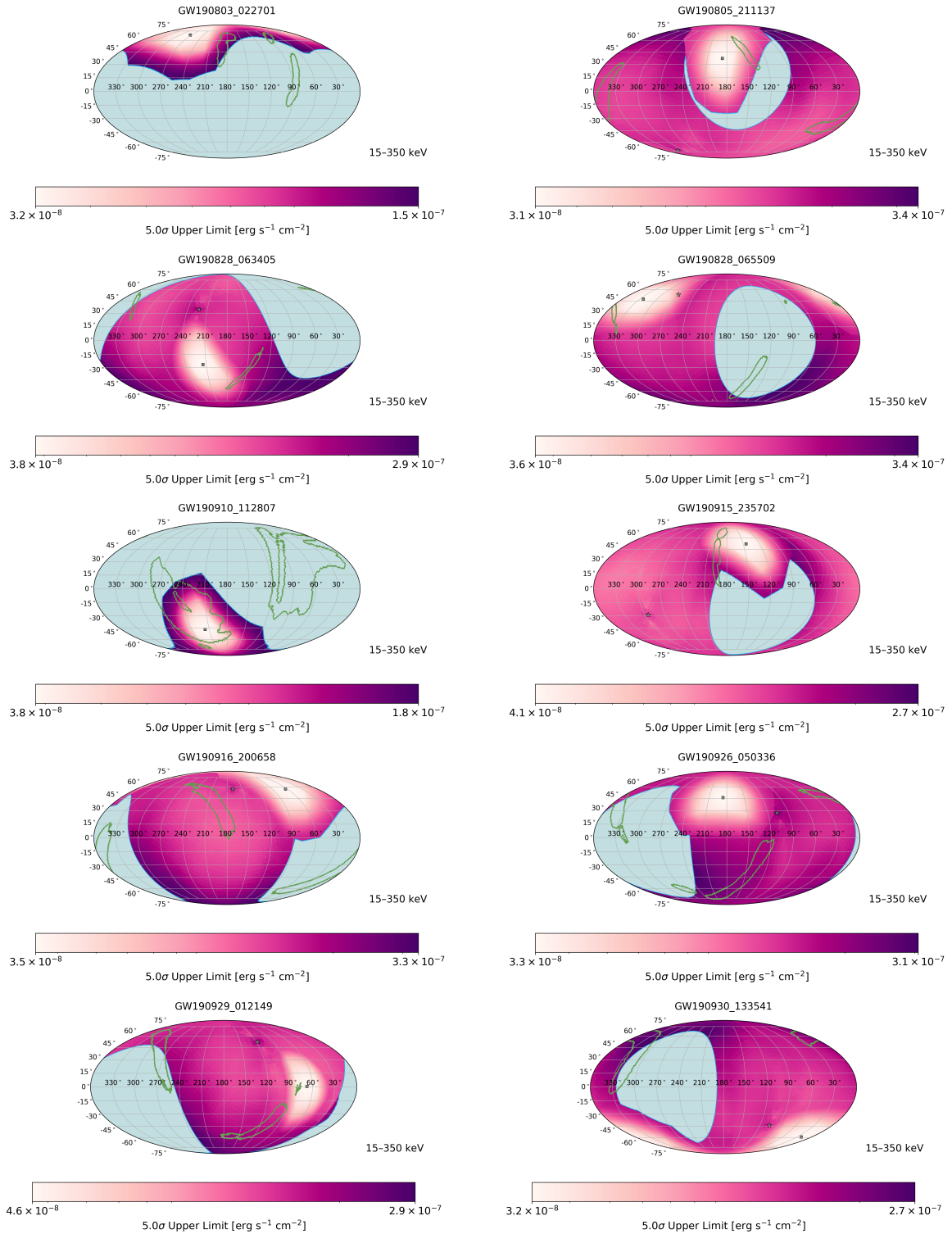


Figure C.2: continued.

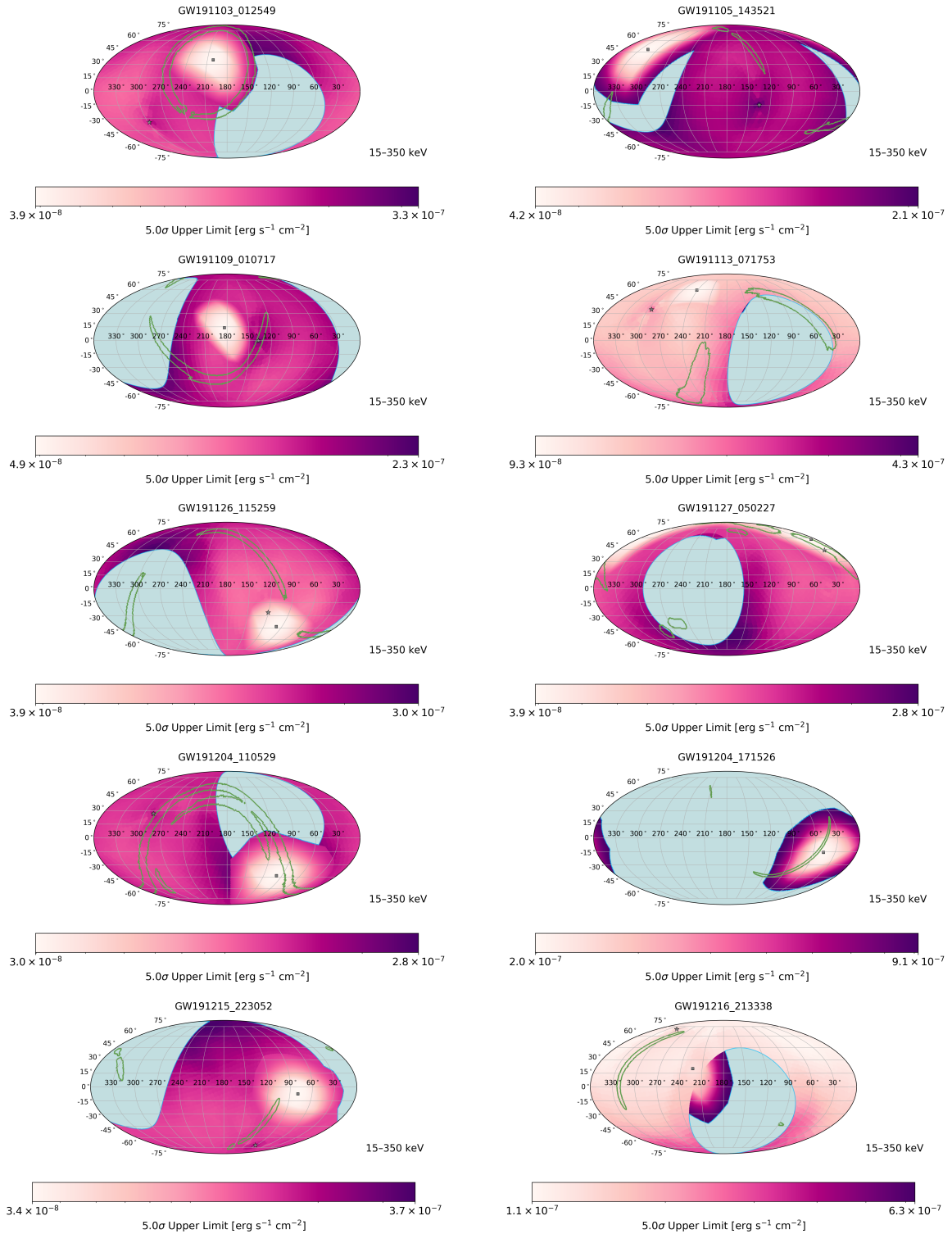


Figure C.2: continued.

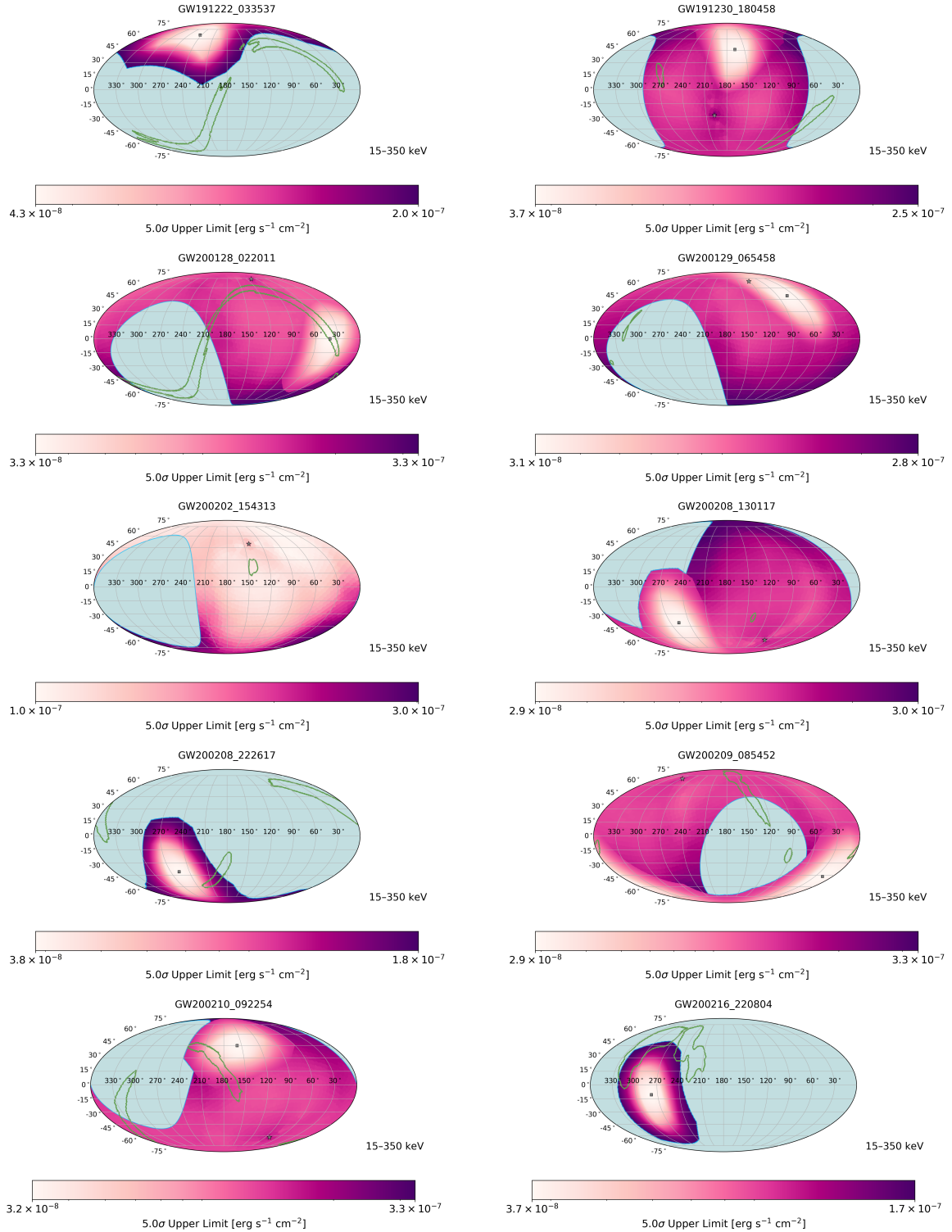
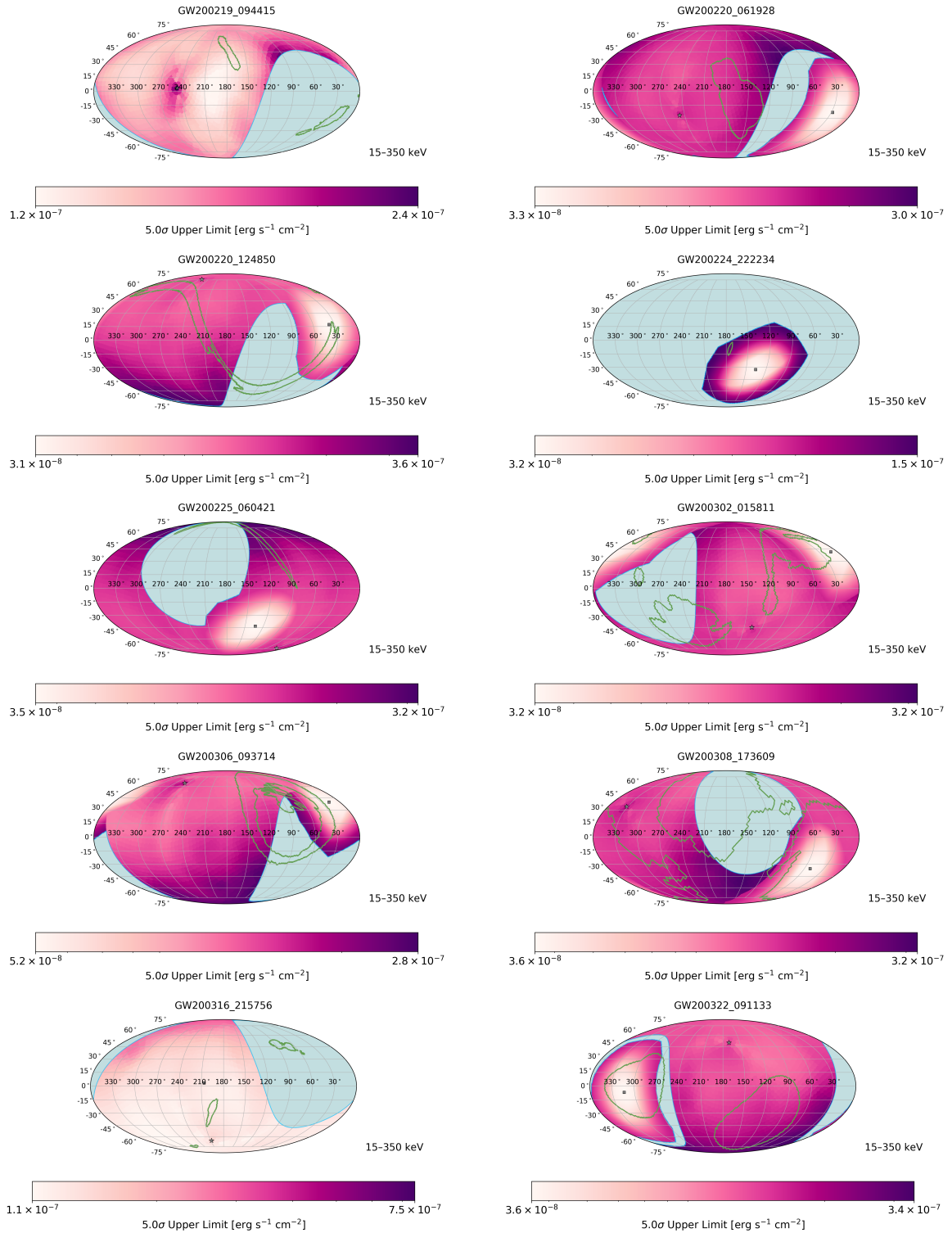


Figure C.2: continued.



Name	Waveform	$F_Q$	$F_{\nu\bar{\nu}}$	$F_{BZ}$	$F_{GW}$	UL
GW190403_051519	IMRPhenomXPHM_comoving	105, 104, 105	9.0, 8.4, 8.6	7.7, 6.5, 6.1	4.5, 3.3, 3.2	178.0
GW190403_051519	PrecessingSpinIMRHM_comoving	99, 94, 94	8.3, 7.8, 7.7	7.1, 5.7, 5.7	4.3, 3.4, 3.3	178.0
GW190403_051519	SEOBNRv4PHM_comoving	88, 80, 76	7.5, 6.5, 6.4	6.3, 5.1, 5.3	4.3, 3.5, 3.4	178.0
GW190412	IMRPhenomPv3HM	*148, 135, 221	*318, 226, 298	46, 27, 23	60, 28, 23	111.0
GW190412	SEOBNRv4PHM	*114, 96, 77	*222, 176, 139	42, 32, 25	41, 28, 21	111.0
GW190413_052954	NRSur7dq4	9.1, 4.5, 4.2	7.7, 4.4, 4.1	7.7, 3.0, 2.5	7.2, 3.0, 2.6	136.0
GW190413_052954	SEOBNRv4PHM	11, 6.0, 5.6	8.5, 4.9, 4.7	8.8, 3.4, 3.1	8.0, 3.3, 3.0	136.0
GW190421_213856	NRSur7dq4	15, 7.4, 7.1	10, 5.5, 5.3	22, 8.9, 8.2	17, 7.3, 6.7	144.0
GW190421_213856	SEOBNRv4PHM	15, 8.5, 7.6	9.2, 5.8, 5.3	18, 9.6, 8.8	14, 7.5, 6.8	144.0
GW190426_190642	IMRPhenomXPHM_comoving	45, 52, 48	3.2, 3.1, 3.0	78, 26, 24	27, 8.7, 7.9	134.0
GW190426_190642	PrecessingSpinIMRHM_comoving	29, 34, 31	2.7, 2.4, 2.4	84, 28, 26	28, 9.3, 8.7	134.0
GW190426_190642	SEOBNRv4PHM_comoving	18, 12, 11	2.1, 1.4, 1.3	91, 33, 27	29, 10, 9.2	134.0
GW190503_185404	NRSur7dq4	50, 22, 20	37, 17, 15	74, 26, 23	59, 20, 17	133.0
GW190512_180714	SEOBNRv4PHM	41, 18, 17	95, 45, 42	17, 6.2, 5.6	25, 9.2, 8.1	176.0
GW190513_205428	NRSur7dq4	44, 19, 17	37, 18, 17	16, 8.1, 7.2	19, 7.8, 6.7	113.0
GW190513_205428	SEOBNRv4PHM	43, 24, 22	34, 20, 19	17, 9.9, 9.3	18, 8.9, 8.1	113.0
GW190514_065416	NRSur7dq4	5.0, 2.6, 2.4	3.8, 2.3, 2.1	8.8, 3.8, 3.4	6.5, 3.1, 2.8	135.0
GW190517_055101	NRSur7dq4	*282, 150, 139	131, 70, 65	26, 11, 9.6	46, 17, 15	134.0
GW190517_055101	SEOBNRv4PHM	*341, 168, 151	139, 68, 63	28, 8.9, 7.7	50, 16, 15	134.0
GW190519_153544	NRSur7dq4	47, 18, 16	13, 5.8, 5.1	40, 8.7, 6.5	27, 6.5, 5.2	126.0
GW190519_153544	SEOBNRv4PHM	47, 19, 18	11, 5.7, 5.2	34, 13, 9.5	24, 8.0, 6.0	126.0
GW190521	IMRPhenomPv2	114, 61, 55	75, 41, 38	131, 59, 57	110, 48, 44	219.0
GW190521	NRSur7dq4	116, 47, 43	78, 34, 31	130, 49, 45	116, 43, 39	219.0
GW190521	SEOBNRv4PHM	99, 53, 51	64, 35, 34	99, 47, 44	92, 43, 40	219.0
GW190521_074359	NRSur7dq4	7.4, 3.7, 3.4	1.4, 0.76, 0.71	42, 12, 10	15, 5.3, 4.2	151.0
GW190521_074359	SEOBNRv4PHM	20, 17, 15	2.5, 1.7, 1.6	82, 29, 24	27, 9.1, 7.3	151.0
GW190527_092055	NRSur7dq4	37, 16, 14	27, 13, 12	18, 8.3, 7.4	18, 7.8, 7.0	191.0
GW190602_175927	NRSur7dq4	18, 11, 10	5.7, 3.6, 3.4	48, 24, 22	24, 12, 11	189.0
GW190602_175927	SEOBNRv4PHM	20, 14, 14	5.9, 4.3, 4.2	50, 29, 26	25, 14, 12	189.0
GW190630_185205	NRSur7dq4	*197, 79, 72	*194, 82, 76	136, 56, 51	151, 58, 53	130.0
GW190630_185205	SEOBNRv4PHM	*173, 80, 77	*169, 81, 78	120, 54, 49	133, 57, 52	130.0
GW190701_203306	NRSur7dq4	20, 12, 11	10, 6.7, 6.2	49, 28, 26	30, 16, 15	128.0
GW190701_203306	SEOBNRv4PHM	21, 14, 13	9.6, 6.9, 6.6	45, 28, 26	28, 16, 15	128.0
GW190706_222641	NRSur7dq4	17, 8.4, 7.7	4.3, 2.4, 2.3	12, 5.1, 4.5	8.1, 3.0, 2.5	163.0
GW190706_222641	SEOBNRv4PHM	16, 12, 12	4.0, 3.0, 3.0	13, 7.8, 7.3	8.3, 4.0, 3.7	163.0
GW190707_093326	IMRPhenomPv2	211, 133, 124	*1152, 739, 702	28, 16, 15	78, 45, 43	160.0
GW190707_093326	SEOBNRv4P	183, 112, 101	*1004, 632, 574	22, 13, 11	66, 39, 34	160.0
GW190708_232457	SEOBNRv4PHM	167, 91, 85	*463, 255, 240	39, 19, 17	80, 39, 36	193.0
GW190719_215514	NRSur7dq4	31, 12, 11	16, 8.2, 7.7	5.2, 2.2, 2.0	6.6, 2.4, 2.1	185.0
GW190719_215514	SEOBNRv4PHM	43, 23, 20	19, 11, 10	7.6, 4.5, 4.3	8.5, 4.7, 4.5	185.0
GW190720_000836	IMRPhenomPv2	*331, 263, 267	*1289, 844, 828	23, 12, 12	67, 29, 27	119.0
GW190720_000836	SEOBNRv4P	*218, 121, 113	*957, 557, 523	18, 9.0, 8.5	53, 26, 24	119.0
GW190727_060333	NRSur7dq4	19, 10, 9.6	12, 7.1, 6.6	11, 5.3, 4.7	11, 5.0, 4.6	174.0
GW190728_064510	IMRPhenomPv2	*209, 111, 113	*962, 477, 469	17, 7.6, 7.2	51, 18, 16	121.0
GW190728_064510	SEOBNRv4P	*195, 81, 74	*945, 419, 388	16, 6.0, 5.4	51, 18, 17	121.0
GW190731_140936	NRSur7dq4	15, 8.8, 8.3	9.8, 6.1, 5.7	16, 7.7, 7.0	13, 6.7, 6.1	140.0
GW190805_211137	IMRPhenomXPHM_comoving	40, 22, 21	11, 7.0, 7.1	14, 4.4, 3.9	13, 4.6, 4.2	143.0
GW190805_211137	PrecessingSpinIMRHM_comoving	36, 22, 22	10, 6.7, 7.2	14, 5.7, 5.5	12, 5.2, 5.3	143.0
GW190805_211137	SEOBNRv4PHM_comoving	32, 23, 22	9.6, 6.7, 7.5	15, 6.3, 6.9	12, 5.5, 6.1	143.0

Table C.1: Table showing the 0.95 percentile fluxes from different models of BBH emission. Units are  $10^{-9}$  erg cm $^{-2}$  s $^{-1}$ . The three numbers in each cell represent the isotropic emission, the uniform-distributed jet opening angle and the fixed jet opening angle. The upper limits (UL) are the  $3\sigma$ , 10–1000 keV range values from Table 5.5. Stars mark instances where the isotropic emission exceeds the UL in more than 10% of the cases.

Table C.1: continued.

Name	Waveform	$F_Q$	$F_{\nu\bar{\nu}}$	$F_{BZ}$	$F_{GW}$	UL
GW190828_063405	NRSur7dq4	55, 21, 19	45, 19, 17	24, 7.4, 6.4	31, 9.6, 8.3	181.0
GW190828_063405	SEOBNRv4PHM	49, 29, 28	39, 22, 22	19, 7.2, 6.6	25, 9.6, 8.9	181.0
GW190828_065509	SEOBNRv4PHM	34, 22, 22	78, 50, 48	12, 6.2, 5.6	16, 7.7, 6.8	200.0
GW190915_235702	IMRPhenomPv2	58, 22, 19	45, 20, 18	35, 12, 11	34, 11, 10	186.0
GW190915_235702	SEOBNRv4P	48, 32, 31	41, 27, 25	32, 12, 10	33, 14, 12	186.0
GW190916_200658	IMRPhenomXPHM_comoving	18, 10, 9.5	9.1, 5.6, 5.1	16, 8.6, 7.3	11, 5.7, 4.8	131.0
GW190916_200658	PrecessingSpinIMRHM_comoving	18, 10, 10	9.2, 5.5, 5.3	15, 9.3, 9.0	11, 5.9, 5.4	131.0
GW190916_200658	SEOBNRv4PHM_comoving	19, 11, 11	9.1, 5.8, 5.6	15, 8.9, 8.5	11, 5.9, 5.5	131.0
GW190924_021846	IMRPhenomPv2	*331, 264, 318	*2872, 1880, 1903	21, 14, 14	63, 31, 28	147.0
GW190924_021846	SEOBNRv4P	*297, 128, 116	*2942, 1323, 1211	17, 6.7, 6.0	69, 27, 24	147.0
GW190926_050336	IMRPhenomXPHM_comoving	11, 2.5, 2.2	9.4, 2.9, 2.6	16, 4.1, 3.2	11, 2.7, 2.2	210.0
GW190926_050336	PrecessingSpinIMRHM_comoving	11, 3.5, 3.5	8.9, 3.4, 3.3	14, 4.1, 3.4	10, 3.0, 2.5	210.0
GW190926_050336	SEOBNRv4PHM_comoving	10, 4.3, 4.7	8.2, 3.5, 3.8	13, 4.1, 3.7	9.1, 2.9, 2.9	210.0
GW190929_012149	IMRPhenomPv2	56, 25, 24	13, 7.7, 7.7	96, 55, 50	26, 7.9, 7.3	175.0
GW190929_012149	SEOBNRv4P	47, 8.2, 7.6	10, 2.9, 2.7	59, 14, 12	20, 4.6, 4.0	175.0
GW190930_133541	IMRPhenomPv2	*367, 240, 258	*1408, 791, 784	26, 13, 13	62, 26, 23	239.0
GW190930_133541	SEOBNRv4P	*280, 130, 121	*1325, 630, 583	23, 9.8, 9.1	67, 27, 24	239.0
GW191103_012549	C01:IMRPhenomXPHM	*332, 230, 230	*1349, 817, 801	15, 8.8, 8.6	53, 25, 24	198.0
GW191103_012549	C01:SEOBNRv4PHM	*303, 171, 158	*1355, 772, 710	16, 9.0, 8.3	58, 29, 26	198.0
GW191105_143521	C01:IMRPhenomXPHM	86, 43, 42	*509, 261, 247	8.5, 3.5, 3.3	26, 10, 9.5	169.0
GW191105_143521	C01:SEOBNRv4PHM	84, 35, 31	*509, 230, 208	8.3, 3.0, 2.7	26, 10, 8.6	169.0
GW191109_010717	C01:IMRPhenomXPHM	169, 11, 10	43, 5.5, 5.0	*437, 55, 43	217, 28, 22	155.0
GW191109_010717	C01:SEOBNRv4PHM	47, 24, 22	16, 10.0, 9.5	*198, 112, 102	89, 48, 43	155.0
GW191113_071753	C01:IMRPhenomXPHM	35, 20, 20	86, 52, 51	25, 8.3, 7.3	16, 5.8, 5.3	172.0
GW191113_071753	C01:SEOBNRv4PHM	74, 36, 35	118, 71, 62	17, 8.5, 8.0	14, 6.4, 5.7	172.0
GW191126_115259	C01:IMRPhenomXPHM	103, 67, 68	*394, 251, 244	5.6, 2.9, 2.7	18, 9.2, 8.4	136.0
GW191126_115259	C01:SEOBNRv4PHM	104, 58, 52	*419, 235, 214	6.5, 3.1, 2.7	21, 10.0, 8.8	136.0
GW191127_050227	C01:IMRPhenomXPHM	59, 57, 61	15, 11, 11	48, 45, 41	11, 8.9, 8.8	140.0
GW191127_050227	C01:SEOBNRv4PHM	32, 16, 16	16, 7.2, 7.1	20, 10, 11	13, 4.8, 4.5	140.0
GW191204_110529	C01:IMRPhenomXPHM	107, 56, 51	118, 69, 64	46, 27, 25	57, 33, 30	142.0
GW191204_110529	C01:SEOBNRv4PHM	119, 74, 70	121, 77, 82	42, 27, 31	55, 33, 36	142.0
GW191215_223052	C01:IMRPhenomXPHM	34, 13, 11	54, 21, 18	19, 4.9, 4.1	25, 6.3, 5.4	153.0
GW191215_223052	C01:SEOBNRv4PHM	31, 13, 12	49, 20, 19	17, 5.1, 4.3	22, 6.6, 5.8	153.0
GW191216_213338	C01:IMRPhenomXPHM	*1098, 694, 684	*5893, 3583, 3466	96, 60, 54	*287, 152, 140	148.0
GW191216_213338	C01:SEOBNRv4PHM	*1180, 602, 545	*6516, 3308, 3024	93, 45, 40	*311, 150, 135	148.0
GW191230_180458	C01:IMRPhenomXPHM	10, 3.2, 2.9	4.6, 1.9, 1.7	18, 5.4, 4.9	11, 3.4, 3.1	139.0
GW191230_180458	C01:SEOBNRv4PHM	8.4, 4.2, 4.1	3.8, 2.2, 2.1	14, 5.0, 4.5	9.3, 3.4, 3.0	139.0
GW200128_022011	C01:IMRPhenomXPHM	35, 14, 11	18, 8.4, 7.0	32, 11, 9.8	27, 10, 8.3	142.0
GW200128_022011	C01:SEOBNRv4PHM	36, 27, 21	15, 12, 9.6	26, 17, 11	23, 17, 10	142.0
GW200129_065458	C01:IMRPhenomXPHM	*220, 149, 145	*170, 108, 105	113, 64, 59	*128, 62, 57	142.0
GW200129_065458	C01:SEOBNRv4PHM	*235, 114, 103	*211, 101, 88	165, 77, 59	*188, 88, 71	142.0
GW200202_154313	C01:IMRPhenomXPHM	*666, 365, 350	*4383, 2340, 2214	50, 23, 21	*174, 78, 71	121.0
GW200202_154313	C01:SEOBNRv4PHM	*703, 328, 300	*4700, 2230, 2051	50, 22, 20	*185, 79, 72	121.0
GW200208_130117	C01:IMRPhenomXPHM	18, 9.2, 8.4	16, 8.6, 7.9	25, 11, 9.6	21, 9.2, 7.8	136.0
GW200208_130117	C01:SEOBNRv4PHM	17, 11, 11	14, 9.6, 9.2	22, 11, 10	19, 9.9, 9.0	136.0
GW200209_085452	C01:IMRPhenomXPHM	21, 4.4, 4.0	16, 4.6, 4.3	25, 4.6, 4.2	21, 4.3, 4.0	135.0
GW200209_085452	C01:SEOBNRv4PHM	10, 5.8, 5.6	8.4, 4.8, 4.8	12, 4.3, 3.9	10, 4.0, 3.7	135.0
GW200219_094415	C01:IMRPhenomXPHM	11, 3.1, 2.7	8.9, 3.1, 2.8	16, 3.7, 3.2	13, 3.2, 2.7	152.0
GW200219_094415	C01:SEOBNRv4PHM	10, 4.9, 4.6	7.7, 3.9, 3.7	11, 4.2, 3.8	9.7, 3.4, 3.2	152.0
GW200220_061928	C01:IMRPhenomXPHM	8.3, 3.4, 3.1	1.3, 0.64, 0.61	52, 11, 10	12, 3.8, 3.4	165.0
GW200220_061928	C01:SEOBNRv4PHM	10, 5.6, 5.3	1.4, 0.84, 0.8	34, 12, 10	12, 4.6, 4.1	165.0
GW200220_124850	C01:IMRPhenomXPHM	13, 4.5, 4.3	8.8, 3.7, 3.5	16, 6.4, 6.0	12, 5.0, 4.8	128.0
GW200220_124850	C01:SEOBNRv4PHM	11, 5.1, 5.3	8.0, 3.9, 3.9	18, 7.0, 7.5	13, 5.2, 5.5	128.0

Table C.1: continued.

Name	Waveform	$F_Q$	$F_{\nu\bar{\nu}}$	$F_{BZ}$	$F_{GW}$	UL
GW200225_060421	C01:IMRPhenomXPHM	97, 45, 40	224, 114, 107	33, 15, 14	53, 26, 24	236.0
GW200225_060421	C01:SEOBNRv4PHM	71, 47, 47	174, 103, 102	25, 13, 12	43, 21, 20	236.0
GW200302_015811	C01:IMRPhenomXPHM	62, 27, 26	60, 30, 29	62, 28, 26	53, 24, 22	162.0
GW200302_015811	C01:SEOBNRv4PHM	66, 34, 35	58, 30, 30	54, 23, 21	48, 21, 18	162.0
GW200306_093714	C01:IMRPhenomXPHM	133, 73, 67	113, 60, 56	19, 10, 9.7	24, 9.9, 9.1	146.0
GW200306_093714	C01:SEOBNRv4PHM	132, 86, 82	102, 64, 61	20, 9.8, 8.1	23, 10, 9.5	146.0
GW200308_173609	C01:IMRPhenomXPHM	51, 54, 51	24, 23, 22	74, 20, 12	7.3, 2.3, 2.2	192.0
GW200308_173609	C01:SEOBNRv4PHM	71, 57, 67	32, 25, 25	13, 3.5, 3.3	4.7, 2.6, 2.1	192.0
GW200316_215756	C01:IMRPhenomXPHM	112, 67, 62	*482, 256, 237	13, 6.4, 5.3	29, 10, 9.2	134.0
GW200316_215756	C01:SEOBNRv4PHM	103, 45, 41	*484, 224, 205	10, 3.6, 3.2	28, 10, 9.1	134.0
GW200322_091133	C01:IMRPhenomXPHM	147, 468, 499	72, 55, 64	42, 24, 27	8.7, 3.1, 3.7	154.0
GW200322_091133	C01:SEOBNRv4PHM	3.7, 0.53, 0.22	2.0, 0.45, 0.17	4.8, 0.9, 0.37	0.77, 0.76, 0.26	154.0

## C.2 Isotropic luminosity upper limits

Table C.2: Isotropic-equivalent luminosity upper limits for the 6 events from O3 with  $p_{\text{astro}} > 0.5$  that are classified with a possible neutron star component in Section 5.3. These are computed using the  $5\sigma$  marginalized flux upper limit from Table 5.4.

Event Name	$D_L$ [Gpc] Median	$5\sigma L_{\text{iso}}$ U.L. [ $\text{erg s}^{-1}$ ] 10-1000 keV
GW190425	0.15	$8.38 \times 10^{47}$
GW190814	0.23	$8.16 \times 10^{47}$
GW190917_114630	0.72	$2.64 \times 10^{49}$
GW191219_163120	0.55	$8.53 \times 10^{48}$
GW200115_042309	0.29	$3.31 \times 10^{48}$
GW200210_092254	0.94	$1.94 \times 10^{49}$

## C.3 Marginal events

Here we present the remaining  $3\sigma$  and  $5\sigma$  flux upper limit maps computed for the 6 marginal GW events ( $\text{FAR} < 2 \text{ yr}^{-1}$ ,  $p_{\text{astro}} < 0.5$ ) from O3 that are presented in Table 5.2. These are constructed according to the method described in Section 5.1. Both sets of upper limits assume the spectral shape of potential emission follows the normal spectral template from Table 5.3 with a 1 s emission duration. The  $5\sigma$  flux upper limit map for GW200105\_203549 is not present in Figure C.4 because it is already presented in Figure 5.4 of the main text.

Table C.3: Isotropic-equivalent luminosity upper limits for events from O3 with  $p_{\text{astro}} > 0.5$  that are classified as probable BBH mergers in Section 5.3. These are computed using the  $5\sigma$  marginalized flux upper limit from Table 5.5. Events without data in both *Fermi*-GBM and *Swift*-BAT are denoted with a dash.

Event Name	$D_L$ [Gpc]	$5\sigma L_{\text{iso}}$ U.L. [erg s $^{-1}$ ]	Event Name	$D_L$ [Gpc]	$5\sigma L_{\text{iso}}$ U.L. [erg s $^{-1}$ ]
	Median	10-1000 keV		Median	10-1000 keV
GW190403_051519	8.28	$2.36 \times 10^{51}$	GW191103_012549	0.99	$3.94 \times 10^{49}$
GW190408_181802	1.54	$2.01 \times 10^{50}$	GW191105_143521	1.15	$5.08 \times 10^{49}$
GW190412	0.72	$1.36 \times 10^{49}$	GW191109_010717	1.29	$5.94 \times 10^{49}$
GW190413_052954	3.32	$3.36 \times 10^{50}$	GW191113_071753	1.37	$7.33 \times 10^{49}$
GW190413_134308	3.80	$4.28 \times 10^{50}$	GW191126_115259	1.62	$7.93 \times 10^{49}$
GW190421_213856	2.59	$2.09 \times 10^{50}$	GW191127_050227	3.4	$2.46 \times 10^{50}$
GW190426_190642	4.58	$6.47 \times 10^{50}$	GW191129_134029	0.79	-
GW190503_185404	1.52	$7.05 \times 10^{49}$	GW191204_110529	1.8	$8.37 \times 10^{49}$
GW190512_180714	1.46	$8.47 \times 10^{49}$	GW191204_171526	0.65	$4.11 \times 10^{49}$
GW190513_205428	2.21	$1.28 \times 10^{50}$	GW191215_223052	1.93	$1.16 \times 10^{50}$
GW190514_065416	3.89	$3.14 \times 10^{50}$	GW191216_213338	0.34	$3.78 \times 10^{48}$
GW190517_055101	1.79	$7.89 \times 10^{49}$	GW191222_033537	3.0	$4.06 \times 10^{50}$
GW190519_153544	2.60	$1.91 \times 10^{50}$	GW191230_180458	4.3	$5.80 \times 10^{50}$
GW190521	3.31	$3.52 \times 10^{50}$	GW200112_155838	1.25	-
GW190521_074359	1.08	$3.98 \times 10^{49}$	GW200128_022011	3.4	$2.94 \times 10^{50}$
GW190527_092055	2.52	$2.65 \times 10^{50}$	GW200129_065458	0.90	$1.28 \times 10^{49}$
GW190602_175927	2.84	$3.39 \times 10^{50}$	GW200202_154313	0.41	$4.71 \times 10^{48}$
GW190620_030421	2.91	$2.81 \times 10^{50}$	GW200208_130117	2.23	$1.49 \times 10^{50}$
GW190630_185205	0.87	$2.22 \times 10^{49}$	GW200208_222617	4.1	$4.21 \times 10^{50}$
GW190701_203306	2.09	$1.21 \times 10^{50}$	GW200209_085452	3.4	$3.21 \times 10^{50}$
GW190706_222641	3.63	$4.78 \times 10^{50}$	GW200216_220804	3.8	$5.03 \times 10^{50}$
GW190707_093326	0.85	$2.61 \times 10^{49}$	GW200219_094415	3.4	$3.88 \times 10^{50}$
GW190708_232457	0.93	$3.69 \times 10^{49}$	GW200220_061928	6.0	$1.24 \times 10^{51}$
GW190719_215514	3.73	$5.28 \times 10^{50}$	GW200220_124850	4.0	$4.16 \times 10^{50}$
GW190720_000836	0.77	$1.62 \times 10^{49}$	GW200224_222234	1.71	$8.97 \times 10^{49}$
GW190725_174728	1.03	-	GW200225_060421	1.15	$7.17 \times 10^{49}$
GW190727_060333	3.07	$3.55 \times 10^{50}$	GW200302_015811	1.48	$6.31 \times 10^{49}$
GW190728_064510	0.88	$1.75 \times 10^{49}$	GW200306_093714	2.1	$1.41 \times 10^{50}$
GW190731_140936	3.33	$3.48 \times 10^{50}$	GW200308_173609	5.4	$1.21 \times 10^{51}$
GW190803_022701	3.19	$2.81 \times 10^{50}$	GW200311_115853	1.17	-
GW190805_211137	6.13	$1.11 \times 10^{51}$	GW200316_215756	1.12	$3.72 \times 10^{49}$
GW190828_063405	2.07	$1.61 \times 10^{50}$	GW200322_091133	3.6	$4.28 \times 10^{50}$
GW190828_065509	1.54	$7.58 \times 10^{49}$			
GW190910_112807	1.52	$4.54 \times 10^{49}$			
GW190915_235702	1.75	$8.36 \times 10^{49}$			
GW190916_200658	4.94	$6.93 \times 10^{50}$			
GW190924_021846	0.55	$6.25 \times 10^{48}$			
GW190925_232845	0.93	-			
GW190926_050336	3.28	$4.81 \times 10^{50}$			
GW190929_012149	3.13	$3.71 \times 10^{50}$			
GW190930_133541	0.77	$3.26 \times 10^{49}$			

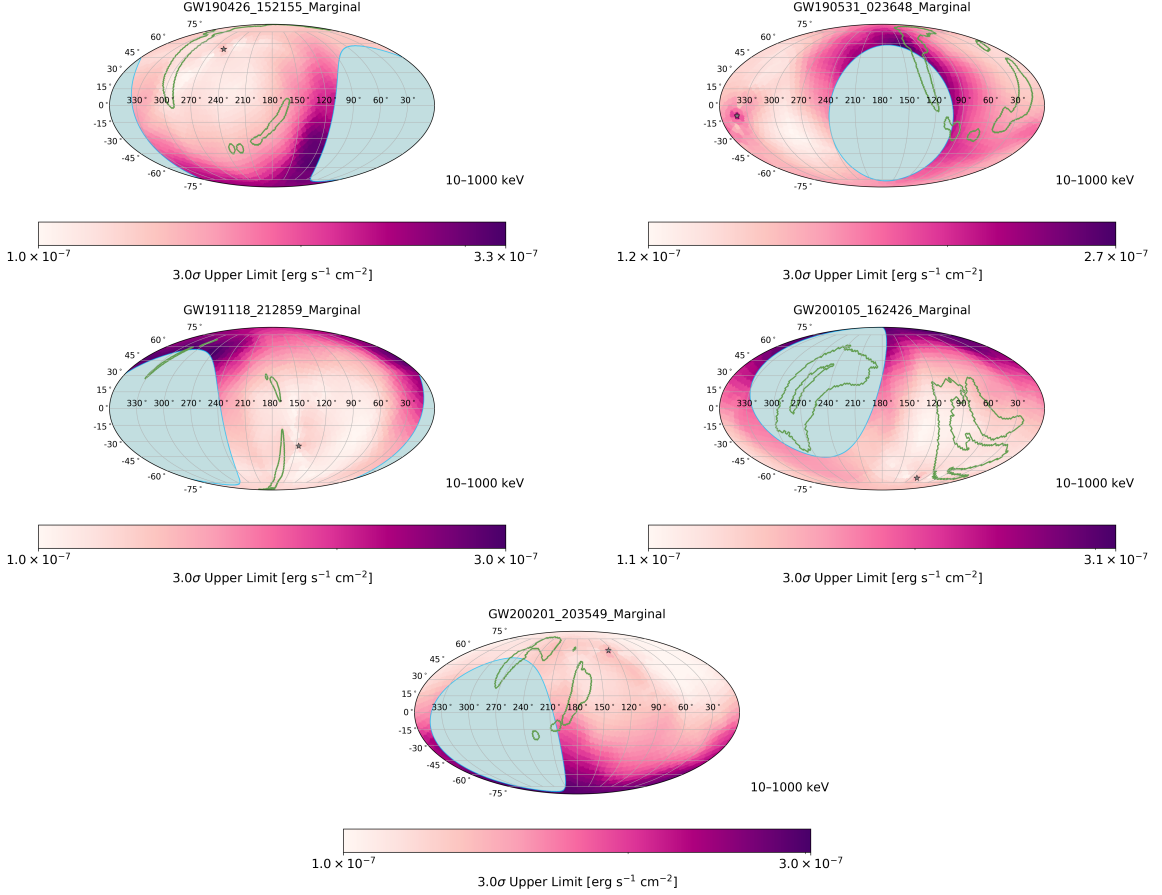


Figure C.3: The  $3\sigma$  flux upper-limit as a function of sky position for the 6 marginal events from O3. The purple gradient represents the combined *Fermi*-GBM and *Swift*-BAT flux upper limits for source positions at each point on the sky. The star symbol represents the zenith direction of *Fermi*-GBM, the square symbol represents the center of the *Swift*-BAT FoV, and the green contour represents the 90% credible area of the LVK localization. The blue region is the non-visible portion of the sky which is occulted by the Earth for *Fermi*-GBM and outside the *Swift*-BAT FoV. No map is provided for GW200311\_103121 because *Fermi*-GBM was in the SAA and, therefore, data are not available at the time of this event.

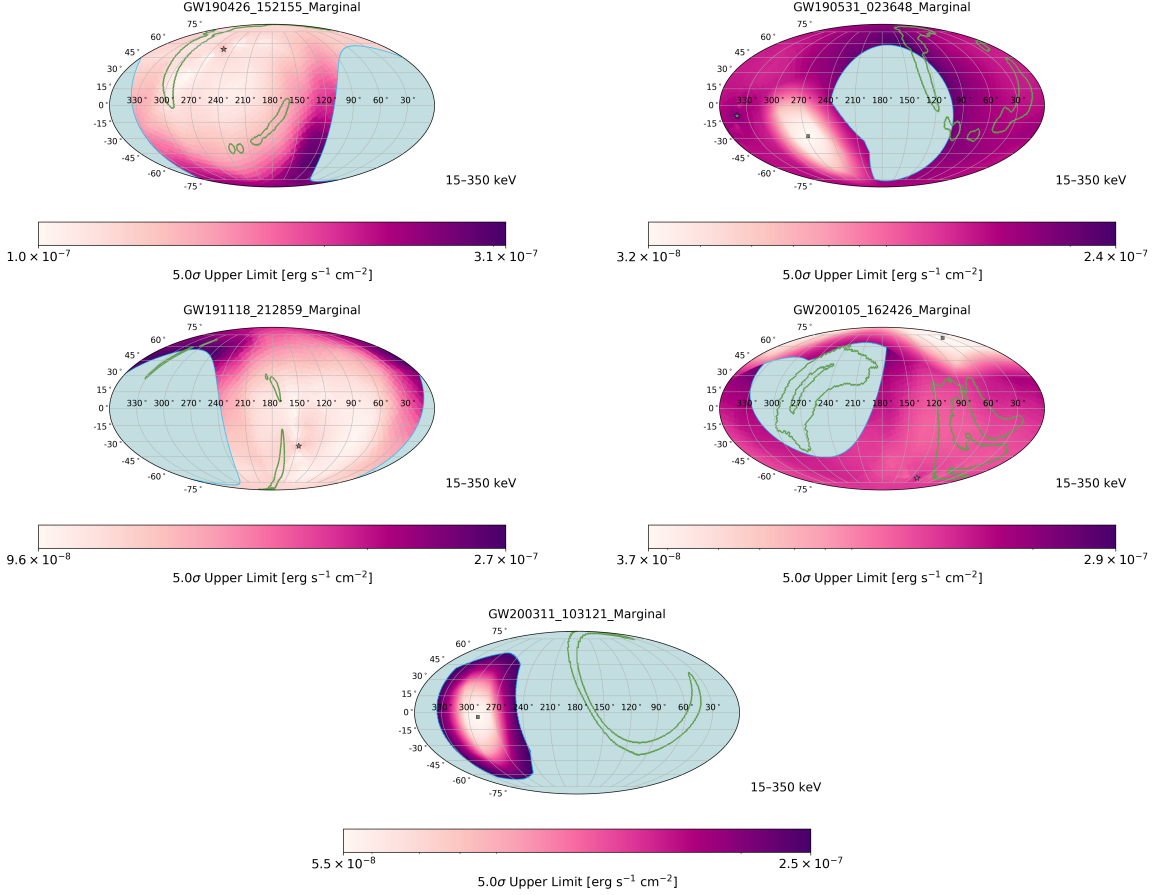


Figure C.4: The  $5\sigma$  confidence level flux upper limit skymaps for the marginal GW events from O3. The  $3\sigma$  flux upper-limit as a function of sky position for the 6 events from O3 identified with a possible neutron star component and  $p_{\text{astro}} > 0.5$ . The purple gradient represents the combined *Fermi*-GBM and *Swift*-BAT flux upper limits for source positions at each point on the sky. The star symbol represents the zenith direction of *Fermi*-GBM, the square symbol represents the center of the *Swift*-BAT FoV, and the green contour represents the 90% credible area of the LVK localization. The blue region is the non-visible portion of the sky which is occulted by the Earth for *Fermi*-GBM and outside the *Swift*-BAT FoV.

## Appendix D: Appendices for Chapter 6

### D.1 IceCube PSF and CAPS correction

We derive the IceCube PSF profile for the selected samples from the smearing matrices provided with the official data release [259], considering the response functions for year 2012–2018 configuration (IC86\_II\_effectiveArea), and selecting the Northern hemisphere only (declination bins above  $-5^\circ$ ). The response functions are weighted by the product of IceCube’s effective area and an unbroken  $E^{-2}$  power law in order to properly account for the relative contributions from high and low energy events. The resulting PSFs are fit with a univariate spline [300], resulting in a smooth description of IceCube’s pointing averaged over the assumed power law spectrum. An example of the obtained PSF is shown in Fig. D.1.

We compute the window functions from the obtained PSF profile using Eq. 6.7. The result is shown in the top plot of Fig. D.1 (blue line): as expected, the plot shows that the correction due to IceCube angular resolution is significantly more important than that for *Fermi*-LAT’s. Therefore, we emphasize the importance of deriving the correct PSF profile from IceCube data with respect to the Gaussian approximation. In the middle and bottom plots of Fig. D.1, we compare the Gaussian vs. data-driven profiles of the IceCube PSF and the derived  $W_{beam}$  respectively. At the small angular scales (large multipoles) the Gaussian profile is clearly misrepresenting the true angular smearing of the IceCube data.

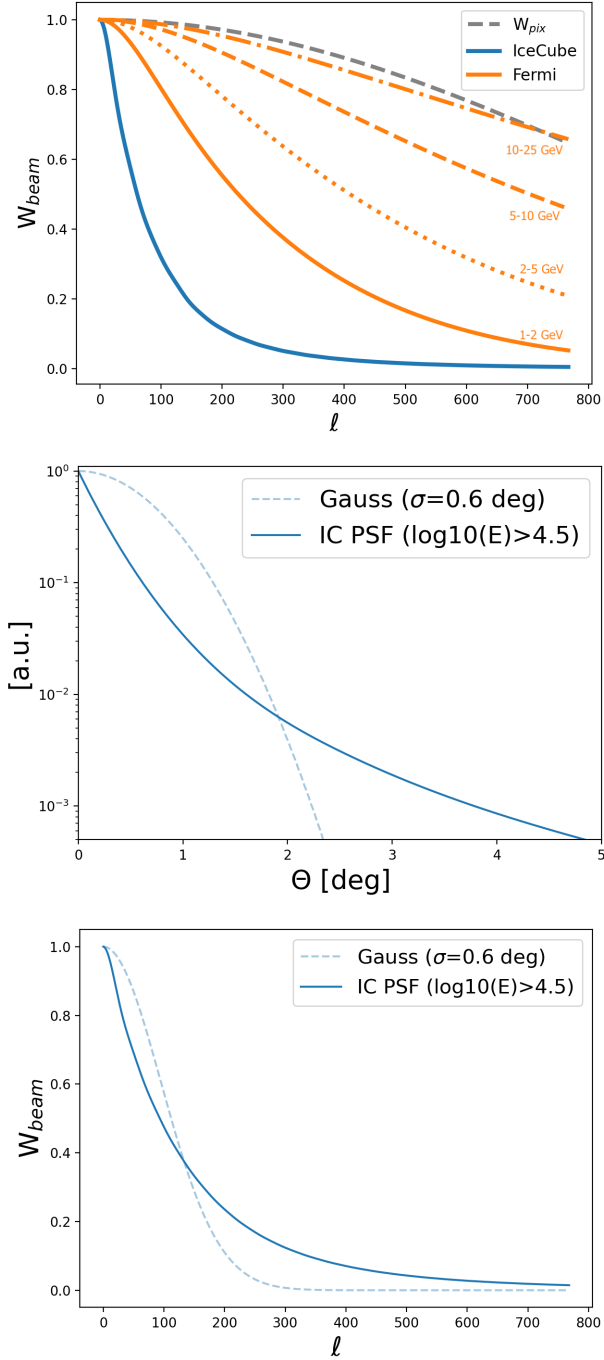


Figure D.1: Top: Window beam functions applied to the maps in order to correct for the instrumental angular resolution. In orange we show the correction functions for the four *Fermi*-LAT energy bins, while in blue is the correction for the IceCube map. In gray we show the pixel window function used to account for the finite pixeling of the maps. Middle: Comparison between the PSF profile from the public data release [259] and a Gaussian profile with  $\sigma = 0.6$  deg. Bottom: Comparison between the beam window functions derived from the PSF and Gaussian profiles shown in the middle panel.

## D.2 Additional plots

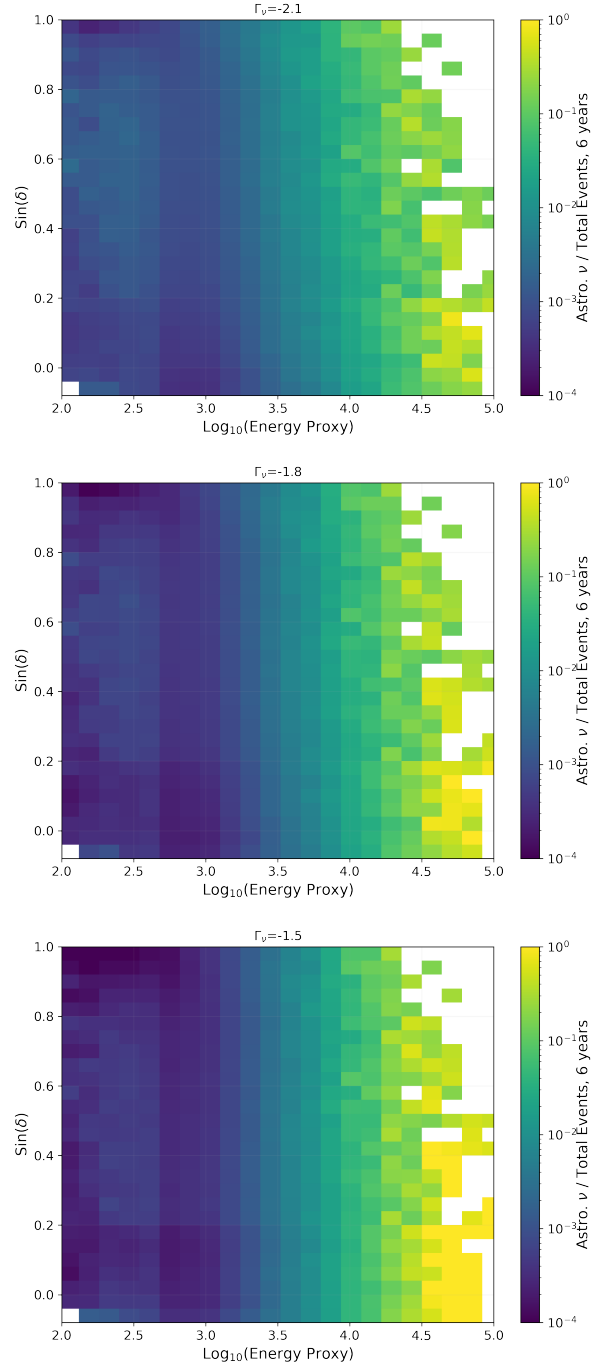


Figure D.2: Variation of IceCube sensitivity in the Northern hemisphere assuming different spectral indices of the power-law spectrum for the astrophysical signal (the normalization is kept the same as in [285]). The plots are generated using the same method described in Section 6.2.3. Energy Proxy is in units of GeV.

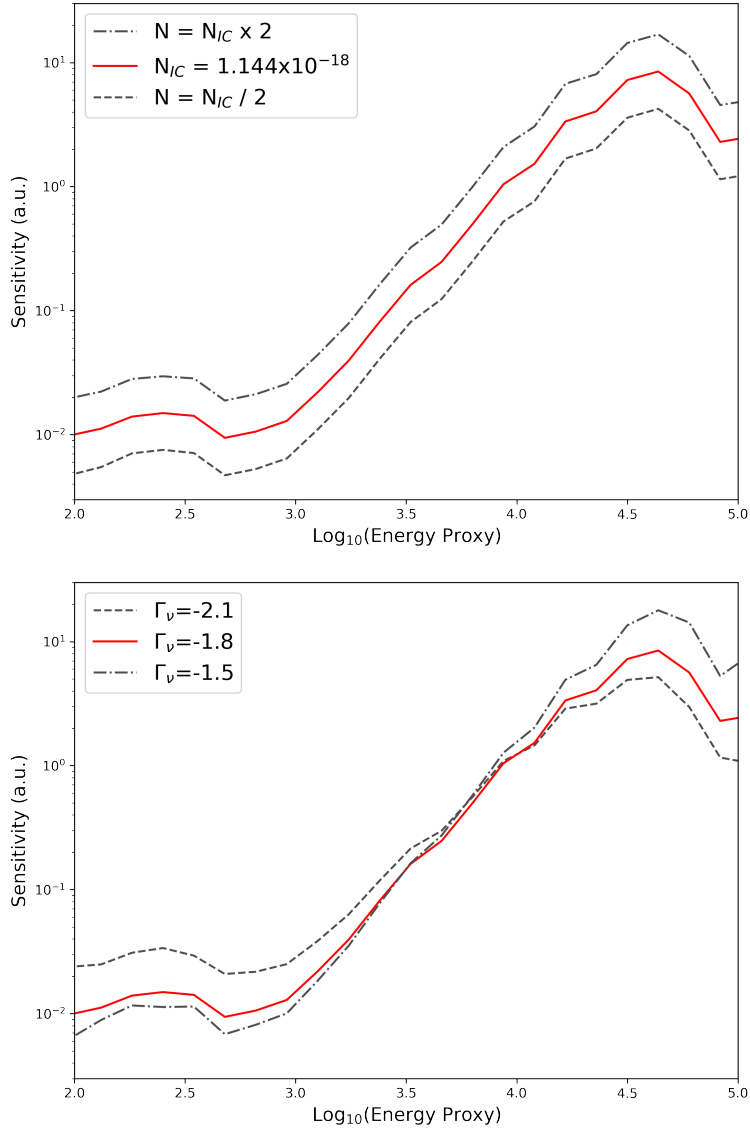


Figure D.3: Variation of IceCube sensitivity as a function of the energy for the Northern hemisphere. In general, a change in the spectrum normalization (as investigated in this work), translates in a rigid proportional shift of the sensitivity up or down. On the other hand, if the normalization is fixed to the measured value [285] at 1 TeV, harder (steeper) spectra slightly enhance the sensitivity at higher (lower) energies, while reducing it at lower (higher) energies. When considering the average sensitivity between 100 GeV and 100 TeV, the softer spectrum with  $\Gamma = -2.1$  decreases the sensitivity by  $\sim 1\%$  compared to the case with  $\Gamma = -1.8\%$ ; on the other hand, the presence of an additional component with a harder spectrum ( $\Gamma = -1.5$ ) would improve the sensitivity by  $\sim 30\%$ . Energy Proxy is in units of GeV.

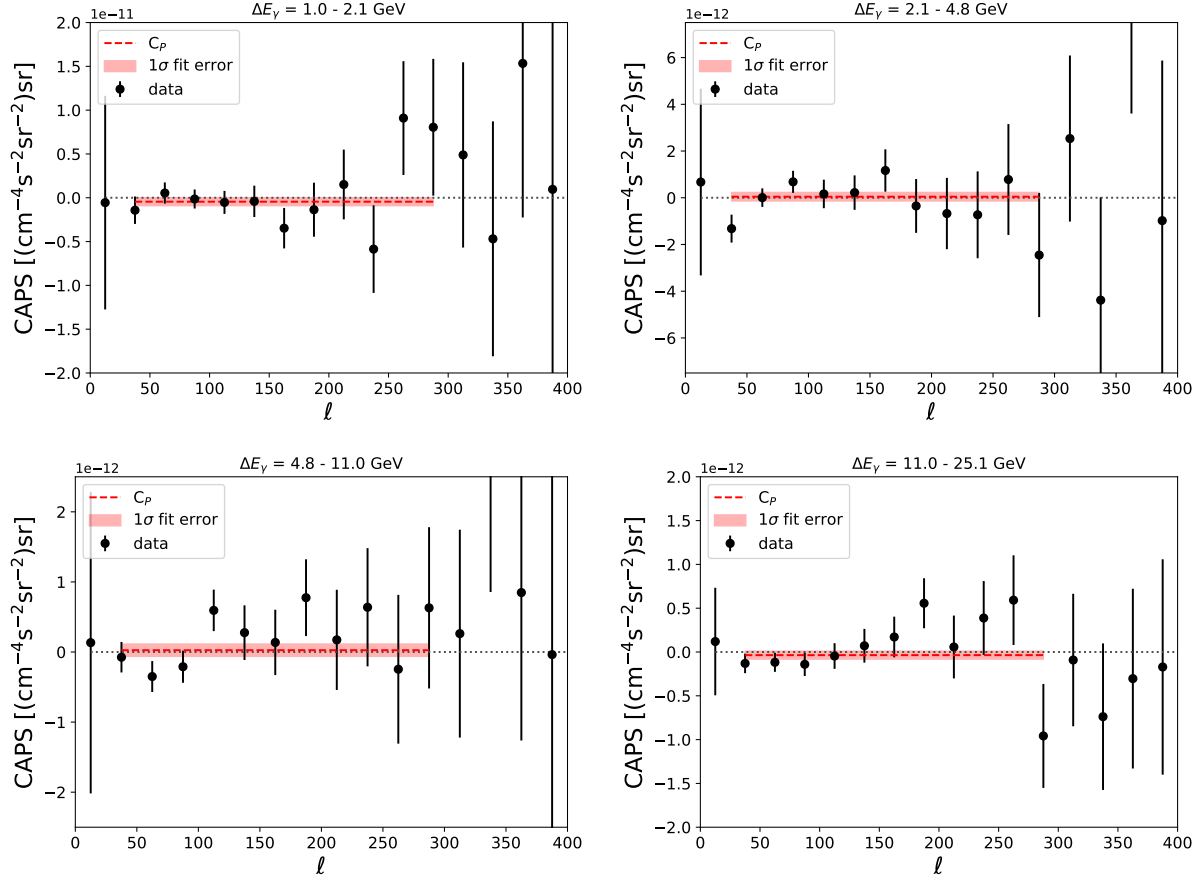


Figure D.4: CAPS for the real *Fermi*-LAT and IceCube maps.

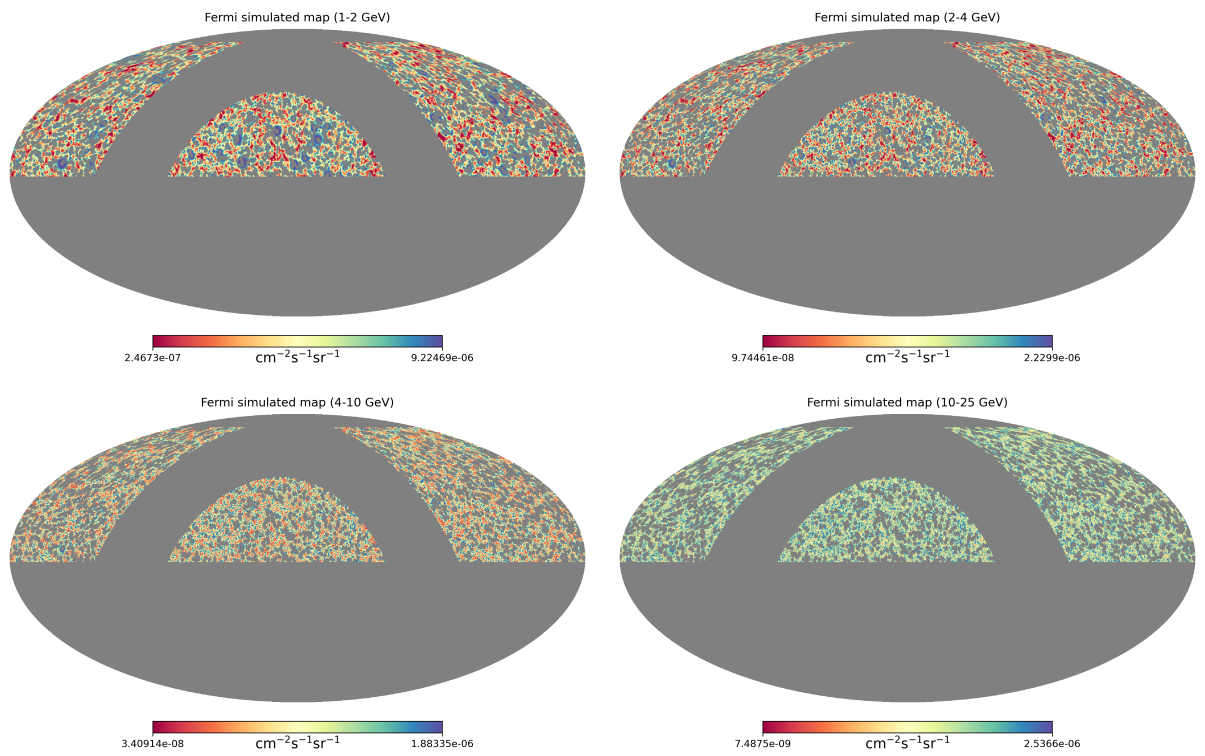


Figure D.5: Simulated *Fermi*-LAT UGRB maps for the four energy bins considered. The colorbar is in unit of flux  $\text{cm}^{-2}\text{s}^{-1}\text{sr}^{-1}$ .

## Appendix E: Facilities and Software used in this Dissertation

### E.1 Facilities

1. *Fermi* Gamma-ray Space Observatory
2. IceCube Neutrino Observatory
3. LIGO/Virgo/KAGRA
4. Neil Gehrels *Swift* Observatory (Burst Alert Telescope)

### E.2 Software

1. Anaconda [301]
2. astropy [302]
3. Atom [303]
4. AxionLimits [304]
5. gammaALPs [305]
6. gmf [306]
7. Grammarly [307]
8. HEALPix [308]
9. healpy [309]
10. fermipy [310]
11. *Fermi* Science Tools [311]

12. jupyter [312]
13. matplotlib [313]
14. NITRATES [226]
15. NumPy [314]
16. pandas [315]
17. PolSpice [316]
18. Procreate [317]
19. PyXSPEC [318]
20. SciPy [319]
21. TexStudio [320]
22. threeML [321]
23. XSPEC [146]
24. Zotero [322]

## Bibliography

- [1] M. Crnogorčević, R. Caputo, M. Meyer, N. Omodei, and M. Gustafsson. Searching for axionlike particles from core-collapse supernovae with Fermi LAT’s low-energy technique. *Phys. Rev. D*, 104(10):103001, 2021.
- [2] Michela Negro, Milena Crnogorčević, Eric Burns, Eric Charles, Lea Marcotulli, and Regina Caputo. A Cross-correlation Study between IceCube Neutrino Events and the FERMI Unresolved Gamma-Ray Sky. *Astrophysical Journal*, 951(1):83, July 2023.
- [3] Hrishikesh Joglekar, Mayank N. Vahia, and Aniket Sule. Oldest sky-chart with supernova record. 2011.
- [4] Victor Hess. On the Observations of the Penetrating Radiation during Seven Balloon Flights. 7 2018.
- [5] W. L. Kraushaar and G. W. Clark. Search for Primary Cosmic Gamma Rays with the Satellite Explorer XI. *Physical Review Letters*, 8(3):106–109, February 1962.
- [6] W. L. Kraushaar, G. W. Clark, G. P. Garmire, R. Borken, P. Higbie, V. Leong, and T. Thorsos. High-Energy Cosmic Gamma-Ray Observations from the OSO-3 Satellite. *Astrophysical Journal*, 177:341, November 1972.
- [7] S. Abdollahi, F. Acero, L. Baldini, J. Ballet, D. Bastieri, R. Bellazzini, B. Berenji, A. Berretta, E. Bissaldi, R. D. Blandford, E. Bloom, R. Bonino, A. Brill, R. J. Britto, P. Bruel, T. H. Burnett, S. Buson, R. A. Cameron, R. Caputo, P. A. Caraveo, D. Castro, S. Chaty, C. C. Cheung, G. Chiaro, N. Cibrario, S. Ciprini, J. Coronado-Blázquez, M. Crnogorcevic, S. Cutini, F. D’Ammando, S. De Gaetano, S. W. Digel, N. Di Lalla, F. Dirirsa, L. Di Venere, A. Domínguez, V. Fallah Ramazani, S. J. Fegan, E. C. Ferrara, A. Fiori, H. Fleischhack, A. Franckowiak, Y. Fukazawa, S. Funk, P. Fusco, G. Galanti, V. Gammaldi, F. Gargano, S. Garrappa, D. Gasparrini, F. Giacchino, N. Giglietto, F. Giordano, M. Giroletti, T. Glanzman, D. Green, I. A. Grenier, M. H. Grondin, L. Guillemot, S. Guiriec, M. Gustafsson, A. K. Harding, E. Hays, J. W. Hewitt, D. Horan, X. Hou, G. Jóhannesson, C. Karwin, T. Kayanoki, M. Kerr, M. Kuss, D. Landriu, S. Larsson, L. Latronico, M. Lemoine-Goumard, J. Li, I. Liodakis, F. Longo, F. Loparco, B. Lott, P. Lubrano, S. Maldera, D. Malyshev, A. Manfreda, G. Martí-Devesa, M. N. Mazziotta, I. Mereu, M. Meyer, P. F. Michelson, N. Mirabal, W. Mitthumsiri, T. Mizuno, A. A. Moiseev, M. E. Monzani, A. Morselli, I. V. Moskalenko, M. Negro, E. Nuss, N. Omodei, M. Orienti, E. Orlando, D. Paneque, Z. Pei, J. S. Perkins, M. Persic, M. Pesce-Rollins, V. Petrosian, R. Pillera, H. Poon, T. A. Porter, G. Principe, S. Rainò, R. Rando, B. Rani,

- M. Razzano, S. Razzaque, A. Reimer, O. Reimer, T. Reposeur, M. Sánchez-Conde, P. M. Saz Parkinson, L. Scotton, D. Serini, C. Sgrò, E. J. Siskind, D. A. Smith, G. Spandre, P. Spinelli, K. Sueoka, D. J. Suson, H. Tajima, D. Tak, J. B. Thayer, D. J. Thompson, D. F. Torres, E. Troja, J. Valverde, K. Wood, and G. Zaharijas. Incremental Fermi Large Area Telescope Fourth Source Catalog. *Astrophysical Journal Supplement*, 260(2):53, June 2022.
- [8] S. Bowyer, E. T. Byram, T. A. Chubb, and H. Friedman. Lunar occultation of x-ray emission from the crab nebula. *Science*, 146(3646):912–917, 1964.
  - [9] R. C. Haymes, D. V. Ellis, G. J. Fishman, J. D. Kurfess, and W. H. Tucker. Observation of Gamma Radiation from the Crab Nebula. *Astrophysical Journal Letters*, 151:L9, January 1968.
  - [10] T. H. Markert, C. R. Canizares, G. W. Clark, F. K. Li, P. L. Northridge, G. F. Sprott, and G. F. Wargo. OSO-7 observations of high galactic latitude X-ray sources. *Astrophysical Journal*, 206:265–272, May 1976.
  - [11] Ray W. Klebesadel, Ian B. Strong, and Roy A. Olson. Observations of Gamma-Ray Bursts of Cosmic Origin. *Astrophysical Journal Letters*, 182:L85, June 1973.
  - [12] K. S. Hirata et al. Observation in the Kamiokande-II Detector of the Neutrino Burst from Supernova SN 1987a. *Phys. Rev. D*, 38:448–458, 1988.
  - [13] R. M. Bionta et al. Observation of a Neutrino Burst in Coincidence with Supernova SN 1987a in the Large Magellanic Cloud. *Phys. Rev. Lett.*, 58:1494, 1987.
  - [14] E. N. Alexeyev, L. N. Alexeyeva, I. V. Krivosheina, and V. I. Volchenko. Detection of the neutrino signal from SN 1987A in the LMC using the INR Baksan underground scintillation telescope. *Physics Letters B*, 205(2-3):209–214, April 1988.
  - [15] M. Planck. Ueber das gesetz der energieverteilung im normalspectrum. *Annalen der Physik*, 309(3):553–563, 1901.
  - [16] A. Einstein. Über einen die erzeugung und verwandlung des lichtes betreffenden heuristischen gesichtspunkt. *Annalen der Physik*, 17(6):132–148, 1905.
  - [17] N. Bohr. On the constitution of atoms and molecules. *Philosophical Magazine*, 26(151):1–25, 1913.
  - [18] H. Yukawa. On the interaction of elementary particles. i. *Proceedings of the Physico-Mathematical Society of Japan*, 17:48–57, 1935.
  - [19] E. Fermi. Versuch einer theorie der  $\beta$ -strahlen. *Zeitschrift für Physik*, 88(3-4):161–177, 1934.
  - [20] Sheldon Glashow. Partial-symmetries of weak interactions. *Nuclear Physics*, 22:579–588, 1961.

- [21] Steven Weinberg. A model of leptons. *Physical Review Letters*, 19:1264–1266, 1967.
- [22] A. Salam. Weak and electromagnetic interactions. In N. Svartholm, editor, *Elementary particle theory: Proceedings of the Nobel Symposium held at Björkborn, Sweden, 1968*, page 367, 1968.
- [23] Gerard 't Hooft. Renormalizable lagrangians for massive yang-mills fields. *Nuclear Physics B*, 35:167–188, 1971.
- [24] Howard Georgi and Sheldon L. Glashow. Unity of all elementary particle forces. *Physical Review Letters*, 32:438–441, 1974.
- [25] G. Aad et al. Measurement of the w boson mass with the atlas detector. *Physical Review Letters*, 110(2):021803, 2013.
- [26] B. Abi et al. Measurement of the positive muon anomalous magnetic moment to 0.46 ppm. *Physical Review Letters*, 126(14):141801, 2021.
- [27] M. Kobayashi and T. Maskawa. Cp violation in the renormalizable theory of weak interaction. *Physical Review Letters*, 31(10):1285–1287, 1973.
- [28] C. L. Bennett and et al. Cobe-dmr: A measurement of the cmb power spectrum at angular scales of 10 arcminutes to 5 degrees. *The Astrophysical Journal*, 464:L1–L4, 1996.
- [29] E. Komatsu and et al. Wmap: Seven-year wilkinson microwave anisotropy probe (wmap) observations: cosmological interpretation. *The Astrophysical Journal Supplement Series*, 192:18, 2011.
- [30] P. A. R. Ade and et al. Planck 2015 results. xiii. cosmological parameters. *Astronomy & Astrophysics*, 594:A13, 2016.
- [31] B. P. Abbott, R. Abbott, T. D. Abbott, F. Acernese, K. Ackley, C. Adams, T. Adams, P. Addesso, R. X. Adhikari, V. B. Adya, C. Affeldt, M. Afrough, B. Agarwal, M. Agathos, K. Agatsuma, N. Aggarwal, O. D. Aguiar, L. Aiello, A. Ain, P. Ajith, B. Allen, G. Allen, A. Allocca, P. A. Altin, A. Amato, A. Ananyeva, S. B. Anderson, W. G. Anderson, S. V. Angelova, S. Antier, S. Appert, K. Arai, M. C. Araya, J. S. Areeda, N. Arnaud, K. G. Arun, S. Ascenzi, G. Ashton, M. Ast, S. M. Aston, P. Astone, D. V. Atallah, P. Aufmuth, C. Aulbert, K. AultONeal, C. Austin, A. Avila-Alvarez, S. Babak, and P. and Bacon. Gw170817: Observation of gravitational waves from a binary neutron star inspiral. *PhRvL*, 119:161101, Oct 2017.
- [32] Raffaella Margutti and Ryan Chornock. First multimessenger observations of a neutron star merger. *ARA&A*, 59(1):155–202, 2021.
- [33] IceCube Collaboration. Neutrino emission from the direction of the blazar TXS 0506+056 prior to the IceCube-170922A alert. *Science*, 361(6398):147–151, 2018.
- [34] Engineering National Academies of Sciences and Medicine. *Astro2020: Decadal Survey on Astronomy and Astrophysics*. National Academies Press, 2021.

- [35] M. Ackermann et al. Dark Matter Constraints from Observations of 25 Milky Way Satellite Galaxies with the Fermi Large Area Telescope. *Phys. Rev. D*, 89:042001, 2014.
- [36] M. Ackermann et al. Searching for Dark Matter Annihilation from Milky Way Dwarf Spheroidal Galaxies with Six Years of Fermi Large Area Telescope Data. *Phys. Rev. Lett.*, 115(23):231301, 2015.
- [37] Manuel Meyer and Tanja Petrushevska. Search for Axionlike-Particle-Induced Prompt  $\gamma$ -Ray Emission from Extragalactic Core-Collapse Supernovae with the *Fermi* Large Area Telescope. *Phys. Rev. Lett.*, 124(23):231101, 2020. [Erratum: Phys.Rev.Lett. 125, 119901 (2020)].
- [38] C. Meegan et al. The Fermi Gamma-Ray Burst Monitor. *The Astrophysical Journal*, 702(1):791–804, Aug 2009.
- [39] W. B. Atwood, A. A. Abdo, M. Ackermann, W. Althouse, B. Anderson, M. Axelsson, L. Baldini, J. Ballet, D. L. Band, G. Barbiellini, and et al. The Large Area Telescope on the Fermi Gamma-Ray Space Telescope Mission. *The Astrophysical Journal*, 697:1071–1102, June 2009.
- [40] David J. Thompson and Kent Wood. Exploring the extreme universe with the fermi gamma-ray space telescope. *Physics Today*, 63(4):34, 2010.
- [41] David N. Burrows, J. E. Hill, J. A. Nousek, J. A. Kennea, A. Wells, J. P. Osborne, A. F. Abbey, A. Beardmore, K. Mukerjee, A. D. T. Short, G. Chincarini, S. Campana, O. Citterio, A. Moretti, C. Pagani, G. Tagliaferri, P. Giommi, M. Capalbi, F. Tamburelli, L. Angelini, G. Cusumano, H. W. Bräuninger, W. Burkert, and G. D. Hartner. The Swift X-Ray Telescope. *Space Science Reviews*, 120(3-4):165–195, October 2005.
- [42] Peter W. A. Roming, Thomas E. Kennedy, Keith O. Mason, John A. Nousek, Lindy Ahr, Richard E. Bingham, Patrick S. Broos, Mary J. Carter, Barry K. Hancock, Howard E. Huckle, S. D. Hunsberger, Hajime Kawakami, Ronnie Killough, T. Scott Koch, Michael K. McLellan, Kelly Smith, Philip J. Smith, Juan Carlos Soto, Patricia T. Boyd, Alice A. Breeveld, Stephen T. Holland, Mariya Ivanushkina, Michael S. Pryzby, Martin D. Still, and Joseph Stock. The Swift Ultra-Violet/Optical Telescope. *Space Science Reviews*, 120(3-4):95–142, October 2005.
- [43] Scott D. Barthelmy, Louis M. Barbier, Jay R. Cummings, Ed E. Fenimore, Neil Gehrels, Derek Hullinger, Hans A. Krimm, Craig B. Markwardt, David M. Palmer, Ann Parsons, Goro Sato, Masaya Suzuki, Tadayuki Takahashi, Makota Tashiro, and Jack Tueller. The Burst Alert Telescope (BAT) on the SWIFT Midex Mission. *Space Science Reviews*, 120(3-4):143–164, October 2005.
- [44] B. P. Abbott et al. Ligo: The laser interferometer gravitational-wave observatory. *Reports on Progress in Physics*, 72(7):076901, 2009.
- [45] The Virgo Collaboration. Advanced virgo: a second-generation interferometric gravitational wave detector. *Classical and Quantum Gravity*, 32(2):024001, 2015.

- [46] T. Akutsu et al. KAGRA: 2.5 Generation Interferometric Gravitational Wave Detector. *Nature Astron.*, 3(1):35–40, 2019.
- [47] B. P. Abbott et al. Prospects for observing and localizing gravitational-wave transients with Advanced LIGO, Advanced Virgo and KAGRA. *Living Rev. Rel.*, 21(1):3, 2018.
- [48] J. Aasi et al. Advanced LIGO. *Class. Quant. Grav.*, 32:074001, 2015.
- [49] R. Abbott, T. D. Abbott, F. Acernese, K. Ackley, C. Adams, N. Adhikari, R. X. Adhikari, V. B. Adya, C. Affeldt, D. Agarwal, M. Agathos, K. Agatsuma, N. Aggarwal, O. D. Aguiar, L. Aiello, A. Ain, P. Ajith, S. Akcay, T. Akutsu, S. Albanesi, A. Allocca, P. A. Altin, A. Amato, C. Anand, S. Anand, A. Ananyeva, S. B. Anderson, W. G. Anderson, M. Ando, T. Andrade, N. Andres, T. Andrić, S. V. Angelova, S. Ansoldi, J. M. Antelis, S. Antier, S. Appert, Koji Arai, Koya Arai, Y. Arai, S. Araki, A. Araya, M. C. Araya, J. S. Areeda, M. Arène, N. Aritomi, N. Arnaud, M. Arogeti, S. M. Aronson, K. G. Arun, H. Asada, Y. Asali, G. Ashton, Y. Aso, M. Assiduo, S. M. Aston, P. Astone, F. Aubin, C. Austin, S. Babak, F. Badaracco, M. K. M. Bader, C. Badger, S. Bae, Y. Bae, A. M. Baer, S. Bagnasco, Y. Bai, L. Baiotti, J. Baird, R. Bajpai, M. Ball, G. Ballardin, S. W. Ballmer, A. Balsamo, G. Baltus, S. Banagiri, D. Bankar, J. C. Barayoga, C. Barbieri, B. C. Barish, D. Barker, P. Barneo, F. Barone, B. Barr, L. Barsotti, M. Barsuglia, D. Barta, J. Bartlett, M. A. Barton, I. Bartos, R. Bassiri, A. Basti, M. Bawaj, J. C. Bayley, A. C. Baylor, M. Bazzan, B. Bécsy, V. M. Bedakihale, M. Bejger, I. Belahcene, V. Benedetto, D. Beniwal, T. F. Bennett, J. D. Bentley, M. BenYaala, F. Bergamin, B. K. Berger, S. Bernuzzi, C. P. L. Berry, D. Bersanetti, A. Bertolini, J. Betzwieser, D. Beveridge, R. Bhandare, U. Bhardwaj, D. Bhattacharjee, S. Bhaumik, I. A. Bilenko, G. Billingsley, S. Bini, R. Birney, O. Birnholtz, S. Biscans, M. Bischi, S. Biscoveanu, A. Bisht, B. Biswas, M. Bitossi, M. A. Bi-zouard, J. K. Blackburn, C. D. Blair, D. G. Blair, R. M. Blair, F. Bobba, N. Bode, M. Boer, G. Bogaert, M. Boldrini, L. D. Bonavena, F. Bondu, E. Bonilla, R. Bonnand, P. Booker, B. A. Boom, R. Bork, V. Boschi, N. Bose, S. Bose, V. Bossilkov, V. Boudart, Y. Bouffanais, A. Bozzi, C. Bradaschia, P. R. Brady, A. Bramley, A. Branch, M. Branchesi, J. Brandt, J. E. Brau, M. Breschi, T. Briant, J. H. Briggs, A. Brillet, M. Brinkmann, P. Brockill, A. F. Brooks, J. Brooks, D. D. Brown, S. Brunett, G. Bruno, R. Bruntz, J. Bryant, T. Bulik, H. J. Bulten, A. Buonanno, R. Buscicchio, D. Buskulic, C. Buy, R. L. Byer, G. S. Cabourn Davies, L. Cadonati, G. Cagnoli, C. Cahillane, J. Calderón Bustillo, J. D. Callaghan, T. A. Callister, E. Calloni, J. Cameron, J. B. Camp, M. Canepa, S. Canevarolo, M. Cannavaciulo, K. C. Cannon, H. Cao, Z. Cao, E. Capocasa, E. Capote, G. Carapella, F. Carbognani, J. B. Carlin, M. F. Carney, M. Carpinelli, G. Carrillo, G. Carullo, T. L. Carver, J. Casanueva Diaz, C. Casentini, G. Castaldi, S. Caudill, M. Cavaglià, F. Cavalier, R. Cavalieri, M. Ceasar, G. Celli, P. Cerdá-Durán, E. Cesarini, W. Chaibi, K. Chakravarti, S. Chalathadka Subrahmanya, E. Champion, C. H. Chan, C. Chan, C. L. Chan, K. Chan, M. Chan, K. Chandra, P. Chanal, S. Chao, C. E. A. Chapman-Bird, P. Charlton, E. A. Chase, E. Chassande-Mottin, C. Chatterjee, Debarati Chatterjee, Deep Chatterjee, M. Chaturvedi, S. Chaty, K. Chatziliaoannou, C. Chen, H. Y. Chen, J. Chen, K. Chen, X. Chen, Y. B. Chen, Y. R. Chen, Z. Chen, H. Cheng, C. K. Cheong, H. Y. Cheung, H. Y. Chia, F. Chiadini, C-Y. Chiang, G. Chiarini, R. Chierici, A. Chincarini, M. L. Chiofalo, A. Chiummo, G. Cho, H. S. Cho, R. K. Choudhary, S. Choudhary, N. Christensen, H. Chu, Q. Chu, Y-K. Chu,

S. Chua, K. W. Chung, G. Ciani, P. Ciecielag, M. Cieślar, M. Cifaldi, A. A. Ciobanu, R. Ciolfi, F. Cipriano, A. Cirone, F. Clara, E. N. Clark, J. A. Clark, L. Clarke, P. Clearwater, S. Clesse, F. Cleva, E. Coccia, E. Codazzo, P. F. Cohadon, D. E. Cohen, L. Cohen, M. Colleoni, C. G. Collette, A. Colombo, M. Colpi, C. M. Compton, Jr. Constancio, M., L. Conti, S. J. Cooper, P. Corban, T. R. Corbitt, I. Cordero-Carrión, S. Corezzi, K. R. Corley, N. Cornish, D. Corre, A. Corsi, S. Cortese, C. A. Costa, R. Cotesta, M. W. Coughlin, J. P. Coulon, S. T. Countryman, B. Cousins, P. Couvares, D. M. Coward, M. J. Cowart, D. C. Coyne, R. Coyne, J. D. E. Creighton, T. D. Creighton, A. W. Criswell, M. Croquette, S. G. Crowder, J. R. Cudell, T. J. Cullen, A. Cumming, R. Cummings, L. Cunningham, E. Cuoco, M. Curyło, P. Dabadie, T. Dal Canton, S. Dall’Osso, G. Dálya, A. Dana, L. M. DaneshgaranBajastani, B. D’Angelo, B. Danila, S. Danilishin, S. D’Antonio, K. Danzmann, C. Darsow-Fromm, A. Dasgupta, L. E. H. Datrier, S. Datta, V. Dattilo, I. Dave, M. Davier, D. Davis, M. C. Davis, E. J. Daw, P. F. de Alarcón, R. Dean, D. DeBra, M. Deenadayalan, J. Degallaix, M. De Laurentis, S. Deléglise, V. Del Favero, F. De Lillo, N. De Lillo, W. Del Pozzo, L. M. DeMarchi, F. De Matteis, V. D’Emilio, N. Demos, T. Dent, A. Depasse, R. De Pietri, R. De Rosa, C. De Rossi, R. DeSalvo, R. De Simone, S. Dhurandhar, M. C. Díaz, Jr. Diaz-Ortiz, M., N. A. Didio, T. Dietrich, L. Di Fiore, C. Di Fronzo, C. Di Giorgio, F. Di Giovanni, M. Di Giovanni, T. Di Girolamo, A. Di Lieto, B. Ding, S. Di Pace, I. Di Palma, F. Di Renzo, A. K. Divakarla, A. Dmitriev, Z. Doctor, L. D’Onofrio, F. Donovan, K. L. Dooley, S. Doravari, I. Dorrington, M. Drago, J. C. Driggers, Y. Drori, J. G. Ducoin, P. Dupej, O. Durante, D. D’Urso, P. A. Duverne, S. E. Dwyer, C. Eassa, P. J. Easter, M. Ebersold, T. Eckhardt, G. Eddolls, B. Edelman, T. B. Edo, O. Edy, A. Effler, S. Eguchi, J. Eichholz, S. S. Eikenberry, M. Eisenmann, R. A. Eisenstein, A. Ejlli, E. Engelby, Y. Enomoto, L. Errico, R. C. Essick, H. Estellés, D. Estevez, Z. Etienne, T. Etzel, M. Evans, T. M. Evans, B. E. Ewing, V. Fafone, H. Fair, S. Fairhurst, A. M. Farah, S. Farinon, B. Farr, W. M. Farr, N. W. Farrow, E. J. Fauchon-Jones, G. Favaro, M. Favata, M. Fays, M. Fazio, J. Feicht, M. M. Fejer, E. Fenyvesi, D. L. Ferguson, A. Fernandez-Galiana, I. Ferrante, T. A. Ferreira, F. Fidecaro, P. Figura, I. Fiori, M. Fishbach, R. P. Fisher, R. Fittipaldi, V. Fiumara, R. Flaminio, E. Floden, H. Fong, J. A. Font, B. Fornal, P. W. F. Forsyth, A. Franke, S. Frasca, F. Frasconi, C. Frederick, J. P. Freed, Z. Frei, A. Freise, R. Frey, P. Fritschel, V. V. Frolov, G. G. Fronzé, Y. Fujii, Y. Fujikawa, M. Fukunaga, M. Fukushima, P. Fulda, M. Fyffe, H. A. Gabbard, W. E. Gabella, B. U. Gadre, J. R. Gair, J. Gais, S. Galauadage, R. Gamba, D. Ganapathy, A. Ganguly, D. Gao, S. G. Gaonkar, B. Garaventa, F. García, C. García-Núñez, C. García-Quirós, F. Garufi, B. Gateley, S. Gaudio, V. Gayathri, G. G. Ge, G. Gemme, A. Gennai, J. George, R. N. George, O. Gerberding, L. Gergely, P. Gewecke, S. Ghonge, Abhirup Ghosh, Archisman Ghosh, Shaon Ghosh, Shrobana Ghosh, B. Giacomazzo, L. Giacoppo, J. A. Giaime, K. D. Giardina, D. R. Gibson, C. Gier, M. Giesler, P. Giri, F. Gissi, J. Glanzer, A. E. Gleckl, P. Godwin, E. Goetz, R. Goetz, N. Gohlke, J. Golomb, B. Goncharov, G. González, A. Gopakumar, M. Gosselin, R. Gouaty, D. W. Gould, B. Grace, A. Grado, M. Granata, V. Granata, A. Grant, S. Gras, P. Grassia, C. Gray, R. Gray, G. Greco, A. C. Green, R. Green, A. M. Gretarsson, E. M. Gretarsson, D. Griffith, W. Griffiths, H. L. Griggs, G. Grignani, A. Grimaldi, S. J. Grimm, H. Grote, S. Grunewald, P. Gruning, D. Guerra, G. M. Guidi, A. R. Guimaraes, G. Guixé, H. K. Gulati, H. K. Guo, Y. Guo, Anchal Gupta, Anuradha Gupta, P. Gupta, E. K. Gustafson, R. Gustafson, F. Guzman, S. Ha,

L. Haegel, A. Hagiwara, S. Haino, O. Halim, E. D. Hall, E. Z. Hamilton, G. Hammond, W. B. Han, M. Haney, J. Hanks, C. Hanna, M. D. Hannam, O. Hannuksela, H. Hansen, T. J. Hansen, J. Hanson, T. Harder, T. Hardwick, K. Haris, J. Harms, G. M. Harry, I. W. Harry, D. Hartwig, K. Hasegawa, B. Haskell, R. K. Hasskew, C. J. Haster, K. Hattori, K. Haughian, H. Hayakawa, K. Hayama, F. J. Hayes, J. Healy, A. Heidmann, A. Heidt, M. C. Heintze, J. Heinze, J. Heinzel, H. Heitmann, F. Hellman, P. Hello, A. F. Helmling-Cornell, G. Hemming, M. Hendry, I. S. Heng, E. Hennes, J. Hennig, M. H. Hennig, A. G. Hernandez, F. Hernandez Vivanco, M. Heurs, S. Hild, P. Hill, Y. Himemoto, A. S. Hines, Y. Hiranuma, N. Hirata, E. Hirose, S. Hochheim, D. Hofman, J. N. Hohmann, D. G. Holcomb, N. A. Holland, K. Holley-Bockelmann, I. J. Hollows, Z. J. Holmes, K. Holt, D. E. Holz, Z. Hong, P. Hopkins, J. Hough, S. Hourihane, E. J. Howell, C. G. Hoy, D. Hoyland, A. Hreibi, B-H. Hsieh, Y. Hsu, G-Z. Huang, H-Y. Huang, P. Huang, Y-C. Huang, Y. J. Huang, Y. Huang, M. T. Hübner, A. D. Huddart, B. Hughey, D. C. Y. Hui, V. Hui, S. Husa, S. H. Huttner, R. Huxford, T. Huynh-Dinh, S. Ide, B. Idzkowski, A. Iess, B. Ikenoue, S. Imam, K. Inayoshi, C. Ingram, Y. Inoue, K. Ioka, M. Isi, K. Isleif, K. Ito, Y. Itoh, B. R. Iyer, K. Izumi, V. JaberianHamedan, T. Jacqmin, S. J. Jadhav, S. P. Jadhav, A. L. James, A. Z. Jan, K. Jani, J. Janquart, K. Janssens, N. N. Janthalur, P. Jaranowski, D. Jariwala, R. Jaume, A. C. Jenkins, K. Jenner, C. Jeon, M. Jeunon, W. Jia, H. B. Jin, G. R. Johns, N. K. Johnson-McDaniel, A. W. Jones, D. I. Jones, J. D. Jones, P. Jones, R. Jones, R. J. G. Jonker, L. Ju, P. Jung, K. Jung, J. Junker, V. Juste, K. Kaihotsu, T. Kajita, M. Kakizaki, C. V. Kalaghatgi, V. Kalogera, B. Kamai, M. Kamiizumi, N. Kanda, S. Kandhasamy, G. Kang, J. B. Kanner, Y. Kao, S. J. Kapadia, D. P. Kapasi, S. Karat, C. Karathanasis, S. Karki, R. Kashyap, M. Kasprzack, W. Kastaun, S. Katsanevas, E. Kat-savounidis, W. Katzman, T. Kaur, K. Kawabe, K. Kawaguchi, N. Kawai, T. Kawasaki, F. Kéfélian, D. Keitel, J. S. Key, S. Khadka, F. Y. Khalili, S. Khan, E. A. Khazanov, N. Khetan, M. Khursheed, N. Kijbunchoo, C. Kim, J. C. Kim, J. Kim, K. Kim, W. S. Kim, Y. M. Kim, C. Kimball, N. Kimura, M. Kinley-Hanlon, R. Kirchhoff, J. S. Kissel, N. Kita, H. Kitazawa, L. Kleybolte, S. Klimenko, A. M. Knee, T. D. Knowles, E. Knyazev, P. Koch, G. Koekoek, Y. Kojima, K. Kokeyama, S. Koley, P. Kolitsidou, M. Kolstein, K. Komori, V. Kondrashov, A. K. H. Kong, A. Kontos, N. Koper, M. Korobko, K. Kotake, M. Kovalam, D. B. Kozak, C. Kozakai, R. Kozu, V. Kringel, N. V. Krishnendu, A. Królak, G. Kuehn, F. Kuei, P. Kuijer, S. Kulkarni, A. Kumar, P. Kumar, Rahul Kumar, Rakesh Kumar, J. Kume, K. Kuns, C. Kuo, H-S. Kuo, Y. Kuromiya, S. Kuroyanagi, K. Kusayanagi, S. Kuwahara, K. Kwak, P. Lagabbe, D. Laghi, E. Lalande, T. L. Lam, A. Lamberts, M. Landry, B. B. Lane, R. N. Lang, J. Lange, B. Lantz, I. La Rosa, A. Lartaux-Vollard, P. D. Lasky, M. Laxen, A. Lazzarini, C. Lazzaro, P. Leaci, S. Leavey, Y. K. Lecoeuche, H. K. Lee, H. M. Lee, H. W. Lee, J. Lee, K. Lee, R. Lee, J. Lehmann, A. Lemaître, M. Leonardi, N. Leroy, N. Letendre, C. Levesque, Y. Levin, J. N. Leviton, K. Leyde, A. K. Y. Li, B. Li, J. Li, K. L. Li, T. G. F. Li, X. Li, C-Y. Lin, F-K. Lin, F-L. Lin, H. L. Lin, L. C. C. Lin, F. Linde, S. D. Linker, J. N. Linley, T. B. Littenberg, G. C. Liu, J. Liu, K. Liu, X. Liu, F. Llamas, M. Llorens-Monteagudo, R. K. L. Lo, A. Lockwood, M. Loh, L. T. London, A. Longo, D. Lopez, M. Lopez Portilla, M. Lorenzini, V. Lorette, M. Lormand, G. Losurdo, T. P. Lott, J. D. Lough, C. O. Lousto, G. Lovelace, J. F. Lucaccioni, H. Lück, D. Lumaca, A. P. Lundgren, L. W. Luo, J. E. Lynam, R. Macas, M. MacInnis, D. M. Macleod, I. A. O. MacMillan, A. Macquet, I. Magaña Hernan-

dez, C. Magazzù, R. M. Magee, R. Maggiore, M. Magnozzi, S. Mahesh, E. Majorana, C. Makarem, I. Maksimovic, S. Maliakal, A. Malik, N. Man, V. Mandic, V. Mangano, J. L. Mango, G. L. Mansell, M. Manske, M. Mantovani, M. Mapelli, F. Marchesoni, M. Marchio, F. Marion, Z. Mark, S. Márka, Z. Márka, C. Markakis, A. S. Markosyan, A. Markowitz, E. Maros, A. Marquina, S. Marsat, F. Martelli, I. W. Martin, R. M. Martin, M. Martinez, V. A. Martinez, V. Martinez, K. Martinovic, D. V. Martynov, E. J. Marx, H. Masalehdan, K. Mason, E. Massera, A. Masserot, T. J. Massinger, M. Masso-Reid, S. Mastrogiovanni, A. Matas, M. Mateu-Lucena, F. Matichard, M. Matiushechkina, N. Mavalala, J. J. McCann, R. McCarthy, D. E. McClelland, P. K. McClincy, S. McCormick, L. McCuller, G. I. McGhee, S. C. McGuire, C. McIsaac, J. McIver, T. McRae, S. T. McWilliams, D. Meacher, M. Mehmet, A. K. Mehta, Q. Meijer, A. Melatos, D. A. Melchor, G. Mendell, A. Menendez-Vazquez, C. S. Menoni, R. A. Mercer, L. Mereni, K. Merfeld, E. L. Merilh, J. D. Merritt, M. Merzougui, S. Meshkov, C. Messenger, C. Messick, P. M. Meyers, F. Meylahn, A. Mhaske, A. Miani, H. Miao, I. Michaloliakos, C. Michel, Y. Michimura, H. Middleton, L. Milano, A. L. Miller, A. Miller, B. Miller, M. Millhouse, J. C. Mills, E. Milotti, O. Minazzoli, Y. Minenkov, N. Mio, Ll. M. Mir, M. Miravet-Tenés, C. Mishra, T. Mishra, T. Mistry, S. Mitra, V. P. Mitrofanov, G. Mitselmakher, R. Mittleman, O. Miyakawa, A. Miyamoto, Y. Miyazaki, K. Miyo, S. Miyoki, Geoffrey Mo, L. M. Modaffer, E. Moguel, K. Mogushi, S. R. P. Mohapatra, S. R. Mohite, I. Molina, M. Molina-Ruiz, M. Mondin, M. Montani, C. J. Moore, D. Moraru, F. Morawski, A. More, C. Moreno, G. Moreno, Y. Mori, S. Morisaki, Y. Moriwaki, G. Morrás, B. Mours, C. M. Mow-Lowry, S. Mozzon, F. Muciaccia, Arunava Mukherjee, D. Mukherjee, Soma Mukherjee, Subroto Mukherjee, Suvodip Mukherjee, N. Mukund, A. Mullavy, J. Munch, E. A. Muñiz, P. G. Murray, R. Musenich, S. Muusse, S. L. Nadji, K. Nagano, S. Nagano, A. Nagar, K. Nakamura, H. Nakano, M. Nakano, R. Nakashima, Y. Nakayama, V. Napolano, I. Nardecchia, T. Narikawa, L. Naticchioni, B. Nayak, R. K. Nayak, R. Negishi, B. F. Neil, J. Neilson, G. Nelemans, T. J. N. Nelson, M. Nery, P. Neubauer, A. Neunzert, K. Y. Ng, S. W. S. Ng, C. Nguyen, P. Nguyen, T. Nguyen, L. Nguyen Quynh, W. T. Ni, S. A. Nichols, A. Nishizawa, S. Nissanke, E. Nitoglia, F. Nocera, M. Norman, C. North, S. Nozaki, J. F. Nuño Siles, L. K. Nuttall, J. Oberling, B. D. O'Brien, Y. Obuchi, J. O'Dell, E. Oelker, W. Ogaki, G. Oganesyan, J. J. Oh, K. Oh, S. H. Oh, M. Ohashi, N. Ohishi, M. Ohkawa, F. Ohme, H. Ohta, M. A. Okada, Y. Okutani, K. Okutomi, C. Olivetto, K. Oohara, C. Ooi, R. Oram, B. O'Reilly, R. G. Ormiston, N. D. Ormsby, L. F. Ortega, R. O'Shaughnessy, E. O'Shea, S. Oshino, S. Os-sokine, C. Osthelder, S. Otabe, D. J. Ottaway, H. Overmier, A. E. Pace, G. Pagano, M. A. Page, G. Pagliaroli, A. Pai, S. A. Pai, J. R. Palamos, O. Palashov, C. Palomba, H. Pan, K. Pan, P. K. Panda, H. Pang, P. T. H. Pang, C. Pankow, F. Pannarale, B. C. Pant, F. H. Panther, F. Paoletti, A. Paoli, A. Paolone, A. Parisi, H. Park, J. Park, W. Parker, D. Pas-cucci, A. Pasqualetti, R. Passaquieti, D. Passuello, M. Patel, M. Pathak, B. Patricelli, A. S. Patron, S. Paul, E. Payne, M. Pedraza, M. Pegoraro, A. Pele, F. E. Peña Arellano, S. Penn, A. Perego, A. Pereira, T. Pereira, C. J. Perez, C. Périgois, C. C. Perkins, A. Per-reca, S. Perriès, J. Petermann, D. Pettersson, H. P. Pfeiffer, K. A. Pham, K. S. Phukon, O. J. Piccinni, M. Pichot, M. Piendibene, F. Piergiovanni, L. Pierini, V. Pierro, G. Pillant, M. Pillas, F. Pilo, L. Pinard, I. M. Pinto, M. Pinto, B. Piotrzkowski, K. Piotrzkowski, M. Pirello, M. D. Pitkin, E. Placidi, L. Planas, W. Plastino, C. Pluchar, R. Poggiani,

E. Polini, D. Y. T. Pong, S. Ponrathnam, P. Popolizio, E. K. Porter, R. Poulton, J. Powell, M. Pracchia, T. Pradier, A. K. Prajapati, K. Prasai, R. Prasanna, G. Pratten, M. Principe, G. A. Prodi, L. Prokhorov, P. Prosposito, L. Prudenzi, A. Puecher, M. Punturo, F. Puosi, P. Puppo, M. Pürer, H. Qi, V. Quetschke, R. Quitzow-James, N. Qutob, F. J. Raab, G. Raaijmakers, H. Radkins, N. Radulesco, P. Raffai, S. X. Rail, S. Raja, C. Rajan, K. E. Ramirez, T. D. Ramirez, A. Ramos-Buades, J. Rana, P. Rapagnani, U. D. Rapol, A. Ray, V. Raymond, N. Raza, M. Razzano, J. Read, L. A. Rees, T. Regimbau, L. Rei, S. Reid, S. W. Reid, D. H. Reitze, P. Relton, A. Renzini, P. Rettegno, A. Reza, M. Rezac, F. Ricci, D. Richards, J. W. Richardson, L. Richardson, G. Riemschneider, K. Riles, S. Rinaldi, K. Rink, M. Rizzo, N. A. Robertson, R. Robie, F. Robinet, A. Rocchi, S. Rodriguez, L. Rolland, J. G. Rollins, M. Romanelli, R. Romano, C. L. Romel, A. Romero-Rodríguez, I. M. Romero-Shaw, J. H. Romie, S. Ronchini, L. Rosa, C. A. Rose, D. Rosińska, M. P. Ross, S. Rowan, S. J. Rowlinson, S. Roy, Santosh Roy, Soumen Roy, D. Rozza, P. Ruggi, K. Ruiz-Rocha, K. Ryan, S. Sachdev, T. Sadecki, J. Sadiq, N. Sago, S. Saito, Y. Saito, K. Sakai, Y. Sakai, M. Sakellariadou, Y. Sakuno, O. S. Salafia, L. Salconi, M. Saleem, F. Salemi, A. Samajdar, E. J. Sanchez, J. H. Sanchez, L. E. Sanchez, N. Sanchis-Gual, J. R. Sanders, A. Sanuy, T. R. Saravanan, N. Sarin, B. Sassolas, H. Satari, B. S. Sathyaprakash, S. Sato, T. Sato, O. Sauter, R. L. Savage, T. Sawada, D. Sawant, H. L. Sawant, S. Sayah, D. Schaetzl, M. Scheel, J. Scheuer, M. Schiworski, P. Schmidt, S. Schmidt, R. Schnabel, M. Schneewind, R. M. S. Schofield, A. Schönbeck, B. W. Schulte, B. F. Schutz, E. Schwartz, J. Scott, S. M. Scott, M. Seglar-Arroyo, T. Sekiguchi, Y. Sekiguchi, D. Sellers, A. S. Sengupta, D. Sentenac, E. G. Seo, V. Sequino, A. Sergeev, Y. Setyawati, T. Shaffer, M. S. Shahriar, B. Shams, L. Shao, A. Sharma, P. Sharma, P. Shawhan, N. S. Shcheblanov, S. Shibagaki, M. Shikauchi, R. Shimizu, T. Shimoda, K. Shimode, H. Shinkai, T. Shishido, A. Shoda, D. H. Shoemaker, D. M. Shoemaker, S. ShyamSundar, M. Sieniawska, D. Sigg, L. P. Singer, D. Singh, N. Singh, A. Singha, A. M. Sintes, V. Sipala, V. Skliris, B. J. J. Slagmolen, T. J. Slaven-Blair, J. Smetana, J. R. Smith, R. J. E. Smith, J. Soldateschi, S. N. Somala, K. Somiya, E. J. Son, K. Soni, S. Soni, V. Sordini, F. Sorrentino, N. Sorrentino, H. Sotani, R. Soulard, T. Souradeep, E. Sowell, V. Spagnuolo, A. P. Spencer, M. Spera, R. Srinivasan, A. K. Srivastava, V. Srivastava, K. Staats, C. Stachie, D. A. Steer, J. Steinhoff, J. Steinlechner, S. Steinlechner, S. P. Stevenson, D. J. Stops, M. Stover, K. A. Strain, L. C. Strang, G. Stratta, A. Strunk, R. Sturani, A. L. Stuver, S. Sudhagar, V. Sudhir, R. Sugimoto, H. G. Suh, A. G. Sullivan, J. M. Sullivan, T. Z. Summerscales, H. Sun, L. Sun, S. Sunil, A. Sur, J. Suresh, P. J. Sutton, Takamasa Suzuki, Toshikazu Suzuki, B. L. Swinkels, M. J. Szczepańczyk, P. Szewczyk, M. Tacca, H. Tagoshi, S. C. Tait, H. Takahashi, R. Takahashi, A. Takamori, S. Takano, H. Takeda, M. Takeda, C. J. Talbot, C. Talbot, H. Tanaka, Kazuyuki Tanaka, Kenta Tanaka, Taiki Tanaka, Takahiro Tanaka, A. J. Tanasiaczuk, S. Tanioka, D. B. Tanner, D. Tao, L. Tao, E. N. Tapia San Martín, C. Taranto, J. D. Tasson, S. Telada, R. Tenorio, J. E. Terhune, L. Terkowski, M. P. Thirugnanasambandam, L. Thomas, M. Thomas, P. Thomas, J. E. Thompson, S. R. Thondapu, K. A. Thorne, E. Thrane, Shubhanshu Tiwari, Srishti Tiwari, V. Tiwari, A. M. Toivonen, K. Toland, A. E. Tolley, T. Tomaru, Y. Tomigami, T. Tomura, M. Tonelli, A. Torres-Forné, C. I. Torrie, I. Tosta e Melo, D. Töyrä, A. Trapananti, F. Travasso, G. Traylor, M. Trevor, M. C. Tringali, A. Tripathhee, L. Troiano, A. Trovato, L. Trozzo, R. J. Trudeau, D. S. Tsai, D. Tsai, K. W. Tsang, T. Tsang, J-S. Tsao, M. Tse,

R. Tso, K. Tsubono, S. Tsuchida, L. Tsukada, D. Tsuna, T. Tsutsui, T. Tsuzuki, K. Turbang, M. Turconi, D. Tuyenbayev, A. S. Ubhi, N. Uchikata, T. Uchiyama, R. P. Udall, A. Ueda, T. Uehara, K. Ueno, G. Ueshima, C. S. Unnikrishnan, F. Uraguchi, A. L. Urban, T. Ushiba, A. Utina, H. Vahlbruch, G. Vajente, A. Vajpeyi, G. Valdes, M. Valentini, V. Valsan, N. van Bakel, M. van Beuzekom, J. F. J. van den Brand, C. Van Den Broeck, D. C. Vander-Hyde, L. van der Schaaf, J. V. van Heijningen, J. Vanosky, M. H. P. M. van Putten, N. van Remortel, M. Vardaro, A. F. Vargas, V. Varma, M. Vasúth, A. Vecchio, G. Vedovato, J. Veitch, P. J. Veitch, J. Venneberg, G. Venugopalan, D. Verkindt, P. Verma, Y. Verma, D. Veske, F. Vetrano, A. Viceré, S. Vidyant, A. D. Viets, A. Vijaykumar, V. Villa-Ortega, J. Y. Vinet, A. Virtuoso, S. Vitale, T. Vo, H. Vocca, E. R. G. von Reis, J. S. A. von Wrangel, C. Vorvick, S. P. Vyatchanin, L. E. Wade, M. Wade, K. J. Wagner, R. C. Walet, M. Walker, G. S. Wallace, L. Wallace, S. Walsh, J. Wang, J. Z. Wang, W. H. Wang, R. L. Ward, J. Warner, M. Was, T. Washimi, N. Y. Washington, J. Watchi, B. Weaver, S. A. Webster, M. Weinert, A. J. Weinstein, R. Weiss, C. M. Weller, R. A. Weller, F. Wellmann, L. Wen, P. Webels, K. Wette, J. T. Whelan, D. D. White, B. F. Whiting, C. Whittle, D. Wilken, D. Williams, M. J. Williams, N. Williams, A. R. Williamson, J. L. Willis, B. Willke, D. J. Wilson, W. Winkler, C. C. Wipf, T. Włodarczyk, G. Woan, J. Woehler, J. K. Wofford, I. C. F. Wong, C. Wu, D. S. Wu, H. Wu, S. Wu, D. M. Wysocki, L. Xiao, W-R. Xu, T. Yamada, H. Yamamoto, Kazuhiro Yamamoto, Kohei Yamamoto, T. Yamamoto, K. Yamashita, R. Yamazaki, F. W. Yang, L. Yang, Y. Yang, Yang Yang, Z. Yang, M. J. Yap, D. W. Yeeles, A. B. Yelikar, M. Ying, K. Yokogawa, J. Yokoyama, T. Yokozawa, J. Yoo, T. Yoshioka, Hang Yu, Haocun Yu, H. Yuzurihara, A. Zadrożny, M. Zanolin, S. Zeidler, T. Zelenova, J. P. Zendri, M. Zevin, M. Zhan, H. Zhang, J. Zhang, L. Zhang, T. Zhang, Y. Zhang, C. Zhao, G. Zhao, Y. Zhao, Yue Zhao, Y. Zheng, R. Zhou, Z. Zhou, X. J. Zhu, Z. H. Zhu, A. B. Zimmerman, Y. Zlochower, M. E. Zucker, and J. Zweizig. GWTC-3: Compact Binary Coalescences Observed by LIGO and Virgo During the Second Part of the Third Observing Run. [arXiv e-prints](#), page arXiv:2111.03606, November 2021.

- [50] M. G. Aartsen et al. The IceCube Neutrino Observatory: Instrumentation and Online Systems. [JINST](#), 12(03):P03012, 2017.
- [51] R D Peccei. [Discrete and Global Symmetries in Particle Physics](#), volume 521 of [Lecture Notes in Physics](#). Springer Berlin Heidelberg, 1999.
- [52] R. Peccei and H. Quinn. CP conservation in the presence of pseudoparticles. [Phys. Rev. Lett.](#), 38:1440–1443, Jun 1977.
- [53] Curtis G Callan Jr, Roger F Dashen, and David J Gross. The structure of the gauge theory vacuum. [Physics Letters](#), 63B(3):334–340, 1976.
- [54] Georg G Raffelt. Axions. In [Stars as Laboratories for Fundamental Physics](#), pages 199–228. The University of Chicago Press, 1996.
- [55] C Abel, S Afach, NJ Ayres, E Babcock, CA Baker, G Ban, G Bison, K Bodek, P Boer, M Burghoff, and et al. Improved limit on the electric dipole moment of the neutron. [Physical Review Letters](#), 124(8):081803, 2020.

- [56] Steven Weinberg. The cosmological constant problem. *Rev. Mod. Phys.*, 61:1–23, Jan 1989.
- [57] Leandros Perivolaropoulos and Foteini Skara. Challenges for  $\Lambda$ CDM: An update. *New Astron. Rev.*, 95:101659, 2022.
- [58] Seth Koren. New Approaches to the Hierarchy Problem and their Signatures from Microscopic to Cosmic PhD thesis, UC, Santa Barbara (main), 2020.
- [59] R. Peccei and H. Quinn. Constraints imposed by CP conservation in the presence of pseudoparticles. *Phys. Rev. D*, 16:1791–1797, Sep 1977.
- [60] Jihn E. Kim. Weak interaction singlet and strong CP invariance. *Phys. Rev. Lett.*, 43:103, 1979.
- [61] M. A. Shifman, A. I. Vainshtein, and V. I. Zakharov. Can confinement ensure natural CP invariance of strong interactions? *Nucl. Phys.*, B166:493–506, 1980.
- [62] P. Arias, D. Cadamuro, M. Goodsell, J. Jaeckel, J. Redondo, and A. Ringwald. WISPy cold dark matter. *Journal of Cosmology and Astro-Particle Physics*, 2012:013, Jun 2012.
- [63] V. Trimble. Existence and nature of dark matter in the universe. *Annual Review of Astronomy and Astrophysics*, 25:425–472, 1987.
- [64] Joseph P. Conlon and M. C. David Marsh. Excess Astrophysical Photons from a 0.1–1 keV Cosmic Axion Background. *Phys. Rev. Lett.*, 111(15):151301, 2013.
- [65] Stephen Angus, Joseph P. Conlon, M. C. David Marsh, Andrew J. Powell, and Lukas T. Witkowski. Soft X-ray Excess in the Coma Cluster from a Cosmic Axion Background. *JCAP*, 09:026, 2014.
- [66] Andrew J. Powell. A Cosmic ALP Background and the Cluster Soft X-ray Excess in A665, A2199 and A2255. *JCAP*, 09:017, 2015.
- [67] David Kraljic, Markus Rummel, and Joseph P. Conlon. ALP conversion and the soft X-ray excess in the outskirts of the Coma cluster. *Journal of Cosmology and Astroparticle Physics*, 2015(01):011–011, Jan 2015.
- [68] Michele Cicoli, Joseph P. Conlon, M. C. David Marsh, and Markus Rummel. 3.55 keV photon line and its morphology from a 3.55 keV axionlike particle line. *Phys. Rev. D*, 90:023540, 2014.
- [69] A. Mirizzi and D. Montanino. Stochastic conversions of TeV photons into axion-like particles in extragalactic magnetic fields. *JCAP*, 0912:004, 2009.
- [70] M. Meyer, D. Horns, and M. Raue. First lower limits on the photon-axion-like particle coupling from very high energy gamma-ray observations. *Physical Review D*, 87:035027, Feb 2013.

- [71] Giorgio Galanti, Marco Roncadelli, Alessandro De Angelis, and Giovanni F. Bignami. Hint at an axion-like particle from the redshift dependence of blazar spectra, 2020.
- [72] Kazunori Kohri and Hideo Kodama. Axion-Like Particles and Recent Observations of the Cosmic Infrared Background Radiation, 2017.
- [73] Jianeng Zhou, Zhongxiang Wang, Feng Huang, and Liang Chen. A possible blazar spectral irregularity case caused by photon–axionlike-particle oscillations, 2 2021.
- [74] Maurizio Giannotti, Igor Irastorza, Javier Redondo, and Andreas Ringwald. Cool WISPs for stellar cooling excesses, 2016.
- [75] Maurizio Giannotti. Hints of new physics from stars, 2016.
- [76] Maurizio Giannotti, Igor G. Irastorza, Javier Redondo, Andreas Ringwald, and Ken’ichi Saikawa. Stellar Recipes for Axion Hunters, 2017.
- [77] Christopher Dessert, Andrew J. Long, and Benjamin R. Safdi. No evidence for axions from Chandra observation of magnetic white dwarf, 4 2021.
- [78] Alexander Friedland, Maurizio Giannotti, and Michael Wise. Constraining the Axion-Photon Coupling with Massive Stars. *Phys. Rev. Lett.*, 110(6):061101, 2013.
- [79] Adrian Ayala, Inma Domínguez, Maurizio Giannotti, Alessandro Mirizzi, and Oscar Straniero. Revisiting the bound on axion-photon coupling from Globular Clusters. *Phys. Rev. Lett.*, 113(19):191302, 2014.
- [80] Christopher Dessert, Joshua W. Foster, and Benjamin R. Safdi. X-ray Searches for Axions from Super Star Clusters. *Phys. Rev. Lett.*, 125(26):261102, 2020.
- [81] M. Ajello et al. Search for Spectral Irregularities due to Photon–Axionlike-Particle Oscillations with the Fermi Large Area Telescope. *Phys. Rev. Lett.*, 116(16):161101, 2016.
- [82] Ji-Gui Cheng, Ya-Jun He, Yun-Feng Liang, Rui-Jing Lu, and En-Wei Liang. Revisiting the analysis of axion-like particles with the Fermi-LAT gamma-ray observation of NGC1275, 10 2020.
- [83] M.C. David Marsh, Helen R. Russell, Andrew C. Fabian, Brian R. McNamara, Paul Nulsen, and Christopher S. Reynolds. A new bound on axion-like particles. *Journal of Cosmology and Astroparticle Physics*, 2017(12):036–036, Dec 2017.
- [84] D. Malyshev, A. Neronov, D. Semikoz, A. Santangelo, and J. Jochum. Improved limit on axion-like particles from  $\gamma$ -ray data on Perseus cluster, 5 2018.
- [85] Christopher S. Reynolds, M. C. David Marsh, Helen R. Russell, Andrew C. Fabian, Robyn Smith, Francesco Tombesi, and Sylvain Veilleux. Astrophysical limits on very light axion-like particles from Chandra grating spectroscopy of NGC 1275, 2019.

- [86] Júlia Sisk-Reynés, James H. Matthews, Christopher S. Reynolds, Helen R. Russell, Robyn N. Smith, and M. C. David Marsh. New constraints on light axion-like particles using Chandra transmission grating spectroscopy of the powerful cluster-hosted quasar H1821+643. *Monthly Notices of the Royal Astronomical Society*, 510(1):1264–1277, February 2022.
- [87] CAST Collaboration, S. Andriamonje, et al. An improved limit on the axion-photon coupling from the cast experiment. *JCAP*, 04:010, 2007.
- [88] CAST Collaboration, V. Anastassopoulos, et al. New cast limit on the axion-photon interaction. *Nature Phys.*, 13:584, 2017.
- [89] Klaus Ehret et al. New ALPs Results on Hidden-Sector Lightweights. *Phys. Lett.*, B689:149–155, 2010.
- [90] M. Diaz Ortiz et al. Design of the ALPS II optical system. *Phys. Dark Univ.*, 35:100968, 2022.
- [91] E. Armengaud et al. Physics potential of the International Axion Observatory (IAXO). *JCAP*, 06:047, 2019.
- [92] I. Shilon, A. Dudarev, H. Silva, U. Wagner, and H. H. J. ten Kate. The Superconducting Toroid for the New International AXion Observatory (IAXO). *IEEE Trans. Appl. Supercond.*, 24(3):4500104, 2014.
- [93] Jonathan L. Ouellet et al. First Results from ABRACADABRA-10 cm: A Search for Sub- $\mu$ eV Axion Dark Matter. *Phys. Rev. Lett.*, 122(12):121802, 2019.
- [94] Chiara P. Salemi et al. Search for Low-Mass Axion Dark Matter with ABRACADABRA-10 cm. *Phys. Rev. Lett.*, 127(8):081801, 2021.
- [95] S. J. Asztalos, G. Carosi, C. Hagmann, D. Kinion, K. van Bibber, M. Hotz, L. J. Rosenberg, G. Rybka, J. Hoskins, J. Hwang, P. Sikivie, D. B. Tanner, R. Bradley, J. Clarke, and ADMX Collaboration. SQUID-Based Microwave Cavity Search for Dark-Matter Axions. *Phys. Rev. Lett.*, 104(4):041301, January 2010.
- [96] N. Du et al. A Search for Invisible Axion Dark Matter with the Axion Dark Matter Experiment. *Phys. Rev. Lett.*, 120(15):151301, 2018.
- [97] C. Boutan et al. Piezoelectrically Tuned Multimode Cavity Search for Axion Dark Matter. *Phys. Rev. Lett.*, 121(26):261302, 2018.
- [98] T. Braine et al. Extended Search for the Invisible Axion with the Axion Dark Matter Experiment. *Phys. Rev. Lett.*, 124(10):101303, 2020.
- [99] C. Bartram et al. Search for Invisible Axion Dark Matter in the 3.3–4.2  $\mu$ eV Mass Range. *Phys. Rev. Lett.*, 127(26):261803, 2021.

- [100] Alexander V. Gramolin, Deniz Aybas, Dorian Johnson, Janos Adam, and Alexander O. Sushkov. Search for axion-like dark matter with ferromagnets. *Nature Phys.*, 17(1):79–84, 2021.
- [101] V. Pelassa, R. Preece, F. Piron, N. Omodei, and S. Guiriec. The LAT Low-Energy technique for Fermi Gamma-Ray Bursts spectral analysis, 2010.
- [102] J. E. Kim and G. Carosi. Axions and the strong CP problem. *Reviews of Modern Physics*, 82:557–601, Jan 2010.
- [103] Joerg Jaeckel and Andreas Ringwald. The low-energy frontier of particle physics. *Annual Review of Nuclear and Particle Science*, 60(1):405–437, Nov 2010.
- [104] A. Ringwald. Axions and axion-like particles, 2014.
- [105] David J.E. Marsh. Axion cosmology. *Physics Reports*, 643:1–79, Jul 2016.
- [106] S. Weinberg. A new light boson? *Phys. Rev. Lett.*, 40:223–226, Jan 1978.
- [107] Frank Wilczek. Problem of Strong  $P$  and  $T$  Invariance in the Presence of Instantons. *Phys. Rev. Lett.*, 40:279–282, 1978.
- [108] Georg Raffelt and Leo Stodolsky. Mixing of the Photon with Low Mass Particles. *Phys. Rev.*, D37:1237, 1988.
- [109] E. Aprile et al. Excess electronic recoil events in XENON1T. *Phys. Rev. D*, 102(7):072004, 2020.
- [110] Luca Di Luzio, Marco Fedele, Maurizio Giannotti, Federico Mescia, and Enrico Nardi. Solar axions cannot explain the XENON1T excess. *Phys. Rev. Lett.*, 125(13):131804, 2020.
- [111] Christina Gao, Jia Liu, Lian-Tao Wang, Xiao-Ping Wang, Wei Xue, and Yi-Ming Zhong. Reexamining the Solar Axion Explanation for the XENON1T Excess. *Phys. Rev. Lett.*, 125(13):131806, 2020.
- [112] Kiwoon Choi, Sang Hui Im, and Chang Sub Shin. Recent progress in physics of axions or axion-like particles, 12 2020.
- [113] John Preskill, Mark B. Wise, and Frank Wilczek. Cosmology of the Invisible Axion. *Phys. Lett.*, 120B:127–132, 1983.
- [114] L. F. Abbott and P. Sikivie. A Cosmological Bound on the Invisible Axion. *Phys. Lett.*, 120B:133–136, 1983.
- [115] Michael Dine and Willy Fischler. The Not So Harmless Axion. *Phys. Lett.*, 120B:137–141, 1983.
- [116] Leanne D. Duffy, P. Sikivie, D. B. Tanner, Stephen J. Asztalos, C. Hagmann, D. Kinion, L. J Rosenberg, K. van Bibber, D. B. Yu, and R. F. Bradley. A high resolution search for dark-matter axions. *Phys. Rev.*, D74:012006, 2006.

- [117] H. Primakoff. Photo-production of neutral mesons in nuclear electric fields and the mean life of the neutral meson. *Phys. Rev.*, 81:899–899, Mar 1951.
- [118] T. Fischer, S. C. Whitehouse, A. Mezzacappa, F. K. Thielemann, and M. Liebendorfer. Protoneutron star evolution and the neutrino driven wind in general relativistic neutrino radiation hydrodynamics simulations. *Astron. Astrophys.*, 517:A80, 2010.
- [119] Georg G. Raffelt. Astrophysical axion bounds diminished by screening effects. *Phys. Rev.*, D33:897, 1986.
- [120] J.W. Brockway, E.D. Carlson, and G.G. Raffelt. SN 1987A gamma-ray limits on the conversion of pseudoscalars. *Physics Letters B*, 383:439–443, Feb 1996.
- [121] J. A. Grifols, E. Massó, and R. Toldrà. Gamma Rays from SN 1987A due to Pseudoscalar Conversion. *Physical Review D*, 77:2372–2375, Sep 1996.
- [122] A. Payez, C. Evoli, T. Fischer, M. Giannotti, A. Mirizzi, and A. Ringwald. Revisiting the SN1987A gamma-ray limit on ultralight axion-like particles. *Journal of Cosmology and Astro-Particle Physics*, 2015:006, Feb 2015.
- [123] M. Meyer, M. Giannotti, A. Mirizzi, J. Conrad, and M. A. Sánchez-Conde. Fermi Large Area Telescope as a Galactic Supernovae Axionscope. *Physical Review Letters*, 118:011103, Jan 2017.
- [124] Tsvi Piran. The physics of gamma-ray bursts. *Reviews of Modern Physics*, 76(4):1143–1210, Jan 2005.
- [125] J. P. Norris, T. L. Cline, U. D. Desai, and B. J. Teegarden. Frequency of fast, narrow gamma-ray bursts. *Nature*, 308:434, March 1984.
- [126] C. Kouveliotou, C. A. Meegan, G. J. Fishman, N. P. Bhat, M. S. Briggs, T. M. Koshut, W. S. Paciesas, and G. N. Pendleton. Identification of two classes of gamma-ray bursts. *The Astrophysical Journal Letters*, 413:L101–L104, August 1993.
- [127] E. Berger. Short-Duration Gamma-Ray Bursts. *Annual Review of Astronomy and Astrophysics*, 52:43–105, Aug 2014.
- [128] W. Fong and E. Berger. The locations of short gamma-ray bursts as evidence for compact object binary progenitors. *The Astrophysical Journal*, 776(1):18, sep 2013.
- [129] W. Fong, E. Berger, R. Margutti, and B. A. Zauderer. A Decade of Short-duration Gamma-ray Burst Broadband Afterglows: Energetics, Circumburst Densities, and jet Opening Angles. *Astrophys. J.*, 815(2):102, 2015.
- [130] B. P. Abbott et al. Gravitational Waves and Gamma-rays from a Binary Neutron Star Merger: GW170817 and GRB 170817A. *Astrophys. J.*, 848(2):L13, 2017.
- [131] T. J. Galama et al. An unusual supernova in the error box of the  $\gamma$ -ray burst of 25 April 1998. *Nature*, 395(6703):670–672, Oct 1998.

- [132] Ferdinando Patat et al. The Metamorphosis of SN1998bw. *Astrophys. J.*, 555:900–917, 2001.
- [133] S. E. Woosley and J. S. Bloom. The Supernova Gamma-Ray Burst Connection. *Ann. Rev. Astron. Astrophys.*, 44:507–556, 2006.
- [134] E. Bissaldi, F. Calura, F. Matteucci, F. Longo, and G. Barbiellini. The connection between gamma-ray bursts and supernovae Ib/c. *Astronomy & Astrophysics*, 471(2):585–597, Aug 2007.
- [135] Massimo Della Valle. Supernovae and Gamma-Ray Bursts: A Decade of Observations. *International Journal of Modern Physics D*, 20(10):1745–1754, Jan 2011.
- [136] Zach Cano, Shan-Qin Wang, Zi-Gao Dai, and Xue-Feng Wu. The Observer’s Guide to the Gamma-Ray Burst Supernova Connection. *Adv. Astron.*, 2017:8929054, 2017.
- [137] Alexandra Dobrynina, Alexander Kartavtsev, and Georg Raffelt. Photon-photon dispersion of TeV gamma rays and its role for photon-ALP conversion. *Phys. Rev. D*, 91:083003, 2015. [Erratum: Phys.Rev.D 95, 109905 (2017)].
- [138] R. Buehler, G. Gallardo, G. Maier, A. Domínguez, M. López, and M. Meyer. Search for the imprint of axion-like particles in the highest-energy photons of hard  $\gamma$ -ray blazars. *JCAP*, 09:027, 2020.
- [139] Maxim Libanov and Sergey Troitsky. On the impact of magnetic-field models in galaxy clusters on constraints on axion-like particles from the lack of irregularities in high-energy spectra of astrophysical sources, 2020.
- [140] Manuel A. Buen-Abad, JiJi Fan, and Chen Sun. Constraints on Axions from Cosmic Distance Measurements, 11 2020.
- [141] R. Jansson and G.R. Farrar. A New Model of the Galactic Magnetic Field. *The Astrophysical Journal*, 757:14, Sep 2012.
- [142] M. Meyer. GammaALPs: calculating the conversion probability between photons and axions/axion-like particles in various astrophysical magnetic fields. <https://github.com/me-manu/gammaALPs>, 2021.
- [143] Manuel Meyer, Dieter Horns, and Martin Raue. First lower limits on the photon-axion-like particle coupling from very high energy gamma-ray observations. *Physical Review D*, 87(3), Feb 2013.
- [144] Pierluca Carenza, Carmelo Evoli, Maurizio Giannotti, Alessandro Mirizzi, and Daniele Montanino. Turbulent axion-photon conversions in the Milky-Way, 4 2021.
- [145] M. Ajello et al. A Decade of Gamma-Ray Bursts Observed by Fermi-LAT: The Second GRB Catalog. *The Astrophysical Journal*, 878(1):52, jun 2019.
- [146] Keith Arnaud, Ben Dorman, and Craig Gordon. XSPEC: An X-ray spectral fitting package, October 1999.

- [147] M. Ajello et al. Impulsive and Long Duration High-Energy Gamma-ray Emission From the Very Bright 2012 March 7 Solar Flares. *Astrophys. J.*, 789(1):20, 2014.
- [148] Shin'ichiro Ando, John F. Beacom, and Hasan Yuksel. Detection of neutrinos from supernovae in nearby galaxies. *Phys. Rev. Lett.*, 95:171101, 2005.
- [149] Matthew D. Kistler, Hasan Yüksel, Shin'ichiro Ando, John F. Beacom, and Yoichiro Suzuki. Core-collapse astrophysics with a five-megaton neutrino detector. *Physical Review D*, 83(12), Jun 2011.
- [150] D. F. Cowen, A. Franckowiak, and M. Kowalski. Estimating the explosion time of core-collapse supernovae from their optical light curves. *Astroparticle Physics*, 33:19–23, Feb 2010.
- [151] S. E. Woosley. Models for gamma-ray burst progenitors and central engines, 2011.
- [152] Y. F. Huang, Z. G. Dai, and T. Lu. Failed gamma-ray bursts and orphan afterglows. *Mon. Not. Roy. Astron. Soc.*, 332:735, 2002.
- [153] D. Band, J. Matteson, L. Ford, B. Schaefer, D. Palmer, B. Teegarden, T. Cline, M. Briggs, W. Paciesas, G. Pendleton, G. Fishman, C. Kouveliotou, C. Meegan, R. Wilson, and P. Lestrade. BATSE Observations of Gamma-Ray Burst Spectra. I. Spectral Diversity, Aug 1993.
- [154] Giacomo Vianello. The Significance of an Excess in a Counting Experiment: Assessing the Impact of Systematic Uncertainties and the Case with a Gaussian Background, May 2018.
- [155] S. S. Wilks. The large-sample distribution of the likelihood ratio for testing composite hypotheses. *Ann. Math. Statist.*, 9(1):60–62, 03 1938.
- [156] Glen Cowan, Kyle Cranmer, Eilam Gross, and Ofer Vitells. Asymptotic formulae for likelihood-based tests of new physics. *Eur. Phys. J. C*, 71:1554, 2011. [Erratum: Eur.Phys.J.C 73, 2501 (2013)].
- [157] Grzegorz Pojmanski. The All Sky Automated Survey. Variable stars in the 0h - 6h quarter of the southern hemisphere. *Acta Astron.*, 52:397–427, 2002.
- [158] B. J. Shappee et al. The Man Behind the Curtain: X-rays Drive the UV through NIR Variability in the 2013 AGN Outburst in NGC 2617. *Astrophys. J.*, 788:48, 2014.
- [159] J. L. Tonry, L. Denneau, A. N. Heinze, B. Stalder, K. W. Smith, S. J. Smartt, C. W. Stubbs, H. J. Weiland, and A. Rest. ATLAS: A High-cadence All-sky Survey System, June 2018.
- [160] P. R. Woniak, W. T. Vestrand, C. W. Akerlof, R. Balsano, J. Bloch, D. Casperson, S. Fletcher, G. Gisler, R. Kehoe, K. Kinemuchi, et al. Northern Sky Variability Survey (NSVS): Public Data Release. *The Astronomical Journal*, 127(4):2436–2449, Apr 2004.

- [161] A. J. Drake, S. G. Djorgovski, A. Mahabal, E. Beshore, S. Larson, M. J. Graham, R. Williams, E. Christensen, M. Catelan, A. Boattini, et al. First Results from the Catalina Real-time Transient Survey (CRTS). *The Astrophysical Journal*, 696(1):870–884, Apr 2009.
- [162] Nicholas M. Law, Shrinivas R. Kulkarni, Richard G. Dekany, Eran O. Ofek, Robert M. Quimby, Peter E. Nugent, Jason Surace, Carl C. Grillmair, Joshua S. Bloom, Mansi M. Kasliwal, et al. The Palomar Transient Factory (PTF): System Overview, Performance, and First Results. *Publications of the Astronomical Society of the Pacific*, 121(886):1395–1408, Dec 2009.
- [163] B. B. Zhang, B. Zhang, E.W. Liang, Y.Z. Fan, X.F. Wu, A. Pe'er, A. a Maxham, H. Gao, and Y.M. Dong. A Comprehensive Analysis of Fermi Gamma-ray Burst Data. I. Spectral Components and the Possible Physical Origins of LAT/GBM GRBs. *The Astrophysical Journal*, 730:141, Apr 2011.
- [164] Sylvain Guiriec et al. Detection of a Thermal Spectral Component in the Prompt Emission of GRB 100724B. *Astron. J.*, 727:L33, 2011.
- [165] Louis Lyons. Open statistical issues in Particle Physics. *Ann. Appl. Stat.*, 2:887–915, 2008.
- [166] Andrew Levan. Long-GRB progenitors. In *Gamma-Ray Bursts*, 2514-3433, pages 5–1 to 5–18. IOP Publishing, 2018.
- [167] T. W. Holoien et al. The ASAS-SN bright supernova catalogue - I. 2013-2014. 464(3):2672–2686, January 2017.
- [168] Eric C. Bellm et al. The Zwicky Transient Facility: System Overview, Performance, and First Results. 131(995):018002, January 2019.
- [169] M. M. Fausnaugh et al. Early Time Light Curves of 18 Bright Type Ia Supernovae Observed with TESS, April 2019.
- [170] LSST Science Collaboration. LSST Science Book, Version 2.0, December 2009.
- [171] V. Tatischeff et al. The e-ASTROGAM gamma-ray space mission. volume 9905 of *Society of Photo-Optical Instrumentation Engineers (SPIE) Conference Series*, page 99052N, Jul 2016.
- [172] A. Moiseev et al. Compton-Pair Production Space Telescope (ComPair) for MeV Gamma-ray Astronomy. *arXiv e-prints*, page arXiv:1508.07349, Aug 2015.
- [173] Xin Wu, Meng Su, Alessandro Bravar, Jin Chang, Yizhong Fan, Martin Pohl, and Roland Walter. PANGU: A High Resolution Gamma-ray Space Telescope. *Proc. SPIE Int. Soc. Opt. Eng.*, 9144:91440F, 2014.
- [174] Regina Caputo et al. All-sky Medium Energy Gamma-ray Observatory: Exploring the Extreme Multimessenger Universe, 2019.

- [175] Steven P. Harris, Jean-Francois Fortin, Kuver Sinha, and Mark G. Alford. Axions in neutron star mergers. *JCAP*, 07:023, 2020.
- [176] LIGO Scientific Collaboration and Virgo Collaboration. GW170817: Observation of Gravitational Waves from a Binary Neutron Star Inspiral. *Physical Review Letters*, 119:161101, Oct 2017.
- [177] Bing Zhang. *The Physics of Gamma-Ray Bursts*. 2018.
- [178] Sylvia Zhu. Precursors in gamma-ray bursts observed by *Fermi*. Digital Object Identifier: <https://doi.org/10.13016/M2CH9N>, 2016.
- [179] J. D. Scargle. Bayesian Blocks: A New Approach to Adaptive Multiband Measurement of Time Series. *Astrophysical Journal*, 764(2):167, June 2013.
- [180] G. Vianello, G. Fitzpatrick, S. Foley, A. J. Horst, D. Kocevski, and J. L. Racusin. Time-Resolved Spectroscopy of GRB 080916C Using Bayesian Blocks. *Astrophysical Journal*, 777(1):61, October 2013.
- [181] G. Vianello, P. Ogle, W. H. Baumgartner, C. B. Markwardt, D. Stern, J. Tueller, M. Ajello, and N. Gehrels. Bayesian Blocks as a Tool for Characterizing the Variability of AGN Light Curves. *Astrophysical Journal*, 858(2):94, May 2018.
- [182] S. Dichiara, J. Gropp, J. A. Kennea, and et al. Gen circ. 32632. *GCN Circulars*, 32632, 2022.
- [183] S. Lesage et al. Fermi-GBM Discovery of GRB 221009A: An Extraordinarily Bright GRB from Onset to Afterglow. 3 2023.
- [184] A. de Ugarte Postigo, L. Izzo, G. Pugliese, and et al. Grb coordinates network, 32648, 1. *GRB Coordinates Network*, 32648(1), 2022.
- [185] Y. Huang, S. Hu, S. Chen, and et al. Grb coordinates network, 32677, 1. *GRB Coordinates Network*, 32677(1), 2022.
- [186] Giorgio Galanti, Marco Roncadelli, and Fabrizio Tavecchio. Assessment of ALP scenarios for GRB 221009A. 11 2022.
- [187] Pierluca Carenza and M. C. David Marsh. On ALP scenarios and GRB 221009A. 11 2022.
- [188] Ali Baktash, Dieter Horns, and Manuel Meyer. Interpretation of multi-TeV photons from GRB221009A. 10 2022.
- [189] A. Goldstein, P. Veres, E. Burns, M. S. Briggs, R. Hamburg, D. Kocevski, C. A. Wilson-Hodge, R. D. Preece, S. Poolakkil, O. J. Roberts, C. M. Hui, V. Connaughton, J. Racusin, A. von Kienlin, T. Dal Canton, N. Christensen, T. Littenberg, K. Siellez, L. Blackburn, J. Broida, E. Bissaldi, W. H. Cleveland, M. H. Gibby, M. M. Giles, R. M. Kippen, S. McBreen, J. McEnery, C. A. Meegan, W. S. Paciesas, and M. Stanbro. An Ordinary Short Gamma-Ray Burst with Extraordinary Implications: Fermi-GBM Detection of GRB 170817A. *Astrophysical Journal Letters*, 848(2):L14, October 2017.

- [190] V. Savchenko, C. Ferrigno, E. Kuulkers, A. Bazzano, E. Bozzo, S. Brandt, J. Chenevez, T. J. L. Courvoisier, R. Diehl, A. Domingo, L. Hanlon, E. Jourdain, A. von Kienlin, P. Laurent, F. Lebrun, A. Lutovinov, A. Martin-Carrillo, S. Mereghetti, L. Natalucci, J. Rodi, J. P. Roques, R. Sunyaev, and P. Ubertini. INTEGRAL Detection of the First Prompt Gamma-Ray Signal Coincident with the Gravitational-wave Event GW170817. *Astrophysical Journal Letters*, 848(2):L15, October 2017.
- [191] B. P. Abbott, R. Abbott, T. D. Abbott, F. Acernese, K. Ackley, C. Adams, T. Adams, P. Addesso, R. X. Adhikari, V. B. Adya, and et al. Gravitational Waves and Gamma-Rays from a Binary Neutron Star Merger: GW170817 and GRB 170817A. *Astrophysical Journal Letters*, 848(2):L13, October 2017.
- [192] B. P. Abbott, R. Abbott, T. D. Abbott, S. Abraham, F. Acernese, K. Ackley, C. Adams, R. X. Adhikari, V. B. Adya, C. Affeldt, M. Agathos, K. Agatsuma, N. Aggarwal, O. D. Aguiar, L. Aiello, A. Ain, P. Ajith, G. Allen, A. Allocca, M. A. Aloy, P. A. Altin, A. Amato, A. Ananyeva, S. B. Anderson, W. G. Anderson, S. V. Angelova, S. Antier, S. Appert, K. Arai, M. C. Araya, J. S. Areeda, M. Arène, N. Arnaud, K. G. Arun, S. Ascenzi, G. Ashton, S. M. Aston, P. Astone, F. Aubin, P. Aufmuth, K. AultONEal, C. Austin, V. Avendano, A. Avila-Alvarez, S. Babak, P. Bacon, F. Badaracco, M. K. M. Bader, S. Bae, P. T. Baker, F. Baldaccini, G. Ballardin, S. W. Ballmer, S. Banagiri, J. C. Barayoga, S. E. Barclay, B. C. Barish, D. Barker, K. Barkett, S. Barnum, F. Barone, B. Barr, L. Barsotti, M. Barsuglia, D. Barta, J. Bartlett, I. Bartos, R. Bassiri, A. Basti, M. Bawaj, J. C. Bayley, M. Bazzan, B. Bécsy, M. Bejger, I. Belahcene, A. S. Bell, D. Beniwal, B. K. Berger, G. Bergmann, S. Bernuzzi, J. J. Bero, C. P. L. Berry, D. Bersanetti, A. Bertolini, J. Betzwieser, R. Bhandare, J. Bidler, I. A. Bilenko, S. A. Bilgili, G. Billingsley, J. Birch, R. Birney, O. Birnholtz, S. Biscans, S. Biscoveanu, A. Bisht, M. Bitossi, M. A. Bizouard, J. K. Blackburn, J. Blackman, C. D. Blair, D. G. Blair, R. M. Blair, S. Bloemen, N. Bode, M. Boer, Y. Boetzel, G. Bogaert, F. Bondu, E. Bonilla, R. Bonnand, P. Booker, B. A. Boom, C. D. Booth, R. Bork, and V. and Boschi. Gwtc-1: A gravitational-wave transient catalog of compact binary mergers observed by ligo and virgo during the first and second observing runs. *PhRvX*, 9:031040, Sep 2019.
- [193] R. Abbott, T. D. Abbott, S. Abraham, F. Acernese, K. Ackley, A. Adams, C. Adams, R. X. Adhikari, V. B. Adya, C. Affeldt, M. Agathos, K. Agatsuma, N. Aggarwal, O. D. Aguiar, L. Aiello, A. Ain, P. Ajith, S. Akcay, G. Allen, A. Allocca, P. A. Altin, A. Amato, S. Anand, A. Ananyeva, S. B. Anderson, W. G. Anderson, S. V. Angelova, S. Ansoldi, J. M. Antelis, S. Antier, S. Appert, K. Arai, M. C. Araya, J. S. Areeda, M. Arène, N. Arnaud, S. M. Aronson, K. G. Arun, Y. Asali, S. Ascenzi, G. Ashton, S. M. Aston, P. Astone, F. Aubin, P. Aufmuth, K. AultONEal, C. Austin, V. Avendano, S. Babak, F. Badaracco, M. K. M. Bader, S. Bae, A. M. Baer, S. Bagnasco, J. Baird, M. Ball, G. Ballardin, S. W. Ballmer, A. Bals, A. Balsamo, G. Baltus, S. Banagiri, D. Bankar, R. S. Bankar, J. C. Barayoga, C. Barbieri, B. C. Barish, D. Barker, P. Barneo, S. Barnum, F. Barone, B. Barr, L. Barsotti, M. Barsuglia, D. Barta, J. Bartlett, I. Bartos, R. Bassiri, A. Basti, M. Bawaj, J. C. Bayley, M. Bazzan, B. R. Becher, B. Bécsy, V. M. Bedakihale, M. Bejger, I. Belahcene, D. Beniwal, M. G. Benjamin, T. F. Bennett, J. D. Bentley, F. Bergamin, B. K. Berger, G. Bergmann, S. Bernuzzi, C. P. L. Berry, D. Bersanetti, A. Bertolini,

J. Betzwieser, R. Bhandare, A. V. Bhandari, D. Bhattacharjee, J. Bidler, I. A. Bilenko, G. Billingsley, R. Birney, O. Birnholtz, S. Biscans, M. Bischi, S. Biscoveanu, A. Bisht, M. Bitossi, M. A. Bizouard, J. K. Blackburn, J. Blackman, C. D. Blair, D. G. Blair, R. M. Blair, O. Blanch, F. Bobba, N. Bode, M. Boer, Y. Boetzel, G. Bogaert, M. Boldrini, F. Bondu, E. Bonilla, R. Bonnand, P. Booker, B. A. Boom, R. Bork, V. Boschi, S. Bose, V. Bossilkov, V. Boudart, Y. Bouffanais, A. Bozzi, C. Bradaschia, P. R. Brady, A. Bramley, M. Branchesi, J. E. Brau, M. Breschi, T. Briant, J. H. Briggs, F. Brightenti, A. Brillet, M. Brinkmann, P. Brockill, A. F. Brooks, J. Brooks, D. D. Brown, S. Brunett, G. Bruno, R. Bruntz, A. Buikema, T. Bulik, H. J. Bulten, A. Buonanno, R. Buscicchio, D. Buskulic, R. L. Byer, M. Cabero, L. Cadonati, M. Caesar, G. Cagnoli, C. Cahillane, J. Calderón Bustillo, J. D. Callaghan, T. A. Callister, E. Calloni, J. B. Camp, M. Canepa, K. C. Cannon, H. Cao, J. Cao, G. Carapella, F. Carbognani, M. F. Carney, M. Carpinelli, G. Carullo, T. L. Carver, J. Casanueva Diaz, C. Casentini, S. Caudill, M. Cavaglià, F. Cavalier, R. Cavalieri, G. Cella, P. Cerdá-Durán, E. Cesarini, W. Chaibi, K. Chakravarti, C. L. Chan, C. Chan, K. Chandra, P. Chanial, S. Chao, P. Charlton, E. A. Chase, E. Chassande-Mottin, D. Chatterjee, D. Chattopadhyay, M. Chaturvedi, K. Chatzioannou, A. Chen, H. Y. Chen, X. Chen, Y. Chen, H. P. Cheng, C. K. Cheong, H. Y. Chia, F. Chiadini, R. Chierici, A. Chin-carini, A. Chiummo, G. Cho, H. S. Cho, M. Cho, S. Choate, N. Christensen, Q. Chu, S. Chua, K. W. Chung, S. Chung, G. Ciani, P. Ciecielag, M. Cieślar, M. Cifaldi, A. A. Ciobanu, R. Ciolfi, F. Cipriano, A. Cirone, F. Clara, E. N. Clark, J. A. Clark, L. Clarke, P. Clearwater, S. Clesse, F. Cleva, E. Coccia, P. F. Cohadon, D. E. Cohen, M. Colleoni, C. G. Collette, C. Collins, M. Colpi, M. Constancio, L. Conti, S. J. Cooper, P. Corban, T. R. Corbitt, I. Cordero-Carrión, S. Corezzi, K. R. Corley, N. Cornish, D. Corre, A. Corsi, S. Cortese, C. A. Costa, R. Cotesta, M. W. Coughlin, S. B. Coughlin, J. P. Coulon, S. T. Countryman, B. Cousins, P. Couvares, P. B. Covas, D. M. Coward, M. J. Cowart, D. C. Coyne, R. Coyne, J. D. E. Creighton, T. D. Creighton, M. Croquette, S. G. Crowder, J. R. Cudell, T. J. Cullen, A. Cumming, R. Cummings, L. Cunningham, E. Cuoco, M. Curyło, T. Dal Canton, G. Dálya, A. Dana, L. M. DaneshgaranBajastani, B. D'Angelo, B. Danila, S. L. Danilishin, S. D'Antonio, K. Danzmann, C. Darsow-Fromm, A. Dasgupta, L. E. H. Datrier, V. Dattilo, I. Dave, M. Davier, G. S. Davies, D. Davis, E. J. Daw, R. Dean, D. De-Bra, M. Deenadayalan, J. Degallaix, M. De Laurentis, S. Deléglise, V. Del Favero, F. De Lillo, N. De Lillo, W. Del Pozzo, L. M. DeMarchi, F. De Matteis, V. D'Emilio, N. Demos, T. Denker, T. Dent, A. Depasse, R. De Pietri, R. De Rosa, C. De Rossi, R. DeSalvo, O. de Varona, S. Dhurandhar, M. C. Díaz, M. Diaz-Ortiz, N. A. Didio, T. Dietrich, L. Di Fiore, C. DiFronzo, C. Di Giorgio, F. Di Giovanni, M. Di Giovanni, T. Di Girolamo, A. Di Lieto, B. Ding, S. Di Pace, I. Di Palma, F. Di Renzo, A. K. Divakarla, A. Dmitriev, Z. Doctor, L. D'Onofrio, F. Donovan, K. L. Dooley, S. Doravari, I. Dorrington, T. P. Downes, M. Drago, J. C. Driggers, Z. Du, J. G. Ducoin, P. Dupej, O. Durante, D. D'Urso, P. A. Duverne, S. E. Dwyer, P. J. Easter, G. Eddolls, B. Edelman, T. B. Edo, O. Edy, A. Effler, J. Eichholz, S. S. Eikenberry, M. Eisenmann, R. A. Eisenstein, A. Ejlli, L. Errico, R. C. Essick, H. Estellés, D. Estevez, Z. B. Etienne, T. Etzel, M. Evans, T. M. Evans, B. E. Ewing, V. Fafone, H. Fair, S. Fairhurst, X. Fan, A. M. Farah, S. Farinon, B. Farr, W. M. Farr, E. J. Fauchon-Jones, M. Favata, M. Fays, M. Fazio, J. Feicht, M. M. Fejer, F. Feng, E. Fenyvesi, D. L. Ferguson, A. Fernandez-Galiana, I. Ferrante, T. A. Ferreira, F. Fidecaro, P. Figura, I. Fiori, D. Fiorucci, M. Fishbach, R. P. Fisher, J. M. Fishner, R. Fit-

tipaldi, M. Fitz-Axen, V. Fiumara, R. Flaminio, E. Floden, E. Flynn, H. Fong, J. A. Font, P. W. F. Forsyth, J. D. Fournier, S. Frasca, F. Frasconi, Z. Frei, A. Freise, R. Frey, V. Frey, P. Fritschel, V. V. Frolov, G. G. Fronzé, P. Fulda, M. Fyffe, H. A. Gabbard, B. U. Gadre, S. M. Gaebel, J. R. Gair, J. Gais, S. Galaudage, R. Gamba, D. Ganapathy, A. Ganguly, S. G. Gaonkar, B. Garaventa, C. García-Quirós, F. Garufi, B. Gateley, S. Gaudio, V. Gayathri, G. Gemme, A. Gennai, D. George, J. George, R. N. George, L. Gergely, S. Ghonge, Abhirup Ghosh, Archisman Ghosh, S. Ghosh, B. Giacomazzo, L. Giacoppo, J. A. Giaime, K. D. Giardina, D. R. Gibson, C. Gier, K. Gill, P. Giri, J. Glanzer, A. E. Gleckl, P. Godwin, E. Goetz, R. Goetz, N. Gohlke, B. Goncharov, G. González, A. Gopakumar, S. E. Gossan, M. Gosselin, R. Gouaty, B. Grace, A. Grado, M. Granata, V. Granata, A. Grant, S. Gras, P. Grassia, C. Gray, R. Gray, G. Greco, A. C. Green, R. Green, E. M. Gretarsson, H. L. Griggs, G. Grignani, A. Grimaldi, E. Grimes, S. J. Grimm, H. Grote, S. Grunewald, P. Gruning, J. G. Guerrero, G. M. Guidi, A. R. Guimaraes, G. Guixé, H. K. Gulati, Y. Guo, Anchal Gupta, Anuradha Gupta, P. Gupta, E. K. Gustafson, R. Gustafson, F. Guzman, L. Haegel, O. Halim, E. D. Hall, E. Z. Hamilton, G. Hammond, M. Haney, M. M. Hanke, J. Hanks, C. Hanna, M. D. Hannam, O. A. Hannuksela, O. Hannuksela, H. Hansen, T. J. Hansen, J. Hanson, T. Harder, T. Hardwick, K. Haris, J. Harms, G. M. Harry, I. W. Harry, D. Hartwig, R. K. Hasskew, C. J. Haster, K. Haughian, F. J. Hayes, J. Healy, A. Heidmann, M. C. Heintze, J. Heinze, J. Heinzel, H. Heitmann, F. Hellman, P. Hello, A. F. Helmling-Cornell, G. Hemming, M. Hendry, I. S. Heng, E. Hennes, J. Hennig, M. H. Hennig, F. Hernandez Vivanco, M. Heurs, S. Hild, P. Hill, A. S. Hines, S. Hochheim, E. Hofgard, D. Hofman, J. N. Hohmann, A. M. Holgado, N. A. Holland, I. J. Hollows, Z. J. Holmes, K. Holt, D. E. Holz, P. Hopkins, C. Horst, J. Hough, E. J. Howell, C. G. Hoy, D. Hoyland, Y. Huang, M. T. Hübner, A. D. Huddart, E. A. Huerta, B. Hughey, V. Hui, S. Husa, S. H. Huttner, B. M. Hutzler, R. Huxford, T. Huynh-Dinh, B. Idzkowski, A. Iess, S. Imperato, H. Inchauspe, C. Ingram, G. Intini, M. Isi, B. R. Iyer, V. Jaberian-Hamedan, T. Jacqmin, S. J. Jadhav, S. P. Jadhav, A. L. James, K. Jani, K. Janssens, N. N. Janthalur, P. Jaranowski, D. Jariwala, R. Jaume, A. C. Jenkins, M. Jeunon, J. Jiang, G. R. Johns, N. K. Johnson-McDaniel, A. W. Jones, D. I. Jones, J. D. Jones, P. Jones, R. Jones, R. J. G. Jonker, L. Ju, J. Junker, C. V. Kalaghatgi, V. Kalogera, B. Kamai, S. Kandhasamy, G. Kang, J. B. Kanner, S. J. Kapadia, D. P. Kapasi, C. Karathanasis, S. Karki, R. Kashyap, M. Kasprzack, W. Kastaun, S. Katsanevas, E. Katsavounidis, W. Katzman, K. Kawabe, F. Kéfélian, D. Keitel, J. S. Key, S. Khadka, F. Y. Khalili, I. Khan, S. Khan, E. A. Khazanov, N. Khetan, M. Khursheed, N. Kijbunchoo, C. Kim, G. J. Kim, J. C. Kim, K. Kim, W. S. Kim, Y. M. Kim, C. Kimball, P. J. King, M. Kinley-Hanlon, R. Kirchhoff, J. S. Kissel, L. Kleybolte, S. Klimenko, T. D. Knowles, E. Knyazev, P. Koch, S. M. Koehlenbeck, G. Koekoek, S. Koley, M. Kolstein, K. Komori, V. Kondrashov, A. Kontos, N. Koper, M. Korobko, W. Z. Korth, M. Kovalam, D. B. Kozak, C. Krämer, V. Kringel, N. V. Krishnendu, A. Królak, G. Kuehn, A. Kumar, P. Kumar, Rahul Kumar, Rakesh Kumar, K. Kuns, S. Kwang, B. D. Lackey, D. Laghi, E. Lalande, T. L. Lam, A. Lamberts, M. Landry, B. B. Lane, R. N. Lang, J. Lange, B. Lantz, R. K. Lanza, I. La Rosa, A. Lartaux-Vollard, P. D. Lasky, M. Laxen, A. Lazzarini, C. Lazzaro, P. Leaci, S. Leavey, Y. K. Lecoeuche, H. M. Lee, H. W. Lee, J. Lee, K. Lee, J. Lehmann, E. Leon, N. Leroy, N. Letendre, Y. Levin, A. Li, J. Li, K. J. L. Li, T. G. F. Li, X. Li, F. Linde, S. D. Linker, J. N. Linley, T. B. Littenberg, J. Liu, X. Liu, M. Llorens-Monteagudo, R. K. L. Lo, A. Lockwood, L. T.

London, A. Longo, M. Lorenzini, V. Loriette, M. Lormand, G. Losurdo, J. D. Lough, C. O. Lousto, G. Lovelace, H. Lück, D. Lumaca, A. P. Lundgren, Y. Ma, R. Macas, M. MacInnis, D. M. Macleod, I. A. O. MacMillan, A. Macquet, I. Magaña Hernandez, F. Magaña-Sandoval, C. Magazzù, R. M. Magee, E. Majorana, I. Maksimovic, S. Malakal, A. Malik, N. Man, V. Mandic, V. Mangano, G. L. Mansell, M. Manske, M. Mantovani, M. Mapelli, F. Marchesoni, F. Marion, S. Márka, Z. Márka, C. Markakis, A. S. Markosyan, A. Markowitz, E. Maros, A. Marquina, S. Marsat, F. Martelli, I. W. Martin, R. M. Martin, M. Martinez, V. Martinez, D. V. Martynov, H. Masalehdan, K. Mason, E. Massera, A. Masserot, T. J. Massinger, M. Masso-Reid, S. Mastrogiovanni, A. Matas, M. Mateu-Lucena, F. Matichard, M. Matiushechkina, N. Mavalvala, E. Maynard, J. J. McCann, R. McCarthy, D. E. McClelland, S. McCormick, L. McCuller, S. C. McGuire, C. McIsaac, J. McIver, D. J. McManus, T. McRae, S. T. McWilliams, D. Meacher, G. D. Meadors, M. Mehmet, A. K. Mehta, A. Melatos, D. A. Melchor, G. Mendell, A. Menendez-Vazquez, R. A. Mercer, L. Mereni, K. Merfeld, E. L. Merilh, J. D. Merritt, M. Merzougui, S. Meshkov, C. Messenger, C. Messick, R. Metzdorff, P. M. Meyers, F. Meylahn, A. Mhaske, A. Miani, H. Miao, I. Michaloliakos, C. Michel, H. Middleton, L. Milano, A. L. Miller, M. Millhouse, J. C. Mills, E. Milotti, M. C. Milovich-Goff, O. Minazzoli, Y. Minenkov, Ll. M. Mir, A. Mishkin, C. Mishra, T. Mistry, S. Mitra, V. P. Mitrofanov, G. Mitselmakher, R. Mittleman, G. Mo, K. Mogushi, S. R. P. Mohapatra, S. R. Mohite, I. Molina, M. Molina-Ruiz, M. Mondin, M. Montani, C. J. Moore, D. Moraru, F. Morawski, G. Moreno, S. Morisaki, B. Mouris, C. M. Mow-Lowry, S. Mozzon, F. Muciaccia, Arunava Mukherjee, D. Mukherjee, Soma Mukherjee, Subroto Mukherjee, N. Mukund, A. Mullavey, J. Munch, E. A. Muñiz, P. G. Murray, S. L. Nadji, A. Nagar, I. Nardecchia, L. Naticchioni, R. K. Nayak, B. F. Neil, J. Neilson, G. Nelemans, T. J. N. Nelson, M. Nery, A. Neunzert, A. H. Nitz, K. Y. Ng, S. Ng, C. Nguyen, P. Nguyen, T. Nguyen, S. A. Nichols, S. Nissanke, F. Nocera, M. Noh, C. North, D. Nothard, L. K. Nuttall, J. Oberling, B. D. O'Brien, J. O'Dell, G. Oganesyan, G. H. Ogin, J. J. Oh, S. H. Oh, F. Ohme, H. Ohta, M. A. Okada, C. Olivetto, P. Oppermann, R. J. Oram, B. O'Reilly, R. G. Ormiston, L. F. Ortega, R. O'Shaughnessy, S. Ossokine, C. Osthelder, D. J. Ottaway, H. Overmier, B. J. Owen, A. E. Pace, G. Pagano, M. A. Page, G. Pagliaroli, A. Pai, S. A. Pai, J. R. Palamos, O. Palashov, C. Palomba, H. Pan, P. K. Panda, T. H. Pang, C. Pankow, F. Pannarale, B. C. Pant, F. Paoletti, A. Paoli, A. Paolone, W. Parker, D. Pasucci, A. Pasqualetti, R. Passaquieti, D. Passuello, M. Patel, B. Patricelli, E. Payne, T. C. Pechsiri, M. Pedraza, M. Pegoraro, A. Pele, S. Penn, A. Perego, C. J. Perez, C. Périgois, A. Perreca, S. Perriès, J. Petermann, D. Petterson, H. P. Pfeiffer, K. A. Pham, K. S. Phukon, O. J. Piccinni, M. Pichot, M. Piendibene, F. Piergiovanni, L. Pierini, V. Pierro, G. Pillant, F. Pilo, L. Pinard, I. M. Pinto, K. Piotrzkowski, M. Pirello, M. Pitkin, E. Placidi, W. Plastino, C. Pluchar, R. Poggiani, E. Polini, D. Y. T. Pong, S. Ponrathnam, P. Popolizio, E. K. Porter, A. Poverman, J. Powell, M. Pracchia, A. K. Prajapati, K. Prasai, R. Prasanna, G. Pratten, T. Prestegard, M. Principe, G. A. Prodi, L. Prokhorov, P. Prosposito, L. Prudenzi, A. Puecher, M. Punturo, F. Puosi, P. Puppo, M. Pürrer, H. Qi, V. Quetschke, P. J. Quinonez, R. Quitzow-James, F. J. Raab, G. Raaijmakers, H. Radkins, N. Radulesco, P. Raffai, H. Rafferty, S. X. Rail, S. Raja, C. Rajan, B. Rajbhandari, M. Rakhmanov, K. E. Ramirez, T. D. Ramirez, A. Ramos-Buades, J. Rana, K. Rao, P. Rapagnani, U. D. Rapol, B. Ratto, V. Raymond, M. Razzano, J. Read, T. Regimbau, L. Rei, S. Reid, D. H.

Reitze, P. Rettegno, F. Ricci, C. J. Richardson, J. W. Richardson, L. Richardson, P. M. Ricker, G. Riemenschneider, K. Riles, M. Rizzo, N. A. Robertson, F. Robinet, A. Rocchi, J. A. Rocha, S. Rodriguez, R. D. Rodriguez-Soto, L. Rolland, J. G. Rollins, V. J. Roma, M. Romanelli, R. Romano, C. L. Romel, A. Romero, I. M. Romero-Shaw, J. H. Romie, S. Ronchini, C. A. Rose, D. Rose, K. Rose, M. J. B. Rosell, D. Rosińska, S. G. Rosofsky, M. P. Ross, S. Rowan, S. J. Rowlinson, Santosh Roy, Soumen Roy, P. Ruggi, K. Ryan, S. Sachdev, T. Sadecki, J. Sadiq, M. Sakellariadou, O. S. Salafia, L. Salconi, M. Saleem, A. Samajdar, E. J. Sanchez, J. H. Sanchez, L. E. Sanchez, N. Sanchis-Gual, J. R. Sanders, L. Sandles, K. A. Santiago, E. Santos, T. R. Saravanan, N. Sarin, B. Sas-solas, B. S. Sathyaprakash, O. Sauter, R. L. Savage, V. Savant, D. Sawant, S. Sayah, D. Schaetzl, P. Schale, M. Scheel, J. Scheuer, A. Schindler-Tyka, P. Schmidt, R. Schnabel, R. M. S. Schofield, A. Schönbeck, E. Schreiber, B. W. Schulte, B. F. Schutz, O. Schwarm, E. Schwartz, J. Scott, S. M. Scott, M. Seglar-Arroyo, E. Seidel, D. Sellers, A. S. Sengupta, N. Sennett, D. Sentenac, V. Sequino, A. Sergeev, Y. Setyawati, T. Shaffer, M. S. Shahriar, S. Sharifi, A. Sharma, P. Sharma, P. Shawhan, H. Shen, M. Shikauchi, R. Shink, D. H. Shoemaker, D. M. Shoemaker, K. Shukla, S. ShyamSundar, M. Sieniawska, D. Sigg, L. P. Singer, D. Singh, N. Singh, A. Singha, A. Singhal, A. M. Sintes, V. Sipala, V. Skliris, B. J. J. Slagmolen, T. J. Slaven-Blair, J. Smetana, J. R. Smith, R. J. E. Smith, S. N. So-mala, E. J. Son, K. Soni, S. Soni, B. Sorazu, V. Sordini, F. Sorrentino, N. Sorrentino, R. Soulard, T. Souradeep, E. Sowell, A. P. Spencer, M. Spera, A. K. Srivastava, V. Srivas-tava, K. Staats, C. Stachie, D. A. Steer, J. Steinhoff, M. Steinke, J. Steinlechner, S. Stein-lechner, D. Steinmeyer, S. P. Stevenson, G. Stolle-McAllister, D. J. Stops, M. Stover, K. A. Strain, G. Stratta, A. Strunk, R. Sturani, A. L. Stuver, J. Südbeck, S. Sudhagar, V. Sudhir, H. G. Suh, T. Z. Summerscales, H. Sun, L. Sun, S. Sunil, A. Sur, J. Suresh, P. J. Sutton, B. L. Swinkels, M. J. Szczepańczyk, M. Tacca, S. C. Tait, C. Talbot, A. J. Tanasijczuk, D. B. Tanner, D. Tao, A. Tapia, E. N. Tapia San Martin, J. D. Tasson, R. Tay-lor, R. Tenorio, L. Terkowski, M. P. Thirugnanasambandam, L. M. Thomas, M. Thomas, P. Thomas, J. E. Thompson, S. R. Thondapu, K. A. Thorne, E. Thrane, Shubhanshu Ti-wari, Srishti Tiwari, V. Tiwari, K. Toland, A. E. Tolley, M. Tonelli, Z. Tornasi, A. Torres-Forné, C. I. Torrie, I. Tosta e Melo, D. Töyrä, A. T. Tran, A. Trapananti, F. Travasso, G. Traylor, M. C. Tringali, A. Tripathee, A. Trovato, R. J. Trudeau, D. S. Tsai, K. W. Tsang, M. Tse, R. Tso, L. Tsukada, D. Tsuna, T. Tsutsui, M. Turconi, A. S. Ubhi, R. P. Udall, K. Ueno, D. Ugolini, C. S. Unnikrishnan, A. L. Urban, S. A. Usman, A. C. Utina, H. Vahlbruch, G. Vajente, A. Vajpeyi, G. Valdes, M. Valentini, V. Valsan, N. van Bakel, M. van Beuzekom, J. F. J. van den Brand, C. Van Den Broeck, D. C. Vander-Hyde, L. van der Schaaf, J. V. van Heijningen, M. Vardaro, A. F. Vargas, V. Varma, S. Vass, M. Vasúth, A. Vecchio, G. Vedovato, J. Veitch, P. J. Veitch, K. Venkateswara, J. Venneberg, G. Venu-gopalan, D. Verkindt, Y. Verma, D. Veske, F. Vetrano, A. Viceré, A. D. Viets, A. Vijayku-mar, V. Villa-Ortega, J. Y. Vinet, S. Vitale, T. Vo, H. Vocca, C. Vorvick, S. P. Vyatchanin, A. R. Wade, L. E. Wade, M. Wade, R. C. Walet, M. Walker, G. S. Wallace, L. Wallace, S. Walsh, J. Z. Wang, S. Wang, W. H. Wang, Y. F. Wang, R. L. Ward, J. Warner, M. Was, N. Y. Washington, J. Watchi, B. Weaver, L. Wei, M. Weinert, A. J. Weinstein, R. Weiss, F. Wellmann, L. Wen, P. Weßels, J. W. Westhouse, K. Wette, J. T. Whelan, D. D. White, L. V. White, B. F. Whiting, C. Whittle, D. M. Wilken, D. Williams, M. J. Williams, A. R. Williamson, J. L. Willis, B. Willke, D. J. Wilson, M. H. Wimmer, W. Winkler, C. C. Wipf,

- G. Woan, J. Woehler, J. K. Wofford, I. C. F. Wong, J. Wrangel, J. L. Wright, D. S. Wu, D. M. Wysocki, L. Xiao, H. Yamamoto, L. Yang, Y. Yang, Z. Yang, M. J. Yap, D. W. Yeeles, A. Yoon, Hang Yu, Haocun Yu, S. H. R. Yuen, A. Zadrożny, M. Zanolin, T. Zelenova, J. P. Zendri, M. Zevin, J. Zhang, L. Zhang, R. Zhang, T. Zhang, C. Zhao, G. Zhao, Y. Zheng, M. Zhou, Z. Zhou, X. J. Zhu, A. B. Zimmerman, Y. Zlochower, M. E. Zucker, J. Zweizig, LIGO Scientific Collaboration, and Virgo Collaboration. GWTC-2: Compact Binary Coalescences Observed by LIGO and Virgo during the First Half of the Third Observing Run. [PhRvX](#), 11(2):021053, April 2021.
- [194] R. Abbott et al. GWTC-2.1: Deep Extended Catalog of Compact Binary Coalescences Observed by LIGO and Virgo During the First Half of the Third Observing Run. 8 2021.
- [195] V. Connaughton, E. Burns, A. Goldstein, L. Blackburn, M. S. Briggs, B. B. Zhang, J. Camp, N. Christensen, C. M. Hui, P. Jenke, T. Littenberg, J. E. McEneany, J. Racusin, P. Shawhan, L. Singer, J. Veitch, C. A. Wilson-Hodge, P. N. Bhat, E. Bissaldi, W. Cleveland, G. Fitzpatrick, M. M. Giles, M. H. Gibby, A. von Kienlin, R. M. Kippen, S. McBreen, B. Mailyan, C. A. Meegan, W. S. Paciesas, R. D. Preece, O. J. Roberts, L. Sparke, M. Stanbro, K. Toelge, and P. Veres. Fermi GBM Observations of LIGO Gravitational-wave Event GW150914. [Astrophysical Journal Letters](#), 826(1):L6, July 2016.
- [196] LSC and Virgo and Fermi-GBM Team. Fermi GBM-190816: A subthreshold GRB candidate potentially associated with a subthreshold LIGO/Virgo compact binary merger candidate. [GRB Coordinates Network](#), 25406:1, August 2019.
- [197] LSC and Virgo and Fermi-GBM Team. Fermi GBM-190816: Updated localization of subthreshold GRB-GW candidate. [GRB Coordinates Network](#), 25465:1, August 2019.
- [198] M. J. Graham, K. E. S. Ford, B. McKernan, N. P. Ross, D. Stern, K. Burdge, M. Coughlin, S. G. Djorgovski, A. J. Drake, D. Duev, M. Kasliwal, A. A. Mahabal, S. van Velzen, J. Belecki, E. C. Bellm, R. Burruss, S. B. Cenko, V. Cunningham, G. Helou, S. R. Kularkci, F. J. Masci, T. Prince, D. Reiley, H. Rodriguez, B. Rusholme, R. M. Smith, and M. T. Soumagnac. Candidate electromagnetic counterpart to the binary black hole merger gravitational-wave event s190521g. [PhRvL](#), 124:251102, Jun 2020.
- [199] Gregory Ashton, Kendall Ackley, Ignacio Magaña Hernandez, and Brandon Piotrkowski. Current observations are insufficient to confidently associate the binary black hole merger GW190521 with AGN J124942.3 + 344929. [CQGra](#), 38(23):235004, December 2021.
- [200] Juan Calderón Bustillo, Samson H. W. Leong, Koustav Chandra, Barry McKernan, and K. E. S. Ford. GW190521 as a black-hole merger coincident with the ZTF19abanrhr flare. 12 2021.
- [201] F. De Paolis, A. A. Nucita, F. Strafella, D. Licchelli, and G. Ingrosso. A quasar microlensing event towards J1249+3449? [Monthly Notices of the Royal Astronomical Society](#), 499(1):L87–L90, December 2020.

- [202] A. Palmese, M. Fishbach, C. J. Burke, J. Annis, and X. Liu. Do LIGO/Virgo Black Hole Mergers Produce AGN Flares? The Case of GW190521 and Prospects for Reaching a Confident Association. *Astrophysical Journal Letters*, 914(2):L34, June 2021.
- [203] R. Chornock, E. Berger, D. Kasen, P. S. Cowperthwaite, M. Nicholl, V. A. Villar, K. D. Alexander, P. K. Blanchard, T. Eftekhari, W. Fong, R. Margutti, P. K. G. Williams, J. Annis, D. Brout, D. A. Brown, H.-Y. Chen, M. R. Drout, B. Farr, R. J. Foley, J. A. Frieman, C. L. Fryer, K. Herner, D. E. Holz, R. Kessler, T. Matheson, B. D. Metzger, E. Quataert, A. Rest, M. Sako, D. M. Scolnic, N. Smith, and M. Soares-Santos. The electromagnetic counterpart of the binary neutron star merger LIGO/virgo GW170817. IV. detection of near-infrared signatures of r-process nucleosynthesis with gemini-south. *ApJ*, 848(2):L19, oct 2017.
- [204] P. S. Cowperthwaite, E. Berger, V. A. Villar, B. D. Metzger, M. Nicholl, R. Chornock, P. K. Blanchard, W. Fong, R. Margutti, M. Soares-Santos, K. D. Alexander, S. Allam, J. Annis, D. Brout, D. A. Brown, R. E. Butler, H.-Y. Chen, H. T. Diehl, Z. Doctor, M. R. Drout, T. Eftekhari, B. Farr, D. A. Finley, R. J. Foley, J. A. Frieman, C. L. Fryer, J. García-Bellido, M. S. S. Gill, J. Guillochon, K. Herner, D. E. Holz, D. Kasen, R. Kessler, J. Marriner, T. Matheson, E. H. Neilsen, E. Quataert, A. Palmese, A. Rest, M. Sako, D. M. Scolnic, N. Smith, D. L. Tucker, P. K. G. Williams, E. Balbinot, J. L. Carlin, E. R. Cook, F. Durret, T. S. Li, P. A. A. Lopes, A. C. C. Lourenço, J. L. Marshall, G. E. Medina, J. Muir, R. R. Muñoz, M. Sauseda, D. J. Schlegel, L. F. Secco, and A. K. Vivas and. The electromagnetic counterpart of the binary neutron star merger LIGO/virgo GW170817. II. UV, optical, and near-infrared light curves and comparison to kilonova models. *ApJ*, 848(2):L17, oct 2017.
- [205] M. Nicholl, E. Berger, D. Kasen, B. D. Metzger, J. Elias, C. Briceño, K. D. Alexander, P. K. Blanchard, R. Chornock, P. S. Cowperthwaite, T. Eftekhari, W. Fong, R. Margutti, V. A. Villar, P. K. G. Williams, W. Brown, J. Annis, A. Bahramian, D. Brout, D. A. Brown, H.-Y. Chen, J. C. Clemens, E. Dennihy, B. Dunlap, D. E. Holz, E. Marchesini, F. Massaro, N. Moskowitz, I. Pelisoli, A. Rest, F. Ricci, M. Sako, M. Soares-Santos, and J. Strader. The electromagnetic counterpart of the binary neutron star merger ligo/virgo gw170817. iii. optical and uv spectra of a blue kilonova from fast polar ejecta. *The Astrophysical Journal Letters*, 848(2):L18, oct 2017.
- [206] M. Soares-Santos, D. E. Holz, J. Annis, R. Chornock, K. Herner, E. Berger, D. Brout, H.-Y. Chen, R. Kessler, M. Sako, S. Allam, D. L. Tucker, R. E. Butler, A. Palmese, Z. Doctor, H. T. Diehl, J. Frieman, B. Yanny, H. Lin, D. Scolnic, P. Cowperthwaite, E. Neilsen, J. Marriner, N. Kuropatkin, W. G. Hartley, F. Paz-Chinchón, K. D. Alexander, E. Balbinot, P. Blanchard, D. A. Brown, J. L. Carlin, C. Conselice, E. R. Cook, A. Drlica-Wagner, M. R. Drout, F. Durret, T. Eftekhari, B. Farr, D. A. Finley, R. J. Foley, W. Fong, C. L. Fryer, J. García-Bellido, M. S . S. Gill, R. A. Gruendl, C. Hanna, D. Kasen, T. S. Li, P. A. A. Lopes, A. C. C. Lourenço, R. Margutti, J. L. Marshall, T. Matheson, G. E. Medina, B. D. Metzger, R. R. Muñoz, J. Muir, M. Nicholl, E. Quataert, A. Rest, M. Sauseda, D. J. Schlegel, L. F. Secco, F. Sobreira, A. Stebbins, V. A. Villar, K. Vivas, A. R. Walker, W. Wester, P. K. G. Williams, A. Zenteno, Y. Zhang, T. M. C. Abbott, F. B. Abdalla, M. Banerji, K. Bechtol, A. Benoit-Lévy, E. Bertin, D. Brooks, E. Buckley-Geer, D. L.

- Burke, A. Carnero Rosell, M. Carrasco Kind, J. Carretero, F. J. Castander, M. Crocce, C. E. Cunha, C. B. D’Andrea, L. N. da Costa, C. Davis, S. Desai, J. P. Dietrich, P. Doel, T. F. Eifler, E. Fernandez, B. Flaugher, P. Fosalba, E. Gaztanaga, D. W. Gerdes, T. Giannantonio, D. A. Goldstein, D. Gruen, J. Gschwend, G. Gutierrez, K. Honscheid, B. Jain, D. J. James, T. Jeltema, M. W. G. Johnson, M. D. Johnson, S. Kent, E. Krause, R. Kron, K. Kuehn, S. Kuhlmann, O. Lahav, M. Lima, M. A. G. Maia, M. March, R. G. McMahon, F. Menanteau, R. Miquel, J. J. Mohr, R. C. Nichol, B. Nord, R. L. C. Ogando, D. Petravick, A. A. Plazas, A. K. Romer, A. Roodman, E. S. Rykoff, E. Sanchez, V. Scarpine, M. Schubnell, I. Sevilla-Noarbe, M. Smith, R. C. Smith, E. Suchyta, M. E. C. Swanson, G. Tarle, D. Thomas, R. C. Thomas, M. A. Troxel, V. Vikram, R. H. Wechsler, J. Weller, (The Dark Energy Survey, and The Dark Energy Camera GW-EM Collaboration). The electromagnetic counterpart of the binary neutron star merger ligo/virgo gw170817. i. discovery of the optical counterpart using the dark energy camera. *The Astrophysical Journal Letters*, 848(2):L16, oct 2017.
- [207] N. R. Tanvir, A. J. Levan, C. González-Fernández, O. Korobkin, I. Mandel, S. Ross-wog, J. Hjorth, P. D’Avanzo, A. S. Fruchter, C. L. Fryer, T. Kangas, B. Milvang-Jensen, S. Rosetti, D. Steeghs, R. T. Wollaeger, Z. Cano, C. M. Copperwheat, S. Covino, V. D’Elia, A. de Ugarte Postigo, P. A. Evans, W. P. Even, S. Fairhurst, R. Figuera Jaimes, C. J. Fontes, Y. I. Fujii, J. P. U. Fynbo, B. P. Gompertz, J. Greiner, G. Hodosan, M. J. Irwin, P. Jakobsson, U. G. Jørgensen, D. A. Kann, J. D. Lyman, D. Malesani, R. G. McMahon, A. Melandri, P. T. O’Brien, J. P. Osborne, E. Palazzi, D. A. Perley, E. Pian, S. Piranomonte, M. Rabus, E. Rol, A. Rowlinson, S. Schulze, P. Sutton, C. C. Thöne, K. Ulaczyk, D. Watson, K. Wiersema, and R. A. M. J. Wijers. The emergence of a lanthanide-rich kilonova following the merger of two neutron stars. *ApJ*, 848(2):L27, oct 2017.
- [208] L. Blackburn, M. S. Briggs, J. Camp, N. Christensen, V. Connaughton, P. Jenke, R. A. Remillard, and J. Veitch. HIGH-ENERGY ELECTROMAGNETIC OFFLINE FOLLOW-UP OF LIGO-VIRGO GRAVITATIONAL-WAVE BINARY COALESCENCE CANDIDATE EVENTS. *The ApJS*, 217(1):8, mar 2015.
- [209] Adam Goldstein, Rachel Hamburg, Joshua Wood, C. Michelle Hui, William H. Cleveland, Daniel Kocevski, Tyson Littenberg, Eric Burns, Tito Dal Canton, Peter Veres, Bagrat Mai-lyan, Christian Malacaria, Michael S. Briggs, and Colleen A. Wilson-Hodge. Updates to the Fermi GBM Targeted Sub-threshold Search in Preparation for the Third Observing Run of LIGO/Virgo. *arXiv e-prints*, page arXiv:1903.12597, March 2019.
- [210] R. Hamburg, C. Fletcher, E. Burns, A. Goldstein, E. Bissaldi, M. S. Briggs, W. H. Cleveland, M. M. Giles, C. M. Hui, D. Kocevski, S. Lesage, B. Mailyan, C. Malacaria, S. Poolakkil, R. Preece, O. J. Roberts, P. Veres, A. von Kienlin, C. A. Wilson-Hodge, J. Wood, Fermi Gamma-Ray Burst Monitor, R. Abbott, T. D. Abbott, S. Abraham, F. Acernese, K. Ackley, C. Adams, R. X. Adhikari, V. B. Adya, C. Affeldt, M. Agathos, K. Agatsuma, N. Aggarwal, O. D. Aguiar, A. Aich, L. Aiello, A. Ain, P. Ajith, G. Allen, A. Allocca, P. A. Altin, A. Amato, S. Anand, A. Ananyeva, S. B. Anderson, W. G. Anderson, S. V. Angelova, S. Ansoldi, S. Antier, S. Appert, K. Arai, M. C. Araya, J. S.

Areeda, M. Arène, N. Arnaud, S. M. Aronson, S. Ascenzi, G. Ashton, S. M. Aston, P. Astone, F. Aubin, P. Aufmuth, K. AultONeal, C. Austin, V. Avendano, S. Babak, P. Bacon, F. Badaracco, M. K. M. Bader, S. Bae, A. M. Baer, J. Baird, F. Baldaccini, G. Ballardin, S. W. Ballmer, A. Bals, A. Balsamo, G. Baltus, S. Banagiri, D. Bankar, R. S. Bankar, J. C. Barayoga, C. Barbieri, B. C. Barish, D. Barker, K. Barkett, P. Barneo, F. Barone, B. Barr, L. Barsotti, M. Barsuglia, D. Barta, J. Bartlett, I. Bartos, R. Bassiri, A. Basti, M. Bawaj, J. C. Bayley, M. Bazzan, B. Bécsy, M. Bejger, I. Belahcene, A. S. Bell, D. Beniwal, M. G. Benjamin, J. D. Bentley, F. Bergamin, B. K. Berger, G. Bergmann, S. Bernuzzi, C. P. L. Berry, D. Bersanetti, A. Bertolini, J. Betzwieser, R. Bhandare, A. V. Bhandari, J. Bidler, E. Biggs, I. A. Bilenko, G. Billingsley, R. Birney, O. Birnholtz, S. Biscans, M. Bischi, S. Biscoveanu, A. Bisht, G. Bissenbayeva, M. Bitossi, M. A. Bizouard, J. K. Blackburn, J. Blackman, C. D. Blair, D. G. Blair, R. M. Blair, F. Bobba, N. Bode, M. Boer, Y. Boetzel, G. Bogaert, F. Bondu, E. Bonilla, R. Bonnand, P. Booker, B. A. Boom, R. Bork, V. Boschi, S. Bose, V. Bossilkov, J. Bosveld, Y. Bouffanais, A. Bozzi, C. Bradaschia, P. R. Brady, A. Bramley, M. Branchesi, J. E. Brau, M. Breschi, T. Briant, J. H. Briggs, F. Brighenti, A. Brillet, M. Brinkmann, P. Brockill, A. F. Brooks, J. Brooks, D. D. Brown, S. Brunett, G. Bruno, R. Bruntz, A. Buikema, T. Bulik, H. J. Bulten, A. Buonanno, D. Buskulic, R. L. Byer, M. Cabero, L. Cadonati, G. Cagnoli, C. Cahillane, J. Calderón Bustillo, J. D. Callaghan, T. A. Callister, E. Calloni, J. B. Camp, M. Canepa, K. C. Cannon, H. Cao, J. Cao, G. Carapella, F. Carbognani, S. Caride, M. F. Carney, G. Carullo, J. Casanueva Diaz, C. Casentini, J. Castañeda, S. Caudill, M. Cavaglià, F. Cavalier, R. Cavalieri, G. Cella, P. Cerdá-Durán, E. Cesarini, O. Chaibi, K. Chakravarti, C. Chan, M. Chan, S. Chao, P. Charlton, E. A. Chase, E. Chassande-Mottin, D. Chatterjee, M. Chaturvedi, H. Y. Chen, X. Chen, Y. Chen, H. P. Cheng, C. K. Cheong, H. Y. Chia, F. Chiadini, R. Chierici, A. Chincarini, A. Chiummo, G. Cho, H. S. Cho, M. Cho, N. Christensen, Q. Chu, S. Chua, K. W. Chung, S. Chung, G. Ciani, P. Ciecielag, M. Cieślar, A. A. Ciobanu, R. Ciolfi, F. Cipriano, A. Cirone, F. Clara, J. A. Clark, P. Clearwater, S. Clesse, F. Cleva, E. Coccia, P. F. Cohadon, D. Cohen, M. Colleoni, C. G. Collette, C. Collins, M. Colpi, Jr. Constancio, M., L. Conti, S. J. Cooper, P. Corban, T. R. Corbitt, I. Cordero-Carrión, S. Corezzi, K. R. Corley, N. Cornish, D. Corre, A. Corsi, S. Cortese, C. A. Costa, R. Cotesta, M. W. Coughlin, S. B. Coughlin, J. P. Coulon, S. T. Countryman, P. Couvares, P. B. Covas, D. M. Coward, M. J. Cowart, D. C. Coyne, R. Coyne, J. D. E. Creighton, T. D. Creighton, J. Cripe, M. Croquette, S. G. Crowder, J. R. Cudell, T. J. Cullen, A. Cumming, R. Cummings, L. Cunningham, E. Cuoco, M. Curylo, T. Dal Canton, G. Dálya, A. Dana, L. M. Daneshgaran-Bajastani, B. D'Angelo, S. L. Danilishin, S. D'Antonio, K. Danzmann, C. Darsow-Fromm, A. Dasgupta, L. E. H. Datrier, V. Dattilo, I. Dave, M. Davier, G. S. Davies, D. Davis, E. J. Daw, D. DeBra, M. Deenadayalan, J. Degallaix, M. De Laurentis, S. Deléglise, M. Delfavero, N. De Lillo, W. Del Pozzo, L. M. DeMarchi, V. D'Emilio, N. Demos, T. Dent, R. De Pietri, R. De Rosa, C. De Rossi, R. DeSalvo, O. de Varona, S. Dhurandhar, M. C. Díaz, Jr. Diaz-Ortiz, M., T. Dietrich, L. Di Fiore, C. Di Fronzo, C. Di Giorgio, F. Di Giovanni, M. Di Giovanni, T. Di Girolamo, A. Di Lieto, B. Ding, S. Di Pace, I. Di Palma, F. Di Renzo, A. K. Divakarla, A. Dmitriev, Z. Doctor, F. Donovan, K. L. Dooley, S. Doravari, I. Dorrington, T. P. Downes, M. Drago, J. C. Driggers, Z. Du, J. G. Ducoin, P. Dupej, O. Durante, D. D'Urso, S. E. Dwyer, P. J. Easter, G. Eddolls, B. Edelman, T. B. Edo, O. Edy, A. Effler, P. Ehrens, J. Eichholz, S. S. Eikenberry, M. Eisenmann,

R. A. Eisenstein, A. Ejlli, L. Errico, R. C. Essick, H. Estelles, D. Estevez, Z. B. Etienne, T. Etzel, M. Evans, T. M. Evans, B. E. Ewing, V. Fafone, S. Fairhurst, X. Fan, S. Farinon, B. Farr, W. M. Farr, E. J. Fauchon-Jones, M. Favata, M. Fays, M. Fazio, J. Feicht, M. M. Fejer, F. Feng, E. Fenyvesi, D. L. Ferguson, A. Fernandez-Galiana, I. Ferrante, E. C. Ferreira, T. A. Ferreira, F. Fidecaro, I. Fiori, D. Fiorucci, M. Fishbach, R. P. Fisher, R. Fittipaldi, M. Fitz-Axen, V. Fiumara, R. Flaminio, E. Floden, E. Flynn, H. Fong, J. A. Font, P. W. F. Forsyth, J. D. Fournier, S. Frasca, F. Frasconi, Z. Frei, A. Freise, R. Frey, V. Frey, P. Fritschel, V. V. Frolov, G. Fronzè, P. Fulda, M. Fyffe, H. A. Gabbard, B. U. Gadre, S. M. Gaebel, J. R. Gair, S. Galaudage, D. Ganapathy, S. G. Gaonkar, C. García-Quirós, F. Garufi, B. Gateley, S. Gaudio, V. Gayathri, G. Gemme, E. Genin, A. Gennai, D. George, J. George, L. Gergely, S. Ghonge, Abhirup Ghosh, Archisman Ghosh, S. Ghosh, B. Giacomazzo, J. A. Giaime, K. D. Giardina, D. R. Gibson, C. Gier, K. Gill, J. Glanzer, J. Gniesmer, P. Godwin, E. Goetz, R. Goetz, N. Gohlke, B. Goncharov, G. González, A. Gopakumar, S. E. Gossan, M. Gosselin, R. Gouaty, B. Grace, A. Grado, M. Granata, A. Grant, S. Gras, P. Grassia, C. Gray, R. Gray, G. Greco, A. C. Green, R. Green, E. M. Gretarsson, H. L. Griggs, G. Grignani, A. Grimaldi, S. J. Grimm, H. Grote, S. Grunewald, P. Gruning, G. M. Guidi, A. R. Guimaraes, G. Guixé, H. K. Gulati, Y. Guo, A. Gupta, Anchal Gupta, P. Gupta, E. K. Gustafson, R. Gustafson, L. Haegel, O. Halim, E. D. Hall, E. Z. Hamilton, G. Hammond, M. Haney, M. M. Hanke, J. Hanks, C. Hanna, M. D. Hannam, O. A. Hannuksela, T. J. Hansen, J. Hanson, T. Harder, T. Hardwick, K. Haris, J. Harms, G. M. Harry, I. W. Harry, R. K. Hasskew, C. J. Haster, K. Haughian, F. J. Hayes, J. Healy, A. Heidmann, M. C. Heintze, J. Heinze, H. Heitmann, F. Hellman, P. Hello, G. Hemming, M. Hendry, I. S. Heng, E. Hennes, J. Hennig, M. Heurs, S. Hild, T. Hinderer, S. Y. Hoback, S. Hochheim, E. Hofgard, D. Hofman, A. M. Holgado, N. A. Holland, K. Holt, D. E. Holz, P. Hopkins, C. Horst, J. Hough, E. J. Howell, C. G. Hoy, Y. Huang, M. T. Hübner, E. A. Huerta, D. Huet, B. Hughey, V. Hui, S. Husa, S. H. Huttner, R. Huxford, T. Huynh-Dinh, B. Idzkowski, A. Iess, H. Inchauspe, C. Ingram, G. Intini, J. M. Isac, M. Isi, B. R. Iyer, T. Jacqmin, S. J. Jadhav, S. P. Jadhav, A. L. James, K. Jani, N. N. Janthalur, P. Jaradowski, D. Jariwala, R. Jaume, A. C. Jenkins, J. Jiang, G. R. Johns, A. W. Jones, D. I. Jones, J. D. Jones, P. Jones, R. Jones, R. J. G. Jonker, L. Ju, J. Junker, C. V. Kalaghatgi, V. Kalogera, B. Kamai, S. Kandhasamy, G. Kang, J. B. Kanner, S. J. Kapadia, S. Karki, R. Kashyap, M. Kasprzack, W. Kastaun, S. Katsanevas, E. Katsavounidis, W. Katzman, S. Kaufer, K. Kawabe, F. Kéfélian, D. Keitel, A. Keivani, R. Kennedy, J. S. Key, S. Khadka, F. Y. Khalili, I. Khan, S. Khan, Z. A. Khan, E. A. Khazanov, N. Khetan, M. Khursheed, N. Kijbunchoo, Chunglee Kim, G. J. Kim, J. C. Kim, K. Kim, W. Kim, W. S. Kim, Y. M. Kim, C. Kimball, P. J. King, M. Kinley-Hanlon, R. Kirchhoff, J. S. Kissel, L. Kleybolte, S. Klimenko, T. D. Knowles, P. Koch, S. M. Koehlenbeck, G. Koekoek, S. Koley, V. Kondrashov, A. Kontos, N. Koper, M. Korobko, W. Z. Korth, M. Kovalam, D. B. Kozak, V. Kringel, N. V. Krishnendu, A. Królak, N. Krupinski, G. Kuehn, A. Kumar, P. Kumar, Rahul Kumar, Rakesh Kumar, S. Kumar, L. Kuo, A. Kutynia, B. D. Lackey, D. Laghi, E. Lalande, T. L. Lam, A. Lamberts, M. Landry, B. B. Lane, R. N. Lang, J. Lange, B. Lantz, R. K. Lanza, I. La Rosa, A. Lartaux-Vollard, P. D. Lasky, M. Laxen, A. Lazzarini, C. Lazzaro, P. Leaci, S. Leavey, Y. K. Lecoeuche, C. H. Lee, H. M. Lee, H. W. Lee, J. Lee, K. Lee, J. Lehmann, N. Leroy, N. Letendre, Y. Levin, A. K. Y. Li, J. Li, K. li, T. G. F. Li, X. Li, F. Linde, S. D. Linker, J. N. Linley, T. B. Littenberg, J. Liu, X. Liu, M. Llorens-Monteagudo,

R. K. L. Lo, A. Lockwood, L. T. London, A. Longo, M. Lorenzini, V. Loriette, M. Lormand, G. Losurdo, J. D. Lough, C. O. Lousto, G. Lovelace, H. Lück, D. Lumaca, A. P. Lundgren, Y. Ma, R. Macas, S. Macfoy, M. MacInnis, D. M. Macleod, I. A. O. MacMillan, A. Macquet, I. Magaña Hernandez, F. Magaña-Sandoval, R. M. Magee, E. Majorana, I. Maksimovic, A. Malik, N. Man, V. Mandic, V. Mangano, G. L. Mansell, M. Manske, M. Mantovani, M. Mapelli, F. Marchesoni, F. Marion, S. Márka, Z. Márka, C. Markakis, A. S. Markosyan, A. Markowitz, E. Maros, A. Marquina, S. Marsat, F. Martelli, I. W. Martin, R. M. Martin, V. Martinez, D. V. Martynov, H. Masalehdan, K. Mason, E. Massera, A. Masserot, T. J. Massinger, M. Masso-Reid, S. Mastrogiovanni, A. Matas, F. Matichard, N. Mavalala, E. Maynard, J. J. McCann, R. McCarthy, D. E. McClelland, S. McCormick, L. McCuller, S. C. McGuire, C. McIsaac, J. McIver, D. J. McManus, T. McRae, S. T. McWilliams, D. Meacher, G. D. Meadors, M. Mehmet, A. K. Mehta, E. Mejuto Villa, A. Melatos, G. Mendell, R. A. Mercer, L. Mereni, K. Merfeld, E. L. Merilh, J. D. Merritt, M. Merzougui, S. Meshkov, C. Messenger, C. Messick, R. Metzdorff, P. M. Meyers, F. Meylahn, A. Mhaske, A. Miani, H. Miao, I. Michaloliakos, C. Michel, H. Middleton, L. Milano, A. L. Miller, M. Millhouse, J. C. Mills, E. Milotti, M. C. Milovich-Goff, O. Minazzoli, Y. Minenkov, A. Mishkin, C. Mishra, T. Mistry, S. Mitra, V. P. Mitrofanov, G. Mitselmakher, R. Mittleman, G. Mo, K. Mogushi, S. R. P. Mohapatra, S. R. Mohite, M. Molina-Ruiz, M. Mondin, M. Montani, C. J. Moore, D. Moraru, F. Morawski, G. Moreno, S. Morisaki, B. Mours, C. M. Mow-Lowry, S. Mozzon, F. Mucciaccia, Arunava Mukherjee, D. Mukherjee, S. Mukherjee, Subroto Mukherjee, N. Mukund, A. Mullavy, J. Munch, E. A. Muñiz, P. G. Murray, A. Nagar, I. Nardecchia, L. Naticchioni, R. K. Nayak, B. F. Neil, J. Neilson, G. Nelemans, T. J. N. Nelson, M. Nery, A. Neunzert, K. Y. Ng, S. Ng, C. Nguyen, P. Nguyen, D. Nichols, S. A. Nichols, S. Nisanke, F. Nocera, M. Noh, C. North, D. Nothard, L. K. Nuttall, J. Oberling, B. D. O'Brien, G. Oganesyan, G. H. Ogin, J. J. Oh, S. H. Oh, F. Ohme, H. Ohta, M. A. Okada, M. Oliver, C. Olivetto, P. Oppermann, Richard J. Oram, B. O'Reilly, R. G. Ormiston, L. F. Ortega, R. O'Shaughnessy, S. Ossokine, C. Osthelder, D. J. Ottaway, H. Overmier, B. J. Owen, A. E. Pace, G. Pagano, M. A. Page, G. Pagliaroli, A. Pai, S. A. Pai, J. R. Palamos, O. Palashov, C. Palomba, H. Pan, P. K. Panda, P. T. H. Pang, C. Pankow, F. Pannarale, B. C. Pant, F. Paoletti, A. Paoli, A. Parida, W. Parker, D. Pascucci, A. Pasqualetti, R. Passaquieti, D. Passuello, B. Patricelli, E. Payne, B. L. Pearlstone, T. C. Pechsiri, A. J. Pedersen, M. Pedraza, A. Pele, S. Penn, A. Perego, C. J. Perez, C. Périgois, A. Perreca, S. Perriès, J. Petermann, H. P. Pfeiffer, M. Phelps, K. S. Phukon, O. J. Piccinni, M. Pichot, M. Piendibene, F. Piergiovanni, V. Pierro, G. Pillant, L. Pinard, I. M. Pinto, K. Piotrkowski, M. Pirello, M. Pitkin, W. Plastino, R. Poggiani, D. Y. T. Pong, S. Ponrathnam, P. Popolizio, E. K. Porter, J. Powell, A. K. Prajapati, K. Prasai, R. Prasanna, G. Pratten, T. Prestegard, M. Principe, G. A. Prodi, L. Prokhorov, M. Punturo, P. Puppo, M. Pürrer, H. Qi, V. Quetschke, P. J. Quinonez, F. J. Raab, G. Raaijmakers, H. Radkins, N. Radulesco, P. Raffai, H. Rafferty, S. Raja, C. Rajan, B. Rajbhandari, M. Rakhmanov, K. E. Ramirez, A. Ramos-Buades, Javed Rana, K. Rao, P. Rapagnani, V. Raymond, M. Razzano, J. Read, T. Regimbau, L. Rei, S. Reid, D. H. Reitze, P. Rettegno, F. Ricci, C. J. Richardson, J. W. Richardson, P. M. Ricker, G. Riemschneider, K. Riles, M. Rizzo, N. A. Robertson, F. Robinet, A. Rocchi, R. D. Rodriguez-Soto, L. Rolland, J. G. Rollins, V. J. Roma, M. Romanelli, R. Romano, C. L. Romel, I. M. Romero-Shaw, J. H. Romie,

C. A. Rose, D. Rose, K. Rose, D. Rosińska, S. G. Rosofsky, M. P. Ross, S. Rowan, S. J. Rowlinson, P. K. Roy, Santosh Roy, Soumen Roy, P. Ruggi, G. Rutins, K. Ryan, S. Sachdev, T. Sadecki, M. Sakellariadou, O. S. Salafia, L. Salconi, M. Saleem, A. Samajdar, E. J. Sanchez, L. E. Sanchez, N. Sanchis-Gual, J. R. Sanders, K. A. Santiago, E. Santos, N. Sarin, B. Sassolas, B. S. Sathyaprakash, O. Sauter, R. L. Savage, V. Savant, D. Sawant, S. Sayah, D. Schaetzl, P. Schale, M. Scheel, J. Scheuer, P. Schmidt, R. Schnabel, R. M. S. Schofield, A. Schönbeck, E. Schreiber, B. W. Schulte, B. F. Schutz, O. Schwarm, E. Schwartz, J. Scott, S. M. Scott, E. Seidel, D. Sellers, A. S. Sengupta, N. Sennett, D. Sentenac, V. Sequino, A. Sergeev, Y. Setyawati, D. A. Shaddock, T. Shaffer, M. S. Shahriar, A. Sharma, P. Sharma, P. Shawhan, H. Shen, M. Shikauchi, R. Shink, D. H. Shoemaker, D. M. Shoemaker, K. Shukla, S. ShyamSundar, K. Siellez, M. Sieniawska, D. Sigg, L. P. Singer, D. Singh, N. Singh, A. Singha, A. Singhal, A. M. Sintes, V. Sipala, V. Skliris, B. J. J. Slagmolen, T. J. Slaven-Blair, J. Smetana, J. R. Smith, R. J. E. Smith, S. Somalia, E. J. Son, S. Soni, B. Sorazu, V. Sordini, F. Sorrentino, T. Souradeep, E. Sowell, A. P. Spencer, M. Spera, A. K. Srivastava, V. Srivastava, K. Staats, C. Stachie, M. Standke, D. A. Steer, M. Steinke, J. Steinlechner, S. Steinlechner, D. Steinmeyer, D. Stocks, D. J. Stops, M. Stover, K. A. Strain, G. Stratta, A. Strunk, R. Sturani, A. L. Stuver, S. Sudhagar, V. Sudhir, T. Z. Summerscales, L. Sun, S. Sunil, A. Sur, J. Suresh, P. J. Sutton, B. L. Swinkels, M. J. Szczepańczyk, M. Tacca, S. C. Tait, C. Talbot, A. J. Tanasićzuk, D. B. Tanner, D. Tao, M. Tápai, A. Tapia, E. N. Tapia San Martin, J. D. Tasson, R. Taylor, R. Tenorio, L. Terkowski, M. P. Thirugnanasambandam, M. Thomas, P. Thomas, J. E. Thompson, S. R. Thondapu, K. A. Thorne, E. Thrane, C. L. Tinsman, T. R. Saravanan, Shubhanshu Tiwari, S. Tiwari, V. Tiwari, K. Toland, M. Tonelli, Z. Tornasi, A. Torres-Forné, C. I. Torrie, I. Tosta e Melo, D. Töyrä, E. A. Trail, F. Travasso, G. Traylor, M. C. Tringali, A. Tripathee, A. Trovato, R. J. Trudeau, K. W. Tsang, M. Tse, R. Tso, L. Tsukada, D. Tsuna, T. Tsutsui, M. Turconi, A. S. Ubhi, K. Ueno, D. Ugolini, C. S. Unnikrishnan, A. L. Urban, S. A. Usman, A. C. Utina, H. Vahlbruch, G. Vajente, G. Valdes, M. Valentini, N. van Bakel, M. van Beuzekom, J. F. J. van den Brand, C. Van Den Broeck, D. C. Vander-Hyde, L. van der Schaaf, J. V. Van Heijningen, A. A. van Veggel, M. Vardaro, V. Varma, S. Vass, M. Vasúth, A. Vecchio, G. Vedovato, J. Veitch, P. J. Veitch, K. Venkateswara, G. Venugopalan, D. Verkindt, D. Veske, F. Vetrano, A. Viceré, A. D. Viets, S. Vinciguerra, D. J. Vine, J. Y. Vinet, S. Vitale, Francisco Hernandez Vivanco, T. Vo, H. Vocca, C. Vorvick, S. P. Vyatchanin, A. R. Wade, L. E. Wade, M. Wade, R. Walet, M. Walker, G. S. Wallace, L. Wallace, S. Walsh, J. Z. Wang, S. Wang, W. H. Wang, R. L. Ward, Z. A. Warren, J. Warner, M. Was, J. Watchi, B. Weaver, L. W. Wei, M. Weinert, A. J. Weinstein, R. Weiss, F. Wellmann, L. Wen, P. Weßels, J. W. Westhouse, K. Wette, J. T. Whelan, B. F. Whiting, C. Whittle, D. M. Wilken, D. Williams, J. L. Willis, B. Willke, W. Winkler, C. C. Wipf, H. Wittel, G. Woan, J. Woehler, J. K. Wofford, C. Wong, J. L. Wright, D. S. Wu, D. M. Wysocki, L. Xiao, H. Yamamoto, L. Yang, Y. Yang, Z. Yang, M. J. Yap, M. Yazback, D. W. Yeeles, Hang Yu, Haocun Yu, S. H. R. Yuen, A. K. Zadrożny, A. Zadrożny, M. Zanolini, T. Zelenova, J. P. Zendri, M. Zevin, J. Zhang, L. Zhang, T. Zhang, C. Zhao, G. Zhao, M. Zhou, Z. Zhou, X. J. Zhu, A. B. Zimmerman, M. E. Zucker, J. Zweizig, LIGO Scientific Collaboration, and Virgo Collaboration. A Joint Fermi-GBM and LIGO/Virgo Analysis of Compact Binary Mergers from the First and Second Gravitational-wave Observing Runs. Astrophysical Journal, 893(2):100, April 2020.

- [211] N. Gehrels, G. Chincarini, P. Giommi, K. O. Mason, J. A. Nousek, A. A. Wells, N. E. White, S. D. Barthelmy, D. N. Burrows, L. R. Cominsky, K. C. Hurley, F. E. Marshall, P. Meszaros, P. W. A. Roming, L. Angelini, L. M. Barbier, T. Belloni, S. Campana, P. A. Caraveo, M. M. Chester, O. Citterio, T. L. Cline, M. S. Cropper, J. R. Cummings, A. J. Dean, E. D. Feigelson, E. E. Fenimore, D. A. Frail, A. S. Fruchter, G. P. Garmire, K. Gentureau, G. Ghisellini, J. Greiner, J. E. Hill, S. D. Hunsberger, H. A. Krimm, S. R. Kulakarni, P. Kumar, F. Lebrun, N. M. Lloyd-Ronning, C. B. Markwardt, B. J. Mattson, R. F. Mushotzky, J. P. Norris, J. Osborne, B. Paczynski, D. M. Palmer, H.-S. Park, A. M. Parsons, J. Paul, M. J. Rees, C. S. Reynolds, J. E. Rhoads, T. P. Sasseen, B. E. Schaefer, A. T. Short, A. P. Smale, I. A. Smith, L. Stella, G. Tagliaferri, T. Takahashi, M. Tashiro, L. K. Townsley, J. Tueller, M. J. L. Turner, M. Vietri, W. Voges, M. J. Ward, R. Willingale, F. M. Zerbi, and W. W. Zhang. TheSwiftGamma-ray burst mission. *ApJ*, 611(2):1005–1020, aug 2004.
- [212] Aaron Tohuvavohu, Jamie A. Kennea, James DeLaunay, David M. Palmer, S. Bradley Cenko, and Scott Barthelmy. Gamma-Ray Urgent Archiver for Novel Opportunities (GUANO): Swift/BAT Event Data Dumps on Demand to Enable Sensitive Subthreshold GRB Searches. *Astrophysical Journal*, 900(1):35, September 2020.
- [213] A. Buikema, C. Cahillane, G. L. Mansell, C. D. Blair, R. Abbott, C. Adams, R. X. Adhikari, A. Ananyeva, S. Appert, K. Arai, J. S. Areeda, Y. Asali, S. M. Aston, C. Austin, A. M. Baer, M. Ball, S. W. Ballmer, S. Banagiri, D. Barker, L. Barsotti, J. Bartlett, B. K. Berger, J. Betzwieser, D. Bhattacharjee, G. Billingsley, S. Biscans, R. M. Blair, N. Bode, P. Booker, R. Bork, A. Bramley, A. F. Brooks, D. D. Brown, K. C. Cannon, X. Chen, A. A. Ciobanu, F. Clara, S. J. Cooper, K. R. Corley, S. T. Countryman, P. B. Covas, D. C. Coyne, L. E. H. Datrier, D. Davis, C. Di Fronzo, K. L. Dooley, J. C. Driggers, P. Dupej, S. E. Dwyer, A. Effler, T. Etzel, M. Evans, T. M. Evans, J. Feicht, A. Fernandez-Galiana, P. Fritschel, V. V. Frolov, P. Fulda, M. Fyffe, J. A. Giaime, K. D. Giardina, P. Godwin, E. Goetz, S. Gras, C. Gray, R. Gray, A. C. Green, E. K. Gustafson, R. Gustafson, J. Hanks, J. Hanson, T. Hardwick, R. K. Hasskew, M. C. Heintze, A. F. Helmling-Cornell, N. A. Holland, J. D. Jones, S. Kandhasamy, S. Karki, M. Kasprzack, K. Kawabe, N. Kijbunchoo, P. J. King, J. S. Kissel, Rahul Kumar, M. Landry, B. B. Lane, B. Lantz, M. Laxen, Y. K. Lecoeuche, J. Leviton, J. Liu, M. Lormand, A. P. Lundgren, R. Macas, M. MacInnis, D. M. Macleod, S. Márka, Z. Márka, D. V. Martynov, K. Mason, T. J. Massinger, F. Matichead, N. Mavalvala, R. McCarthy, D. E. McClelland, S. McCormick, L. McCuller, J. McIver, T. McRae, G. Mendell, K. Merfeld, E. L. Merilh, F. Meylahn, T. Mistry, R. Mittleman, G. Moreno, C. M. Mow-Lowry, S. Mozzon, A. Mullavey, T. J. N. Nelson, P. Nguyen, L. K. Nuttall, J. Oberling, Richard J. Oram, B. O'Reilly, C. Osthelder, D. J. Ottaway, H. Overmier, J. R. Palamos, W. Parker, E. Payne, A. Pele, R. Penhorwood, C. J. Perez, M. Pirello, H. Radkins, K. E. Ramirez, J. W. Richardson, K. Riles, N. A. Robertson, J. G. Rollins, C. L. Romel, J. H. Romie, M. P. Ross, K. Ryan, T. Sadecki, E. J. Sanchez, L. E. Sanchez, T. R. Saravanan, R. L. Savage, D. Schaetzl, R. Schnabel, R. M. S. Schofield, E. Schwartz, D. Sellers, T. Shaffer, D. Sigg, B. J. J. Slagmolen, J. R. Smith, S. Soni, B. Sorazu, A. P. Spencer, K. A. Strain, L. Sun, M. J. Szczepańczyk, M. Thomas, P. Thomas, K. A. Thorne, K. Toland, C. I. Torrie, G. Traylor, M. Tse, A. L. Urban, G. Va-

jente, G. Valdes, D. C. Vander-Hyde, P. J. Veitch, K. Venkateswara, G. Venugopalan, A. D. Viets, T. Vo, C. Vorvick, M. Wade, R. L. Ward, J. Warner, B. Weaver, R. Weiss, C. Whittle, B. Willke, C. C. Wipf, L. Xiao, H. Yamamoto, Hang Yu, Haocun Yu, L. Zhang, M. E. Zucker, and J. Zweizig. Sensitivity and performance of the advanced ligo detectors in the third observing run. PhRvD, 102:062003, Sep 2020.

- [214] B. P. Abbott et al. ApJL, 892(1):L3, mar 2020.
- [215] R. Abbott, T. D. Abbott, S. Abraham, F. Acernese, K. Ackley, C. Adams, R. X. Adhikari, V. B. Adya, C. Affeldt, M. Agathos, K. Agatsuma, N. Aggarwal, O. D. Aguiar, A. Aich, L. Aiello, A. Ain, P. Ajith, S. Akcay, G. Allen, A. Allocca, P. A. Altin, A. Amato, S. Anand, A. Ananyeva, S. B. Anderson, W. G. Anderson, S. V. Angelova, S. Ansoldi, S. Antier, S. Appert, K. Arai, M. C. Araya, J. S. Areeda, M. Arène, N. Arnaud, S. M. Aronson, K. G. Arun, Y. Asali, S. Ascenzi, G. Ashton, S. M. Aston, P. Astone, F. Aubin, P. Aufmuth, K. AultONeal, C. Austin, V. Avendano, S. Babak, P. Bacon, F. Badaracco, M. K. M. Bader, S. Bae, A. M. Baer, J. Baird, F. Baldaccini, G. Ballardin, S. W. Ballmer, A. Bals, A. Balsamo, G. Baltus, S. Banagiri, D. Bankar, R. S. Bankar, J. C. Barayoga, C. Barbieri, B. C. Barish, D. Barker, K. Barkett, P. Barneo, F. Barone, B. Barr, L. Barsotti, M. Barsuglia, D. Barta, J. Bartlett, I. Bartos, R. Bassiri, A. Basti, M. Bawaj, J. C. Bayley, M. Bazzan, B. Bécsy, M. Bejger, I. Belahcene, A. S. Bell, D. Beniwal, M. G. Benjamin, R. Benkel, J. D. Bentley, F. Bergamin, B. K. Berger, G. Bergmann, S. Bernuzzi, C. P. L. Berry, D. Bersanetti, A. Bertolini, J. Betzwieser, R. Bhandare, A. V. Bhandari, J. Bidler, E. Biggs, I. A. Bilenko, G. Billingsley, R. Birney, O. Birnholtz, S. Biscans, M. Bischi, S. Biscoveanu, A. Bisht, G. Bissenbayeva, M. Bitossi, M. A. Bizouard, J. K. Blackburn, J. Blackman, C. D. Blair, D. G. Blair, R. M. Blair, F. Bobba, N. Bode, M. Boer, Y. Boetzel, G. Bogaert, F. Bondu, E. Bonilla, R. Bonnand, P. Booker, B. A. Boom, R. Bork, V. Boschi, S. Bose, V. Bossilkov, J. Bosveld, Y. Bouffanais, A. Bozzi, C. Bradaschia, P. R. Brady, A. Bramley, M. Branchesi, J. E. Brau, M. Breschi, T. Briant, J. H. Briggs, F. Brightenti, A. Brillet, M. Brinkmann, R. Brito, P. Brockill, A. F. Brooks, J. Brooks, D. D. Brown, S. Brunett, G. Bruno, R. Bruntz, A. Buikema, T. Bulik, H. J. Bulten, A. Buonanno, D. Buskulic, R. L. Byer, M. Cabero, L. Cadonati, G. Cagnoli, C. Cahillane, J. Calderón Bustillo, J. D. Callaghan, T. A. Callister, E. Calloni, J. B. Camp, M. Canepa, K. C. Cannon, H. Cao, J. Cao, G. Carapella, F. Carbognani, S. Caride, M. F. Carney, G. Carullo, J. Casanueva Diaz, C. Casentini, J. Castañeda, S. Caudill, M. Cavaglià, F. Cavalier, R. Cavalieri, G. Celli, P. Cerdá-Durán, E. Cesarini, O. Chaibi, K. Chakravarti, C. Chan, M. Chan, S. Chao, P. Charlton, E. A. Chase, E. Chassande-Mottin, D. Chatterjee, M. Chaturvedi, K. Chatzioannou, H. Y. Chen, X. Chen, Y. Chen, H. P. Cheng, C. K. Cheong, H. Y. Chia, F. Chiadini, R. Chierici, A. Chincarini, A. Chiummo, G. Cho, H. S. Cho, M. Cho, N. Christensen, Q. Chu, S. Chua, K. W. Chung, S. Chung, G. Ciani, P. Cieczielag, M. Cieślar, A. A. Ciobanu, R. Ciolfi, F. Cipriano, A. Cirone, F. Clara, J. A. Clark, P. Clearwater, S. Clesse, F. Cleva, E. Coccia, P. F. Cohadon, D. Cohen, M. Colleoni, C. G. Collette, C. Collins, M. Colpi, Jr. Constancio, M., L. Conti, S. J. Cooper, P. Corban, T. R. Corbitt, I. Cordero-Carrión, S. Corezzi, K. R. Corley, N. Cornish, D. Corre, A. Corsi, S. Cortese, C. A. Costa, R. Cotesta, M. W. Coughlin, S. B. Coughlin, J. P. Coulon, S. T. Countryman, P. Couvares, P. B. Covas, D. M. Coward, M. J. Cowart, D. C. Coyne, R. Coyne, J. D. E. Creighton, T. D.

Creighton, J. Cripe, M. Croquette, S. G. Crowder, J. R. Cudell, T. J. Cullen, A. Cumming, R. Cummings, L. Cunningham, E. Cuoco, M. Curylo, T. Dal Canton, G. Dálya, A. Dana, L. M. Daneshgaran-Bajastani, B. D'Angelo, S. L. Danilishin, S. D'Antonio, K. Danzmann, C. Darsow-Fromm, A. Dasgupta, L. E. H. Datrier, V. Dattilo, I. Dave, M. Davier, G. S. Davies, D. Davis, E. J. Daw, D. DeBra, M. Deenadayalan, J. Degallaix, M. De Laurentis, S. Deléglise, M. Delfavero, N. De Lillo, W. Del Pozzo, L. M. DeMarchi, V. D'Emilio, N. Demos, T. Dent, R. De Pietri, R. De Rosa, C. De Rossi, R. DeSalvo, O. de Varona, S. Dhurandhar, M. C. Díaz, Jr. Diaz-Ortiz, M., T. Dietrich, L. Di Fiore, C. Di Fronzo, C. Di Giorgio, F. Di Giovanni, M. Di Giovanni, T. Di Girolamo, A. Di Lieto, B. Ding, S. Di Pace, I. Di Palma, F. Di Renzo, A. K. Divakarla, A. Dmitriev, Z. Doctor, F. Donovan, K. L. Dooley, S. Doravari, I. Dorrington, T. P. Downes, M. Drago, J. C. Driggers, Z. Du, J. G. Ducoin, P. Dupej, O. Durante, D. D'Urso, S. E. Dwyer, P. J. Easter, G. Eddolls, B. Edelman, T. B. Edo, O. Edy, A. Effler, P. Ehrens, J. Eichholz, S. S. Eikenberry, M. Eisenmann, R. A. Eisenstein, A. Ejlli, L. Errico, R. C. Essick, H. Estelles, D. Estevez, Z. B. Etienne, T. Etzel, M. Evans, T. M. Evans, B. E. Ewing, V. Fafone, S. Fairhurst, X. Fan, S. Farinon, B. Farr, W. M. Farr, E. J. Fauchon-Jones, M. Favata, M. Fays, M. Fazio, J. Feicht, M. M. Fejer, F. Feng, E. Fenyvesi, D. L. Ferguson, A. Fernandez-Galiana, I. Ferrante, E. C. Ferreira, T. A. Ferreira, F. Fidecaro, I. Fiori, D. Fiorucci, M. Fishbach, R. P. Fisher, R. Fittipaldi, M. Fitz-Axen, V. Fiumara, R. Flaminio, E. Floden, E. Flynn, H. Fong, J. A. Font, P. W. F. Forsyth, J. D. Fournier, S. Frasca, F. Frasconi, Z. Frei, A. Freise, R. Frey, V. Frey, P. Fritschel, V. V. Frolov, G. Fronzè, P. Fulda, M. Fyffe, H. A. Gabbard, B. U. Gadre, S. M. Gaebel, J. R. Gair, S. Galaudage, D. Ganapathy, A. Ganguly, S. G. Gaonkar, C. García-Quirós, F. Garufi, B. Gateley, S. Gaudio, V. Gayathri, G. Gemme, E. Genin, A. Gennai, D. George, J. George, L. Gergely, S. Ghonge, Abhirup Ghosh, Archisman Ghosh, S. Ghosh, B. Giacomazzo, J. A. Giaime, K. D. Giardina, D. R. Gibson, C. Gier, K. Gill, J. Glanzer, J. Gniesmer, P. Godwin, E. Goetz, R. Goetz, N. Gohlke, B. Goncharov, G. González, A. Gopakumar, S. E. Gossan, M. Gosselin, R. Gouaty, B. Grace, A. Grado, M. Granata, A. Grant, S. Gras, P. Grassia, C. Gray, R. Gray, G. Greco, A. C. Green, R. Green, E. M. Gretarsson, H. L. Griggs, G. Grignani, A. Grimaldi, S. J. Grimm, H. Grote, S. Grunewald, P. Gruning, G. M. Guidi, A. R. Guimaraes, G. Guixé, H. K. Gulati, Y. Guo, A. Gupta, Anchal Gupta, P. Gupta, E. K. Gustafson, R. Gustafson, L. Haegel, O. Halim, E. D. Hall, E. Z. Hamilton, G. Hammond, M. Haney, M. M. Hanke, J. Hanks, C. Hanna, M. D. Hannam, O. A. Hannuksela, T. J. Hansen, J. Hanson, T. Harder, T. Hardwick, K. Haris, J. Harms, G. M. Harry, I. W. Harry, R. K. Hasskew, C. J. Haster, K. Haughian, F. J. Hayes, J. Healy, A. Heidmann, M. C. Heintze, J. Heinze, H. Heitmann, F. Hellman, P. Hello, G. Hemming, M. Hendry, I. S. Heng, E. Hennes, J. Hennig, M. Heurs, S. Hild, T. Hinderer, S. Y. Hoback, S. Hochheim, E. Hofgard, D. Hofman, A. M. Holgado, N. A. Holland, K. Holt, D. E. Holz, P. Hopkins, C. Horst, J. Hough, E. J. Howell, C. G. Hoy, Y. Huang, M. T. Hübner, E. A. Huerta, D. Huet, B. Hughey, V. Hui, S. Husa, S. H. Huttner, R. Huxford, T. Huynh-Dinh, B. Idzkowski, A. Iess, H. Inchauspe, C. Ingram, G. Intini, J. M. Isac, M. Isi, B. R. Iyer, T. Jacqmin, S. J. Jadhav, S. P. Jadhav, A. L. James, K. Jani, N. N. Janthalur, P. Jaradowski, D. Jariwala, R. Jaume, A. C. Jenkins, J. Jiang, G. R. Johns, N. K. Johnson-McDaniel, A. W. Jones, D. I. Jones, J. D. Jones, P. Jones, R. Jones, R. J. G. Jonker, L. Ju, J. Junker, C. V. Kalaghatgi, V. Kalogera, B. Kamai, S. Kandhasamy, G. Kang, J. B. Kanner, S. J. Kapadia, S. Karki, R. Kashyap, M. Kasprzack, W. Kastaun,

S. Katsanevas, E. Katsavounidis, W. Katzman, S. Kaufer, K. Kawabe, F. Kéfélian, D. Keitel, A. Keivani, R. Kennedy, J. S. Key, S. Khadka, F. Y. Khalili, I. Khan, S. Khan, Z. A. Khan, E. A. Khazanov, N. Khetan, M. Khursheed, N. Kijbunchoo, Chunglee Kim, G. J. Kim, J. C. Kim, K. Kim, W. Kim, W. S. Kim, Y. M. Kim, C. Kimball, P. J. King, M. Kinley-Hanlon, R. Kirchhoff, J. S. Kissel, L. Kleybolte, S. Klimenko, T. D. Knowles, E. Knyazev, P. Koch, S. M. Koehlenbeck, G. Koekoek, S. Koley, V. Kondrashov, A. Kontos, N. Koper, M. Korobko, W. Z. Korth, M. Kovalam, D. B. Kozak, V. Kringel, N. V. Krishnendu, A. Królak, N. Krupinski, G. Kuehn, A. Kumar, P. Kumar, Rahul Kumar, Rakesh Kumar, S. Kumar, L. Kuo, A. Kutynia, B. D. Lackey, D. Laghi, E. Lalande, T. L. Lam, A. Lamberts, M. Landry, P. Landry, B. B. Lane, R. N. Lang, J. Lange, B. Lantz, R. K. Lanza, I. La Rosa, A. Lartaux-Vollard, P. D. Lasky, M. Laxen, A. Lazzarini, C. Lazzaro, P. Leaci, S. Leavey, Y. K. Lecoeuche, C. H. Lee, H. M. Lee, H. W. Lee, J. Lee, K. Lee, J. Lehmann, N. Leroy, N. Letendre, Y. Levin, A. K. Y. Li, J. Li, K. li, T. G. F. Li, X. Li, F. Linde, S. D. Linker, J. N. Linley, T. B. Littenberg, J. Liu, X. Liu, M. Llorens-Monteagudo, R. K. L. Lo, A. Lockwood, L. T. London, A. Longo, M. Lorenzini, V. Loriette, M. Lormand, G. Losurdo, J. D. Lough, C. O. Lousto, G. Lovelace, H. Lück, D. Lumaca, A. P. Lundgren, Y. Ma, R. Macas, S. Macfoy, M. MacInnis, D. M. Macleod, I. A. O. MacMillan, A. Macquet, I. Magaña Hernandez, F. Magaña-Sandoval, R. M. Magee, E. Majorana, I. Maksimovic, A. Malik, N. Man, V. Mandic, V. Mangano, G. L. Mansell, M. Manske, M. Mantovani, M. Mapelli, F. Marchesoni, F. Marion, S. Márka, Z. Márka, C. Markakis, A. S. Markosyan, A. Markowitz, E. Maros, A. Marquina, S. Marsat, F. Martelli, I. W. Martin, R. M. Martin, V. Martinez, D. V. Martynov, H. Masalehdan, K. Mason, E. Massera, A. Masserot, T. J. Massinger, M. Masso-Reid, S. Mastrogiovanni, A. Matas, F. Matichard, N. Mavalvala, E. Maynard, J. J. McCann, R. McCarthy, D. E. McClelland, S. McCormick, L. McCuller, S. C. McGuire, C. McIsaac, J. McIver, D. J. McManus, T. McRae, S. T. McWilliams, D. Meacher, G. D. Meadors, M. Mehmet, A. K. Mehta, E. Mejuto Villa, A. Melatos, G. Mendell, R. A. Mercer, L. Mereni, K. Merfeld, E. L. Merilh, J. D. Merritt, M. Merzougui, S. Meshkov, C. Messenger, C. Messick, R. Metzdorff, P. M. Meyers, F. Meylahn, A. Mhaske, A. Miani, H. Miao, I. Michaloliakos, C. Michel, H. Middleton, L. Milano, A. L. Miller, M. Millhouse, J. C. Mills, E. Milotti, M. C. Milovich-Goff, O. Minazzoli, Y. Minenkov, A. Mishkin, C. Mishra, T. Mistry, S. Mitra, V. P. Mitrofanov, G. Mitselmakher, R. Mittleman, G. Mo, K. Mogushi, S. R. P. Mohapatra, S. R. Mohite, M. Molina-Ruiz, M. Mondin, M. Montani, C. J. Moore, D. Moraru, F. Morawski, G. Moreno, S. Morisaki, B. Mours, C. M. Mow-Lowry, S. Mozzon, F. Mucciaccia, Arunava Mukherjee, D. Mukherjee, S. Mukherjee, Subroto Mukherjee, N. Mukund, A. Mullavy, J. Munch, E. A. Muñiz, P. G. Murray, A. Nagar, I. Nardecchia, L. Naticchioni, R. K. Nayak, B. F. Neil, J. Neilson, G. Nelemans, T. J. N. Nelson, M. Nery, A. Neunzert, K. Y. Ng, S. Ng, C. Nguyen, P. Nguyen, D. Nichols, S. A. Nichols, S. Nisanke, F. Nocera, M. Noh, C. North, D. Nothard, L. K. Nuttall, J. Oberling, B. D. O'Brien, G. Oganesyan, G. H. Ogin, J. J. Oh, S. H. Oh, F. Ohme, H. Ohta, M. A. Okada, M. Oliver, C. Olivetto, P. Oppermann, Richard J. Oram, B. O'Reilly, R. G. Ormiston, L. F. Ortega, R. O'Shaughnessy, S. Ossokine, C. Osthelder, D. J. Ottaway, H. Overmier, B. J. Owen, A. E. Pace, G. Pagano, M. A. Page, G. Pagliaroli, A. Pai, S. A. Pai, J. R. Palamos, O. Palashov, C. Palomba, H. Pan, P. K. Panda, P. T. H. Pang, C. Pankow, F. Pannarale, B. C. Pant, F. Paoletti, A. Paoli, A. Parida, W. Parker, D. Pascucci, A. Pasqualetti,

R. Passaquieti, D. Passuello, B. Patricelli, E. Payne, B. L. Pearlstone, T. C. Pechsiri, A. J. Pedersen, M. Pedraza, A. Pele, S. Penn, A. Perego, C. J. Perez, C. Périgois, A. Perreca, S. Perriès, J. Petermann, H. P. Pfeiffer, M. Phelps, K. S. Phukon, O. J. Piccinni, M. Pitchot, M. Piendibene, F. Piergiovanni, V. Pierro, G. Pillant, L. Pinard, I. M. Pinto, K. Piotrkowski, M. Pirello, M. Pitkin, W. Plastino, R. Poggiani, D. Y. T. Pong, S. Ponrathnam, P. Popolizio, E. K. Porter, J. Powell, A. K. Prajapati, K. Prasai, R. Prasanna, G. Pratten, T. Prestegard, M. Principe, G. A. Prodi, L. Prokhorov, M. Punturo, P. Puppo, M. Pürrer, H. Qi, V. Quetschke, P. J. Quinonez, F. J. Raab, G. Raaijmakers, H. Radkins, N. Radulesco, P. Raffai, H. Rafferty, S. Raja, C. Rajan, B. Rajbhandari, M. Rakhmanov, K. E. Ramirez, A. Ramos-Buades, Javed Rana, K. Rao, P. Rapagnani, V. Raymond, M. Razzano, J. Read, T. Regimbau, L. Rei, S. Reid, D. H. Reitze, P. Rettegno, F. Ricci, C. J. Richardson, J. W. Richardson, P. M. Ricker, G. Riemschneider, K. Riles, M. Rizzo, N. A. Robertson, F. Robinet, A. Rocchi, R. D. Rodriguez-Soto, L. Rolland, J. G. Rollins, V. J. Roma, M. Romanelli, R. Romano, C. L. Romel, I. M. Romero-Shaw, J. H. Romie, C. A. Rose, D. Rose, K. Rose, D. Rosińska, S. G. Rosofsky, M. P. Ross, S. Rowan, S. J. Rowlinson, P. K. Roy, Santosh Roy, Soumen Roy, P. Ruggi, G. Rutins, K. Ryan, S. Sachdev, T. Sadecki, M. Sakellariadou, O. S. Salafia, L. Salconi, M. Saleem, F. Salemi, A. Samajdar, E. J. Sanchez, L. E. Sanchez, N. Sanchis-Gual, J. R. Sanders, K. A. Santiago, E. Santos, N. Sarin, B. Sassolas, B. S. Sathyaprakash, O. Sauter, R. L. Savage, V. Savant, D. Sawant, S. Sayah, D. Schaetzl, P. Schale, M. Scheel, J. Scheuer, P. Schmidt, R. Schnabel, R. M. S. Schofield, A. Schönbeck, E. Schreiber, B. W. Schulte, B. F. Schutz, O. Schwarm, E. Schwartz, J. Scott, S. M. Scott, E. Seidel, D. Sellers, A. S. Sengupta, N. Sennett, D. Sentenac, V. Sequino, A. Sergeev, Y. Setyawati, D. A. Shaddock, T. Shaffer, M. S. Shahriar, A. Sharma, P. Sharma, P. Shawhan, H. Shen, M. Shikauchi, R. Shink, D. H. Shoemaker, D. M. Shoemaker, K. Shukla, S. ShyamSundar, K. Siellez, M. Sieniawska, D. Sigg, L. P. Singer, D. Singh, N. Singh, A. Singha, A. Singhal, A. M. Sintes, V. Sipala, V. Skliris, B. J. J. Slagmolen, T. J. Slaven-Blair, J. Smetana, J. R. Smith, R. J. E. Smith, S. Somala, E. J. Son, S. Soni, B. Sorazu, V. Sordini, F. Sorrentino, T. Souradeep, E. Sowell, A. P. Spencer, M. Spera, A. K. Srivastava, V. Srivastava, K. Staats, C. Stachie, M. Standke, D. A. Steer, J. Steinhoff, M. Steinke, J. Steinlechner, S. Steinlechner, D. Steinmeyer, S. Stevenson, D. Stocks, D. J. Stops, M. Stover, K. A. Strain, G. Stratta, A. Strunk, R. Sturani, A. L. Stuver, S. Sudhagar, V. Sudhir, T. Z. Summerscales, L. Sun, S. Sunil, A. Sur, J. Suresh, P. J. Sutton, B. L. Swinkels, M. J. Szczepańczyk, M. Tacca, S. C. Tait, C. Talbot, A. J. Tanasiyczuk, D. B. Tanner, D. Tao, M. Tápai, A. Tapia, E. N. Tapia San Martin, J. D. Tasson, R. Taylor, R. Tenorio, L. Terkowski, M. P. Thirugnanasambandam, M. Thomas, P. Thomas, J. E. Thompson, S. R. Thondapu, K. A. Thorne, E. Thrane, C. L. Tinsman, T. R. Saravanan, Shubhanshu Tiwari, S. Tiwari, V. Tiwari, K. Toland, M. Tonelli, Z. Tornasi, A. Torres-Forné, C. I. Torrie, I. Tosta e Melo, D. Töyrä, E. A. Trail, F. Travasso, G. Traylor, M. C. Tringali, A. Tripathee, A. Trovato, R. J. Trudeau, K. W. Tsang, M. Tse, R. Tso, L. Tsukada, D. Tsuna, T. Tsutsui, M. Turconi, A. S. Ubhi, K. Ueno, D. Ugolini, C. S. Unnikrishnan, A. L. Urban, S. A. Usman, A. C. Utina, H. Vahlbruch, G. Vajente, G. Valdes, M. Valentini, N. van Bakel, M. van Beuzekom, J. F. J. van den Brand, C. Van Den Broeck, D. C. Vander-Hyde, L. van der Schaaf, J. V. Van Heijningen, A. A. van Veggel, M. Vardaro, V. Varma, S. Vass, M. Vasúth, A. Vecchio, G. Vedovato, J. Veitch, P. J. Veitch, K. Venkateswara, G. Venugopalan, D. Verkindt, D. Veske, F. Vetrano, A. Viceré,

A. D. Viets, S. Vinciguerra, D. J. Vine, J. Y. Vinet, S. Vitale, Francisco Hernandez Vivanco, T. Vo, H. Vocca, C. Vorvick, S. P. Vyatchanin, A. R. Wade, L. E. Wade, M. Wade, R. Walet, M. Walker, G. S. Wallace, L. Wallace, S. Walsh, J. Z. Wang, S. Wang, W. H. Wang, R. L. Ward, Z. A. Warden, J. Warner, M. Was, J. Watchi, B. Weaver, L. W. Wei, M. Weinert, A. J. Weinstein, R. Weiss, F. Wellmann, L. Wen, P. Weßels, J. W. Westhouse, K. Wette, J. T. Whelan, B. F. Whiting, C. Whittle, D. M. Wilken, D. Williams, J. L. Willis, B. Willke, W. Winkler, C. C. Wipf, H. Wittel, G. Woan, J. Woehler, J. K. Wofford, C. Wong, J. L. Wright, D. S. Wu, D. M. Wysocki, L. Xiao, H. Yamamoto, L. Yang, Y. Yang, Z. Yang, M. J. Yap, M. Yazback, D. W. Yeeles, Hang Yu, Haocun Yu, S. H. R. Yuen, A. K. Zadrożny, A. Zadrożny, M. Zanolin, T. Zelenova, J. P. Zendri, M. Zevin, J. Zhang, L. Zhang, T. Zhang, C. Zhao, G. Zhao, M. Zhou, Z. Zhou, X. J. Zhu, A. B. Zimmerman, M. E. Zucker, J. Zweizig, LIGO Scientific Collaboration, and Virgo Collaboration. GW190814: Gravitational Waves from the Coalescence of a 23 Solar Mass Black Hole with a 2.6 Solar Mass Compact Object. *Astrophysical Journal Letters*, 896(2):L44, June 2020.

- [216] Charles Meegan, Giselher Lichti, P. N. Bhat, Elisabetta Bissaldi, Michael S. Briggs, Valerie Connaughton, Roland Diehl, Gerald Fishman, Jochen Greiner, Andrew S. Hoover, Alexander J. van der Horst, Andreas von Kienlin, R. Marc Kippen, Chryssa Kouveliotou, Sheila McBreen, W. S. Paciesas, Robert Preece, Helmut Steinle, Mark S. Wallace, Robert B. Wilson, and Colleen Wilson-Hodge. THEFERMIGAMMA-RAY BURST MONITOR. *ApJ*, 702(1):791–804, aug 2009.
- [217] Michael S. Briggs, Shaolin Xiong, Valerie Connaughton, Dave Tierney, Gerard Fitzpatrick, Suzanne Foley, J. Eric Grove, Alexandre Chekhtman, Melissa Gibby, Gerald J. Fishman, Shelia McBreen, Vandiver L. Chaplin, Sylvain Guiriec, Emily Layden, P. N. Bhat, Maximilian Hughes, Jochen Greiner, Andreas von Kienlin, R. Marc Kippen, Charles A. Meegan, William S. Paciesas, Robert D. Preece, Colleen Wilson-Hodge, Robert H. Holzworth, and Michael L. Hutchins. Terrestrial gamma-ray flashes in the fermi era: Improved observations and analysis methods. *JGRA*, 118(6):3805–3830, 2013.
- [218] Bing Zhang. The delay time of gravitational wave — gamma-ray burst associations. *FrPhy*, 14(6), Jul 2019.
- [219] D. Kocevski, E. Burns, A. Goldstein, T. Dal Canton, M. S. Briggs, L. Blackburn, P. Veres, C. M. Hui, R. Hamburg, O. J. Roberts, C. A. Wilson-Hodge, V. Connaughton, J. Racusin, T. Littenberg, A. von Kienlin, and E. Bissaldi. Analysis of sub-threshold short gamma-ray bursts in fermi GBM data. *ApJ*, 862(2):152, aug 2018.
- [220] A. Goldstein, E. Burns, R. Hamburg, V. Connaughton, P. Veres, M. S. Briggs, C. M. Hui, and The GBM-LIGO Collaboration. Updates to the fermi-gbm short grb targeted offline search in preparation for ligo’s second observing run, 2016.
- [221] D. Band, J. Matteson, L. Ford, B. Schaefer, D. Palmer, B. Teegarden, T. Cline, M. Briggs, W. Paciesas, G. Pendleton, G. Fishman, C. Kouveliotou, C. Meegan, R. Wilson, and P. Lestrade. BATSE Observations of Gamma-Ray Burst Spectra. I. Spectral Diversity. *Astrophysical Journal*, 413:281, August 1993.

- [222] A. von Kienlin, C. A. Meegan, W. S. Paciesas, P. N. Bhat, E. Bissaldi, M. S. Briggs, E. Burns, W. H. Cleveland, M. H. Gibby, M. M. Giles, A. Goldstein, R. Hamburg, C. M. Hui, D. Kocevski, B. Mailyan, C. Malacaria, S. Poolakkil, R. D. Preece, O. J. Roberts, P. Veres, and C. A. Wilson-Hodge. The fourth fermi-GBM gamma-ray burst catalog: A decade of data. *ApJ*, 893(1):46, apr 2020.
- [223] S. Poolakkil, R. Preece, C. Fletcher, A. Goldstein, P. N. Bhat, E. Bissaldi, M. S. Briggs, E. Burns, W. H. Cleveland, M. M. Giles, C. M. Hui, D. Kocevski, S. Lesage, B. Mailyan, C. Malacaria, W. S. Paciesas, O. J. Roberts, P. Veres, A. von Kienlin, and C. A. Wilson-Hodge. The fermi-GBM gamma-ray burst spectral catalog: 10 yr of data. *ApJ*, 913(1):60, may 2021.
- [224] E. E. Fenimore, K. McLean, D. Palmer, S. Barthelmy, N. Gehrels, H. Krimm, C. Markwardt, A. Parsons, and J. Tueller. Swift’s Ability to Detect Gamma-Ray Bursts. *BaltA*, 13:301–306, January 2004.
- [225] Amy Lien, Takanori Sakamoto, Neil Gehrels, David M. Palmer, Scott D. Barthelmy, Carlo Graziani, and John K. Cannizzo. Probing the Cosmic Gamma-Ray Burst Rate with Trigger Simulations of the Swift Burst Alert Telescope. *Astrophysical Journal*, 783(1):24, March 2014.
- [226] James DeLaunay and Aaron Tohuavavohu. Harvesting BAT-GUANO with NITRATES (Non-Imaging Transient Reconstruction And TEmporal Search): Detecting and localizing the faintest GRBs with a likelihood framework. 11 2021.
- [227] J. Allison, K. Amako, J. Apostolakis, P. Arce, M. Asai, T. Aso, E. Bagli, A. Bagulya, S. Banerjee, G. Barrand, B.R. Beck, A.G. Bogdanov, D. Brandt, J.M.C. Brown, H. Burkhardt, Ph. Canal, D. Cano-Ott, S. Chauvie, K. Cho, G.A.P. Cirrone, G. Cooperman, M.A. Cortés-Giraldo, G. Cosmo, G. Cuttone, G. Depaola, L. Desorgher, X. Dong, A. Dotti, V.D. Elvira, G. Folger, Z. Francis, A. Galoyan, L. Garnier, M. Gayer, K.L. Genser, V.M. Grichine, S. Guatelli, P. Guèye, P. Gumplinger, A.S. Howard, I. Hřivnáčová, S. Hwang, S. Incerti, A. Ivanchenko, V.N. Ivanchenko, F.W. Jones, S.Y. Jun, P. Kaitaniemi, N. Karakatsanis, M. Karamitros, M. Kelsey, A. Kimura, T. Koi, H. Kurashige, A. Lechner, S.B. Lee, F. Longo, M. Maire, D. Mancusi, A. Mantero, E. Mendoza, B. Morgan, K. Murakami, T. Nikitina, L. Pandola, P. Paprocki, J. Perl, I. Petrović, M.G. Pia, W. Pokorski, J.M. Quesada, M. Raine, M.A. Reis, A. Ribon, A. Ristić Fira, F. Romano, G. Russo, G. Santin, T. Sasaki, D. Sawkey, J.I. Shin, I.I. Strakovský, A. Taborda, S. Tanaka, B. Tomé, T. Toshito, H.N. Tran, P.R. Truscott, L. Urban, V. Uzhinsky, J.M. Verbeke, M. Verderi, B.L. Wendt, H. Wenzel, D.H. Wright, D.M. Wright, T. Yamashita, J. Yarba, and H. Yoshida. Recent developments in geant4. *NIMPA*, 835:186–225, 2016.
- [228] Eric Burns. Neutron star mergers and how to study them. *LRR*, 23(1):4, 2020.
- [229] Abraham Loeb. Electromagnetic Counterparts to Black Hole Mergers Detected by LIGO. *Astrophysical Journal Letters*, 819(2):L21, March 2016.
- [230] Rosalba Perna, Davide Lazzati, and Bruno Giacomazzo. Short Gamma-Ray Bursts from the Merger of Two Black Holes. *Astrophysical Journal Letters*, 821(1):L18, April 2016.

- [231] Bing Zhang. Mergers of Charged Black Holes: Gravitational-wave Events, Short Gamma-Ray Bursts, and Fast Radio Bursts. *Astrophysical Journal Letters*, 827(2):L31, August 2016.
- [232] Lixin Dai, Jonathan C. McKinney, and M. Coleman Miller. Energetic constraints on electromagnetic signals from double black hole mergers. *Monthly Notices of the Royal Astronomical Society*, 470(1):L92–L96, May 2017.
- [233] I. Bombaci. The maximum mass of a neutron star. *Astronomy & Astrophysics Journal*, 305:871, January 1996.
- [234] Vassiliki Kalogera and Gordon Baym. The Maximum Mass of a Neutron Star. *Astrophysical Journal Letters*, 470:L61, October 1996.
- [235] Ben Margalit and Brian D. Metzger. Constraining the Maximum Mass of Neutron Stars from Multi-messenger Observations of GW170817. *Astrophysical Journal Letters*, 850(2):L19, December 2017.
- [236] Luciano Rezzolla, Elias R. Most, and Lukas R. Weih. Using gravitational-wave observations and quasi-universal relations to constrain the maximum mass of neutron stars. *The Astrophysical Journal Letters*, 852(2):L25, jan 2018.
- [237] B. P. Abbott, R. Abbott, T. D. Abbott, M. R. Abernathy, F. Acernese, K. Ackley, C. Adams, T. Adams, P. Addesso, R. X. Adhikari, V. B. Adya, C. Affeldt, M. Agathos, K. Agatsuma, N. Aggarwal, O. D. Aguiar, L. Aiello, A. Ain, P. Ajith, T. Akutsu, B. Allen, A. Allocata, P. A. Altin, A. Ananyeva, S. B. Anderson, W. G. Anderson, M. Ando, S. Appert, K. Arai, A. Araya, M. C. Araya, J. S. Areeda, N. Arnaud, K. G. Arun, H. Asada, S. Ascenzi, G. Ashton, Y. Aso, M. Ast, S. M. Aston, P. Astone, S. Atsuta, P. Aufmuth, C. Aulbert, A. Avila-Alvarez, K. Awai, S. Babak, P. Bacon, M. K. M. Bader, L. Baiotti, P. T. Baker, F. Baldaccini, G. Ballardin, S. W. Ballmer, J. C. Barayoga, S. E. Barclay, B. C. Barish, D. Barker, F. Barone, B. Barr, L. Barsotti, M. Barsuglia, D. Barta, J. Bartlett, M. A. Barton, I. Bartos, R. Bassiri, A. Basti, J. C. Batch, C. Baune, V. Bavigadda, M. Bazzan, B. Bécsy, C. Beer, M. Bejger, I. Belahcene, M. Belgin, A. S. Bell, B. K. Berger, G. Bergmann, C. P. L. Berry, D. Bersanetti, A. Bertolini, J. Betzwieser, S. Bhagwat, R. Bhandare, I. A. Bilenko, G. Billingsley, C. R. Billman, J. Birch, R. Birney, O. Birnholtz, S. Biscans, A. Bisht, M. Bitossi, C. Biwer, M. A. Bizouard, J. K. Blackburn, J. Blackman, C. D. Blair, D. G. Blair, R. M. Blair, S. Bloemen, O. Bock, M. Boer, G. Bogaert, A. Bohe, F. Bondu, R. Bonnand, B. A. Boom, R. Bork, V. Boschi, S. Bose, Y. Bouffanais, A. Bozzi, C. Bradaschia, P. R. Brady, V. B. Braginsky, M. Branchesi, J. E. Brau, T. Briant, A. Brillet, M. Brinkmann, V. Brisson, P. Brockill, J. E. Broida, A. F. Brooks, D. A. Brown, D. D. Brown, N. M. Brown, S. Brunett, C. C. Buchanan, A. Buikema, T. Bulik, H. J. Bulten, A. Buonanno, D. Buskulic, C. Buy, R. L. Byer, M. Cabero, L. Cadonati, G. Cagnoli, C. Cahillane, J. Calderón Bustillo, T. A. Callister, E. Calloni, J. B. Camp, K. C. Cannon, H. Cao, J. Cao, C. D. Capano, E. Capocasa, F. Carbognani, S. Caride, J. Casanueva Diaz, C. Casentini, S. Caudill, M. Cavaglià, F. Cavalier, R. Cavalieri, G. Celli, C. B. Cepeda, L. Cerboni Baiardi, G. Cerretani, E. Cesarini, S. J. Chamberlin, M. Chan, S. Chao, P. Charlton, E. Chassande-Mottin, B. D. Cheeseboro, H. Y. Chen, Y. Chen, H. P. Cheng,

A. Chincarini, A. Chiummo, T. Chmiel, H. S. Cho, M. Cho, J. H. Chow, N. Christensen, Q. Chu, A. J. K. Chua, S. Chua, S. Chung, G. Ciani, F. Clara, J. A. Clark, F. Cleva, C. Cocchieri, E. Coccia, P. F. Cohadon, A. Colla, C. G. Collette, L. Cominsky, M. Constancio, L. Conti, S. J. Cooper, T. R. Corbitt, N. Cornish, A. Corsi, S. Cortese, C. A. Costa, M. W. Coughlin, S. B. Coughlin, J. P. Coulon, S. T. Countryman, P. Couvares, P. B. Covas, E. E. Cowan, D. M. Coward, M. J. Cowart, D. C. Coyne, R. Coyne, J. D. E. Creighton, T. D. Creighton, J. Cripe, S. G. Crowder, T. J. Cullen, A. Cumming, L. Cunningham, E. Cuoco, T. Dal Canton, S. L. Danilishin, S. D'Antonio, K. Danzmann, A. Dasgupta, C. F. da Silva Costa, V. Dattilo, I. Dave, M. Davier, G. S. Davies, D. Davis, E. J. Daw, B. Day, R. Day, S. de, D. Debra, G. Debreczeni, J. Degallaix, M. de Laurentis, S. Deléglise, W. Del Pozzo, T. Denker, T. Dent, V. Dergachev, R. De Rosa, R. T. Derosa, R. Desalvo, R. C. Devine, S. Dhurandhar, M. C. Díaz, L. di Fiore, M. di Giovanni, T. di Girolamo, A. di Lieto, S. di Pace, I. di Palma, A. di Virgilio, Z. Doctor, K. Doi, V. Dolique, F. Donovan, K. L. Dooley, S. Doravari, I. Dorrington, R. Douglas, M. Dovale Álvarez, T. P. Downes, M. Drago, R. W. P. Drever, J. C. Driggers, Z. Du, M. Ducrot, S. E. Dwyer, K. Eda, T. B. Edo, M. C. Edwards, A. Effler, H. B. Eggenstein, P. Ehrens, J. Eichholz, S. S. Eikenberry, R. A. Eisenstein, R. C. Essick, Z. Etienne, T. Etzel, M. Evans, T. M. Evans, R. Everett, M. Factourovich, V. Fafone, H. Fair, S. Fairhurst, X. Fan, S. Farinon, B. Farr, W. M. Farr, E. J. Fauchon-Jones, M. Favata, M. Fays, H. Fehrmann, M. M. Fejer, A. Fernández Galiana, I. Ferrante, E. C. Ferreira, F. Ferrini, F. Fidecaro, I. Fiori, D. Fiorucci, R. P. Fisher, R. Flaminio, M. Fletcher, H. Fong, S. S. Forsyth, J. D. Fournier, S. Frasca, F. Frasconi, Z. Frei, A. Freise, R. Frey, V. Frey, E. M. Fries, P. Fritschel, V. V. Frolov, Y. Fujii, M. K. Fujimoto, P. Fulda, M. Fyffe, H. Gabbard, B. U. Gadre, S. M. Gaebel, J. R. Gair, L. Gammaitoni, S. G. Gaonkar, F. Garufi, G. Gaur, V. Gayathri, N. Gehrels, G. Gemme, E. Genin, A. Gennai, J. George, L. Gergely, V. Germain, S. Ghonge, Abhirup Ghosh, Archisman Ghosh, S. Ghosh, J. A. Giaime, K. D. Giardina, A. Giazotto, K. Gill, A. Glaefke, E. Goetz, R. Goetz, L. Gondan, G. González, J. M. Gonzalez Castro, A. Gopakumar, M. L. Gorodetsky, S. E. Gossan, M. Gosselin, R. Gouaty, A. Grado, C. Graef, M. Granata, A. Grant, S. Gras, C. Gray, G. Greco, A. C. Green, P. Groot, H. Grote, S. Grunewald, G. M. Guidi, X. Guo, A. Gupta, M. K. Gupta, K. E. Gushwa, E. K. Gustafson, R. Gustafson, J. J. Hacker, A. Hagiwara, B. R. Hall, E. D. Hall, G. Hammond, M. Haney, M. M. Hanke, J. Hanks, C. Hanna, M. D. Hannam, J. Hanson, T. Hardwick, J. Harms, G. M. Harry, I. W. Harry, M. J. Hart, M. T. Hartman, C. J. Haster, K. Haughian, K. Hayama, J. Healy, A. Heidmann, M. C. Heintze, H. Heitmann, P. Hello, G. Hemming, M. Hendry, I. S. Heng, J. Hennig, J. Henry, A. W. Heptonstall, M. Heurs, S. Hild, E. Hirose, D. Hoak, D. Hofman, K. Holt, D. E. Holz, P. Hopkins, J. Hough, E. A. Houston, E. J. Howell, Y. M. Hu, E. A. Huerta, D. Huet, B. Hughey, S. Husa, S. H. Huttner, T. Huynh-Dinh, N. Indik, D. R. Ingram, R. Inta, K. Ioka, H. N. Isa, J. M. Isac, M. Isi, T. Isogai, Y. Itoh, B. R. Iyer, K. Izumi, T. Jacqmin, K. Jani, P. Jaradowski, S. Jawahar, F. Jiménez-Forteza, W. W. Johnson, D. I. Jones, R. Jones, R. J. G. Jonker, L. Ju, J. Junker, T. Kagawa, T. Kajita, M. Kakizaki, C. V. Kalaghatgi, V. Kalogera, M. Kamiizumi, N. Kanda, S. Kandhasamy, S. Kanemura, M. Kaneyama, G. Kang, J. B. Kanner, S. Karki, K. S. Karvinen, M. Kasprzack, Y. Kataoka, E. Katsavounidis, W. Katzman, S. Kaufer, T. Kaur, K. Kawabe, N. Kawai, S. Kawamura, F. Kéfélian, D. Keitel, D. B. Kelley, R. Kennedy, J. S. Key, F. Y. Khalili, I. Khan, S. Khan, Z. Khan, E. A. Khazanov,

N. Kijbunchoo, C. Kim, H. Kim, J. C. Kim, J. Kim, W. Kim, Y. M. Kim, S. J. Kimbrell, N. Kimura, E. J. King, P. J. King, R. Kirchhoff, J. S. Kissel, B. Klein, L. Kleybolte, S. Klimenko, P. Koch, S. M. Koehlenbeck, Y. Kojima, K. Kokeyama, S. Koley, K. Komori, V. Kondrashov, A. Kontos, M. Korobko, W. Z. Korth, K. Kotake, I. Kowalska, D. B. Kozak, C. Krämer, V. Kringel, B. Krishnan, A. Królak, G. Kuehn, P. Kumar, Rahul Kumar, Rakesh Kumar, L. Kuo, K. Kuroda, A. Kutynia, Y. Kuwahara, B. D. Lackey, M. Landry, R. N. Lang, J. Lange, B. Lantz, R. K. Lanza, A. Lartaux-Vollard, P. D. Lasky, M. Laxen, A. Lazzarini, C. Lazzaro, P. Leaci, S. Leavey, E. O. Lebigot, C. H. Lee, H. K. Lee, H. M. Lee, H. W. Lee, K. Lee, J. Lehmann, A. Lennon, M. Leonardi, J. R. Leong, N. Leroy, N. Letendre, Y. Levin, T. G. F. Li, A. Libson, T. B. Littenberg, J. Liu, N. A. Lockerbie, A. L. Lombardi, L. T. London, J. E. Lord, M. Lorenzini, V. Loriette, M. Lormand, G. Losurdo, J. D. Lough, C. O. Lousto, G. Lovelace, H. Lück, A. P. Lundgren, R. Lynch, Y. Ma, S. Macfoy, B. Machenschalk, M. Macinnis, D. M. MacLeod, F. Magaña-Sandoval, E. Majorana, I. Maksimovic, V. Malvezzi, N. Man, V. Mandic, V. Mangano, S. Mano, G. L. Mansell, M. Manske, M. Mantovani, F. Marchesoni, M. Marchio, F. Marion, S. Márka, Z. Márka, A. S. Markosyan, E. Maros, F. Martelli, L. Martellini, I. W. Martin, D. V. Martynov, K. Mason, A. Masserot, T. J. Massinger, M. Masso-Reid, S. Mastrogiovanni, F. Matichard, L. Matone, N. Matsumoto, F. Matsushima, N. Mavalvala, N. Mazumder, R. McCarthy, D. E. McClelland, S. McCormick, C. McGrath, S. C. McGuire, G. McIntyre, J. McIver, D. J. McManus, T. McRae, S. T. McWilliams, D. Meacher, G. D. Meadors, J. Meidam, A. Melatos, G. Mendell, D. Mendoza-Gandara, R. A. Mercer, E. L. Merilh, M. Merzougui, S. Meshkov, C. Messenger, C. Messick, R. Metzdorff, P. M. Meyers, F. Mezzani, H. Miao, C. Michel, Y. Michimura, H. Middleton, E. E. Mikhailov, L. Milano, A. L. Miller, A. Miller, B. B. Miller, J. Miller, M. Millhouse, Y. Minenkov, J. Ming, S. Mirshekari, C. Mishra, V. P. Mitrofanov, G. Mitselmakher, R. Mittleman, O. Miyakawa, A. Miyamoto, T. Miyamoto, S. Miyoki, A. Moggi, M. Mohan, S. R. P. Mohapatra, M. Montani, B. C. Moore, C. J. Moore, D. Moraru, G. Moreno, W. Morii, S. Morisaki, Y. Moriwaki, S. R. Morriss, B. Mours, C. M. Mow-Lowry, G. Mueller, A. W. Muir, Arunava Mukherjee, D. Mukherjee, S. Mukherjee, N. Mukund, A. Mullavey, J. Munch, E. A. M. Muniz, P. G. Murray, A. Mytidis, S. Nagano, K. Nakamura, T. Nakamura, H. Nakano, Masaya Nakano, Masayuki Nakano, K. Nakao, K. Napier, I. Nardechia, T. Narikawa, L. Naticchioni, G. Nelemans, T. J. N. Nelson, M. Neri, M. Nery, A. Neunzert, J. M. Newport, G. Newton, T. T. Nguyen, W. T. Ni, A. B. Nielsen, S. Nissanke, A. Nitz, A. Noack, F. Nocera, D. Nolting, M. E. N. Normandin, L. K. Nuttall, J. Oberling, E. Ochsner, E. Oelker, G. H. Ogin, J. J. Oh, S. H. Oh, M. Ohashi, N. Ohishi, M. Ohkawa, F. Ohme, K. Okutomi, M. Oliver, K. Ono, Y. Ono, K. Oohara, P. Oppermann, Richard J. Oram, B. O'Reilly, R. O'Shaughnessy, D. J. Ottaway, H. Overmier, B. J. Owen, A. E. Pace, J. Page, A. Pai, S. A. Pai, J. R. Palamos, O. Palashov, C. Palomba, A. Pal-Singh, H. Pan, C. Pankow, F. Pannarale, B. C. Pant, F. Paoletti, A. Paoli, M. A. Papa, H. R. Paris, W. Parker, D. Pascucci, A. Pasqualetti, R. Passaquieti, D. Passuello, B. Patricelli, B. L. Pearlstone, M. Pedraza, R. Pedurand, L. Pekowsky, A. Pele, F. E. Peña Arellano, S. Penn, C. J. Perez, A. Perreca, L. M. Perri, H. P. Pfeiffer, M. Phelps, O. J. Piccinni, M. Pichot, F. Piergiovanni, V. Pierro, G. Pillant, L. Pinard, I. M. Pinto, M. Pitkin, M. Poe, R. Poggiani, P. Popolizio, A. Post, J. Powell, J. Prasad, J. W. W. Pratt, V. Predoi, T. Prestegard, M. Prijatelj, M. Principe, S. Privitera, G. A. Prodi, L. G. Prokhorov, O. Puncken, M. Pun-

turo, P. Puppo, M. Pürrer, H. Qi, J. Qin, S. Qiu, V. Quetschke, E. A. Quintero, R. Quitzow-James, F. J. Raab, D. S. Rabeling, H. Radkins, P. Raffai, S. Raja, C. Rajan, M. Rakhmanov, P. Rapagnani, V. Raymond, M. Razzano, V. Re, J. Read, T. Regimbau, L. Rei, S. Reid, D. H. Reitze, H. Rew, S. D. Reyes, E. Rhoades, F. Ricci, K. Riles, M. Rizzo, N. A. Robertson, R. Robie, F. Robinet, A. Rocchi, L. Rolland, J. G. Rollins, V. J. Roma, R. Romano, J. H. Romie, D. Rosińska, S. Rowan, A. Rüdiger, P. Ruggi, K. Ryan, S. Sachdev, T. Sadecki, L. Sadeghian, N. Sago, M. Saijo, Y. Saito, K. Sakai, M. Sakellariadou, L. Salconi, M. Saleem, F. Salemi, A. Samajdar, L. Sammut, L. M. Sampson, E. J. Sanchez, V. Sandberg, J. R. Sanders, Y. Sasaki, B. Sassolas, B. S. Sathyaprakash, S. Sato, T. Sato, P. R. Saulson, O. Sauter, R. L. Savage, A. Sawadsky, P. Schale, J. Scheuer, E. Schmidt, J. Schmidt, P. Schmidt, R. Schnabel, R. M. S. Schofield, A. Schönbeck, E. Schreiber, D. Schuette, B. F. Schutz, S. G. Schwalbe, J. Scott, S. M. Scott, T. Sekiguchi, Y. Sekiguchi, D. Sellers, A. S. Sengupta, D. Sentenac, V. Sequino, A. Sergeev, Y. Setyawati, D. A. Shaddock, T. J. Shaffer, M. S. Shahriar, B. Shapiro, P. Shawhan, A. Sheperd, M. Shibata, Y. Shikano, T. Shimoda, A. Shoda, D. H. Shoemaker, D. M. Shoemaker, K. Siellez, X. Siemens, M. Sieniawska, D. Sigg, A. D. Silva, A. Singer, L. P. Singer, A. Singh, R. Singh, A. Singhal, A. M. Sintes, B. J. J. Slagmolen, B. Smith, J. R. Smith, R. J. E. Smith, K. Somiya, E. J. Son, B. Sorazu, F. Sorrentino, T. Souradeep, A. P. Spencer, A. K. Srivastava, A. Staley, M. Steinke, J. Steinlechner, S. Steinlechner, D. Steinmeyer, B. C. Stephens, S. P. Stevenson, R. Stone, K. A. Strain, N. Straniero, G. Stratta, S. E. Strigin, R. Sturani, A. L. Stuver, Y. Sugimoto, T. Z. Summerscales, L. Sun, S. Sunil, P. J. Sutton, T. Suzuki, B. L. Swinkels, M. J. Szczepańczyk, M. Tacca, H. Tagoshi, S. Takada, H. Takahashi, R. Takahashi, A. Takamori, D. Talukder, H. Tanaka, K. Tanaka, T. Tanaka, D. B. Tanner, M. Tápai, A. Taracchini, D. Tatsumi, R. Taylor, S. Telada, T. Theeg, E. G. Thomas, M. Thomas, P. Thomas, K. A. Thorne, E. Thrane, T. Tippens, S. Tiwari, V. Tiwari, K. V. Tokmakov, K. Toland, T. Tomaru, C. Tomlinson, M. Tonelli, Z. Tornasi, C. I. Torrie, D. Töyrä, F. Travasso, G. Traylor, D. Trifirò, J. Trinastic, M. C. Tringali, L. Trozzo, M. Tse, R. Tso, K. Tsubono, T. Tsuzuki, M. Turconi, D. Tuyenbayev, T. Uchiyama, T. Uehara, S. Ueki, K. Ueno, D. Ugolini, C. S. Unnikrishnan, A. L. Urban, T. Ushiba, S. A. Usman, H. Vahlbruch, G. Vajente, G. Valdes, N. van Bakel, M. van Beuzekom, J. F. J. van den Brand, C. van den Broeck, D. C. Vander-Hyde, L. van der Schaaf, J. V. van Heijningen, M. H. P. M. van Putten, A. A. van Veggel, M. Vardaro, V. Varma, S. Vass, M. Vasúth, A. Vecchio, G. Vedovato, J. Veitch, P. J. Veitch, K. Venkateswara, G. Venugopalan, D. Verkindt, F. Vetrano, A. Viceré, A. D. Viets, S. Vinciguerra, D. J. Vine, J. Y. Vinet, S. Vitale, T. Vo, H. Vocca, C. Vorvick, D. V. Voss, W. D. Vousden, S. P. Vyatchanin, A. R. Wade, L. E. Wade, M. Wade, T. Wakamatsu, M. Walker, L. Wallace, S. Walsh, G. Wang, H. Wang, M. Wang, Y. Wang, R. L. Ward, J. Warner, M. Was, J. Watchi, B. Weaver, L. W. Wei, M. Weinert, A. J. Weinstein, R. Weiss, L. Wen, P. Weßels, T. Westphal, K. Wette, J. T. Whelan, B. F. Whiting, C. Whittle, D. Williams, R. D. Williams, A. R. Williamson, J. L. Willis, B. Willke, M. H. Wimmer, W. Winkler, C. C. Wipf, H. Wittel, G. Woan, J. Woehler, J. Worden, J. L. Wright, D. S. Wu, G. Wu, W. Yam, H. Yamamoto, K. Yamamoto, T. Yamamoto, C. C. Yancey, K. Yano, M. J. Yap, J. Yokoyama, T. Yokozawa, T. H. Yoon, Hang Yu, Haocun Yu, H. Yuzurihara, M. Yvert, A. Zadrożny, L. Zangrandi, M. Zanolini, S. Zeidler, J. P. Zendri, M. Zevin, L. Zhang, M. Zhang, T. Zhang, Y. Zhang, C. Zhao, M. Zhou, Z. Zhou, S. J. Zhu, X. J. Zhu, M. E. Zucker, J. Zweizig, Ligo Scientific Collaboration

Kagra Collaboration, and VIRGO Collaboration. Prospects for observing and localizing gravitational-wave transients with Advanced LIGO, Advanced Virgo and KAGRA. *Living Reviews in Relativity*, 21(1):3, April 2018.

- [238] Polina Petrov, Leo P. Singer, Michael W. Coughlin, Vishwesh Kumar, Mouza Almualla, Shreya Anand, Mattia Bulla, Tim Dietrich, Francois Foucart, and Nidhal Guessoum. Data-driven Expectations for Electromagnetic Counterpart Searches Based on LIGO/Virgo Public Alerts. *Astrophysical Journal*, 924(2):54, January 2022.
- [239] IceCube Collaboration. Evidence for High-Energy Extraterrestrial Neutrinos at the IceCube Detector. *Science*, 342(6161):1242856, November 2013.
- [240] M. G. Aartsen et al. Characteristics of the diffuse astrophysical electron and tau neutrino flux with six years of IceCube high energy cascade data. *Phys. Rev. Lett.*, 125(12):121104, 2020.
- [241] M. G. Aartsen et al. Multimessenger observations of a flaring blazar coincident with high-energy neutrino IceCube-170922A. *Science*, 361(6398):eaat1378, 2018.
- [242] M. G. Aartsen et al. Neutrino emission from the direction of the blazar TXS 0506+056 prior to the IceCube-170922A alert. *Science*, 361(6398):147–151, 2018.
- [243] IceCube Collaboration. EVIDENCE FOR NEUTRINO EMISSION FROM THE NEARBY ACTIVE GALAXY NGC 1068. *Science*, 378(6619):538–543, November 2022.
- [244] M. G. Aartsen, M. Ackermann, J. Adams, J. A. Aguilar, M. Ahlers, M. Ahrens, C. Alispach, K. Andeen, T. Anderson, I. Ansseau, G. Anton, C. Argüelles, J. Auffenberg, S. Axani, P. Backes, H. Bagherpour, X. Bai, A. Balagopal, A. Barbano, S. W. Barwick, B. Bastian, V. Baum, S. Baur, R. Bay, J. J. Beatty, K.-H. Becker, J. Becker Tjus, S. BenZvi, D. Berley, E. Bernardini, D. Z. Besson, G. Binder, D. Bindig, E. Blaufuss, S. Blot, C. Bohm, M. Börner, S. Böser, O. Botner, J. Böttcher, E. Bourbeau, J. Bourbeau, F. Bradascio, J. Braun, S. Bron, J. Brostean-Kaiser, A. Burgman, J. Buscher, R. S. Busse, T. Carver, C. Chen, E. Cheung, D. Chirkin, S. Choi, K. Clark, L. Classen, A. Coleman, G. H. Collin, J. M. Conrad, P. Coppin, P. Correa, D. F. Cowen, R. Cross, P. Dave, C. De Clercq, J. J. DeLaunay, H. Dembinski, K. Deoskar, S. De Ridder, P. Desiati, K. D. de Vries, G. de Wasseige, M. de With, T. DeYoung, A. Diaz, J. C. Díaz-Vélez, H. Djumovic, M. Dunkman, E. Dvorak, B. Eberhardt, T. Ehrhardt, P. Eller, R. Engel, P. A. Evenson, S. Fahey, A. R. Fazely, J. Felde, K. Filimonov, C. Finley, D. Fox, A. Franckowiak, E. Friedman, A. Fritz, T. K. Gaisser, J. Gallagher, E. Ganster, S. Garrappa, L. Gerhardt, K. Ghorbani, T. Glauch, T. Glüsenkamp, A. Goldschmidt, J. G. Gonzalez, D. Grant, Z. Griffith, S. Griswold, M. Günder, M. Gündüz, C. Haack, A. Hallgren, R. Halliday, L. Halve, F. Halzen, K. Hanson, A. Haungs, D. Hebecker, D. Heereman, P. Heix, K. Helbing, R. Hellauer, F. Henningsen, S. Hickford, J. Hignight, G. C. Hill, K. D. Hoffman, R. Hoffmann, T. Hoinka, B. Hokanson-Fasig, K. Hoshina, F. Huang, M. Huber, T. Huber, K. Hultqvist, M. Hünnefeld, R. Hussain, S. In, N. Iovine, A. Ishihara, G. S. Japaridze, M. Jeong, K. Jero, B. J. P. Jones, F. Jonske, R. Joppe, D. Kang, W. Kang, A. Kappes,

D. Kappesser, T. Karg, M. Karl, A. Karle, U. Katz, M. Kauer, J. L. Kelley, A. Kheirandish, J. Kim, T. Kintscher, J. Kiryluk, T. Kittler, S. R. Klein, R. Koirala, H. Kolanoski, L. Köpke, C. Kopper, S. Kopper, D. J. Koskinen, M. Kowalski, K. Krings, G. Krückl, N. Kulacz, N. Kurahashi, A. Kyriacou, M. Labare, J. L. Lanfranchi, M. J. Larson, F. Lauber, J. P. Lazar, K. Leonard, A. Leszczyńska, M. Leuermann, Q. R. Liu, E. Lohfink, C. J. Lozano Mariscal, L. Lu, F. Lucarelli, J. Lünemann, W. Luszczak, Y. Lyu, W. Y. Ma, J. Madsen, G. Maggi, K. B. M. Mahn, Y. Makino, P. Mallik, K. Mallot, S. Mancina, I. C. Mariş, R. Maruyama, K. Mase, H. S. Matis, R. Maunu, F. McNally, K. Meagher, M. Medici, A. Medina, M. Meier, S. Meighen-Berger, T. Menne, G. Merino, T. Meures, J. Micallef, D. Mockler, G. Momenté, T. Montaruli, R. W. Moore, R. Morse, M. Moulai, P. Muth, R. Nagai, U. Naumann, G. Neer, H. Niederhausen, M. U. Nisa, S. C. Nowicki, D. R. Nygren, A. Obertacke Pollmann, M. Oehler, A. Olivas, A. O'Murchadha, E. O'Sullivan, T. Palczewski, H. Pandya, D. V. Pankova, N. Park, P. Peiffer, C. Pérez de los Heros, S. Philippen, D. Pieloth, E. Pinat, A. Pizzuto, M. Plum, A. Porcelli, P. B. Price, G. T. Przybylski, C. Raab, A. Raissi, M. Rameez, L. Rauch, K. Rawlins, I. C. Rea, R. Reimann, B. Relethford, M. Renschler, G. Renzi, E. Resconi, W. Rhode, M. Richman, S. Robertson, M. Rongen, C. Rott, T. Ruhe, D. Ryckbosch, D. Rysewyk, I. Safa, S. E. Sanchez Herrera, A. Sandrock, J. Sandroos, M. Santander, S. Sarkar, S. Sarkar, K. Satalecka, M. Schaufel, H. Schieler, P. Schlunder, T. Schmidt, A. Schneider, J. Schneider, F. G. Schröder, L. Schumacher, S. Sclafani, D. Seckel, S. Seunarine, S. Shefali, M. Silva, R. Snihur, J. Soedingrekso, D. Soldin, M. Song, G. M. Spiczak, C. Spiering, J. Stachurska, M. Stamatikos, T. Stanev, R. Stein, P. Steinmüller, J. Stettner, A. Steuer, T. Stezelberger, R. G. Stokstad, A. Stößl, N. L. Strotjohann, T. Stürwald, T. Stuttard, G. W. Sullivan, I. Taboada, F. Tenholt, S. Ter-Antonyan, A. Terliuk, S. Tilav, K. Tollefson, L. Tomankova, C. Tönnis, S. Toscano, D. Tosi, A. Trettin, M. Tselengidou, C. F. Tung, A. Turcati, R. Turcotte, C. F. Turley, B. Ty, E. Unger, M. A. Unland Elorrieta, M. Usner, J. Vandenbroucke, W. Van Driessche, D. van Eijk, N. van Eijndhoven, S. Vanheule, J. van Santen, M. Vraeghe, C. Walck, A. Wallace, M. Wallraff, N. Wandkowsky, T. B. Watson, C. Weaver, A. Weindl, M. J. Weiss, J. Weldert, C. Wendt, J. Werthebach, B. J. Whelan, N. Whitehorn, K. Wiebe, C. H. Wiebusch, L. Wille, D. R. Williams, L. Wills, M. Wolf, J. Wood, T. R. Wood, K. Woschnagg, G. Wrede, D. L. Xu, X. W. Xu, Y. Xu, J. P. Yanez, G. Yodh, S. Yoshida, T. Yuan, and M. Zöcklein. Time-integrated neutrino source searches with 10 years of icecube data. *Phys. Rev. Lett.*, 124:051103, Feb 2020.

- [245] Robert Stein et al. A tidal disruption event coincident with a high-energy neutrino. *Nature Astron.*, 5(5):510–518, 2021.
- [246] M. Ackermann, M. Ajello, A. Allafort, E. Antolini, W. B. Atwood, M. Axelsson, L. Baldini, J. Ballet, G. Barbiellini, D. Bastieri, K. Bechtol, R. Bellazzini, B. Berenji, R. D. Blandford, E. D. Bloom, E. Bonamente, A. W. Borgland, E. Bottacini, A. Bouvier, J. Bregeon, M. Brigida, P. Bruel, R. Buehler, T. H. Burnett, S. Buson, G. A. Caliandro, R. A. Cameron, P. A. Caraveo, J. M. Casandjian, E. Cavazzuti, C. Cecchi, E. Charles, C. C. Cheung, J. Chiang, S. Ciprini, R. Claus, J. Cohen-Tanugi, J. Conrad, L. Costamante, S. Cutini, A. de Angelis, F. de Palma, C. D. Dermer, S. W. Digel, E. do Couto e. Silva, P. S. Drell, R. Dubois, L. Escande, C. Favuzzi, S. J. Fegan, E. C. Ferrara, J. Finke, W. B.

Focke, P. Fortin, M. Frailis, Y. Fukazawa, S. Funk, P. Fusco, F. Gargano, D. Gasparrini, N. Gehrels, S. Germani, B. Giebels, N. Giglietto, P. Giommi, F. Giordano, M. Giroletti, T. Glanzman, G. Godfrey, I. A. Grenier, J. E. Grove, S. Guiriec, M. Gustafsson, D. Hadasch, M. Hayashida, E. Hays, S. E. Healey, D. Horan, X. Hou, R. E. Hughes, G. Iafrate, G. Jóhannesson, A. S. Johnson, W. N. Johnson, T. Kamae, H. Katagiri, J. Kataoka, J. Knöldlseder, M. Kuss, J. Lande, S. Larsson, L. Latronico, F. Longo, F. Loparco, B. Lott, M. N. Lovellette, P. Lubrano, G. M. Madejski, M. N. Mazziotta, W. McConville, J. E. McEnery, P. F. Michelson, W. Mitthumsiri, T. Mizuno, A. A. Moiseev, C. Monte, M. E. Monzani, E. Moretti, A. Morselli, I. V. Moskalenko, S. Murgia, T. Nakamori, M. Naumann-Godo, P. L. Nolan, J. P. Norris, E. Nuss, M. Ohno, T. Ohsugi, A. Okumura, N. Omodei, M. Orienti, E. Orlando, J. F. Ormes, M. Ozaki, D. Paneque, D. Parent, M. Pesce-Rollins, M. Pierbattista, S. Piranomonte, F. Piron, G. Pivato, T. A. Porter, S. Rainò, R. Rando, M. Razzano, S. Razzaque, A. Reimer, O. Reimer, S. Ritz, L. S. Rochester, R. W. Romani, M. Roth, D. A. Sanchez, C. Sbarra, J. D. Scargle, T. L. Schalk, C. Sgrò, M. S. Shaw, E. J. Siskind, G. Spandre, P. Spinelli, A. W. Strong, D. J. Suson, H. Tajima, H. Takahashi, T. Takahashi, T. Tanaka, J. G. Thayer, J. B. Thayer, D. J. Thompson, L. Tibaldo, M. Tinivella, D. F. Torres, G. Tosti, E. Troja, Y. Uchiyama, J. Vandebroucke, V. Vasileiou, G. Vianello, V. Vitale, A. P. Waite, E. Wallace, P. Wang, B. L. Winer, D. L. Wood, K. S. Wood, and S. Zimmer. The Second Catalog of Active Galactic Nuclei Detected by the Fermi Large Area Telescope. *Astrophysical Journal*, 743(2):171, December 2011.

- [247] G. Principe, D. Malyshev, J. Ballet, and S. Funk. The first catalog of Fermi-LAT sources below 100 MeV. *Astronomy & Astrophysics Journal*, 618:A22, October 2018.
- [248] M. G. Aartsen et al. The contribution of Fermi-2LAC blazars to the diffuse TeV-PeV neutrino flux. *Astrophys. J.*, 835(1):45, 2017.
- [249] R. Abbasi et al. Search for Astrophysical Neutrinos from 1FLE Blazars with IceCube. *Astrophys. J.*, 938(1):38, 2022.
- [250] Alexander Plavin, Yuri Y. Kovalev, Yuri A. Kovalev, and Sergey Troitsky. Observational Evidence for the Origin of High-energy Neutrinos in Parsec-scale Nuclei of Radio-bright Active Galaxies. *Astrophysical Journal*, 894(2):101, May 2020.
- [251] Sara Buson et al. Beginning a Journey Across the Universe: The Discovery of Extragalactic Neutrino Factories. *Astrophys. J. Lett.*, 933(2):L43, 2022. [Erratum: *Astrophys.J.Lett.* 934, L38 (2022), Erratum: *Astrophys.J.* 934, L38 (2022)].
- [252] M. Ackermann, M. Ajello, L. Baldini, J. Ballet, G. Barbiellini, D. Bastieri, R. Bellazzini, E. Bissaldi, R. D. Blandford, R. Bonino, E. Bottacini, J. Bregeon, P. Bruel, R. Buehler, E. Burns, S. Buson, R. A. Cameron, R. Caputo, P. A. Caraveo, E. Cavazzuti, S. Chen, G. Chiaro, S. Ciprini, D. Costantin, A. Cuoco, S. Cutini, F. D’Ammando, P. de la Torre Luque, F. de Palma, A. Desai, S. W. Digel, N. Di Lalla, M. Di Mauro, L. Di Venere, F. Fana Dirirsa, C. Favuzzi, A. Franckowiak, Y. Fukazawa, S. Funk, P. Fusco, F. Gargano, D. Gasparrini, N. Giglietto, F. Giordano, M. Giroletti, D. Green, I. A. Grenier, L. Guillenmot, S. Guiriec, D. Horan, G. Jóhannesson, M. Kuss, S. Larsson, L. Latronico, J. Li,

I. Liodakis, F. Longo, F. Loparco, P. Lubrano, J. D. Magill, S. Maldera, D. Malyshev, A. Manfreda, M. N. Mazziotta, I. Mereu, P. F. Michelson, W. Mitthumsiri, T. Mizuno, M. E. Monzani, A. Morselli, I. V. Moskalenko, M. Negro, E. Nuss, M. Orienti, E. Orlando, M. Palatiello, V. S. Paliya, D. Paneque, M. Persic, M. Pesce-Rollins, V. Petrosian, F. Piron, T. A. Porter, G. Principe, S. Rainò, R. Rando, M. Razzano, S. Razzaque, A. Reimer, O. Reimer, D. Serini, C. Sgrò, E. J. Siskind, G. Spandre, P. Spinelli, D. J. Suson, H. Tajima, M. Takahashi, J. B. Thayer, L. Tibaldo, D. F. Torres, E. Troja, T. M. Venter, G. Vianello, K. Wood, M. Yassine, G. Zaharijas, S. Ammazzalorso, N. Fornengo, M. Regis, and Fermi-LAT Collaboration. Unresolved Gamma-Ray Sky through its Angular Power Spectrum. *Physical Review Letters*, 121(24):241101, December 2018.

- [253] Silvia Manconi, Michael Korsmeier, Fiorenza Donato, Nicolao Fornengo, Marco Regis, and Hannes Zechlin. Testing gamma-ray models of blazars in the extragalactic sky. *Physical Review D*, 101(10):103026, May 2020.
- [254] Michael Korsmeier, Elena Pinetti, Michela Negro, Marco Regis, and Nicolao Fornengo. Flat-spectrum Radio Quasars and BL Lacs Dominate the Anisotropy of the Unresolved Gamma-Ray Background. *Astrophysical Journal*, 933(2):221, July 2022.
- [255] Tim Linden. Star-forming galaxies significantly contribute to the isotropic gamma-ray background. *Physical Review D*, 96(8):083001, October 2017.
- [256] M. Di Mauro, F. Calore, F. Donato, M. Ajello, and L. Latronico. Diffuse  $\gamma$ -Ray Emission from Misaligned Active Galactic Nuclei. *Astrophysical Journal*, 780(2):161, January 2014.
- [257] Ke Fang, John S. Gallagher, and Francis Halzen. The TeV Diffuse Cosmic Neutrino Spectrum and the Nature of Astrophysical Neutrino Sources. *Astrophysical Journal*, 933(2):190, July 2022.
- [258] W. B. Atwood et al. The large area telescope on the fermi gamma-ray space telescope mission. *The Astrophysical Journal*, 697(2):1071, 2009.
- [259] IceCube Collaboration, R. Abbasi, M. Ackermann, J. Adams, J. A. Aguilar, M. Ahlers, M. Ahrens, C. Alispach, N. M. Amin, K. Andeen, T. Anderson, I. Ansseau, G. Anton, C. Argüelles, S. Axani, X. Bai, A. Balagopal V., A. Barbano, S. W. Barwick, B. Bastian, V. Basu, V. Baum, S. Baur, R. Bay, J. J. Beatty, K. H. Becker, J. Becker Tjus, C. Bellenghi, S. BenZvi, D. Berley, E. Bernardini, D. Z. Besson, G. Binder, D. Bindig, E. Blaufuss, S. Blot, C. Bohm, S. Böser, O. Botner, J. Böttcher, E. Bourbeau, J. Bourbeau, F. Bradascio, J. Braun, S. Bron, J. Brostean-Kaiser, A. Burgman, J. Buscher, R. S. Busse, M. A. Campana, T. Carver, C. Chen, E. Cheung, D. Chirkin, S. Choi, B. A. Clark, K. Clark, L. Classen, A. Coleman, G. H. Collin, J. M. Conrad, P. Coppin, P. Correa, D. F. Cowen, R. Cross, P. Dave, C. De Clercq, J. J. DeLaunay, H. Dembinski, K. Deoskar, S. De Ridder, A. Desai, P. Desiati, K. D. de Vries, G. de Wasseige, M. de With, T. DeYoung, S. Dharamani, A. Diaz, J. C. Díaz-Vélez, H. Dujmovic, M. Dunkman, M. A. DuVernois, E. Dvorak, T. Ehrhardt, P. Eller, R. Engel, P. A. Evenson, S. Fahey, A. R. Fazely, J. Felde, A. T. Fienberg, K. Filimonov, C. Finley, L. Fischer, D. Fox, A. Franckowiak, E. Friedman, A. Fritz,

T. K. Gaisser, J. Gallagher, E. Ganster, S. Garrappa, L. Gerhardt, A. Ghadimi, T. Glauch, T. Glüsenkamp, A. Goldschmidt, J. G. Gonzalez, S. Goswami, D. Grant, T. Grégoire, Z. Griffith, S. Griswold, M. Gündüz, C. Haack, A. Hallgren, R. Halliday, L. Halve, F. Halzen, M. Ha Minh, K. Hanson, J. Hardin, A. Haungs, S. Hauser, D. Hebecker, P. Heix, K. Helbing, R. Hellauer, F. Henningsen, S. Hickford, J. Hignight, C. Hill, G. C. Hill, K. D. Hoffman, R. Hoffmann, T. Hoinka, B. Hokanson-Fasig, K. Hoshina, F. Huang, M. Huber, T. Huber, K. Hultqvist, M. Hünnefeld, R. Hussain, S. In, N. Iovine, A. Ishihara, M. Jansson, G. S. Japaridze, M. Jeong, B. J. P. Jones, F. Jonske, R. Joppe, D. Kang, W. Kang, X. Kang, A. Kappes, D. Kappesser, T. Karg, M. Karl, A. Karle, U. Katz, M. Kauer, M. Kellermann, J. L. Kelley, A. Kheirandish, J. Kim, K. Kin, T. Kintscher, J. Kiryluk, T. Kittler, S. R. Klein, R. Koirala, H. Kolanoski, L. Köpke, C. Kopper, S. Kopper, D. J. Koskinen, P. Koundal, M. Kovacevich, M. Kowalski, K. Krings, G. Krückl, N. Kulacz, N. Kurahashi, A. Kyriacou, C. Lagunas Gualda, J. L. Lanfranchi, M. J. Larson, F. Lauber, J. P. Lazar, K. Leonard, A. Leszczyńska, Y. Li, Q. R. Liu, E. Lohfink, C. J. Lozano Mariscal, L. Lu, F. Lucarelli, A. Ludwig, J. Lünemann, W. Luszczak, Y. Lyu, W. Y. Ma, J. Madsen, G. Maggi, K. B. M. Mahn, Y. Makino, P. Mallik, S. Mancina, I. C. Mariş, R. Maruyama, K. Mase, R. Maunu, F. McNally, K. Meagher, A. Medina, M. Meier, S. Meighen-Berger, J. Merz, J. Micallef, D. Mockler, G. Momenté, T. Montaruli, R. W. Moore, R. Morse, M. Moulai, P. Muth, R. Naab, R. Nagai, U. Naumann, J. Necker, G. Neer, L. V. Nguyêñ, H. Niederhausen, M. U. Nisa, S. C. Nowicki, D. R. Nygren, A. Obertacke Pollmann, M. Oehler, A. Olivas, E. O’Sullivan, H. Pandya, D. V. Pankova, N. Park, G. K. Parker, E. N. Paudel, P. Peiffer, C. Pérez de los Heros, S. Philippen, D. Pieloth, S. Pieper, A. Pizzuto, M. Plum, Y. Popovych, A. Porcelli, M. Prado Rodriguez, P. B. Price, G. T. Przybylski, C. Raab, A. Raissi, M. Rameez, K. Rawlins, I. C. Rea, A. Rehman, R. Reimann, M. Renschler, G. Renzi, E. Resconi, S. Reusch, W. Rhode, M. Richman, B. Riedel, S. Robertson, G. Roellinghoff, M. Rongen, C. Rott, T. Ruhe, D. Ryckbosch, D. Rysewyk Cantu, I. Safa, S. E. Sanchez Herrera, A. Sandrock, J. Sandroos, M. Santander, S. Sarkar, S. Sarkar, K. Satalecka, M. Scharf, M. Schaufel, H. Schieler, P. Schlunder, T. Schmidt, A. Schneider, J. Schneider, F. G. Schröder, L. Schumacher, S. Sclafani, D. Seckel, S. Seunarine, S. Shefali, M. Silva, B. Smithers, R. Snihur, J. Soedingrekso, D. Soldin, M. Song, G. M. Spiczak, C. Spiering, J. Stachurska, M. Stamatikos, T. Stanev, R. Stein, J. Stettner, A. Steuer, T. Stezelberger, R. G. Stokstad, N. L. Strotjohann, T. Stürwald, T. Stuttard, G. W. Sullivan, I. Taboada, F. Tenholt, S. Ter-Antonyan, S. Tilav, K. Tollefson, L. Tomankova, C. Tönnis, S. Toscano, D. Tosi, A. Trettin, M. Tselengidou, C. F. Tung, A. Turcati, R. Turcotte, C. F. Turley, J. P. Twagirayezu, B. Ty, E. Unger, M. A. Unland Elorrieta, J. Vandebroucke, D. van Eijk, N. van Eijndhoven, D. Vannerom, J. van Santen, S. Verpoest, M. Vraeghe, C. Walck, A. Wallace, T. B. Watson, C. Weaver, A. Weindl, M. J. Weiss, J. Weldert, C. Wendt, J. Werthebach, B. J. Whelan, N. Whitehorn, K. Wiebe, C. H. Wiebusch, D. R. Williams, M. Wolf, T. R. Wood, K. Woschnagg, G. Wrede, J. Wulff, X. W. Xu, Y. Xu, J. P. Yanez, S. Yoshida, T. Yuan, Z. Zhang, and M. Zöcklein. IceCube Data for Neutrino Point-Source Searches Years 2008-2018. [arXiv e-prints](#), page arXiv:2101.09836, January 2021.

- [260] P. J. E. Peebles. [The large-scale structure of the universe](#). Princeton University Press, 1980.

- [261] Jun-Qing Xia, Alessandro Cuoco, Enzo Branchini, Mattia Fornasa, and Matteo Viel. A cross-correlation study of the Fermi-LAT  $\gamma$ -ray diffuse extragalactic signal. *Mon.Not.Roy.Astron.Soc.*, 416:2247–2264, 2011.
- [262] A. Cuoco et al. Tomographic imaging of the Fermi-LAT gamma-ray sky through cross-correlations: A wider and deeper look. *Astrophys. J. Suppl.*, 232(10), 2017.
- [263] Simone Ammazzalorso, Nicolao Fornengo, Shunsaku Horiuchi, and Marco Regis. Characterizing the local gamma-ray Universe via angular cross-correlations. *Phys. Rev.*, D98(10):103007, 2018.
- [264] Enzo Branchini, Stefano Camera, Alessandro Cuoco, Nicolao Fornengo, Marco Regis, Matteo Viel, and Jun-Qing Xia. Cross-correlating the  $\gamma$ -ray sky with Catalogs of Galaxy Clusters. *Astrophys. J. Suppl.*, 228(1):8, 2017.
- [265] M. Lisanti, S. Mishra-Sharma, N. L. Rodd, and B. R. Safdi. A Search for Dark Matter Annihilation in Galaxy Groups. *ArXiv e-prints*, August 2017.
- [266] M. Lisanti, S. Mishra-Sharma, N. L. Rodd, B. R. Safdi, and R. H. Wechsler. Mapping Extragalactic Dark Matter Annihilation with Galaxy Surveys: A Systematic Study of Stacked Group Searches. *ArXiv e-prints*, September 2017.
- [267] Rachel Mandelbaum, Hironao Miyatake, Takashi Hamana, Masamune Oguri, Melanie Simet, Robert Armstrong, James Bosch, Ryoma Murata, François Lanusse, Alexie Leauthaud, Jean Coupon, Surhud More, Masahiro Takada, Satoshi Miyazaki, Joshua S Speagle, Masato Shirasaki, Cristóbal Sifón, Song Huang, Atsushi J Nishizawa, Elinor Medezinski, Yuki Okura, Nobuhiro Okabe, Nicole Czakon, Ryuichi Takahashi, William R Coulton, Chiaki Hikage, Yutaka Komiyama, Robert H Lupton, Michael A Strauss, Masayuki Tanaka, and Yousuke Utsumi. The first-year shear catalog of the Subaru Hyper Suprime-Cam Subaru Strategic Program Survey. *pasj*, 70:S25, January 2018.
- [268] Stefano Camera, Mattia Fornasa, Nicolao Fornengo, and Marco Regis. A Novel Approach in the Weakly Interacting Massive Particle Quest: Cross-correlation of Gamma-Ray Anisotropies and Cosmic Shear. *Astrophys.J.*, 771:L5, 2013.
- [269] S. Camera, M. Fornasa, N. Fornengo, and M. Regis. Tomographic-spectral approach for dark matter detection in the cross-correlation between cosmic shear and diffuse  $\gamma$ -ray emission. *JCAP*, 6:029, June 2015.
- [270] Masato Shirasaki, Shunsaku Horiuchi, and Naoki Yoshida. Cross-Correlation of Cosmic Shear and Extragalactic Gamma-ray Background: Constraints on the Dark Matter Annihilation Cross-Section. *Phys.Rev.*, D90:063502, 2014.
- [271] S. Ammazzalorso, D. Gruen, M. Regis, et al. Detection of Cross-Correlation between Gravitational Lensing and  $\gamma$  Rays. *Physical Review Letters*, 124(10):101102, March 2020.
- [272] Nicolao Fornengo, Laurence Perotto, Marco Regis, and Stefano Camera. Evidence of Cross-correlation between the CMB Lensing and the  $\Gamma$ -ray sky. *Astrophys. J.*, 802(1):L1, 2015.

- [273] Ke Fang, Arka Banerjee, Eric Charles, and Yuuki Omori. A Cross-Correlation Study of High-energy Neutrinos and Tracers of Large-Scale Structure. *Astrophys. J.*, 894(2):112, 2020.
- [274] M. G. Aartsen, R. Abbasi, M. Ackermann, J. Adams, J. A. Aguilar, M. Ahlers, M. Ahrens, C. Alispach, P. Allison, N. M. Amin, K. Andeen, T. Anderson, I. Ansseau, G. Anton, C. Argüelles, T. C. Arlen, J. Auffenberg, S. Axani, H. Bagherpour, X. Bai, A. Balagopal V, A. Barbano, I. Bartos, B. Bastian, V. Basu, V. Baum, S. Baur, R. Bay, J. J. Beatty, K. H. Becker, J. Becker Tjus, S. BenZvi, D. Berley, E. Bernardini, D. Z. Besson, G. Binder, D. Bindig, E. Blaufuss, S. Blot, C. Bohm, M. Bohmer, S. Böser, O. Botner, J. Böttcher, E. Bourbeau, J. Bourbeau, F. Bradascio, J. Braun, S. Bron, J. Brosteau-Kaiser, A. Burgman, R. T. Burley, J. Buscher, R. S. Busse, M. Bustamante, M. A. Campana, E. G. Carnie-Bronca, T. Carver, C. Chen, P. Chen, E. Cheung, D. Chirkin, S. Choi, B. A. Clark, K. Clark, L. Classen, A. Coleman, G. H. Collin, A. Connolly, J. M. Conrad, P. Coppin, P. Correa, D. F. Cowen, R. Cross, P. Dave, C. Deaconu, C. De Clercq, J. J. DeLaunay, S. De Kockere, H. Dembinski, K. Deoskar, S. De Ridder, A. Desai, P. Desiati, K. D. de Vries, G. de Wasseige, M. de With, T. DeYoung, S. Dharani, A. Diaz, J. C. Díaz-Vélez, H. Dujmovic, M. Dunkman, M. A. DuVernois, E. Dvorak, T. Ehrhardt, P. Eller, R. Engel, J. J. Evans, P. A. Evenson, S. Fahey, K. Farrag, A. R. Fazely, J. Felde, A. T. Fienberg, K. Filimonov, C. Finley, L. Fischer, D. Fox, A. Franckowiak, E. Friedman, A. Fritz, T. K. Gaisser, J. Gallagher, E. Ganster, D. Garcia-Fernandez, S. Garrappa, A. Gartner, L. Gerhard, R. Gernhaeuser, A. Ghadimi, C. Glaser, T. Glauch, T. Glüsenkamp, A. Goldschmidt, J. G. Gonzalez, S. Goswami, D. Grant, T. Grégoire, Z. Griffith, S. Griswold, M. Gündüz, C. Haack, A. Hallgren, R. Halliday, L. Halve, F. Halzen, J. C. Hanson, K. Hanson, J. Hardin, J. Haugen, A. Haungs, S. Hauser, D. Hebecker, D. Heinen, P. Heix, K. Helbing, R. Hellauer, F. Henningsen, S. Hickford, J. Hignight, C. Hill, G. C. Hill, K. D. Hoffman, B. Hoffmann, R. Hoffmann, T. Hoinka, B. Hokanson-Fasig, K. Holzapfel, K. Hoshina, F. Huang, M. Huber, T. Huber, T. Huege, K. Hughes, K. Hultqvist, M. Hünnefeld, R. Hussain, S. In, N. Iovine, A. Ishihara, M. Jansson, G. S. Japaridze, M. Jeong, B. J. P. Jones, F. Jonske, R. Joppe, O. Kalekin, D. Kang, W. Kang, X. Kang, A. Kappes, D. Kappesser, T. Karg, M. Karl, A. Karle, T. Katori, U. Katz, M. Kauer, A. Keivani, M. Kellermann, J. L. Kelley, A. Kheirandish, J. Kim, K. Kin, T. Kintscher, J. Kiryluk, T. Kittler, M. Kleifges, S. R. Klein, R. Koirala, H. Kolanoski, L. Köpke, C. Kopper, S. Kopper, D. J. Koskinen, P. Koundal, M. Kovacevich, M. Kowalski, C. B. Krauss, K. Krings, G. Krückl, N. Kulacz, N. Kurahashi, C. Lagunas Gualda, R. Lahmann, J. L. Lanfranchi, M. J. Larson, U. Latif, F. Lauber, J. P. Lazar, K. Leonard, A. Leszczyńska, Y. Li, Q. R. Liu, E. Lohfink, J. LoSecco, C. J. Lozano Mariscal, L. Lu, F. Lucarelli, A. Ludwig, J. Lünemann, W. Luszczak, Y. Lyu, W. Y. Ma, J. Madsen, G. Maggi, K. B. M. Mahn, Y. Makino, P. Mallik, S. Mancina, S. Mandalia, I. C. Mariş, S. Marka, Z. Marka, R. Maruyama, K. Mase, R. Maunu, F. McNally, K. Meagher, A. Medina, M. Meier, S. Meighen-Berger, J. Merz, Z. S. Meyers, J. Micallef, D. Mockler, G. Momenté, T. Montaruli, R. W. Moore, R. Morse, M. Moulay, P. Muth, R. Naab, R. Nagai, J. Nam, U. Nauman, J. Necker, G. Neer, A. Nelles, L. V. Nguyén, H. Niederhausen, M. U. Nisa, S. C. Nowicki, D. R. Nygren, E. Oberla, A. Obertacke Pollmann, M. Oehler, A. Olivas, E. O'Sullivan, Y. Pan, H. Pandya, D. V. Pankova, L. Papp, N. Park, G. K. Parker, E. N. Paudel, P. Peiffer,

C. Pérez de los Heros, T. C. Petersen, S. Philippen, D. Pieloth, S. Pieper, J. L. Pinfold, A. Pizzuto, I. Plaisier, M. Plum, Y. Popovych, A. Porcelli, M. Prado Rodriguez, P. B. Price, G. T. Przybylski, C. Raab, A. Raissi, M. Rameez, L. Rauch, K. Rawlins, I. C. Rea, A. Rehman, R. Reimann, M. Renschler, G. Renzi, E. Resconi, S. Reusch, W. Rhode, M. Richman, B. Riedel, M. Riegel, E. J. Roberts, S. Robertson, G. Roellinghoff, M. Ronnen, C. Rott, T. Ruhe, D. Ryckbosch, D. Rysewyk Cantu, I. Safa, S. E. Sanchez Herrera, A. Sandrock, J. Sandroos, P. Sandstrom, M. Santander, S. Sarkar, S. Sarkar, K. Satalecka, M. Scharf, M. Schaufel, H. Schieler, P. Schlunder, T. Schmidt, A. Schneider, J. Schneider, F. G. Schröder, L. Schumacher, S. Sclafani, D. Seckel, S. Seunarine, M. H. Shaevitz, A. Sharma, S. Shefali, M. Silva, D. Smith, B. Smithers, R. Snihur, J. Soedingrekso, D. Soldin, S. Söldner-Rembold, M. Song, D. Southall, G. M. Spiczak, C. Spiering, J. Stachurska, M. Stamatikos, T. Stanev, R. Stein, J. Stettner, A. Steuer, T. Stezelberger, R. G. Stokstad, N. L. Strotjohann, T. Stürwald, T. Stuttard, G. W. Sullivan, I. Taboada, A. Taketa, H. K. M. Tanaka, F. Tenholt, S. Ter-Antonyan, A. Terliuk, S. Tilav, K. Tollefson, L. Tomankova, C. Tönnis, J. Torres, S. Toscano, D. Tosi, A. Trettin, M. Tselengidou, C. F. Tung, A. Turcati, R. Turcotte, C. F. Turley, J. P. Twagirayezu, B. Ty, E. Unger, M. A. Unland Elorrieta, J. Vandenbroucke, D. van Eijk, N. van Eijndhoven, D. Vannerom, J. van Santen, D. Verberic, S. Verpoest, A. Vieregg, M. Vraeghe, C. Walck, T. B. Watson, C. Weaver, A. Weindl, L. Weinstock, M. J. Weiss, J. Weldert, C. Welling, C. Wendt, J. Werthebach, N. Whitehorn, K. Wiebe, C. H. Wiebusch, D. R. Williams, S. A. Wissel, M. Wolf, T. R. Wood, K. Woschnagg, G. Wrede, S. Wren, J. Wulff, X. W. Xu, Y. Xu, J. P. Yanez, S. Yoshida, T. Yuan, Z. Zhang, S. Zierke, and M. Zöcklein. IceCube-Gen2: the window to the extreme Universe. *Journal of Physics G Nuclear Physics*, 48(6):060501, June 2021.

- [275] Andrea Zonca, Leo Singer, Daniel Lenz, Martin Reinecke, Cyrille Rosset, Eric Hivon, and Krzysztof Gorski. healpy: equal area pixelization and spherical harmonics transforms for data on the sphere in python. *Journal of Open Source Software*, 4(35):1298, March 2019.
- [276] K. M. Górski, E. Hivon, A. J. Banday, B. D. Wandelt, F. K. Hansen, M. Reinecke, and M. Bartelmann. HEALPix: A Framework for High-Resolution Discretization and Fast Analysis of Data Distributed on the Sphere. *Astrophysical Journal*, 622:759–771, April 2005.
- [277] I. Szapudi, S. Prunet, D. Pogosyan, A. S. Szalay, and J. R. Bond. Fast Cosmic Microwave Background Analyses via Correlation Functions. *Astrophys.J.Lett.*, 548:L115–L118, February 2001.
- [278] G. Chon, A. Challinor, S. Prunet, E. Hivon, and I. Szapudi. Fast estimation of polarization power spectra using correlation functions. *Mon. Not. Roy. Astron. Soc.*, 350:914–926, May 2004.
- [279] G. Efstathiou. Myths and truths concerning estimation of power spectra: the case for a hybrid estimator. *Mon. Not. Roy. Astron. Soc.*, 349:603–626, April 2004.
- [280] A. Challinor and G. Chon. Error analysis of quadratic power spectrum estimates for cosmic microwave background polarization: sampling covariance. *Mon. Not. Roy. Astron. Soc.*, 360:509–532, June 2005.

- [281] M. Ackermann, M. Ajello, A. Albert, et al. The spectrum of isotropic diffuse gamma-ray emission between 100 MeV and 820 GeV. *Astrophys.J.*, 799(1):86, 2015.
- [282] M. Fornasa, A. Cuoco, J. Zavala, J. M. Gaskins, M. A. Sánchez-Conde, G. Gomez-Vargas, E. Komatsu, T. Linden, F. Prada, F. Zandanel, and A. Morselli. Angular power spectrum of the diffuse gamma-ray emission as measured by the Fermi Large Area Telescope and constraints on its dark matter interpretation. *Physical Review D*, 94(12):123005, December 2016.
- [283] A. Cooray and R. Sheth. Halo models of large scale structure. *Phys.Rep.*, 372:1–129, December 2002.
- [284] M. G. Aartsen, M. Ackermann, J. Adams, J. A. Aguilar, M. Ahlers, M. Ahrens, C. Alispach, K. Andeen, T. Anderson, I. Ansseau, G. Anton, C. Argüelles, J. Auffenberg, S. Axani, P. Backes, H. Bagherpour, X. Bai, A. Balagopal, A. Barbano, S. W. Barwick, B. Bastian, V. Baum, S. Baur, R. Bay, J. J. Beatty, K. H. Becker, J. Becker Tjus, S. BenZvi, D. Berley, E. Bernardini, D. Z. Besson, G. Binder, D. Bindig, E. Blaufuss, S. Blot, C. Bohm, M. Börner, S. Böser, O. Botner, J. Böttcher, E. Bourbeau, J. Bourbeau, F. Bradascio, J. Braun, S. Bron, J. Brostean-Kaiser, A. Burgman, J. Buscher, R. S. Busse, T. Carver, C. Chen, E. Cheung, D. Chirkin, S. Choi, K. Clark, L. Classen, A. Coleman, G. H. Collin, J. M. Conrad, P. Coppin, P. Correa, D. F. Cowen, R. Cross, P. Dave, C. De Clercq, J. J. DeLaunay, H. Dembinski, K. Deoskar, S. De Ridder, P. Desiati, K. D. de Vries, G. de Wasseige, M. de With, T. DeYoung, A. Diaz, J. C. Díaz-Vélez, H. Dujmovic, M. Dunkman, E. Dvorak, B. Eberhardt, T. Ehrhardt, P. Eller, R. Engel, P. A. Evenson, S. Fahey, A. R. Fazely, J. Felde, K. Filimonov, C. Finley, D. Fox, A. Franckowiak, E. Friedman, A. Fritz, T. K. Gaisser, J. Gallagher, E. Ganster, S. Garrappa, L. Gerhardt, K. Ghorbani, T. Glauch, T. Glüsenkamp, A. Goldschmidt, J. G. Gonzalez, D. Grant, Z. Griffith, S. Griswold, M. Günder, M. Gündüz, C. Haack, A. Hallgren, R. Halliday, L. Halve, F. Halzen, K. Hanson, A. Haungs, D. Hebecker, D. Heereman, P. Heix, K. Helbing, R. Hellauer, F. Henningsen, S. Hickford, J. Hignight, G. C. Hill, K. D. Hoffman, R. Hoffmann, T. Hoinka, B. Hokanson-Fasig, K. Hoshina, F. Huang, M. Huber, T. Huber, K. Hultqvist, M. Hünenfeld, R. Hussain, S. In, N. Iovine, A. Ishihara, G. S. Japaridze, M. Jeong, K. Jero, B. J. P. Jones, F. Jonske, R. Joppe, D. Kang, W. Kang, A. Kappes, D. Kappesser, T. Karg, M. Karl, A. Karle, U. Katz, M. Kauer, J. L. Kelley, A. Kheirandish, J. Kim, T. Kintscher, J. Kiryluk, T. Kittler, S. R. Klein, R. Koirlala, H. Kolanoski, L. Köpke, C. Kopper, S. Kopper, D. J. Koskinen, M. Kowalski, K. Krings, G. Krückl, N. Kulacz, N. Kurahashi, A. Kyriacou, M. Labare, J. L. Lanfranchi, M. J. Larson, F. Lauber, J. P. Lazar, K. Leonard, A. Leszczyńska, M. Leuermann, Q. R. Liu, E. Lohfink, C. J. Lozano Mariscal, L. Lu, F. Lucarelli, J. Lünemann, W. Luszczak, Y. Lyu, W. Y. Ma, J. Madsen, G. Maggi, K. B. M. Mahn, Y. Makino, P. Mallik, K. Mallot, S. Mancina, I. C. Mariş, R. Maruyama, K. Mase, H. S. Matis, R. Maunu, F. McNally, K. Meagher, M. Medici, A. Medina, M. Meier, S. Meighen-Berger, T. Menne, G. Merino, T. Meures, J. Micallef, D. Mockler, G. Momenté, T. Montaruli, R. W. Moore, R. Morse, M. Moulai, P. Muth, R. Nagai, U. Naumann, G. Neer, H. Niederhausen, M. U. Nisa, S. C. Nowicki, D. R. Nygren, A. Obertacke Pollmann, M. Oehler, A. Olivas, A. O’Murchadha, E. O’Sullivan, T. Palczewski, H. Pandya, D. V. Pankova, N. Park, P. Peiffer, C. Pérez de los Heros,

S. Philippen, D. Pieloth, E. Pinat, A. Pizzuto, M. Plum, A. Porcelli, P. B. Price, G. T. Przybylski, C. Raab, A. Raissi, M. Rameez, L. Rauch, K. Rawlins, I. C. Rea, R. Reimann, B. Relethford, M. Renschler, G. Renzi, E. Resconi, W. Rhode, M. Richman, S. Robertson, M. Rongen, C. Rott, T. Ruhe, D. Ryckbosch, D. Rysewyk, I. Safa, S. E. Sanchez Herrera, A. Sandrock, J. Sandroos, M. Santander, S. Sarkar, S. Sarkar, K. Satalecka, M. Schaufel, H. Schieler, P. Schlunder, T. Schmidt, A. Schneider, J. Schneider, F. G. Schröder, L. Schumacher, S. Sclafani, D. Seckel, S. Seunarine, S. Shefali, M. Silva, R. Snihur, J. Soedinguerekso, D. Soldin, M. Song, G. M. Spiczak, C. Spiering, J. Stachurska, M. Stamatikos, T. Staney, R. Stein, P. Steinmüller, J. Stettner, A. Steuer, T. Stezelberger, R. G. Stokstad, A. Stößl, N. L. Strotjohann, T. Stürwald, T. Stuttard, G. W. Sullivan, I. Taboada, F. Tenholt, S. Ter-Antonyan, A. Terliuk, S. Tilav, K. Tollefson, L. Tomankova, C. Tönnis, S. Toscano, D. Tosi, A. Trettin, M. Tselengidou, C. F. Tung, A. Turcati, R. Turcotte, C. F. Turley, B. Ty, E. Unger, M. A. Unland Elorrieta, M. Usner, J. Vandembroucke, W. Van Driessche, D. van Eijk, N. van Eijndhoven, S. Vanheule, J. van Santen, M. Vraeghe, C. Walck, A. Wallace, M. Wallraff, N. Wandkowsky, T. B. Watson, C. Weaver, A. Weindl, M. J. Weiss, J. Weldert, C. Wendt, J. Werthebach, B. J. Whelan, N. Whitehorn, K. Wiebe, C. H. Wiebusch, L. Wille, D. R. Williams, L. Wills, M. Wolf, J. Wood, T. R. Wood, K. Woschnagg, G. Wrede, D. L. Xu, X. W. Xu, Y. Xu, J. P. Yanez, G. Yodh, S. Yoshida, T. Yuan, and M. Zöcklein. Time-Integrated Neutrino Source Searches with 10 Years of IceCube Data. *Physical Review Letters*, 124(5):051103, February 2020.

- [285] R. Abbasi, M. Ackermann, J. Adams, J. A. Aguilar, M. Ahlers, M. Ahrens, J. M. Alameddine, C. Alispach, Jr. Alves, A. A., N. M. Amin, K. Andeen, T. Anderson, G. Anton, C. Argüelles, Y. Ashida, S. Axani, X. Bai, A. Balagopal V., A. Barbano, S. W. Barwick, B. Bastian, V. Basu, S. Baur, R. Bay, J. J. Beatty, K. H. Becker, J. Becker Tjus, C. Bellenghi, S. BenZvi, D. Berley, E. Bernardini, D. Z. Besson, G. Binder, D. Bindig, E. Blaufuss, S. Blot, M. Boddenberg, F. Bontempo, J. Borowka, S. Böser, O. Botner, J. Böttcher, E. Bourbeau, F. Bradascio, J. Braun, B. Brinson, S. Bron, J. Brostean-Kaiser, S. Browne, A. Burgman, R. T. Burley, R. S. Busse, M. A. Campana, E. G. Carnie-Bronca, C. Chen, Z. Chen, D. Chirkin, K. Choi, B. A. Clark, K. Clark, L. Classen, A. Coleman, G. H. Collin, J. M. Conrad, P. Coppin, P. Correa, D. F. Cowen, R. Cross, C. Dappen, P. Dave, C. De Clercq, J. J. DeLaunay, D. Delgado López, H. Dembinski, K. Deoskar, A. Desai, P. Desiati, K. D. de Vries, G. de Wasseige, M. de With, T. DeYoung, A. Diaz, J. C. Díaz-Vélez, M. Dittmer, H. Dujmovic, M. Dunkman, M. A. DuVernois, E. Dvorak, T. Ehrhardt, P. Eller, R. Engel, H. Erpenbeck, J. Evans, P. A. Evenson, K. L. Fan, A. R. Fazely, N. Feigl, S. Fiedlschuster, A. T. Fienberg, K. Filimonov, C. Finley, L. Fischer, D. Fox, A. Franckowiak, E. Friedman, A. Fritz, P. Fürst, T. K. Gaisser, J. Gallagher, E. Ganster, A. Garcia, S. Garrappa, L. Gerhardt, A. Ghadimi, C. Glaser, T. Glauch, T. Glüsenkamp, J. G. Gonzalez, S. Goswami, D. Grant, T. Grégoire, S. Griswold, C. Günther, P. Gutjahr, C. Haack, A. Hallgren, R. Halliday, L. Halve, F. Halzen, M. Ha Minh, K. Hanson, J. Hardin, A. A. Harnisch, A. Haungs, D. Hebecker, K. Helbing, F. Henningsen, E. C. Hettinger, S. Hickford, J. Hignight, C. Hill, G. C. Hill, K. D. Hoffman, R. Hoffmann, B. Hokanson-Fasig, K. Hoshina, F. Huang, M. Huber, T. Huber, K. Hultqvist, M. Hünnefeld, R. Hussain, K. Hyman, S. In, N. Iovine, A. Ishihara, M. Jansson, G. S. Japaridze, M. Jeong, M. Jin, B. J. P. Jones, D. Kang, W. Kang, X. Kang, A. Kappes, D. Kappesser, L. Kardum, T. Karg,

M. Karl, A. Karle, U. Katz, M. Kauer, M. Kellermann, J. L. Kelley, A. Kheirandish, K. Kin, T. Kintscher, J. Kiryluk, S. R. Klein, R. Koerala, H. Kolanoski, T. Kontrimas, L. Köpke, C. Kopper, S. Kopper, D. J. Koskinen, P. Koundal, M. Kovacevich, M. Kowalski, T. Kozynets, E. Kun, N. Kurahashi, N. Lad, C. Lagunas Gualda, J. L. Lanfranchi, M. J. Larson, F. Lauber, J. P. Lazar, J. W. Lee, K. Leonard, A. Leszczyńska, Y. Li, M. Linetto, Q. R. Liu, M. Liubarska, E. Lohfink, C. J. Lozano Mariscal, L. Lu, F. Lucarelli, A. Ludwig, W. Luszczak, Y. Lyu, W. Y. Ma, J. Madsen, K. B. M. Mahn, Y. Makino, S. Mancina, I. C. Mariş, I. Martinez-Soler, R. Maruyama, K. Mase, T. McElroy, F. McNally, J. V. Mead, K. Meagher, S. Mechbal, A. Medina, M. Meier, S. Meighen-Berger, J. Micallef, D. Mockler, T. Montaruli, R. W. Moore, R. Morse, M. Moulai, R. Naab, R. Nagai, U. Naumann, J. Necker, L. V. Nguyẽn, H. Niederhausen, M. U. Nisa, S. C. Nowicki, A. Obertacke Pollmann, M. Oehler, B. Oeyen, A. Olivas, E. O'Sullivan, H. Pandya, D. V. Pankova, N. Park, G. K. Parker, E. N. Paudel, L. Paul, C. Pérez de los Heros, L. Peters, J. Peterson, S. Philippen, S. Pieper, M. Pittermann, A. Pizzuto, M. Plum, Y. Popovych, A. Porcelli, M. Prado Rodriguez, P. B. Price, B. Pries, G. T. Przybylski, C. Raab, A. Raissi, M. Rameez, K. Rawlins, I. C. Rea, A. Rehman, P. Reichherzer, R. Reimann, G. Renzi, E. Resconi, S. Reusch, W. Rhode, M. Richman, B. Riedel, E. J. Roberts, S. Robertson, G. Roellinghoff, M. Rongen, C. Rott, T. Ruhe, D. Ryckbosch, D. Rysewyk Cantu, I. Safa, J. Saffer, S. E. Sanchez Herrera, A. Sandrock, J. Sandroos, M. Santander, S. Sarkar, S. Sarkar, K. Satalecka, M. Schaufel, H. Schieler, S. Schindler, T. Schmidt, A. Schneider, J. Schneider, F. G. Schröder, L. Schumacher, G. Schwefer, S. Sclafani, D. Seckel, S. Seunarine, A. Sharma, S. Shefali, M. Silva, B. Skrzypek, B. Smithers, R. Snihur, J. Soedingrekso, D. Soldin, C. Spannfellner, G. M. Spiczak, C. Spiering, J. Stachurska, M. Stamatikos, T. Stanev, R. Stein, J. Stettner, A. Steuer, T. Stezelberger, T. Stürwald, T. Stuttard, G. W. Sullivan, I. Taboada, S. Ter-Antonyan, S. Tilav, F. Tischbein, K. Tollefson, C. Tönnis, S. Toscano, D. Tosi, A. Trettin, M. Tselengidou, C. F. Tung, A. Turcati, R. Turcotte, C. F. Turley, J. P. Twagirayezu, B. Ty, M. A. Unland Elorrieta, N. Valtonen-Mattila, J. Vandebroucke, N. van Eijndhoven, D. Vannerom, J. van Santen, S. Verpoest, C. Walck, T. B. Watson, C. Weaver, P. Weigel, A. Weindl, M. J. Weiss, J. Weldert, C. Wendt, J. Werthebach, M. Weyrauch, N. Whitehorn, C. H. Wiebusch, D. R. Williams, M. Wolf, K. Woschnagg, G. Wrede, J. Wulff, X. W. Xu, J. P. Yanez, S. Yoshida, S. Yu, T. Yuan, Z. Zhang, P. Zhelnin, and IceCube Collaboration. Improved Characterization of the Astrophysical Muon-neutrino Flux with 9.5 Years of IceCube Data. *Astrophysical Journal*, 928(1):50, March 2022.

- [286] J. Stettner et al. Measurement of the diffuse astrophysical muon-neutrino spectrum with ten years of IceCube data. In *36th International Cosmic Ray Conference (ICRC2019)*, volume 36 of *International Cosmic Ray Conference*, page 1017, July 2019.
- [287] L. Marcotulli, M. Di Mauro, and M. Ajello. Source-count Distribution of Gamma-Ray Blazars. *Astrophysical Journal*, 896(1):6, June 2020.
- [288] M. Ajello, D. Gasparrini, M. Sánchez-Conde, G. Zaharijas, M. Gustafsson, et al. The Origin of the Extragalactic Gamma-Ray Background and Implications for Dark-Matter Annihilation. *Astrophysical Journal Letters*, 800(2):L27, 2015.

- [289] M. Ajello, W. B. Atwood, L. Baldini, J. Ballet, G. Barbiellini, D. Bastieri, R. Bellazzini, E. Bissaldi, R. D. Blandford, E. D. Bloom, R. Bonino, J. Bregeon, R. J. Britto, P. Bruel, R. Buehler, S. Buson, R. A. Cameron, R. Caputo, M. Caragiulo, P. A. Caraveo, E. Cavazzuti, C. Cecchi, E. Charles, A. Chekhtman, C. C. Cheung, G. Chiaro, S. Ciprini, J. M. Cohen, D. Costantin, F. Costanza, A. Cuoco, S. Cutini, F. D’Ammando, F. de Palma, R. Desiante, S. W. Digel, N. Di Lalla, M. Di Mauro, L. Di Venere, A. Domínguez, P. S. Drell, D. Dumora, C. Favuzzi, S. J. Fegan, E. C. Ferrara, P. Fortin, A. Franckowiak, Y. Fukazawa, S. Funk, P. Fusco, F. Gargano, D. Gasparrini, N. Giglietto, P. Giommi, F. Giordano, M. Giroletti, T. Glanzman, D. Green, I. A. Grenier, M. H. Grondin, J. E. Grove, L. Guillenmot, S. Guiriec, A. K. Harding, E. Hays, J. W. Hewitt, D. Horan, G. Jóhannesson, S. Ken-sei, M. Kuss, G. La Mura, S. Larsson, L. Latronico, M. Lemoine-Goumard, J. Li, F. Longo, F. Loparco, B. Lott, P. Lubrano, J. D. Magill, S. Maldera, A. Manfreda, M. N. Mazziotta, J. E. McEnery, M. Meyer, P. F. Michelson, N. Mirabal, W. Mitthumsiri, T. Mizuno, A. A. Moiseev, M. E. Monzani, A. Morselli, I. V. Moskalenko, M. Negro, E. Nuss, T. Ohsugi, N. Omodei, M. Orienti, E. Orlando, M. Palatiello, V. S. Paliya, D. Panque, J. S. Perkins, M. Persic, M. Pesce-Rollins, F. Piron, T. A. Porter, G. Principe, S. Rainò, R. Rando, M. Razzano, S. Razzaque, A. Reimer, O. Reimer, T. Reposeur, P. M. Saz Parkinson, C. Sgrò, D. Simone, E. J. Siskind, F. Spada, G. Spandre, P. Spinelli, L. Stawarz, D. J. Suson, M. Takahashi, D. Tak, J. G. Thayer, J. B. Thayer, D. J. Thompson, D. F. Torres, E. Torresi, E. Troja, G. Vianello, K. Wood, and M. Wood. 3FHL: The Third Catalog of Hard Fermi-LAT Sources. *Astrophysical Journal Supplement*, 232(2):18, October 2017.
- [290] Ke Fang and Kohta Murase. Multimessenger Implications of Sub-PeV Diffuse Galactic Gamma-Ray Emission. *Astrophysical Journal*, 919(2):93, October 2021.
- [291] S. S. Wilks. The large-sample distribution of the likelihood ratio for testing composite hypotheses. *Ann.Math.Statist.*, 9:60–62, 1938.
- [292] R. Caputo, C. Prescod-Weinstein, C. Kierans, M. Crnogorčević, S. McDermott, R. Leane, Z. Wadiasingh, T. Jeltema, J. Tomsick, and Y. Tsai. Light Dark Matter Candidates with MeV gamma-ray signatures. *Snowmass2021*, 122, 2020.
- [293] Yang Bai, Sida Lu, and Nicholas Orloffsky. Dark Exoplanets. 3 2023.
- [294] Damiano F. G. Fiorillo and Fabio Iocco. Axions from Neutron Star Mergers. *Phys. Rev. D*, 105:12, 2022.
- [295] T. Dietrich and K. Clough. Cooling binary neutron star remnants via nucleon-nucleon-axion bremsstrahlung. *Phys. Rev. D*, 100(8):083005, 2019.
- [296] A. Hook and J. Huang. Probing axions with neutron star inspirals and other stellar processes. *JHEP*, 06:036, 2018.
- [297] M. Lucca and L. Sagunski. The lifetime of binary neutron star merger remnants. *Journal of High Energy Astrophysics*, 27:33–37, 2020.
- [298] R. Gill, A. Nathanail, and L. Rezzolla. When Did the Remnant of GW170817 Collapse to a Black Hole? *Astrophys. J.*, 876(2):139, 2019.

- [299] Cecilia Chirenti, Simone Dichiara, Amy Lien, M. Coleman Miller, and Robert Preece. Kilohertz quasiperiodic oscillations in short gamma-ray bursts. *Nature*, 613(7943):253–256, January 2023.
- [300] Pauli Virtanen, Ralf Gommers, Travis E. Oliphant, Matt Haberland, Tyler Reddy, David Cournapeau, Evgeni Burovski, Pearu Peterson, Warren Weckesser, Jonathan Bright, Stéfan J. van der Walt, Matthew Brett, Joshua Wilson, K. Jarrod Millman, Nikolay Mayorov, Andrew R. J. Nelson, Eric Jones, Robert Kern, Eric Larson, C J Carey, İlhan Polat, Yu Feng, Eric W. Moore, Jake VanderPlas, Denis Laxalde, Josef Perktold, Robert Cimrman, Ian Henriksen, E. A. Quintero, Charles R. Harris, Anne M. Archibald, Antônio H. Ribeiro, Fabian Pedregosa, Paul van Mulbregt, and SciPy 1.0 Contributors. SciPy 1.0: Fundamental Algorithms for Scientific Computing in Python. *Nature Methods*, 17:261–272, 2020.
- [301] Anaconda software distribution, 2020.
- [302] Astropy Collaboration, Adrian M. Price-Whelan, Pey Lian Lim, Nicholas Earl, Nathaniel Starkman, Larry Bradley, David L. Shupe, Aarya A. Patil, Lia Corrales, C. E. Brasseur, Maximilian Nöthe, Axel Donath, Erik Tollerud, Brett M. Morris, Adam Ginsburg, Eero Vaher, Benjamin A. Weaver, James Tocknell, William Jamieson, Marten H. van Kerwijk, Thomas P. Robitaille, Bruce Merry, Matteo Bachetti, H. Moritz Günther, Thomas L. Aldcroft, Jaime A. Alvarado-Montes, Anne M. Archibald, Attila Bódi, Shreyas Bapat, Geert Barentsen, Juanjo Bazán, Manish Biswas, Médéric Boquien, D. J. Burke, Daria Cara, Mi-hai Cara, Kyle E. Conroy, Simon Conseil, Matthew W. Craig, Robert M. Cross, Kelle L. Cruz, Francesco D’Eugenio, Nadia Dencheva, Hadrien A. R. Devillepoix, Jörg P. Dietrich, Arthur Davis Eigenbrot, Thomas Erben, Leonardo Ferreira, Daniel Foreman-Mackey, Ryan Fox, Nabil Freij, Suyog Garg, Robel Geda, Lauren Glattly, Yash Gondhalekar, Karl D. Gordon, David Grant, Perry Greenfield, Austen M. Groener, Steve Guest, Sebastian Gurovich, Rasmus Handberg, Akeem Hart, Zac Hatfield-Dodds, Derek Homeier, Griffin Hosseinzadeh, Tim Jenness, Craig K. Jones, Prajwel Joseph, J. Bryce Kalmbach, Emir Karamehmetoglu, Mikołaj Kałuszyński, Michael S. P. Kelley, Nicholas Kern, Wolfgang E. Kerzendorf, Eric W. Koch, Shankar Kulumani, Antony Lee, Chun Ly, Zhiyuan Ma, Conor MacBride, Jakob M. Maljaars, Demitri Muna, N. A. Murphy, Henrik Norman, Richard O’Steen, Kyle A. Oman, Camilla Pacifici, Sergio Pascual, J. Pascual-Granado, Rohit R. Patil, Gabriel I. Perren, Timothy E. Pickering, Tanuj Rastogi, Benjamin R. Roulston, Daniel F. Ryan, Eli S. Rykoff, Jose Sabater, Parikshit Sakurikar, Jesús Salgado, Aniket Sanghi, Nicholas Saunders, Volodymyr Savchenko, Ludwig Schwardt, Michael Seifert-Eckert, Albert Y. Shih, Anany Shrey Jain, Gyanendra Shukla, Jonathan Sick, Chris Simpson, Sudheesh Singanamalla, Leo P. Singer, Jaladh Singhal, Manodeep Sinha, Brigitta M. Sipőcz, Lee R. Spitler, David Stansby, Ole Streicher, Jani Šumak, John D. Swinbank, Dan S. Taranu, Nikita Tewary, Grant R. Tremblay, Miguel de Val-Borro, Samuel J. Van Kooten, Zlatan Vasović, Shresth Verma, José Vinícius de Miranda Cardoso, Peter K. G. Williams, Tom J. Wilson, Benjamin Winkel, W. M. Wood-Vasey, Rui Xue, Peter Yoachim, Chen Zhang, Andrea Zonca, and Astropy Project Contributors. The Astropy Project: Sustaining and Growing a Community-oriented Open-source Project and the Latest Major Release (v5.0) of the Core Package. *Astrophysical Journal*, 935(2):167, August 2022.

- [303] GitHub Inc. Atom, 2021.
- [304] Ciaran O'Hare. cajohare/axionlimits: Axionlimits. <https://cajohare.github.io/AxionLimits/>, July 2020.
- [305] Manuel Meyer, James Davies, and Julian Kuhlmann. gammaALPs: An open-source python package for computing photon-axion-like-particle oscillations in astrophysical environments. PoS, ICRC2021:557, 2021.
- [306] Manuel Meyer. me-manu/gmf. <https://github.com/me-manu/gmf/>, 2016.
- [307] Grammarly Inc. Grammarly. <https://www.grammarly.com>, Accessed 9 April 2023.
- [308] K. M. Górski, E. Hivon, A. J. Banday, B. D. Wandelt, F. K. Hansen, M. Reinecke, and M. Bartelmann. HEALPix – a framework for high-resolution discretization and fast analysis of data distributed on the sphere, 2020.
- [309] Andrea Zonca and Krzysztof M. Górski. healpy: High-resolution healpix-based analysis, 2021.
- [310] M. Wood, T. Jogler, and E. Charles. Fermipy: An open-source python package for analysis of fermi-lat data, 2021.
- [311] Fermi-LAT Collaboration. Fermi science tools, 2022.
- [312] Project Jupyter. Jupyter: A multi-language interactive computing environment, 2018.
- [313] John D. Hunter. Matplotlib: A 2d graphics environment, 2022.
- [314] Stéfan van der Walt, S. Chris Colbert, and Gaël Varoquaux. NumPy: A fundamental package for scientific computing with python, 2021.
- [315] Wes McKinney et al. Pandas: Powerful data analysis tools for python, 2021.
- [316] Gayoung Chon and Anthony Challinor. PolSpice: A software package for analyzing cosmic microwave background polarization, 2019.
- [317] Savage Interactive. Procreate, 2021.
- [318] Andreas Zoglauer et al. PyXspec: Python interface to the x-ray spectral fitting package (xspec), 2022.
- [319] Pauli Virtanen, Ralf Gommers, Travis E. Oliphant, et al. SciPy: Open-source scientific tools for python, 2021.
- [320] Tim Schnitzler et al. TeXstudio: A fully featured latex editor, 2021.
- [321] Giacomo Vianello et al. ThreeML: A modern framework for the analysis of multi-wavelength data, 2021.
- [322] Zotero. Zotero, 2021.